FDR4LDYN
Fiducial Data Record for Land Dynamic

ESA RFP/3-18440/24/I-DT-I

ESCAT Quality Assessment, Quality Control, and ASCAT Interoperability Report

DT1-1

Revision History

Revision	Date	Author(s)	Description
0.1	23 October 2024	TU Wien	First complete version
1.0	7 March 2025	TU Wien	Update after creating first preliminary FDR4LDYN data record v0.1

How to cite this document

ESA, *ESCAT Quality Assessment, Quality Control, and ASCAT Interoperability Report*, v1.0, 2024

Table of Contents

1. Quality assessment of of ERS-1 and ERS-2 ESCAT data 4
- 1.1. Data characteristics 4
- 1.2. Pre-processing 9
- 1.3. Data quality flags 10
- 1.4. Spatial and temporal sampling statistics 31
- 1.5. Outlier detection 34
- 1.6. Summary 43

2. Quality control and calibration of ERS-1 and ERS-2 ESCAT data 45
- 2.1. Natural calibration targets for ESCAT backscatter 45
- 2.2. Analysis of breaks and trends 51
  - 2.2.1. Breaks and trends in ERS-1 52
  - 2.2.2. Breaks and trends in ERS-2 55
- 2.3. Intracalibration of beams per sensor 58
- 2.4. Temporal effects of intracalibration 66
- 2.5. Intercalibration between ESCAT and ASCAT 72
- 2.6. Summary 81

3. Interoperability between ERS-1 and ERS-2 ESCAT and Metop ASCAT data 82
- 3.1. Synthetic ESCAT dataset experiment 82
- 3.2. Slope and curvature calculation based on synthetic ESCAT data 84
  - 3.2.1. Climatology-based slope and curvature 84
  - 3.2.2. Time-series-based slope and curvature 85
  - 3.2.3. Parameter adaptations for time-series-based slope and curvature 87
- 3.3. Preliminary processing of ESCAT data 89
  - 3.3.1. Time series analysis 89
  - 3.3.2. Spatial analysis of slope 95
  - 3.3.3. Spatial analysis of curvature 102
- 3.4. Summary 109

4. References 110

Appendices 120

A. Supplementary figures 120
- A.1. ERS-1 outlier detection 120
- A.2. ERS-2 outlier detection 141

1. Quality assessment of of ERS-1 and ERS-2 ESCAT data

1.1. Data characteristics

The ERS-2 scatterometer data products were processed as part of the Scatterometer Instrument Competence Centre (SCIRoCCo) project established by ESA in 2014. The SCIRoCCo project supports and promotes the use of 20 years' worth of ERS Scatterometer (ESCAT) data at medium spatial resolutions (25 km, 50 km). Running from 2014 to 2017, SCIRoCCo focused on improving data quality through sensor inter-calibration, characterization, and validation. The project provides data processing tools, educational resources, and publications to advance applications in soil moisture, ocean winds, sea ice, and climatology. SCIRoCCo supports multi-sensor time series efforts across ESA missions to ensure consistent and high-quality Earth observation data for research and meteorological communities.

The reprocessing of ERS-2 Scatterometer Level 2.0 products was successfully completed on 14 March 2015, using the most recent version of the Advanced Scatterometer Processing System (ASPS) 10.04. Additionally, in May 2018, the dataset was further expanded with the reprocessing of ERS-1 Scatterometer Level 2.0 products [1].

Characteristic	ERS-1	ERS-2
Time Period	25 July 1991 – 3 June 1996	21 April 1995 – 5 July 2011
Frequency	5.3 GHz (C band)	5.3 GHz (C band)
Antenna Azimuth Orientations	Three fixed	Three fixed
Polarizations	V Only	V Only
Beam Resolution	Range Gate	Range Gate
Resolution	25/50 km	25/50 km
Number of pulses per 50 km	256	256
Swath width	500 km	500 km
Incidence Angle	18 – 59°	18 – 59°
Orbit	Sun-synchronous 780 km altitude, 98.52° inclination	Sun-synchronous 780 km altitude, 98.52° inclination

Table 1.1: Operating Characteristics of ERS-1 and ERS-2 AMI in Wind Scatterometer mode

The ERS-1/2 Scatterometer Ocean Wind field and Sea Ice probability (`ASPS20.H/ASPS20.N`) products are provided through the ESA Earth Online Portal[1]. The high-resolution (`ERS.ASPS20.H`) and nominal resolution (`ERS.ASPS20.N`) dataset include radar backscatter (σ^0) for the three instrument beams, wind vector solutions, sea ice probability, and various quality flags. The data have been downloaded and archived at TU Wien and checked for health, completeness, and gaps. The following Tables 1.2 and 1.3 summarize the dataset specifications, as well as, the size and number of files. Although the number of files for ERS-1 is the same for both the high and nominal-resolution products, it slightly differs for ERS-2. There are 16 files missing in case of the nominal resolution ERS-2 dataset compared to the high-resolution product.

---

[1] https://earth.esa.int/eogateway

Attribute	**Details**
Digital Object Identifier (DOI)	European Space Agency, 2019, ERS-1/2 SCATTEROMETER Ocean Wind field and Sea Ice probability [ASPS20.H/ASPS20.N], Version ASPS v10.04. `https://doi.org/10.57780/ers-ee9aba7`
Spatial Coverage	82.00 N, -82.00 S, -180.00 W, 180.00 E
Temporal Coverage	1991-08-01 – 2011-07-04
Date of Launch	1991-07-17 (ERS-1), 1995-04-21 (ERS-2)
Operators	European Space Agency (ESA)
Mission Status	Completed
Orbit Height	782 to 785 km
Orbit Type	Sun-synchronous
Current Processor Version	ASPS 10.04

Table 1.2: Dataset specification of `ERS.ASPS20.H` and `ERS.ASPS20.N`.

Product	**Size (GB)**	**Number of Files**
`ERS1.ASPS20.H`	271.9	23,677
`ERS1.ASPS20.N`	63.6	23,677
`ERS2.ASPS20.H`	799.9	69,621
`ERS2.ASPS20.N`	187.1	69,605

Table 1.3: Dataset size and number of files for `ERS.ASPS20.H` and `ERS.ASPS20.N`.

The ERS-1 satellite operated from July 17, 1991, to March 7, 2000, while its successor, ERS-2, was operational from April 21, 1995, until September 5, 2011. Both missions provided valuable scatterometer data, which were processed into high (25 km) and nominal (50 km) resolution products: `ERS1.ASPS20.H`, `ERS1.ASPS20.N`, `ERS2.ASPS20.H` and `ERS2.ASPS20.N`. The following Table 1.4 lists the first and last available files for both the high and nominal resolution products of ERS-1 and ERS-2, highlighting the time span of the datasets.

Product	**First File**	**Last File**
`ERS1.ASPS20.H`	`1991-08-01 05:14:57`	`1996-06-02 20:49:04`
`ERS1.ASPS20.N`	`1991-08-01 05:14:57`	`1996-06-02 20:49:04`
`ERS2.ASPS20.H`	`1996-03-26 00:10:11`	`2011-07-04 10:59:02`
`ERS2.ASPS20.N`	`1996-03-26 00:10:11`	`2011-07-04 10:59:04`

Table 1.4: First and Last File Dates for ERS-1 and ERS-2 ASPS20 Level 2.0 products.

There are known periods with missing data due to various mission-related issues, most notably for ERS-2 [2]. A list of gaps found in the ERS.ASPS20.H and ERS.ASPS20.N are listed in the Tables 1.5, 1.6, 1.7 and 1.8.

Product	Gaps > 2 hours	Gaps > 3 days
ERS1.ASPS20.H	248	5
Gaps > 3 days details:		
18 days: 1991-12-10 – 1991-12-28 03 days: 1992-06-25 – 1992-06-29 05 days: 1992-07-18 – 1992-07-23 29 days: 1993-05-16 – 1993-06-14 05 days: 1994-03-31 – 1994-04-05		

Table 1.5: Gaps in ERS1.ASPS20.H products.

Product	Gaps > 2 hours	Gaps > 3 days
ERS1.ASPS20.N	248	5
Gaps > 3 days details:		
18 days: 1991-12-10 – 1991-12-28 03 days: 1992-06-25 – 1992-06-29 05 days: 1992-07-18 – 1992-07-23 29 days: 1993-05-16 – 1993-06-14 05 days: 1994-03-31 – 1994-04-05		

Table 1.6: Gaps in ERS1.ASPS20.N products.

Product	Gaps > 2 hours	Gaps > 3 days
ERS2.ASPS20.H	1808	13
Gaps > 3 days details:		
019 days: 1996-06-08 – 1996-06-27 010 days: 1996-07-15 – 1996-07-26 003 days: 1998-06-03 – 1998-06-06 003 days: 2000-02-07 – 2000-02-10 005 days: 2000-06-30 – 2000-07-05 003 days: 2000-10-07 – 2000-10-10 015 days: 2001-01-17 – 2001-02-02 210 days: 2001-11-19 – 2002-06-17 004 days: 2003-03-27 – 2003-03-31 003 days: 2003-05-16 – 2003-05-19 009 days: 2003-06-22 – 2003-07-01 014 days: 2003-07-02 – 2003-07-17 014 days: 2011-02-21 – 2011-03-07		

Table 1.7: Gaps in ERS2.ASPS20.H products.

Product	**Gaps > 2 hours**	**Gaps > 3 days**
ERS2.ASPS20.N	1811	13
Gaps > 3 days details:		
019 days: 1996-06-08 – 1996-06-27		
010 days: 1996-07-15 – 1996-07-26		
003 days: 1998-06-03 – 1998-06-06		
003 days: 2000-02-07 – 2000-02-10		
005 days: 2000-06-30 – 2000-07-05		
003 days: 2000-10-07 – 2000-10-10		
015 days: 2001-01-17 – 2001-02-02		
210 days: 2001-11-19 – 2002-06-17		
004 days: 2003-03-27 – 2003-03-31		
003 days: 2003-05-16 – 2003-05-19		
009 days: 2003-06-22 – 2003-07-01		
014 days: 2003-07-02 – 2003-07-17		
014 days: 2011-02-21 – 2011-03-07		

Table 1.8: Summary of gaps in ERS2.ASPS20.N products.


ERS-1.ASPS20.H | Mission Phase C (618 days) | Missing orbits #840
1992-04-14 06:17:59 - 1993-12-23 10:56:48

ERS-1.ASPS20.H | Mission Phase D (107 days) | Missing orbits #102
1993-12-23 17:39:06 - 1994-04-10 15:58:38

ERS-1.ASPS20.H | Mission Phase E (170 days) | Missing orbits #47
1994-04-10 17:39:05 - 1994-09-28 00:50:19

ERS-1.ASPS20.H | Mission Phase F (174 days) | Missing orbits #49
1994-09-28 02:30:57 - 1995-03-21 09:01:33

ERS-1.ASPS20.H | Mission Phase G (439 days) | Missing orbits #180
1995-03-21 09:01:49 - 1996-06-02 20:49:04

Figure 1.1: Number of missing orbit files per relative orbit number for dataset `ERS-1.ASPS20.H`.

Figure 1.2: Number of missing orbit files per relative orbit number for dataset `ERS-1.ASPS20.N`.

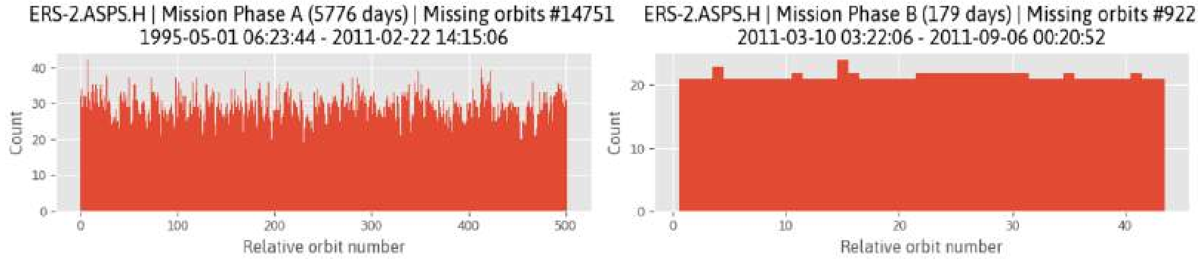

Figure 1.3: Number of missing orbit files per relative orbit number for dataset `ERS-2.ASPS20.H`.

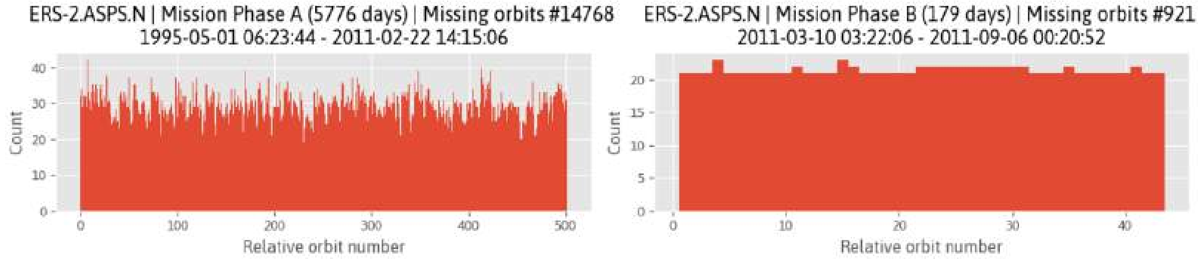

Figure 1.4: Number of missing orbit files per relative orbit number for dataset `ERS-2.ASPS20.N`.

No specific pattern was identified during the investigation of missing orbit files, as illustrated in Figures 1.1, 1.2, 1.3, and 1.4. Absolute orbit numbers were converted to relative orbit numbers to generate statistics on the missing orbit files.

Table 1.9: ERS-1 and ERS-2 mission phases parameters [3].

Sat/Phase	Start Time	Stop Time	Start Orbit	Stop Orbit	Range
ERS-1/A	1991-07-25T20:52:34Z	1991-12-10T22:33:02Z	126	2104	43
ERS-1/B	1991-12-28T07:36:19Z	1992-04-01T04:48:52Z	2354	3713	43
ERS-1/R	1992-04-02T15:58:35Z	1992-04-14T07:58:35Z	3735	3901	501
ERS-1/C	1992-04-14T06:17:59Z	1993-12-23T10:56:48Z	3901	12749	501
ERS-1/D	1993-12-23T17:39:06Z	1994-04-10T15:58:38Z	12754	14300	43
ERS-1/E	1994-04-10T17:39:05Z	1994-09-28T00:50:19Z	14302	16745	2411
ERS-1/F	1994-09-28T02:30:57Z	1995-03-21T09:01:33Z	16747	19247	2411
ERS-1/G	1995-03-21T09:01:49Z	2000-03-11T00:33:05Z	19248	45251	501
ERS-2/A	1995-05-01T06:23:44Z	2011-02-22T14:15:06Z	146	82829	501
ERS-2/B	2011-03-10T22:06:55Z	2011-09-06T00:20:52Z	83064	85630	43

1.2. Pre-processing

The scatterometer data were resampled to a fixed Earth grid using a nearest-neighbor search. The nearest neighbor method preserves the integrity of the original data and ensures that quality flags and measurements remain consistent. The fixed Earth target grid, known as the Fibonacci grid, features points arranged based on the Fibonacci ratio. Unlike other spiral-constructed grids, the Fibonacci grid is defined by a longitudinal turn between consecutive points along the spiral, equal to the golden angle ($360° \cdot \left(1 - \phi^{-1}\right) \simeq 137.5°$) or its complementary ($360° \cdot \phi^{-1} \simeq 222.5°$) [4]. The spatial sampling distance depends on the number of grid points (12.5 km: N = 1,650,000; 25 km: N = 430,000). The grid point locations are computed on a spherical Earth and then converted to WGS84 ellipsoidal coordinates (EPSG:4326).

The Fibonacci grid used for the high-resolution data (`ERS.ASPS20.H`) has a spacing of approximately 12.5 km, while for nominal resolution data (`ERS.ASPS20.N`) the grid spacing is around 25 km. The scatterometer data has been resampled over land only, except Antarctica.

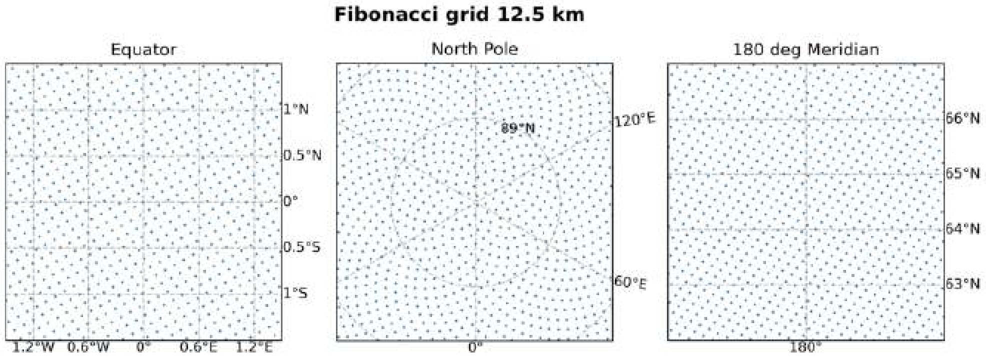

Figure 1.5: Fibonacci grid with 12.5 km sampling (N=1,650,000) showcasing 3 different areas: Equator (left), North Pole (center), and 180° meridian.

The resampled high-resolution (`ERS.ASPS20.H`) and nominal resolution (`ERS.ASPS20.N`) dataset are stored in a contiguous ragged array netCDF format which follows the Climate-Forecast (CF) conventions.

The contiguous ragged array format consists of one-dimensional arrays, each holding time series observations for a collection of grid points. A counting array, called `row_size`, is also stored in the netCDF file and indicates the number of observations per grid point. The `row_size` variable functions as a pointer, enabling the extraction of single or multiple time series from the netCDF file. To maintain a balance in both the number and size of netCDF files, the data is globally partitioned into 5×5° cells leading to approximately 1,000 netCDF files.

Since ERS-1 and ERS-2 data share the same format (fields and data types), the ERS-2 data has been appended to the ERS-1 data after resampling. In this process, a new variable, `spacecraft_id`, has been introduced to differentiate between the two satellites.

Apart from the gaps reported in Tables 1.5, 1.6, 1.7, and 1.8, no data integrity issues (e.g., corrupt files) were identified during pre-processing. However, duplicate observations had to be removed at the equator, as resampling data at the end of the previous swath and the start of the next swath led to multiple observations being assigned to the same grid point.

1.3. Data quality flags

Backscatter observations and quality flags have been analyzed using the high-resolution (`ERS.ASPS20.H`) and nominal resolution (`ERS.ASPS20.N`) contiguous ragged time series datasets. Global statistics were computed for the flags listed in Tables 1.10 and 1.11. Results are presented only for the high-resolution product (`ERS.ASPS20.H`), as no significant differences were found when compared to the nominal resolution product (`ERS.ASPS20.N`). Wind-related flags included in Node Confidence Data 2 (ncd2) were not analyzed.

Table 1.10: Node Confidence Data 1 flags.

NCD1 Flags
Fore/Mid/Aft beam backscatter flag
Doppler frequency shift flag
Doppler Compensation Center of Gravity (CoG) flag
Doppler Compensation Standard Deviation (StDev) flag
Yaw error angle flag
Frame checksum flag

Table 1.11: Node Confidence Data 2 flags.

NCD2 Flags
Internal calibration flag
Arcing flag
Noise power flag
Radiometric accuracy (Kp) flag
Distance from C-band model flag
Wind speed bias flag
Wind direction bias flag
Low wind flag
High wind flag
Ambiguity removal flag

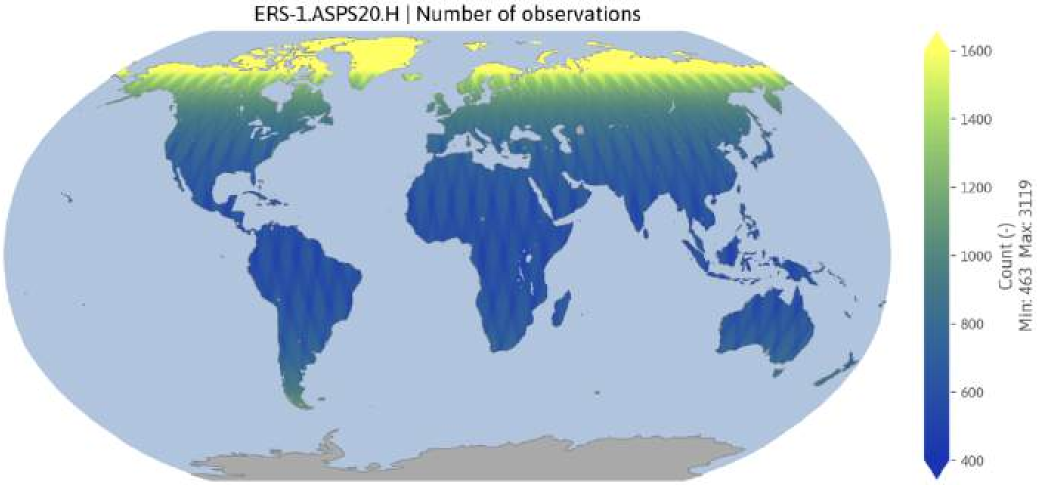

Figure 1.6: Absolute number of observations for dataset `ERS-1.ASPS20.H` (including NaN).

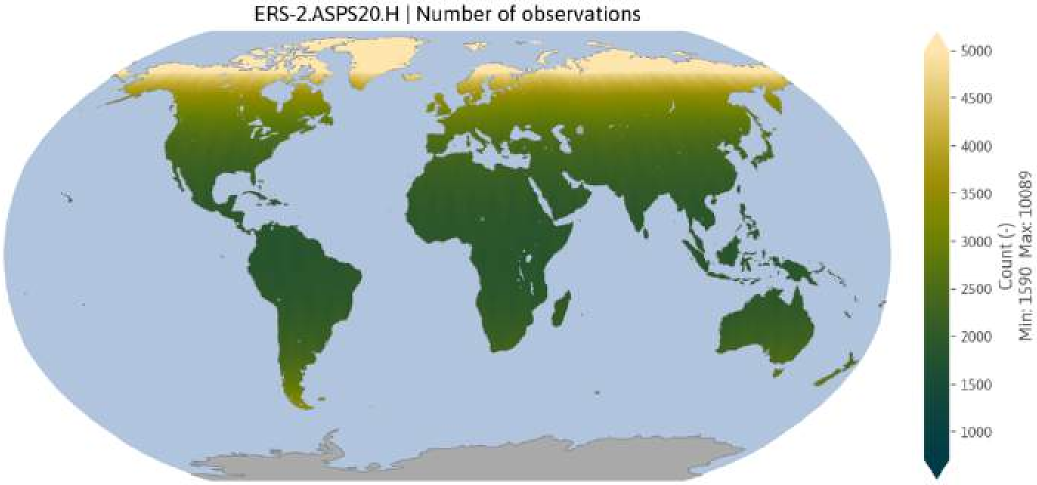

Figure 1.7: Absolute number of observations for dataset `ERS-2.ASPS20.H` (including NaN).

The absolute number of observations for `ERS-1.ASPS20.H` is displayed in Figure 1.6, whereas Figure 1.7 presents the observations for `ERS-2.ASPS20.H`. For ERS-1, 95% of the observations range between 500 and 1900, whereas for ERS-2, 95% of the observations range between 1800 and 6400. As expected, the number of observations increases with latitude due to the polar orbit of the ERS-1 and ERS-2 satellites. These encompass both valid and invalid data, representing the theoretical maximum number of observations. No unexpected patterns are evident in the two global maps.

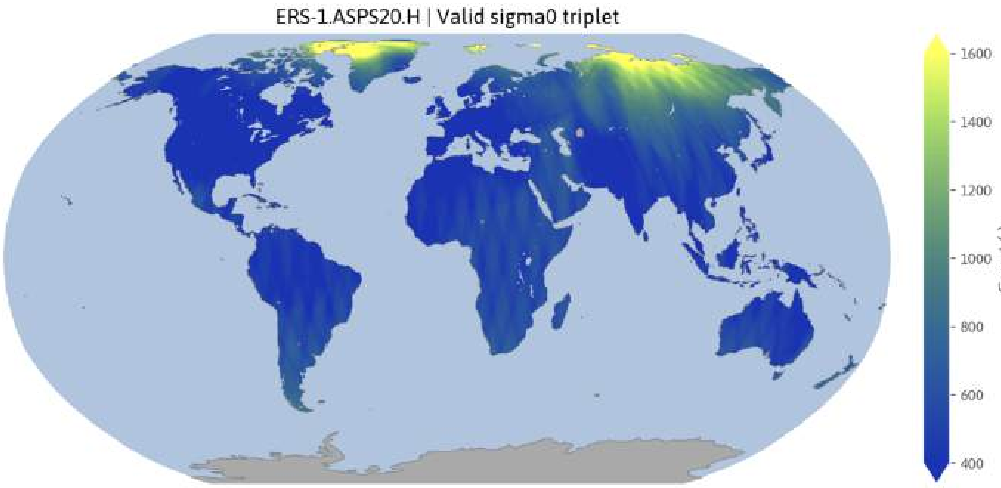

Figure 1.8: Number of valid backscatter triplet observations for dataset `ERS-1.ASPS20.H`.

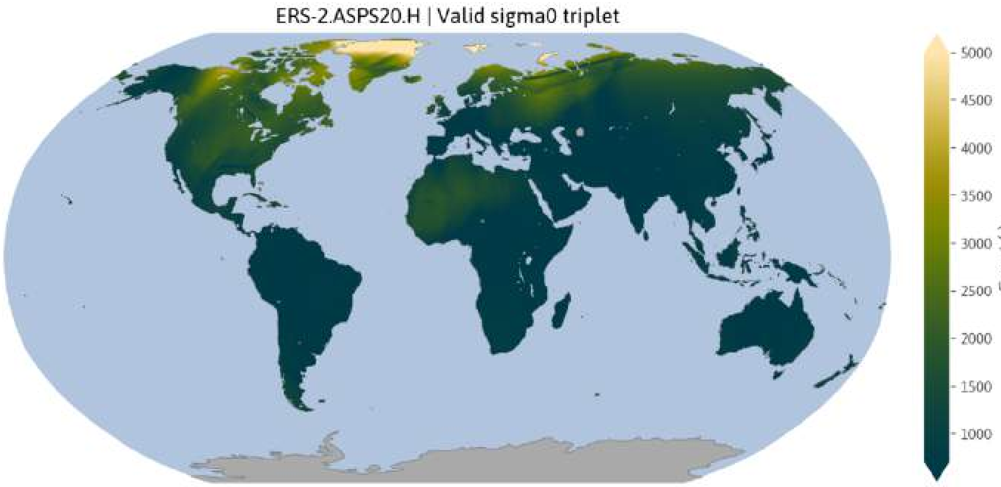

Figure 1.9: Number of valid backscatter triplet observations for dataset `ERS-2.ASPS20.H`.

The number of valid backscatter triplet observations for dataset `ERS-1.ASPS20.H` is shown in Figure 1.8, whereas Figure 1.9 illustrated the valid observations for `ERS-2.ASPS20.H`. For ERS-1, 95% of the observations range between 300 and 1400, whereas for ERS-2, 95% of the observations range between 500 and 3000. In the case of ERS-1, there are noticeably fewer valid backscatter observations over North America, Europe, West Africa, and Central Asia. In contrast, ERS-2 presents a different scenario. Following the loss of its tape recorder in 2003, the mission shifted from global to regional coverage. Consequently, the number of valid backscatter observations significantly decreased in regions outside the range of ground stations. Mainly North America, Europe, North Africa, East Asia and Australia were part of the regional mission scenario.

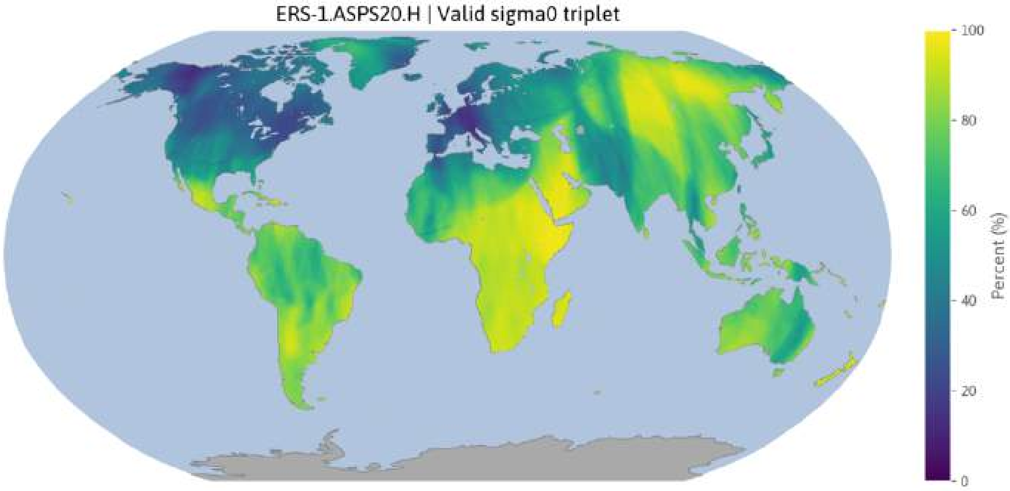

Figure 1.10: Percent valid backscatter triplet observations for dataset `ERS-1.ASPS20.H`.

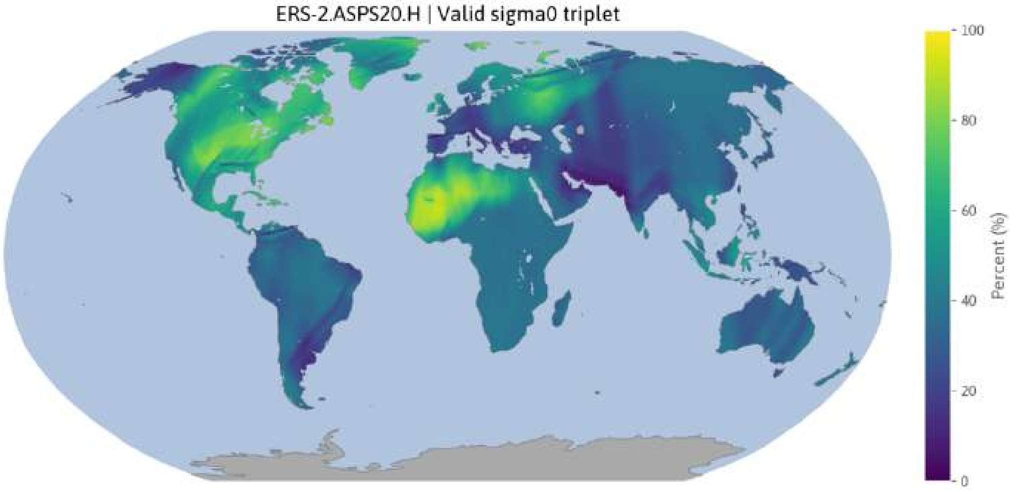

Figure 1.11: Percent valid backscatter triplet observations for dataset `ERS-2.ASPS20.H`.

Figure 1.10 and 1.11 highlight the areas previously mentioned by showing the relative number of valid backscatter observations in per cent. There is a smaller number of valid backscatter observations in North America, Europe, West Africa and Central Asia for ERS-1. In the case of ERS-2, mainly South America, Central and South Africa, as well as Europe, Asia and Australia.

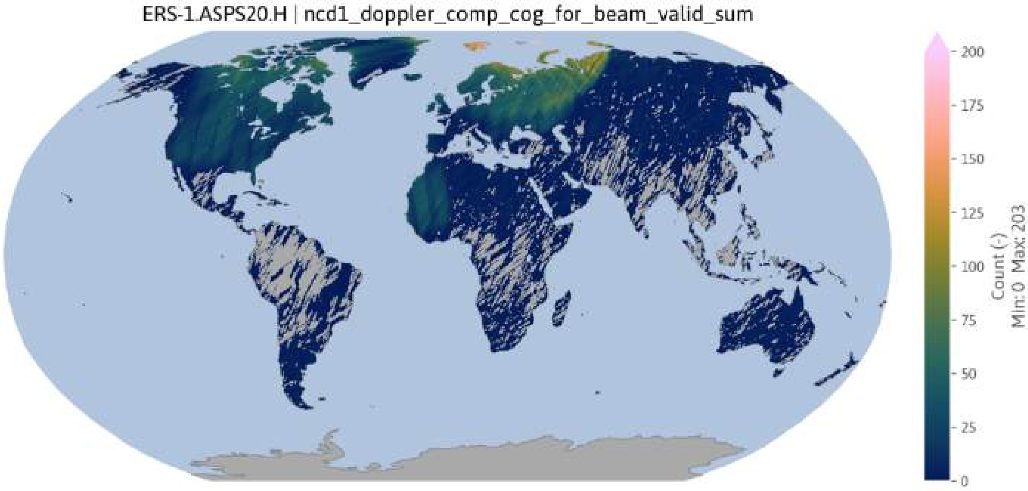

Figure 1.12: Fore beam doppler compensation center of gravity flag for dataset `ERS-1.ASPS20.H`.

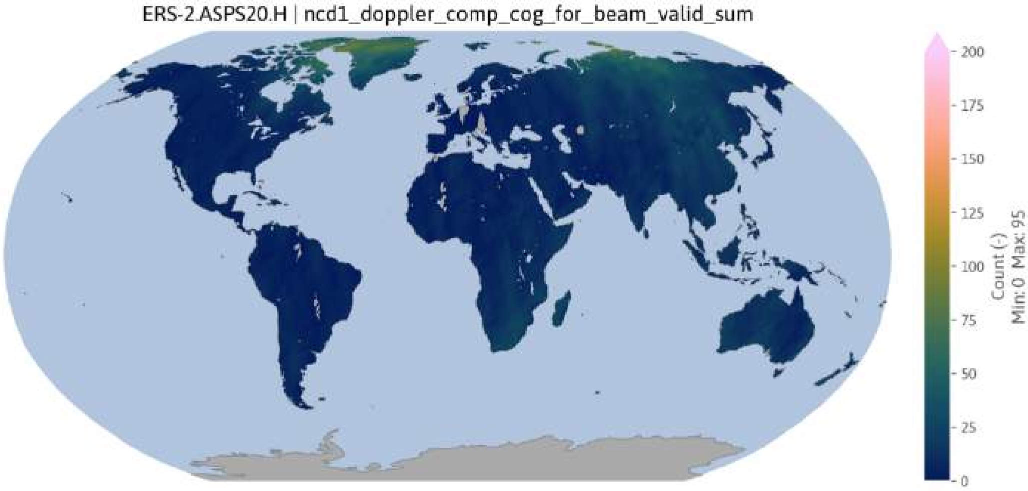

Figure 1.13: Fore beam doppler compensation center of gravity flag for dataset `ERS-2.ASPS20.H`.

Part of the instrument monitoring parameters includes the power spectrum characteristics, such as the center of gravity and standard deviation. Figure 1.12 and 1.13 display the absolute number of instances where the Doppler compensation center of gravity flag was raised in the case of the Fore beam. Both satellites show few occurrences, with ERS-1 indicating a cluster in North America, Europe, and West Africa, while ERS-2 shows a focus in Greenland, Asia and parts of Africa. The same pattern can also be seen in the Doppler compensation standard deviation flag in Figure 1.14 and 1.15, as well as the Doppler frequency shift flag in Figure 1.16 and 1.15. Among the three Doppler flags, the Doppler frequency shift flag has the highest number of marked observations (635) in the case of ERS-1.

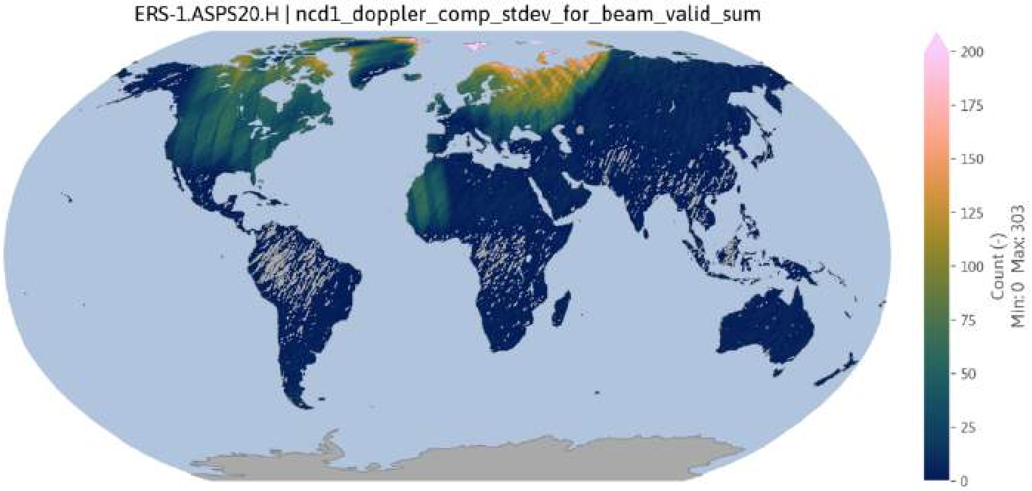

Figure 1.14: Fore beam doppler compensation standard deviation flag for dataset `ERS-1.ASPS20.H`.

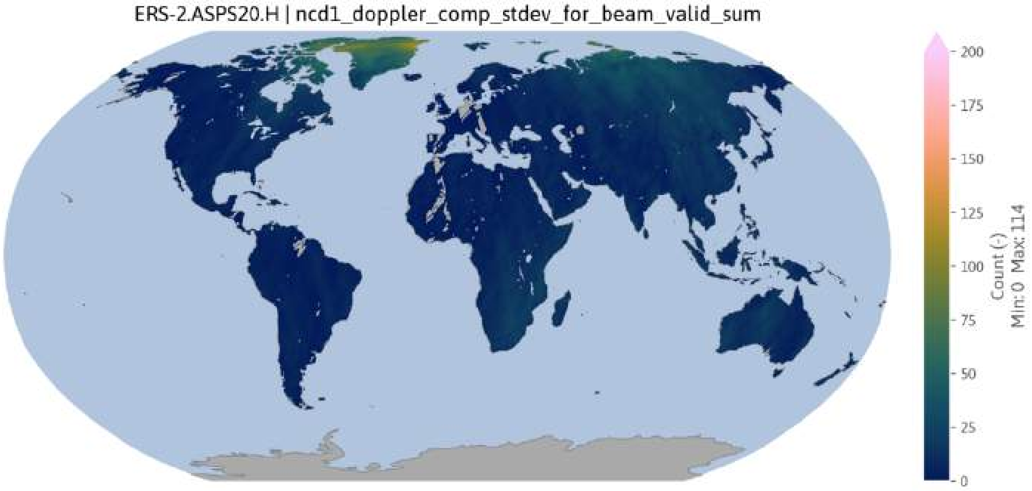

Figure 1.15: Fore beam doppler compensation standard deviation flag for dataset `ERS-2.ASPS20.H`.

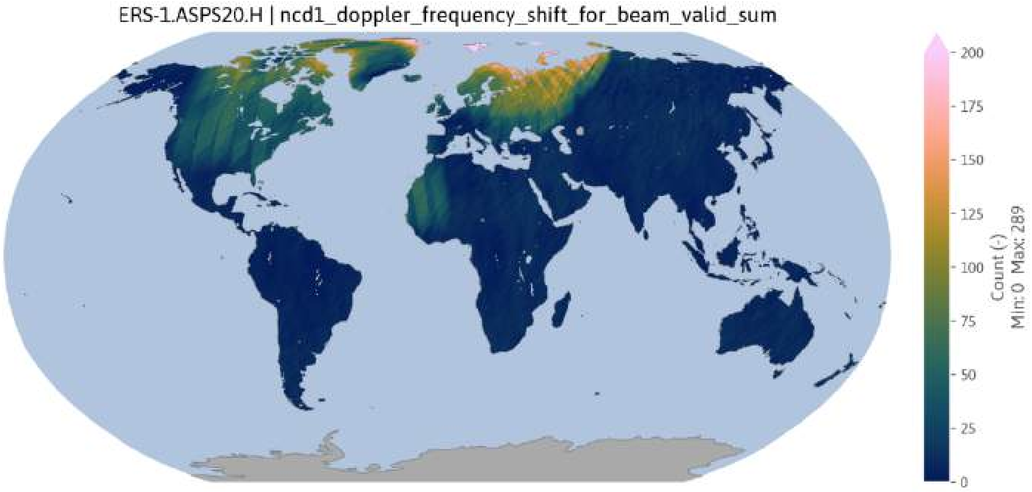

Figure 1.16: Fore beam doppler frequency shift flag for dataset `ERS-1.ASPS20.H`.

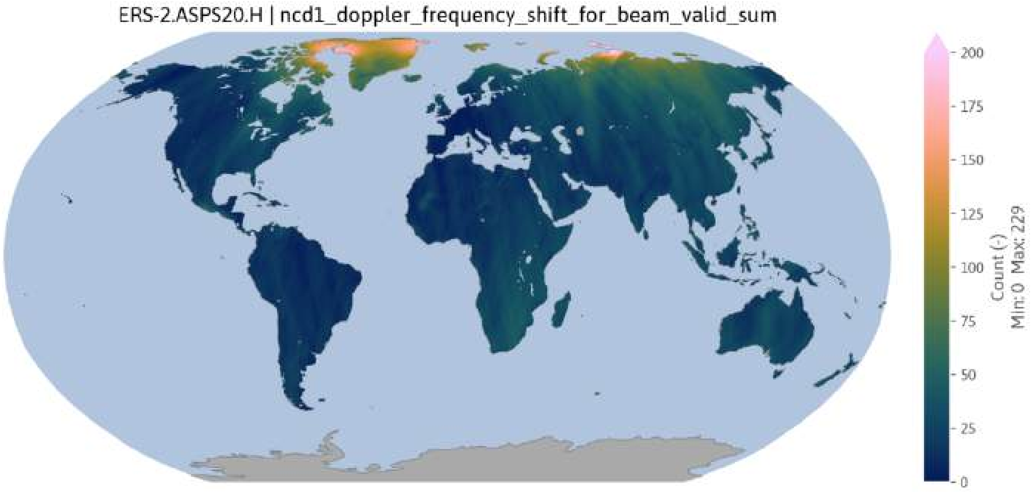

Figure 1.17: Fore beam doppler frequency shift flag for dataset `ERS-2.ASPS20.H`.

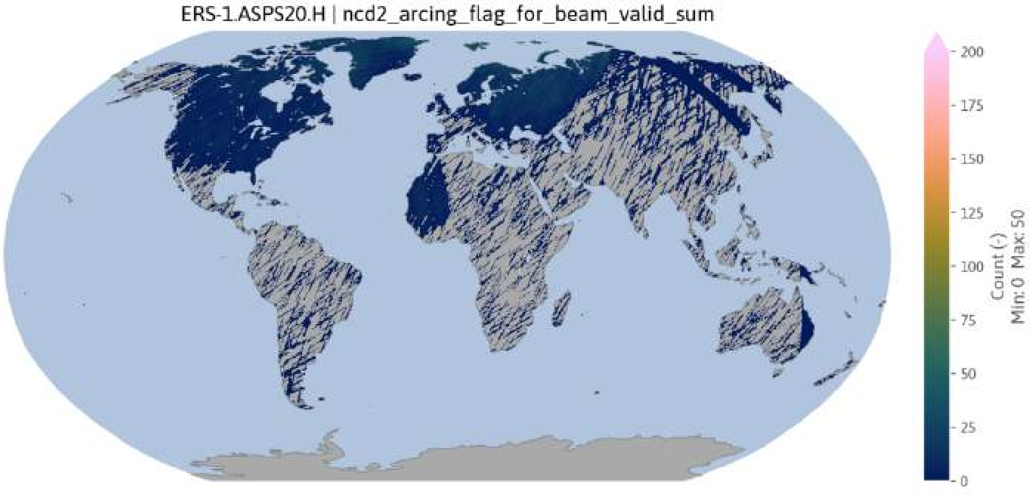

Figure 1.18: Fore beam arcing flag for dataset `ERS-1.ASPS20.H`.

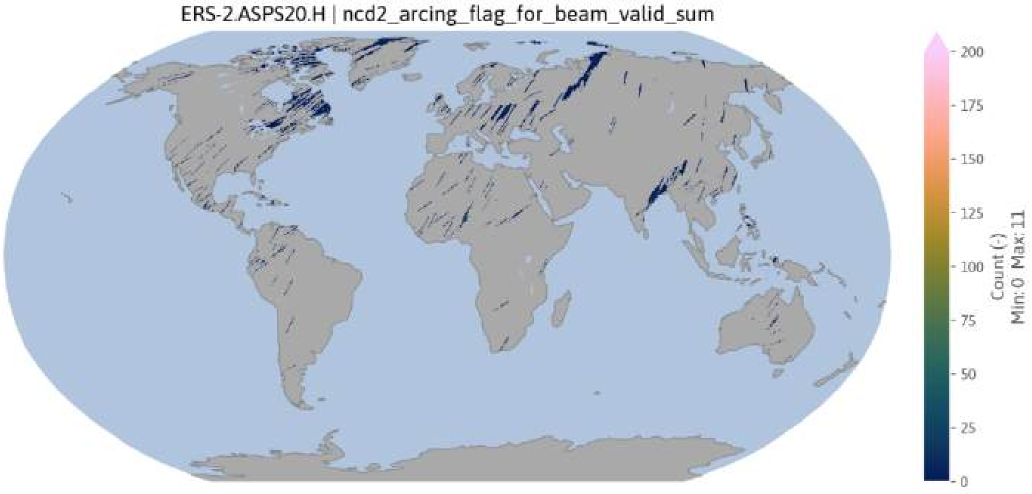

Figure 1.19: Fore beam arcing flag for dataset `ERS-2.ASPS20.H`.

The arcing flag indicates instances of High Power Amplifier (HPA) arcing, which occurs due to unintended electrical discharges within the HPA, temporarily disrupting its operation. To prevent damage, the HPA is automatically powered down during arcing and restarted after a few seconds. During this period, no transmit or internal calibration pulses are generated, resulting in missing data for the affected measurement block. The absolute number of arcing occurrences in the fore beam is very low (Figure 1.18 and 1.19). Similar to the previously mentioned Doppler flags, ERS-1 also exhibits a cluster of occurrences in North America, Europe, and West Africa.

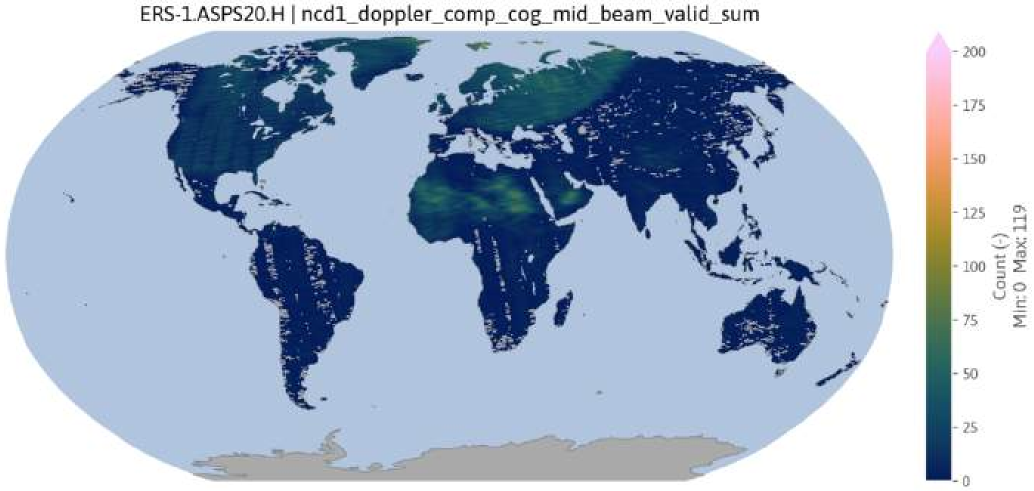

Figure 1.20: Mid beam doppler compensation center of gravity flag for dataset `ERS-1.ASPS20.H`.

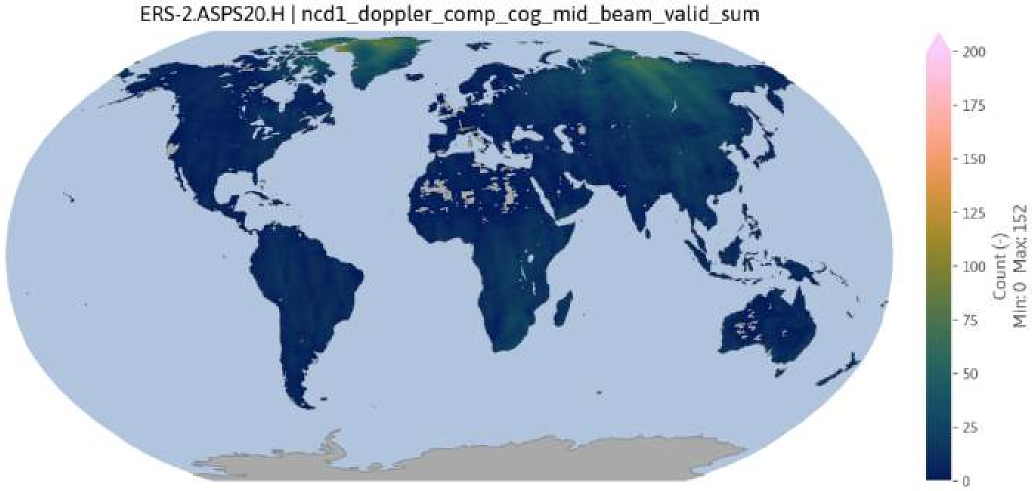

Figure 1.21: Mid beam doppler compensation center of gravity flag for dataset `ERS-2.ASPS20.H`.

The mid beam Doppler compensation center of gravity flag and standard deviation flag are visualized in Figure 1.20, 1.21, 1.22 and 1.23. A similar spatial distribution and number of absolute occurrences are observed for both ERS-1 and ERS-2. However, one notable exception is the clustering of raised mid-beam Doppler flags over the Sahara Desert in the case of ERS-1.

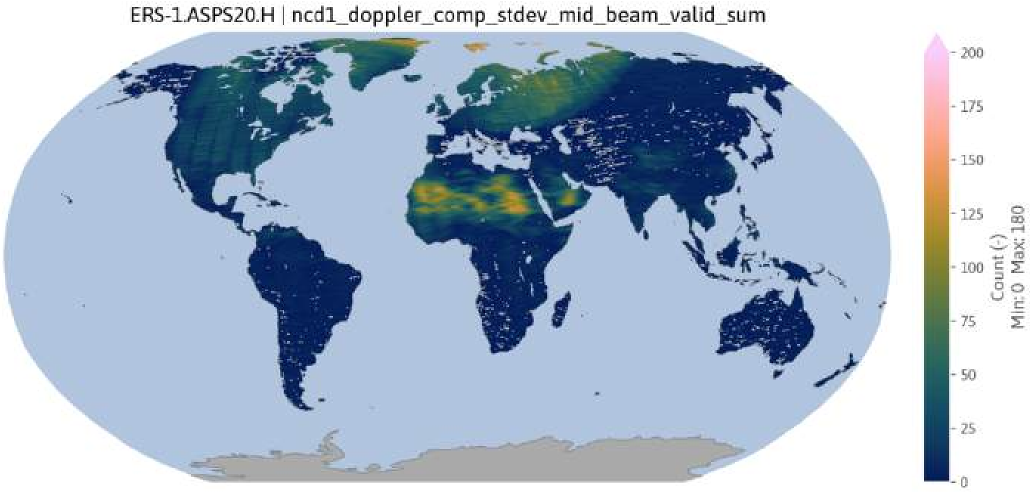

Figure 1.22: Mid beam doppler compensation standard deviation flag for dataset `ERS-1.ASPS20.H`.

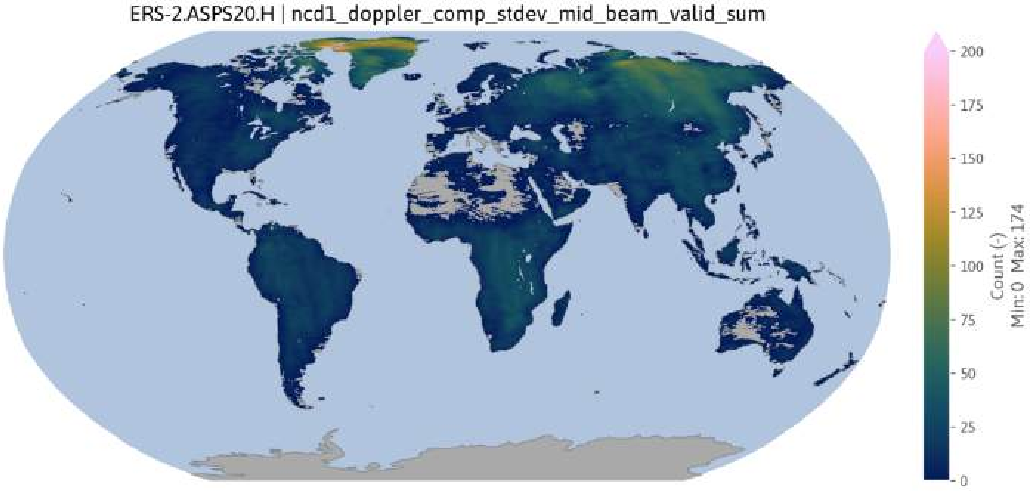

Figure 1.23: Mid beam doppler compensation standard deviation flag for dataset `ERS-2.ASPS20.H`.

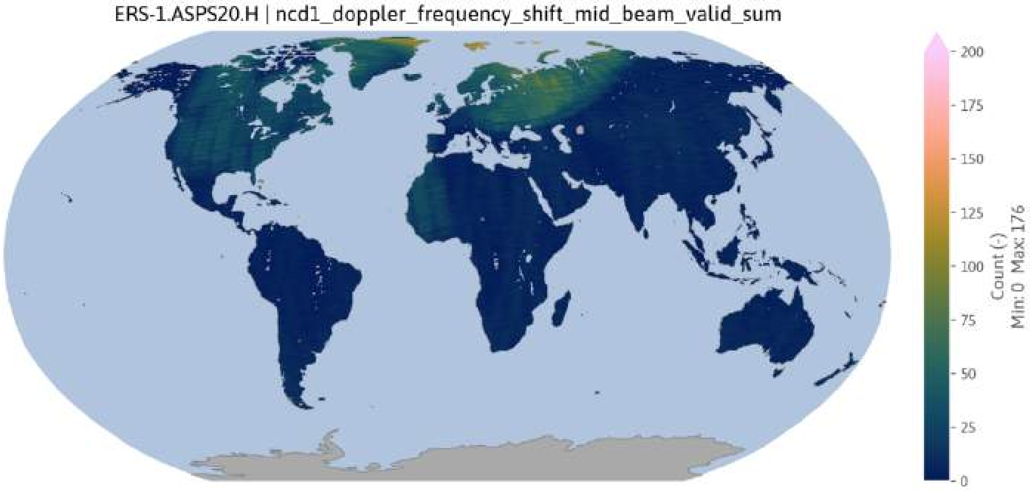

Figure 1.24: Mid beam doppler frequency shift flag for dataset `ERS-1.ASPS20.H`.

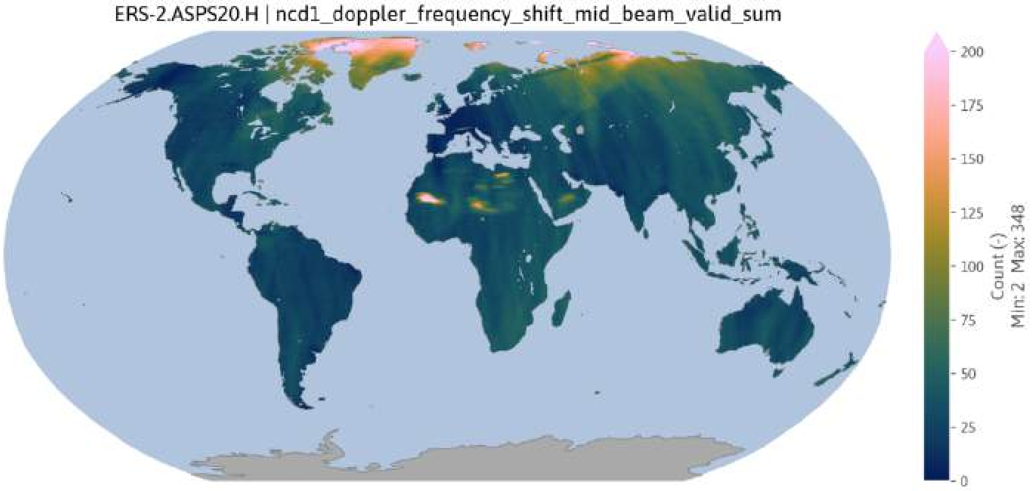

Figure 1.25: Mid beam doppler frequency shift flag for dataset `ERS-2.ASPS20.H`.

The Doppler frequency flag for the mid beam (Figure 1.24 and 1.25) is again spatially consistent with the previous Doppler flags, apart from the fact that in this case the Sahara desert is more prominent for ERS-2 instead of ERS-1.

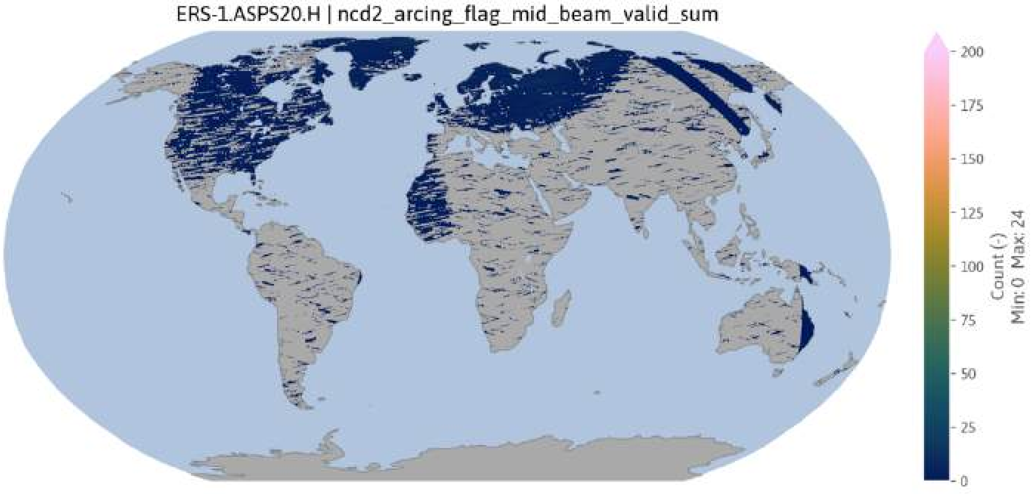

Figure 1.26: Mid beam arcing flag for dataset `ERS-1.ASPS20.H`.

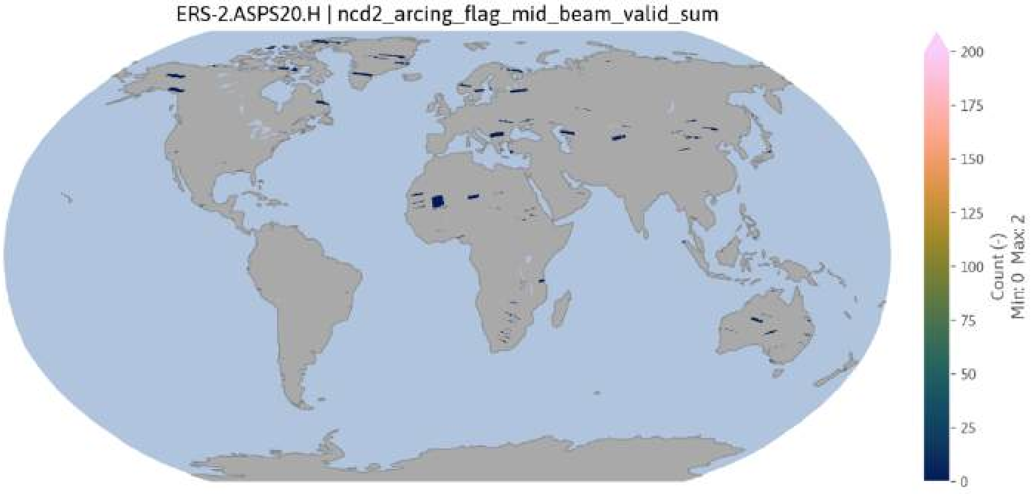

Figure 1.27: Mid beam arcing flag for dataset `ERS-2.ASPS20.H`.

The arcing flag in the mid beam (Figure 1.26 and 1.27) is very consistent with the spatial pattern seen in the fore beam. The maximum number of absolute occurrences is only twice for ERS-2.

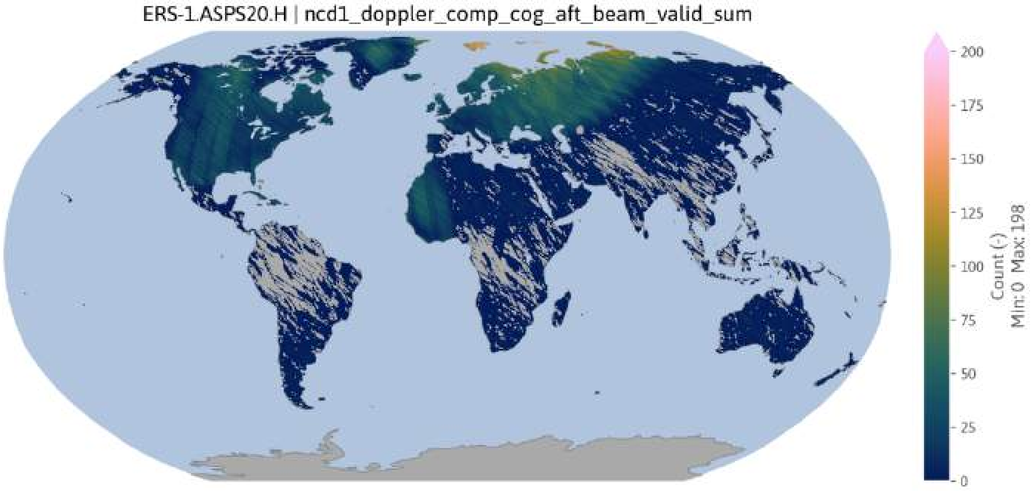

Figure 1.28: Aft beam doppler compensation center of gravity flag for dataset `ERS-1.ASPS20.H`.

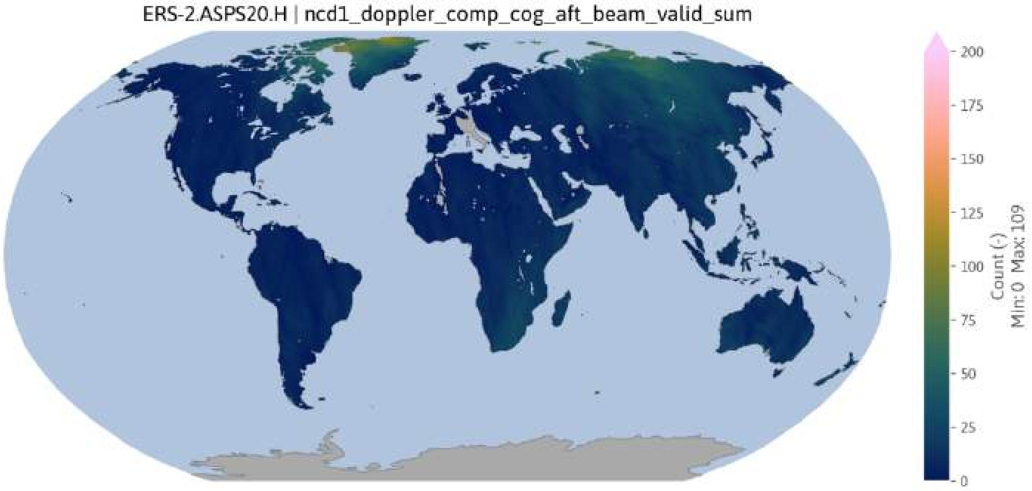

Figure 1.29: Aft beam doppler compensation center of gravity flag for dataset `ERS-2.ASPS20.H`.

The aft beam Doppler compensation center of gravity flag and standard deviation flag are visualized in Figure 1.28, 1.29, 1.30 and 1.31. There are no major differences compared to the fore and mid beam Doppler flags shown before. This is also true for the Doppler frequency shift flag displayed in Figure 1.32 and 1.33, as well as the arcing flag illustrated in Figure 1.34 and 1.35.

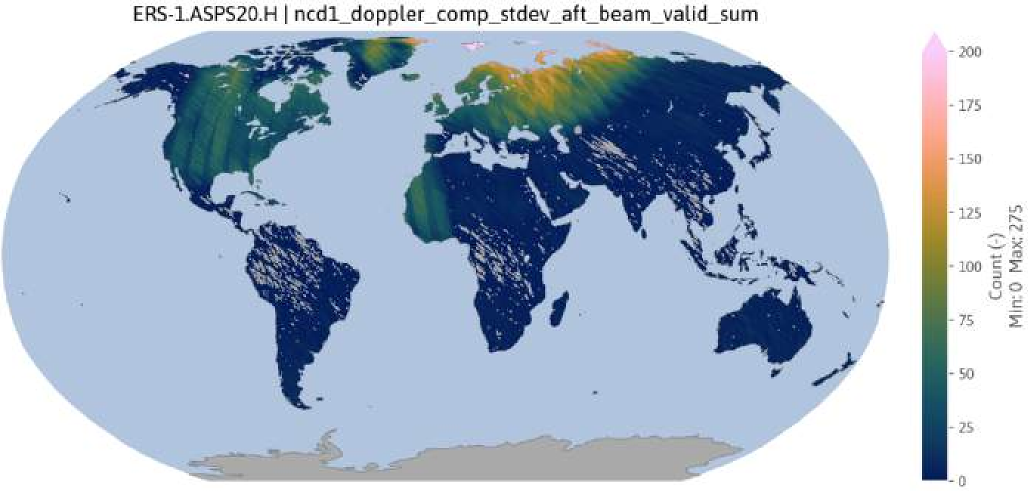

Figure 1.30: Aft beam doppler compensation standard deviation flag for dataset `ERS-1.ASPS20.H`.

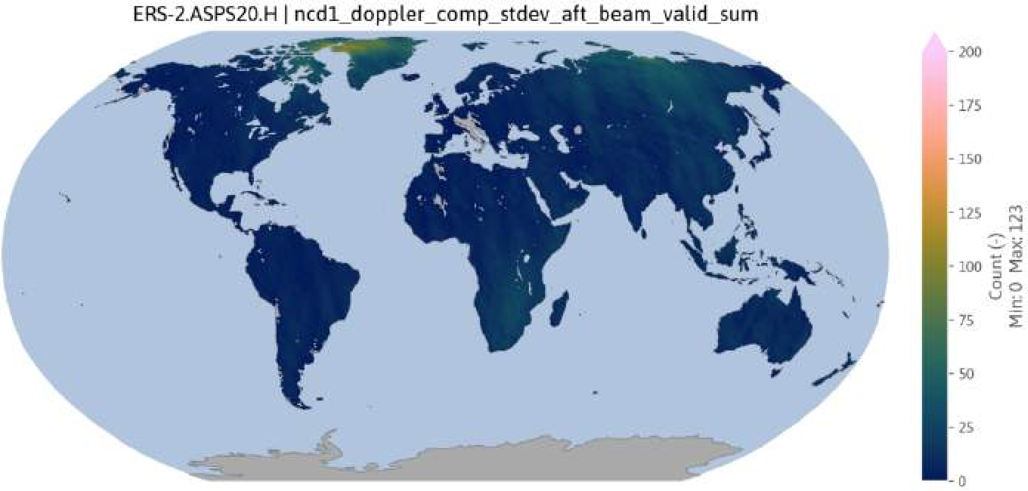

Figure 1.31: Aft beam doppler compensation standard deviation flag for dataset `ERS-2.ASPS20.H`.

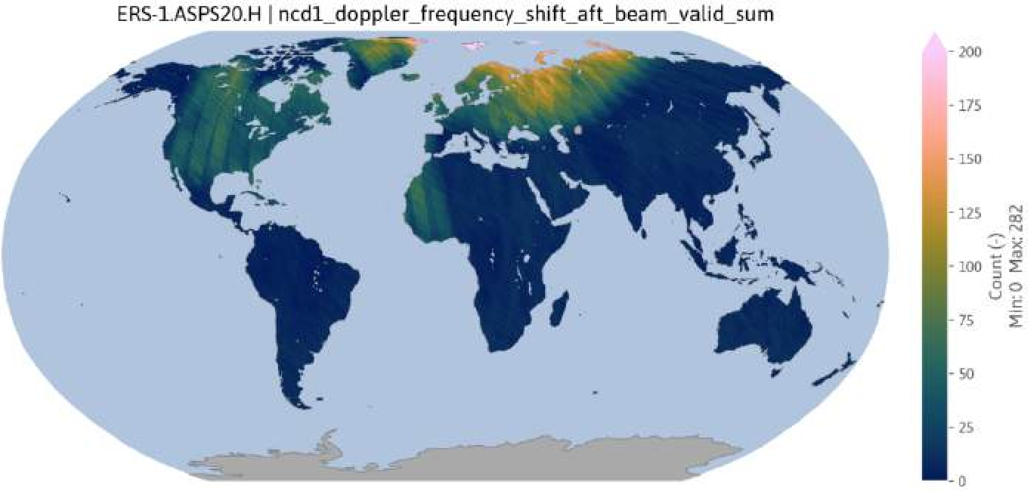

Figure 1.32: Aft beam doppler frequency shift flag for dataset `ERS-1.ASPS20.H`.

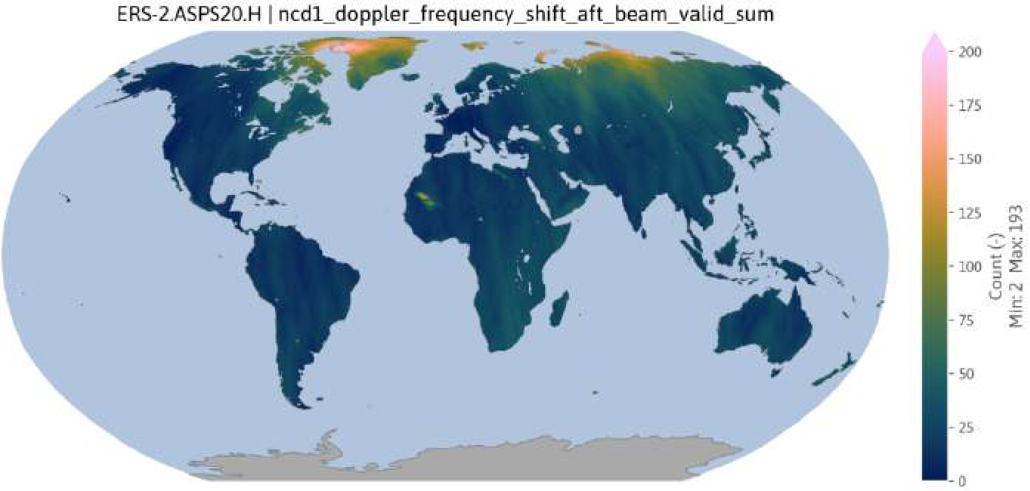

Figure 1.33: Aft beam doppler frequency shift flag for dataset `ERS-2.ASPS20.H`.

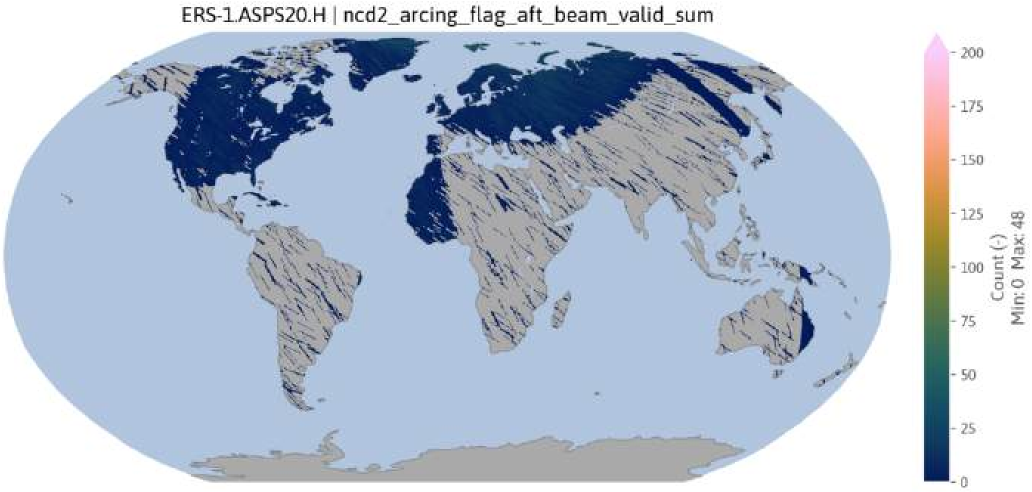

Figure 1.34: Aft beam arcing flag for dataset `ERS-1.ASPS20.H`.

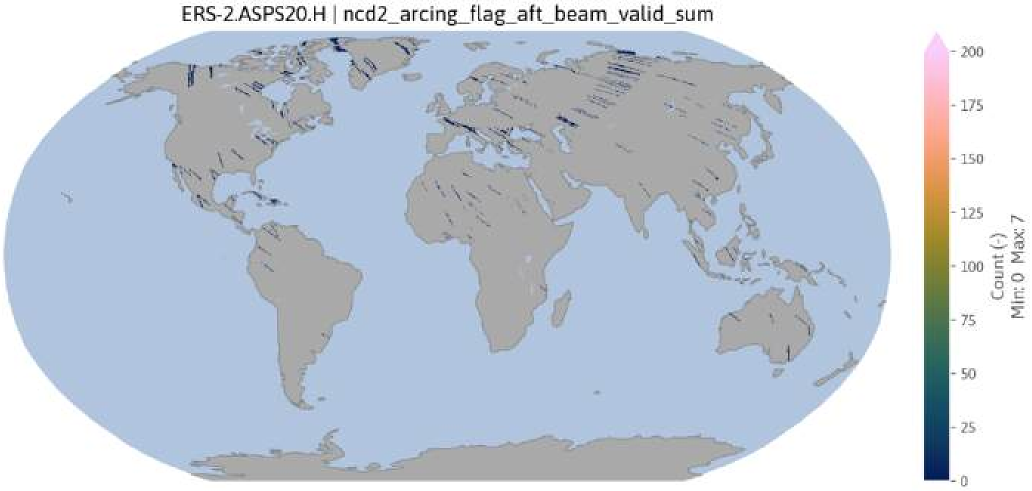

Figure 1.35: Aft beam arcing flag for dataset `ERS-2.ASPS20.H`.

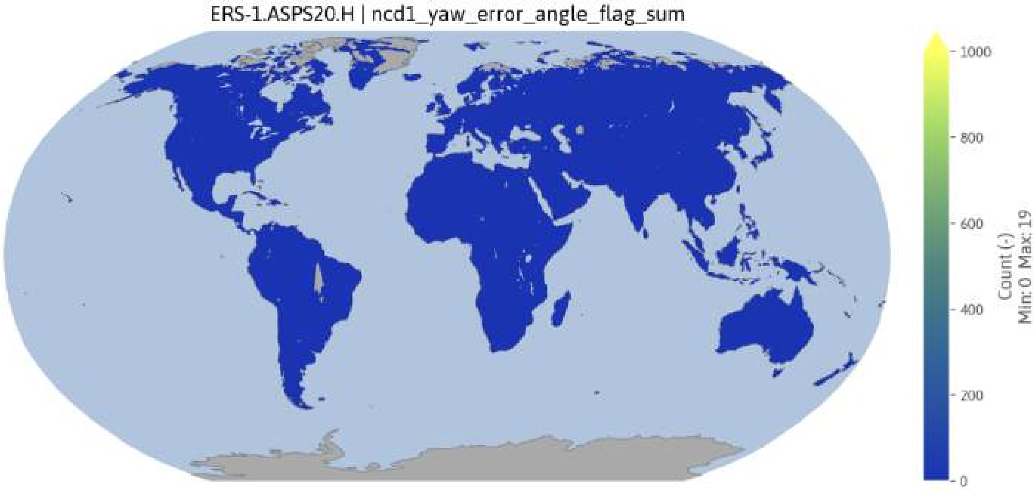

Figure 1.36: Yaw error flag for dataset `ERS-1.ASPS20.H`.

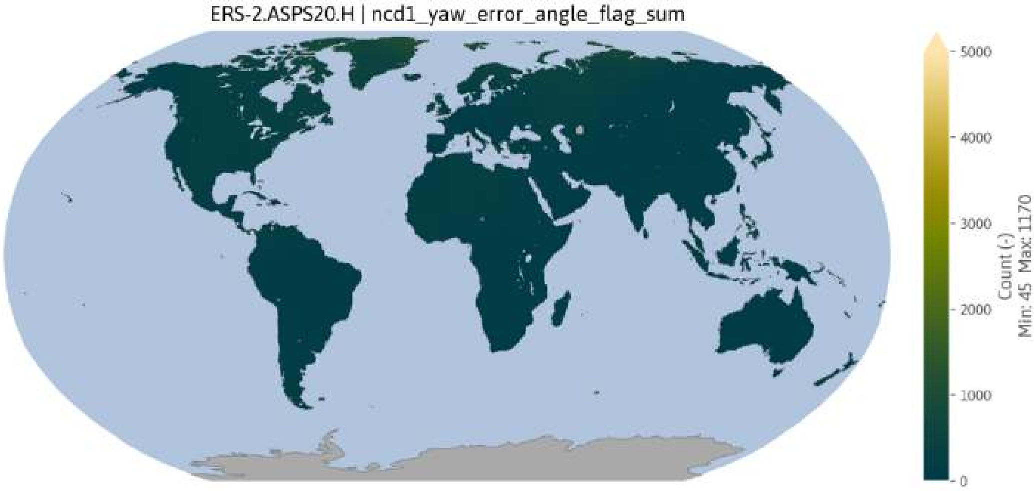

Figure 1.37: Yaw error flag for dataset `ERS-2.ASPS20.H`.

The yaw error angle represents the deviation of the satellite's orientation from its intended yaw direction. It affects both the accuracy of Doppler frequency compensation and the correct positioning of radar measurements on the ground. In the case of ERS-2, 3 of 6 on-board gyroscopes failed in 2000 and the satellite operated in a degraded mode, requiring estimation of the yaw error angle to adjust for Doppler shifts and ensure proper signal processing and sample positioning. The number of absolute yaw error angle flags raised for ERS-2 can be seen in Figure 1.37. Approximately 90% of the time series contain between 100 and 600 observations flagged with the yaw error angle, predominantly concentrated in a specific period shortly after 2000.

No major issues regarding on-board gyroscopes have been reported for ERS-1 and the number of yaw error angle flags raised is very low (Figure 1.36) compared to ERS-1.

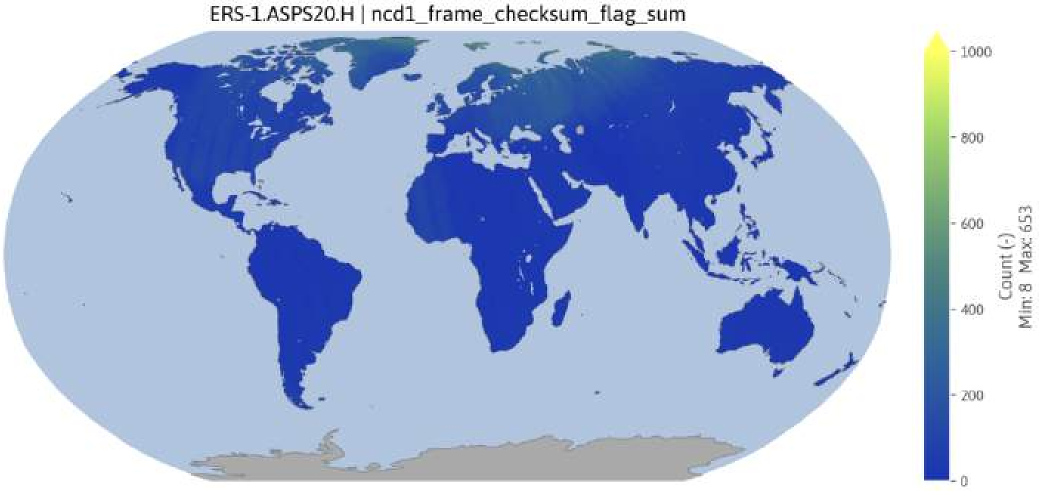

Figure 1.38: Frame checksum flag for dataset `ERS-1.ASPS20.H`.

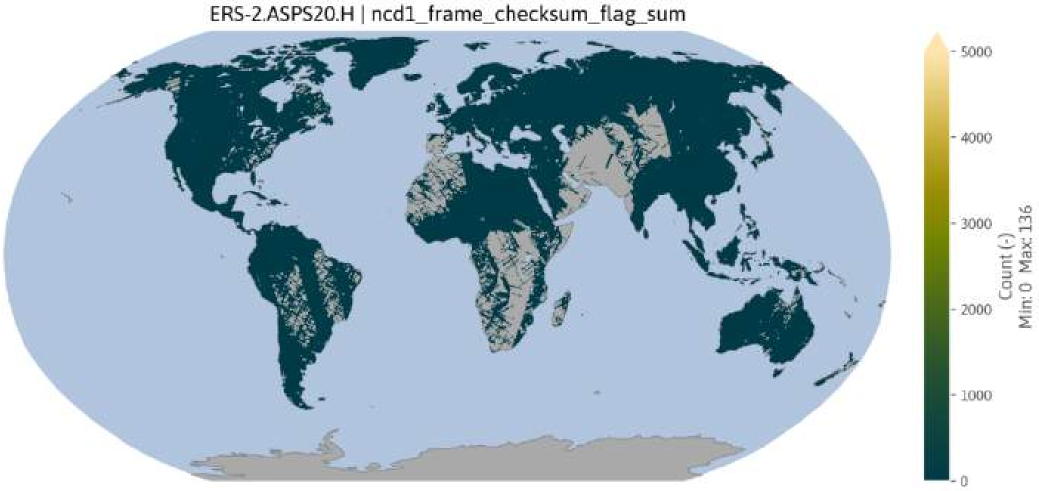

Figure 1.39: Frame checksum flag for dataset `ERS-2.ASPS20.H`.

A checksum analysis on Low Rate (LR) frames is performed by the Frame Synchronizer. When errors occur, the system flags the event, replaces faulty data with defaults, and tracks error counts. If errors exceed a threshold, the checksum flag is set to signal degraded data quality. In the case of ERS-1, approximately 90% of the time series contain between 20 and 100 observations flagged with a checksum error. A clustering of a higher number of occurrences (approximately between 500 and 600) can be found in North America, Europe and West Africa, similar to the spatial patterns found in the Doppler flags. A very small number of observations are flagged with a checksum error for ERS-2, with 90% of the time series showing around 5 to 15 flagged observations.

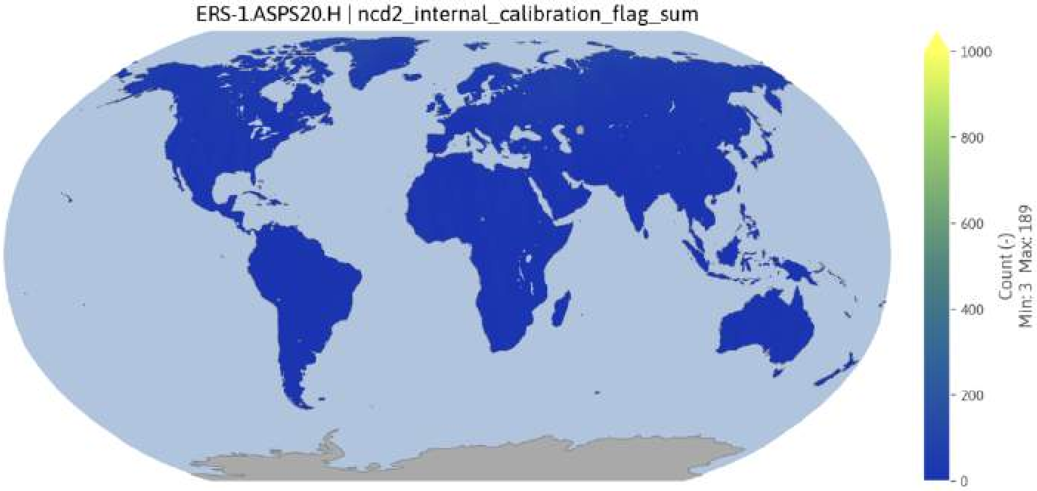

Figure 1.40: Internal calibration flag for dataset `ERS-1.ASPS20.H`.

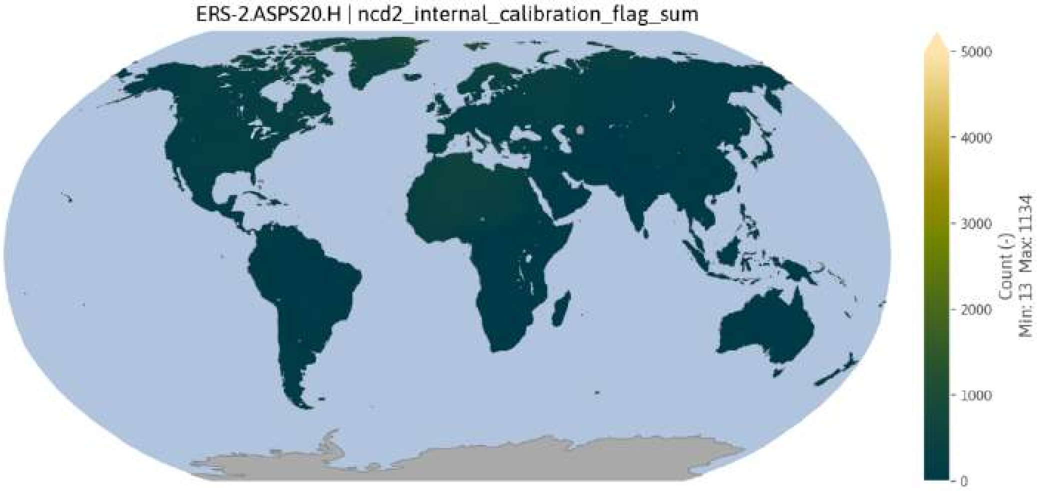

Figure 1.41: Internal calibration flag for dataset `ERS-2.ASPS20.H`.

Quality control also involves monitoring the internal calibration levels to ensure they remain within predefined limits throughout data processing. Figure 1.40 and 1.41 display the internal calibration flags for both ERS-1 and ERS-2. Neither of them shows a large number of occurrences or particular spatial clustering.

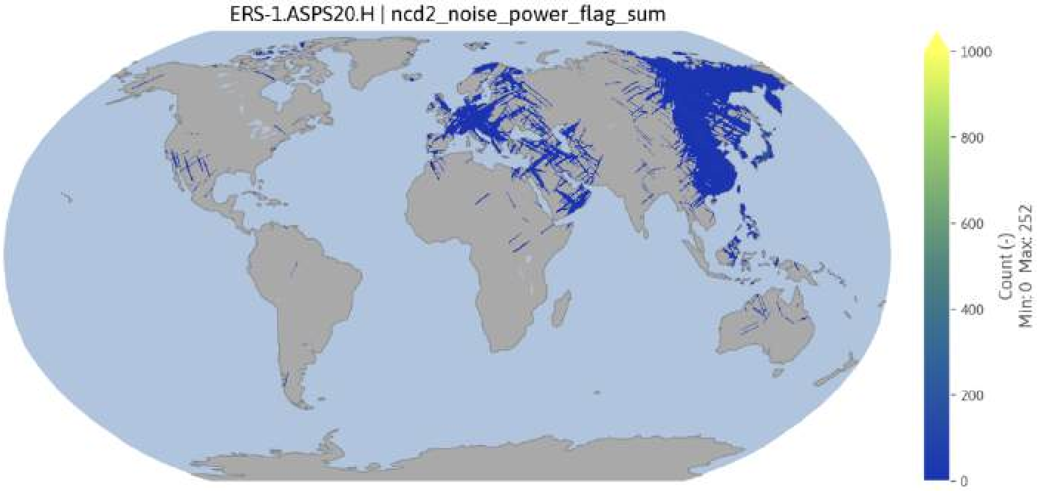

Figure 1.42: Noise power flag for dataset `ERS-1.ASPS20.H`.

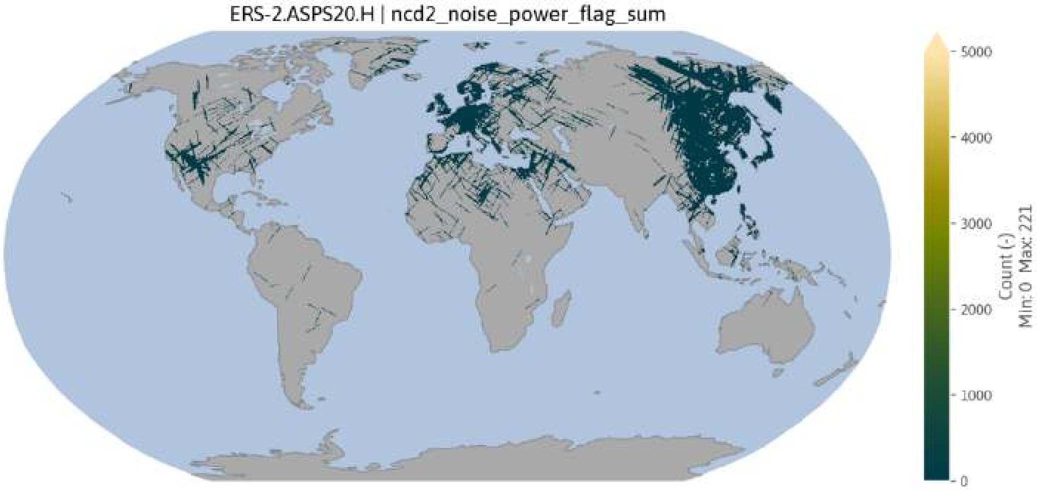

Figure 1.43: Noise power flag for dataset `ERS-2.ASPS20.H`.

The noise power flag reflects whether the noise power levels in the I and Q channels exceed predefined thresholds. For both satellites, the number of observations with a raised noise power flag is very low as indicated in Figure 1.42 and 1.43. Interestingly, there is a noticeable clustering of these flagged observations over North America, Europe and East Asia in both cases.

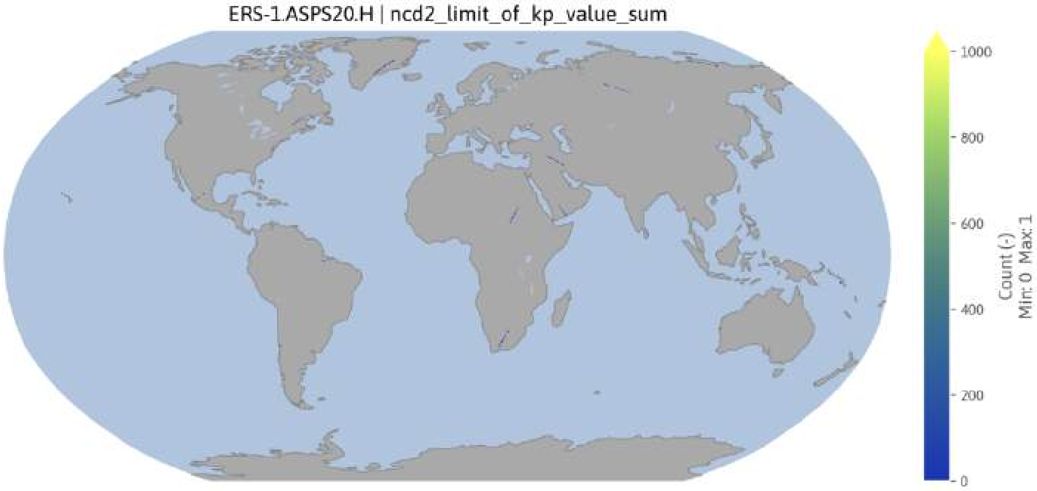

Figure 1.44: Kp flag for dataset `ERS-1.ASPS20.H`.

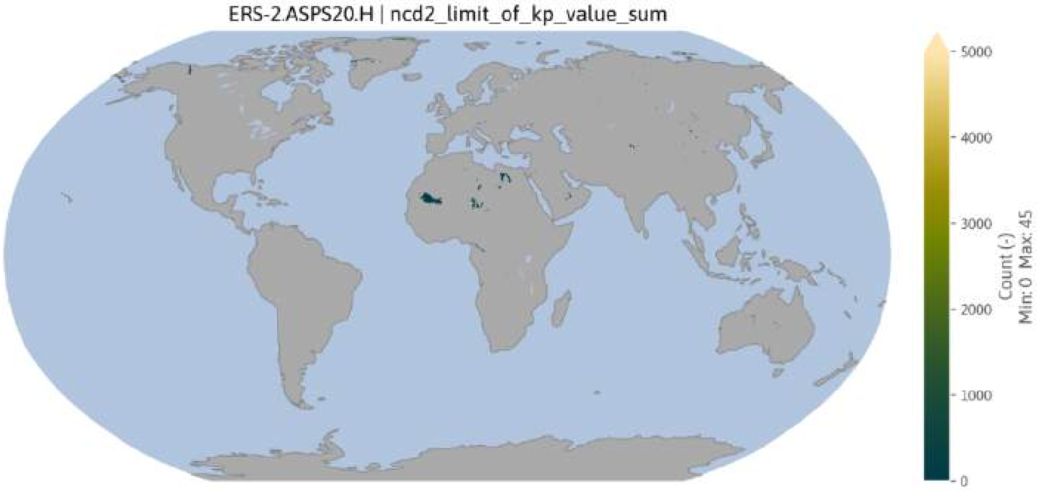

Figure 1.45: Kp flag for dataset `ERS-2.ASPS20.H`.

The Kp flag monitors the Kp value limit for each beam (fore, mid, and aft). Before wind extraction, the Kp value is estimated and compared to a predefined threshold. If any beam exceeds this threshold, the flag is raised. The number of times the flag is raised over land is very low (Figure 1.44 and 1.45). For ERS-2, there appears to be slight clustering in the sandy regions of the Sahara Desert.

1.4. Spatial and temporal sampling statistics

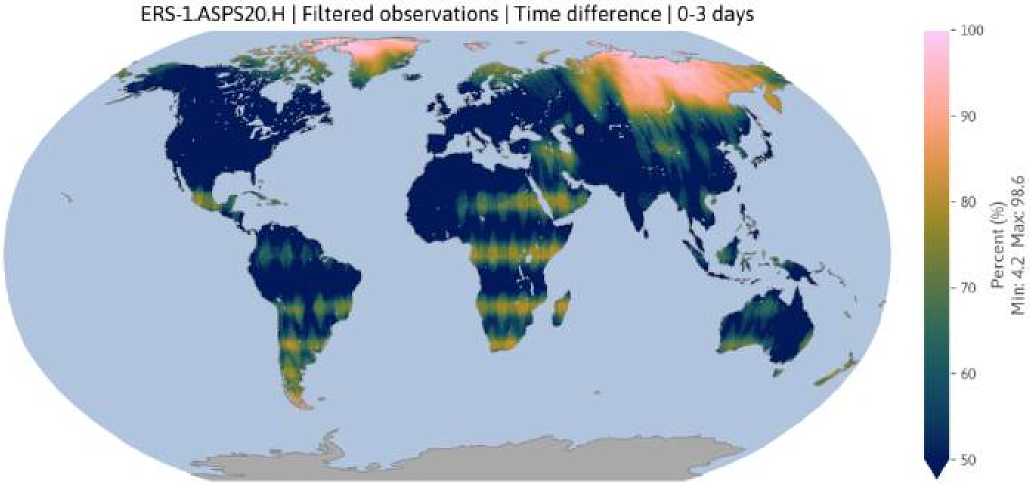

Figure 1.46: Relative number of observations with a time difference between 0 and 3 days for the dataset `ERS-1.ASPS20.H`.

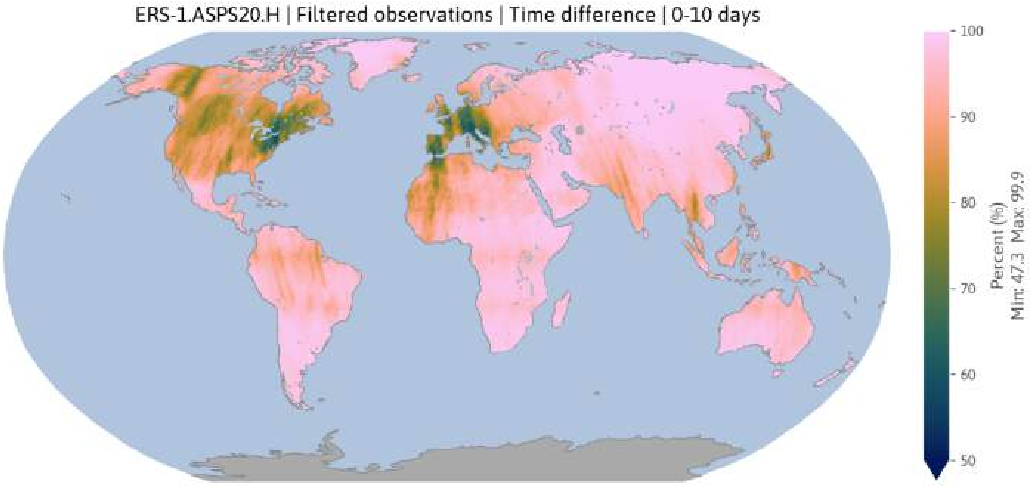

Figure 1.47: Relative number of observations with a time difference between 0 and 10 days for the dataset `ERS-1.ASPS20.H`.

In order to analyze the spatial and temporal sampling characteristics, the time difference between successive observations was calculated. Figure 1.46 shows the percentage of observations with a time difference between 0 and 3 days. The spatial sampling pattern is typical for a polar-orbiting satellite, though a higher number of observations in North America, Europe, and Southwest Asia exhibit longer time intervals between consecutive observations.

Examining the same statistic for a time difference of 0 to 10 days (Figure 1.47) reveals that 90% to 100% of observations have a time difference of less than 10 days. For this time range, a distinct latitude pattern is no longer apparent.

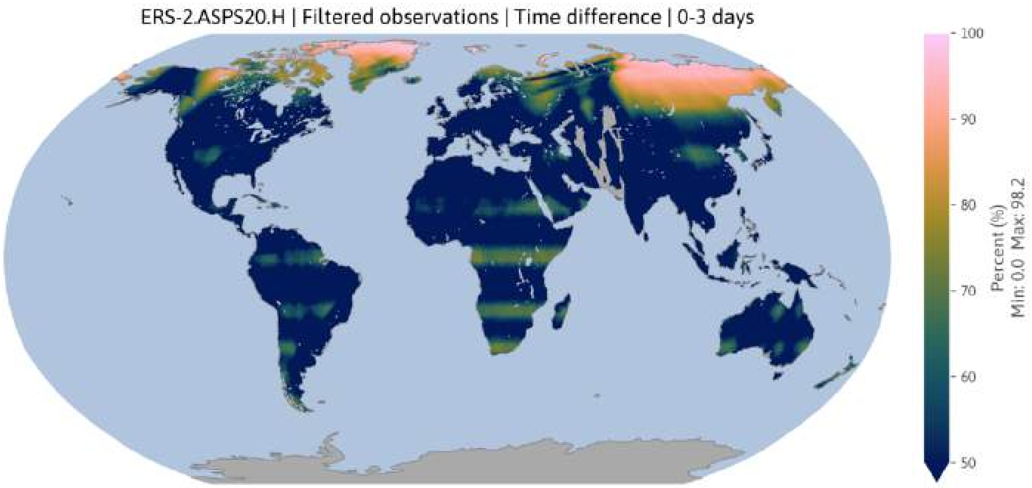

Figure 1.48: Relative number of observations with a time difference between 0 and 3 days for the dataset `ERS-2.ASPS20.H`.

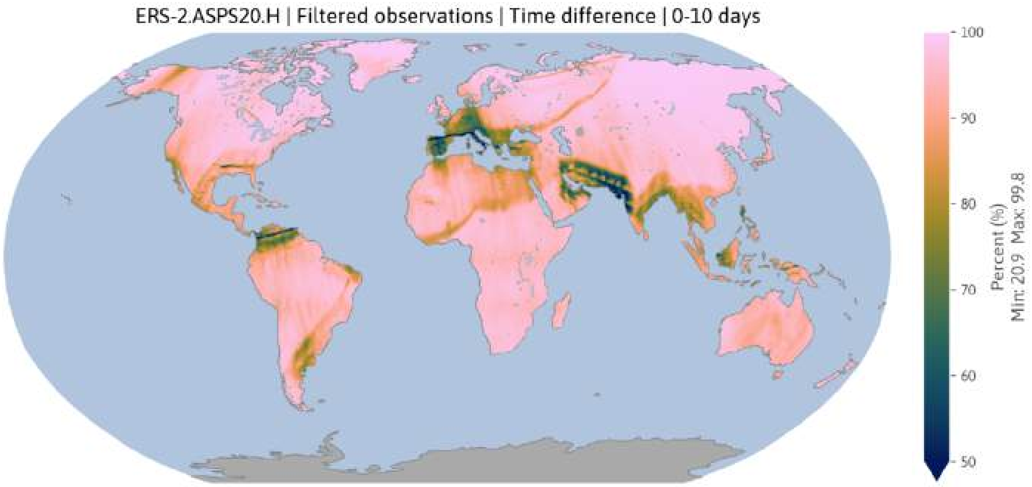

Figure 1.49: Relative number of observations with a time difference between 0 and 10 days for the dataset `ERS-2.ASPS20.H`.

ERS-2 exhibits a similar spatial pattern for a time difference of 0 to 3 days, with a clear dependency on latitude (Figure 1.48). Likewise, the statistics for 0 to 10 days show that 90% to 100% of observations occur within this time frame (Figure 1.49).

It is important to note that these statistics may not detect larger gaps if they occur only in a few isolated cases. However, if such gaps occur regularly, the statistics would reflect them.

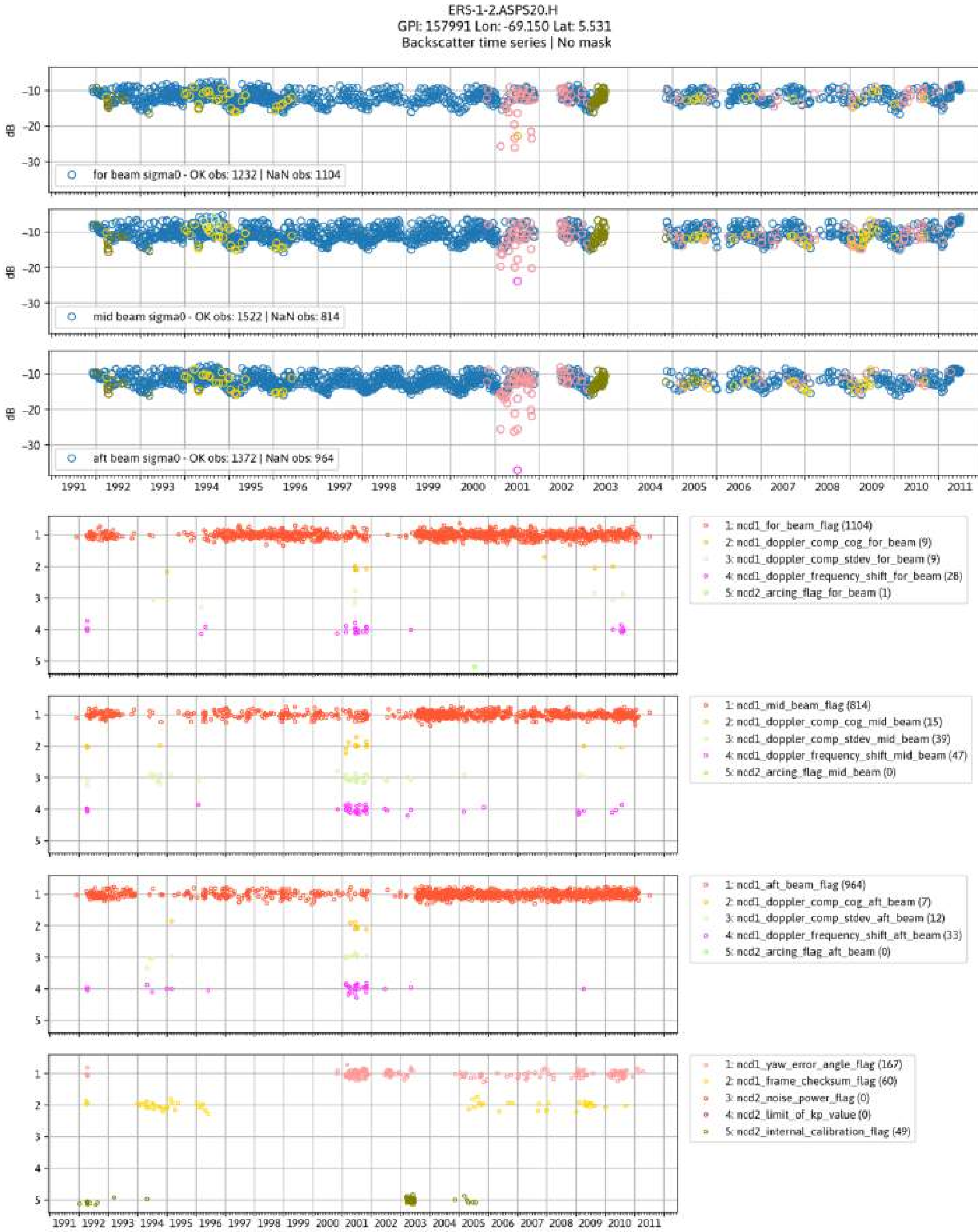

Figure 1.50: `ERS-1-2.ASPS20.H` time series example for a location in Colombia 5.53° N -69.15° W.

A time series example is shown in Figure 1.50. The time series (top) displays the fore, mid, and aft beam backscatter, along with the corresponding individual flags (below) for a location in Colombia, South America (5.53° N -69.15° W). Backscatter observations flagged for yaw error angle appear as outliers in 2001, but no significant issues are evident for the other flags.

1.5. Outlier detection

A global outlier detection method was employed to identify any flagged and unflagged outliers. Quantile regression [5], [6] was used to model the 5th and 95th percentiles of the incidence angle dependency of backscatter and detect outliers. The Fore, Mid, and Aft beams were evaluated separately. An observation σ_i^0 with predictor θ_i is considered an outlier if its squared difference from the quantile regression estimate $\hat{Q}_\tau(\theta_i)$ is larger than 4 dB:

$$(\sigma_i^0 - \hat{Q}_{0.05}(\theta_i))^2 > 4\,\mathrm{dB} \tag{1}$$

$$(\sigma_i^0 - \hat{Q}_{0.95}(\theta_i))^2 > 4\,\mathrm{dB} \tag{2}$$

where $\hat{Q}_{0.05}(\theta_i)$ and $\hat{Q}_{0.95}(\theta_i)$ are the estimated 5th and 95th percentiles from quantile regression. The threshold of 4 dB was empirically determined by examining individual time series observations.

In the case of `ERS-1.ASPS20.H`, the majority of lower outliers correspond to individual observations flagged by various node confidence data fields, including the Doppler compensation COG, Doppler compensation standard deviation, Doppler frequency shift, frame checksum, yaw error angle, and internal calibration flag (see Figure 1.52). A spatial visualization of lower outliers reveals that erroneous data is often confined to specific orbits or segments thereof (see Appendix A.1, Figure A.1-A.15). However, there seem to be a number of lower outliers that are not flagged by any of the node confidence data fields, mostly clustered around higher latitudes (e.g., Greenland or northern Russia). As can be seen in Figure 1.51, such outliers can be related to natural signal variations. The year 1995 was exceptionally warm for Greenland, with an increase in surface melt extent, particularly along Greenland's southern and western coasts. These melting events were likely responsible for the significant drop in the backscatter signal, although some of the observations were flagged.

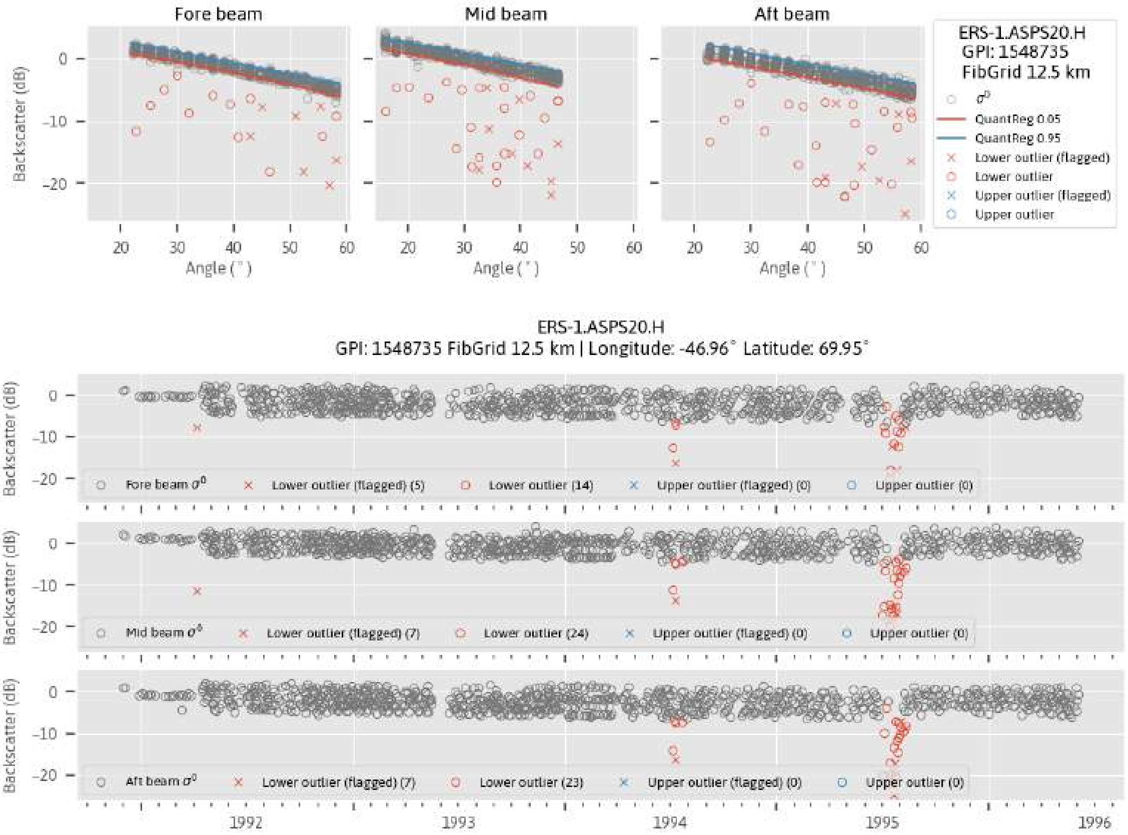

Figure 1.51: `ERS-1.ASPS20.H` σ^0 time series and incidence angle relationship for a grid point in Greenland (GPI: 1548735, FibGrid 12.5 km)

Upper outliers, on the other hand, do not seem to be as frequent, except for the Mid beam (see Figure 1.54). No obvious orbit patterns are visible, and outliers seem to cluster in the center of Greenland and East Africa. The Mid beam shows additional outliers over North America, Eastern Europe, and Australia (see Appendix A.1, Figure A.2–A.16). While some locations (e.g. Africa, Greenland, Australia, Asia) might have upper outlier detected due to natural signal variations, the majority shows that multiple node confidence data fields (Doppler compensation COG, Doppler compensation stdev, Doppler frequency shift) are set in case of the Mid beam (see Figure A.4, A.10 and A.16) and to a much lesser extent for the Fore and Aft beam (see Figure A.2, A.8 and A.14 and Figure A.6, A.12 and A.18).

A site in northern Russia (GPI: 1541998, FibGrid 12.5 km, 69.28° N, 62.85° E) does not exhibit any distinct natural target variations in the time series (Figure 1.53) that could account for the upper outliers, which are predominantly observed in the Mid beam. Hence, as indicated by the node confidence data fields, these σ^0 observations are flagged as being of poor quality.

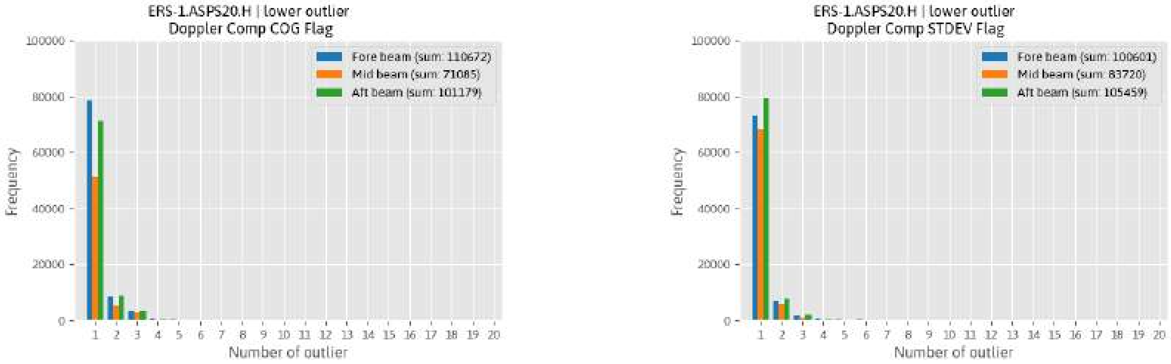

(a) Doppler compensation COG

(b) Doppler compensation standard deviation

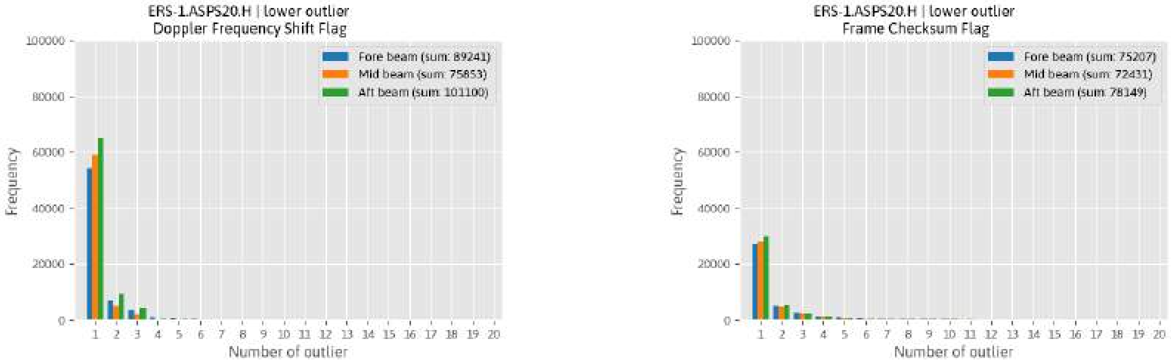

(c) Doppler frequency shift

(d) Frame checksum

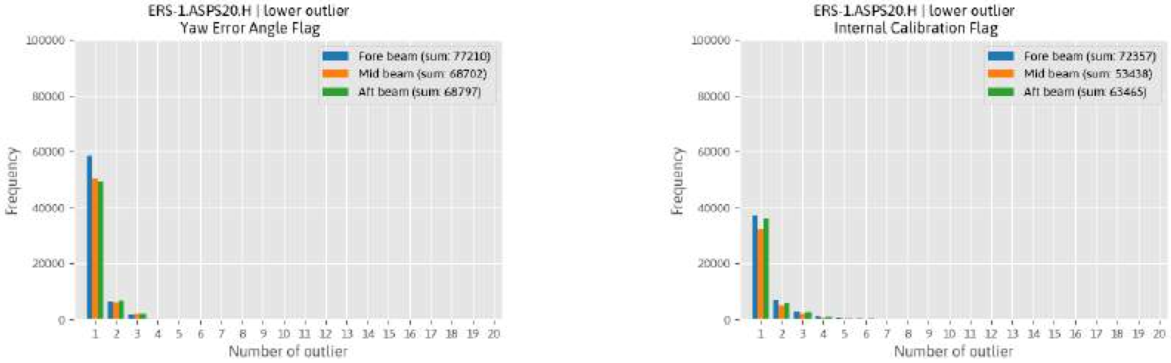

(e) Yaw error angle

(f) Internal calibration flag

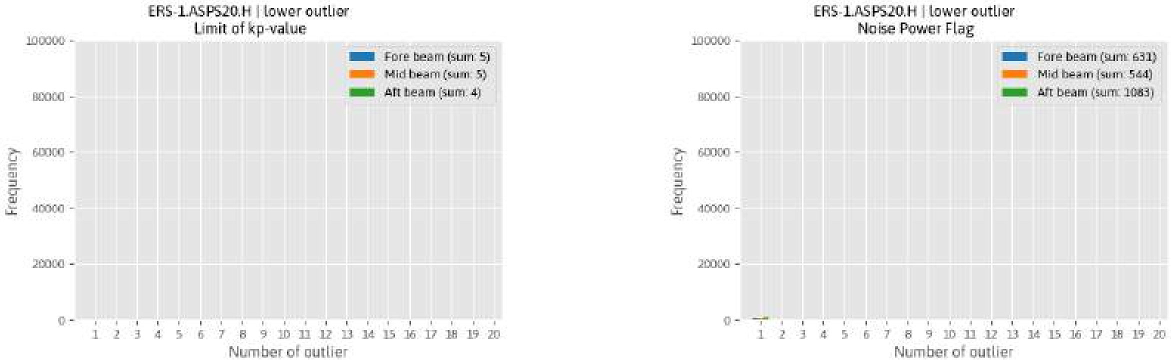

(g) Limit of kp-value

(h) Noise power flag

Figure 1.52: Count of lower outliers flagged by node confidence flag - `ERS-1.ASPS20.H`.

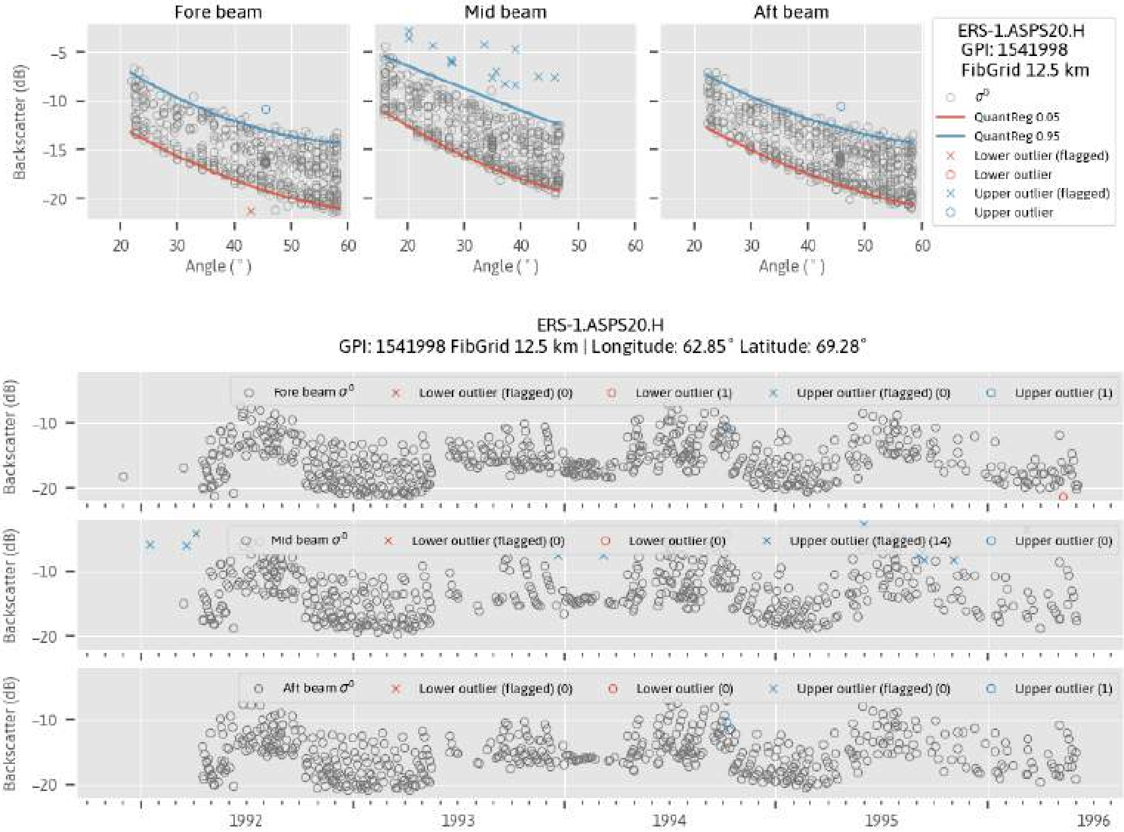

Figure 1.53: `ERS-1.ASPS20.H` σ^0 time series and incidence angle relationship for a grid point in northern Russia (GPI: 1541998, FibGrid 12.5 km)

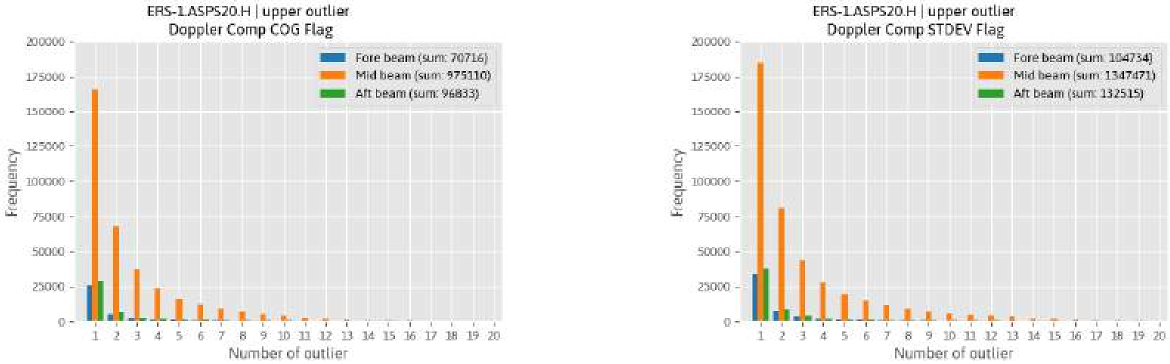

(a) Doppler compensation COG

(b) Doppler compensation standard deviation

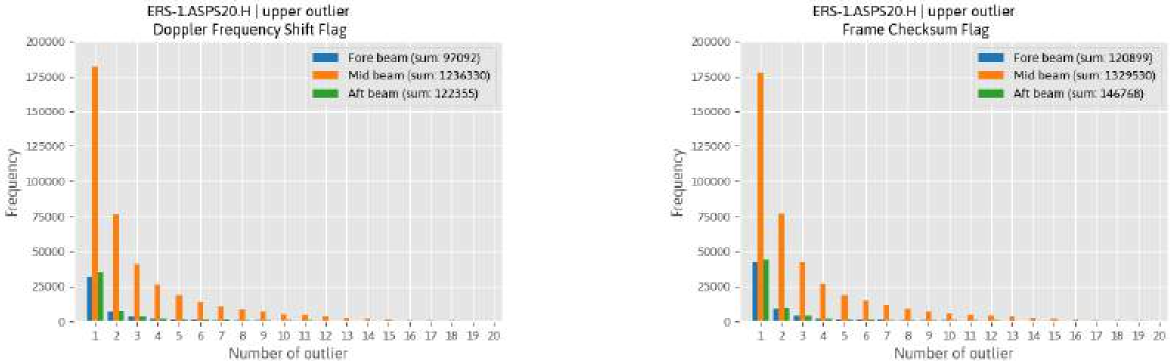

(c) Doppler frequency shift

(d) Frame checksum

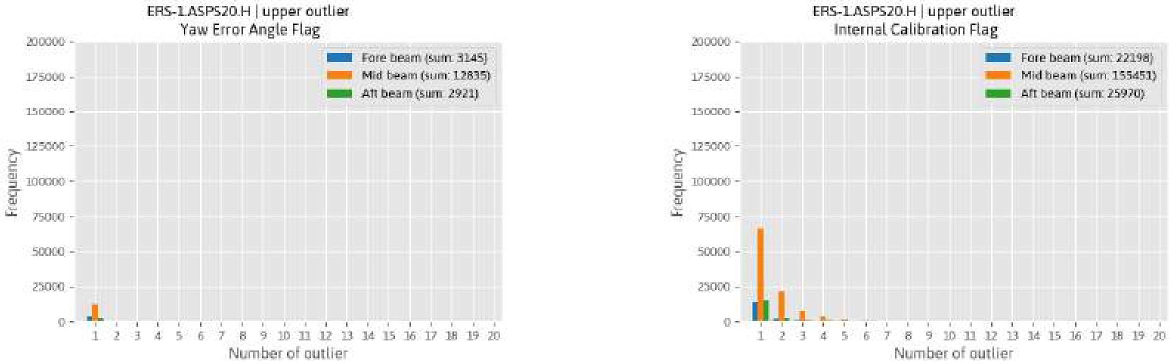

(e) Yaw error angle

(f) Internal calibration flag

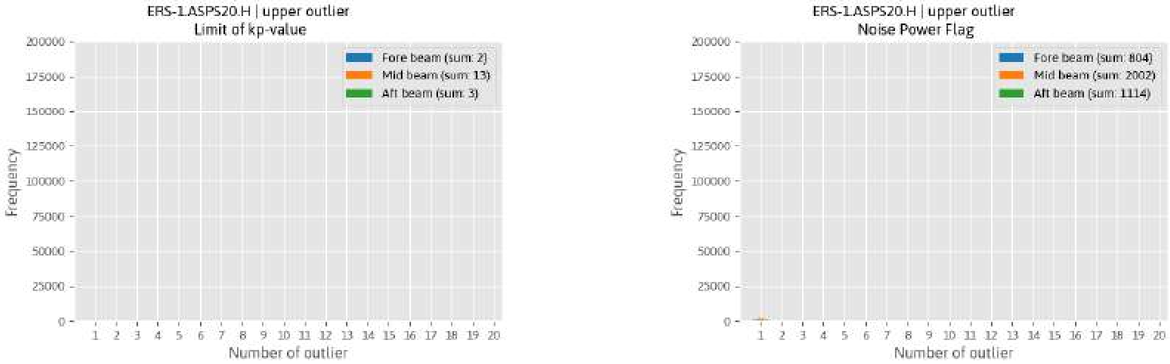

(g) Limit of kp-value

(h) Noise power flag

Figure 1.54: Count of upper outliers flagged by node confidence flag - `ERS-1.ASPS20.H`.

In the case of `ERS-2.ASPS20.H`, the Fore, Mid and Aft beam have a similar number of lower outlier (see Figure 1.56) and overall more outliers compared to `ERS-1.ASPS20.H`. The highest number of outliers is associated with the node confidence data fields: Doppler compensation COG, Doppler compensation standard deviation, Doppler frequency shift, and yaw error angle flag. In contrast, the frame checksum and internal calibration flag typically indicate only a single outlier per grid point, likely due to individual lower-quality orbits.

Spatial maps reveal a similar cluster of lower outliers in regions such as Greenland, northern Russia, and the sandy deserts of Africa, most likely due to natural signal variations or anomalies. (see Appendix A.2, Figure A.43–A.84). An example σ^0 time series is shown in Figure 1.55 for a grid point located in northern Africa. Approximately half of the lower outliers are flagged, while the other half appear to have been recorded at a very high incidence angle in the case of the Fore and Aft beam, which could explain why they are considered outliers.

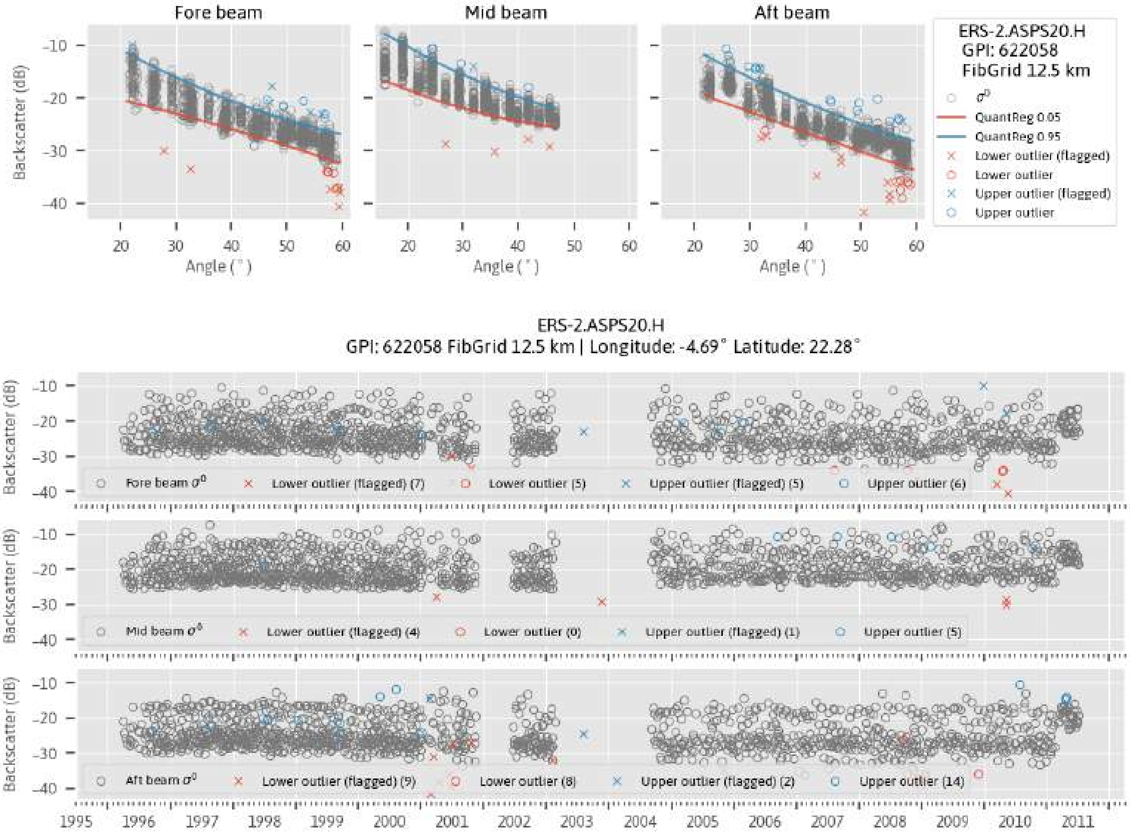

Figure 1.55: `ERS-2.ASPS20.H` σ^0 time series and incidence angle relationship for a grid point in northern Africa (GPI: 622058, FibGrid 12.5 km)

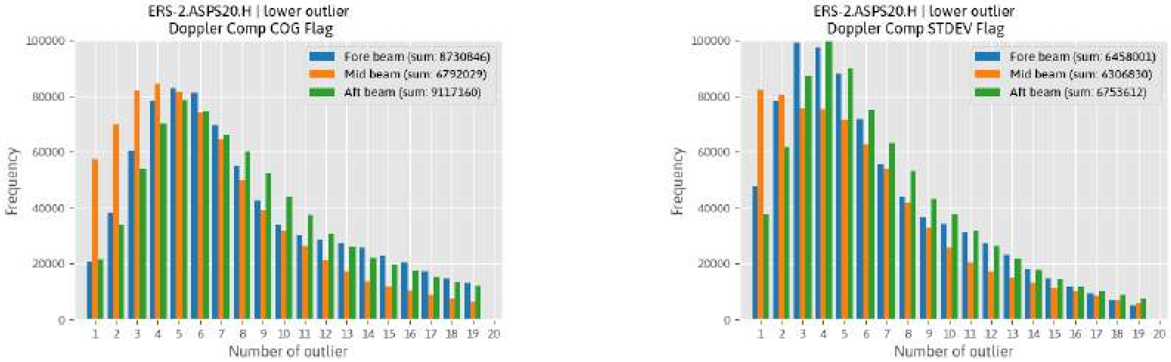

(a) Doppler compensation COG

(b) Doppler compensation standard deviation

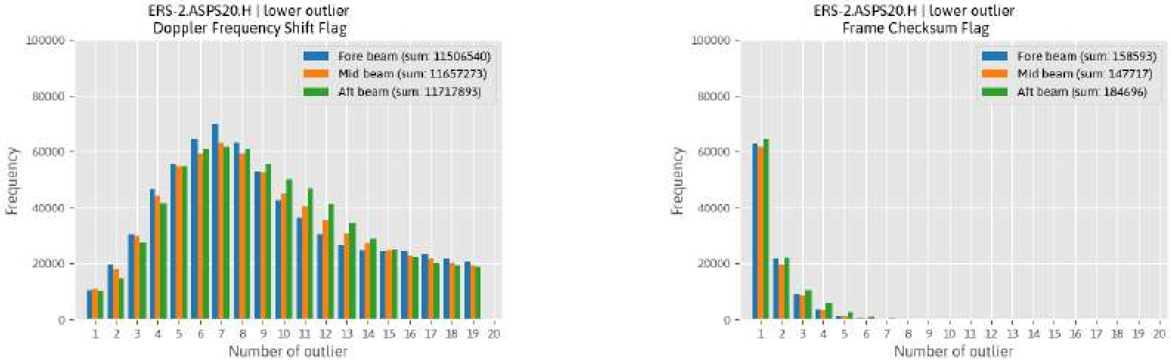

(c) Doppler frequency shift

(d) Frame checksum

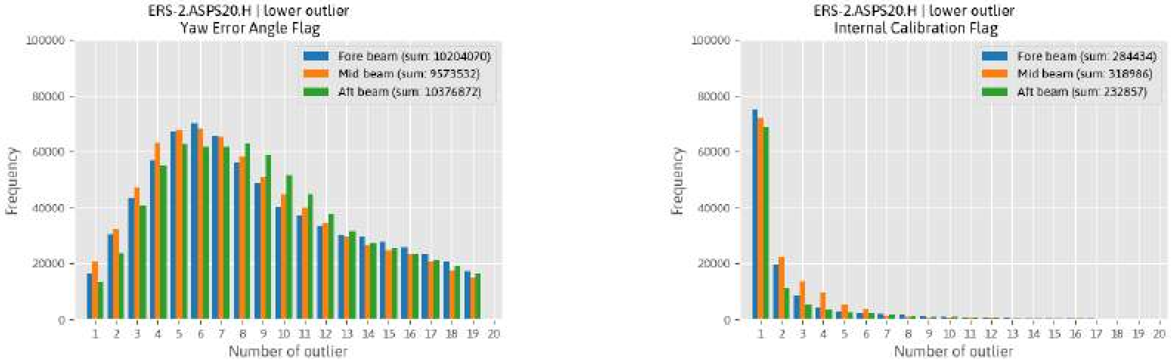

(e) Yaw error angle

(f) Internal calibration flag

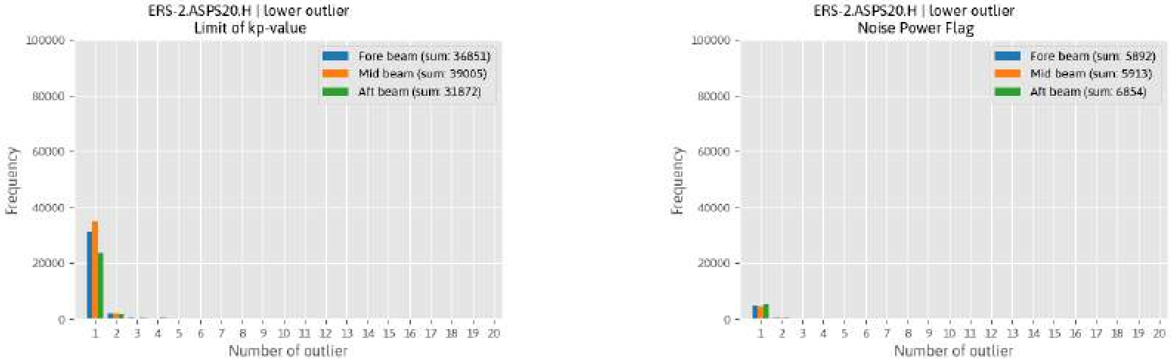

(g) Limit of kp-value

(h) Noise power flag

Figure 1.56: Count of lower outliers flagged by node confidence flag - `ERS-2.ASPS20.H`.

Similar to `ERS-1.ASPS20.H`, `ERS-2.ASPS20.H` also appears to have significantly fewer upper outliers compared to lower outliers. In addition, no Mid beam anomaly is observed, unlike in `ERS-1.ASPS20.H`. Histograms show that these outliers seem to be isolated instances indicative of erroneous orbits rather than forming a distinct cluster (see Figure 1.58).

Spatial maps of the upper outlier confirm this assumption, since no particular pattern can be found except for the yaw error angle flag(see Appendix A.2, Figure A.43–A.84). A small cluster of upper outliers is scattered across Africa, Australia, and Asia, consistently appearing in all three beams. An example of a σ^0 time series for a location in northeastern Africa is shown in Figure 1.57. Fore and Aft beam outliers appear to be signal anomalies exceeding the 4 dB threshold, which may be too conservative for regions with consistently low backscatter signals. In the case of the Mid beam, most of the outliers occur at incidence angles between 32–34°, where Bragg scattering plays a dominant role. Wind-driven ripples forming on sand dunes can enhance radar backscatter, leading to these observations being identified as outliers.

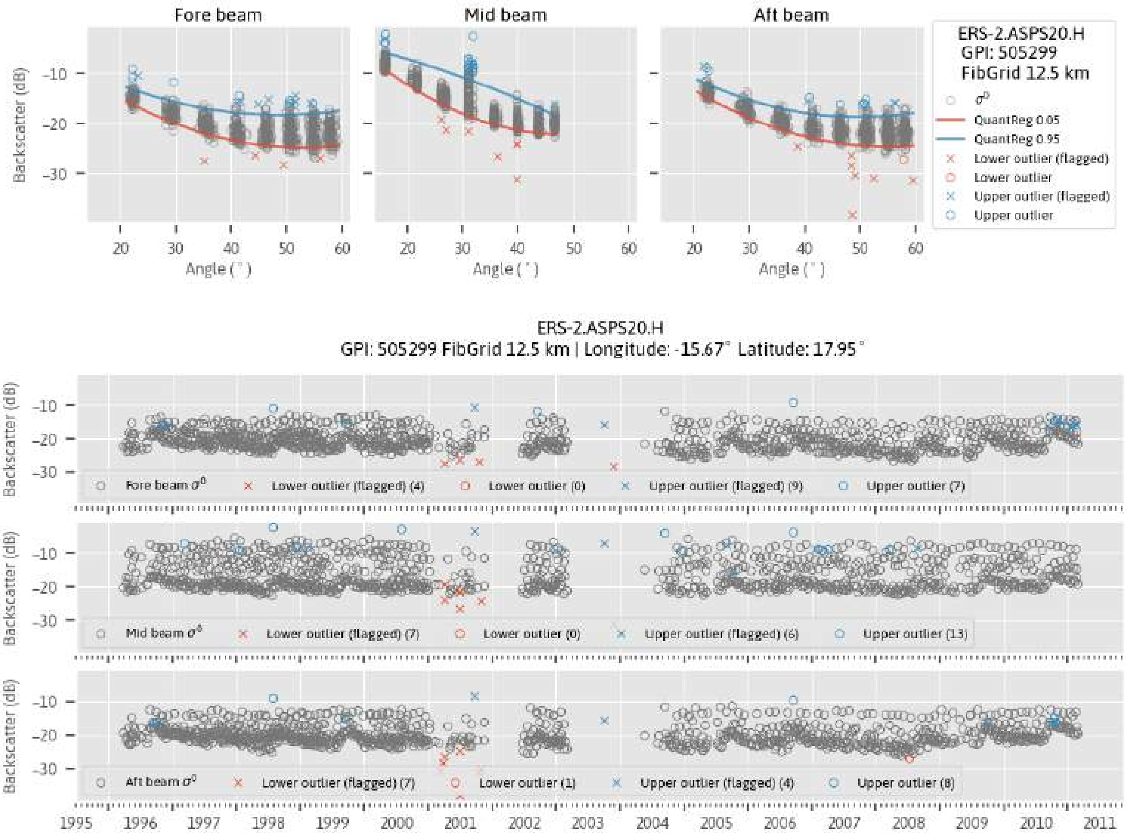

Figure 1.57: `ERS-2.ASPS20.H` σ^0 time series and incidence angle relationship for a grid point in northern Africa (GPI: 505299, FibGrid 12.5 km)

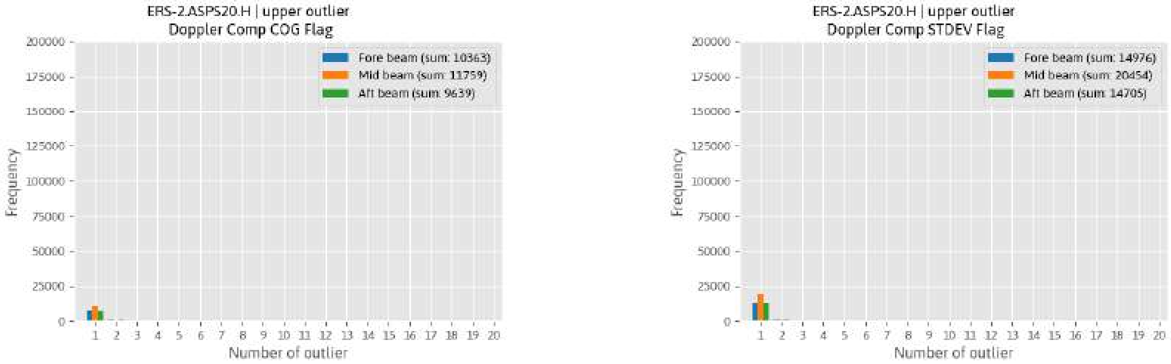

(a) Doppler compensation COG

(b) Doppler compensation standard deviation

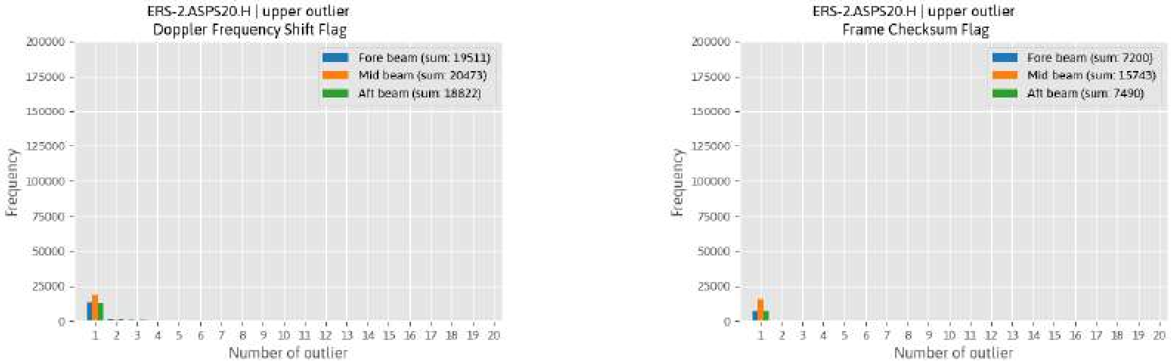

(c) Doppler frequency shift

(d) Frame checksum

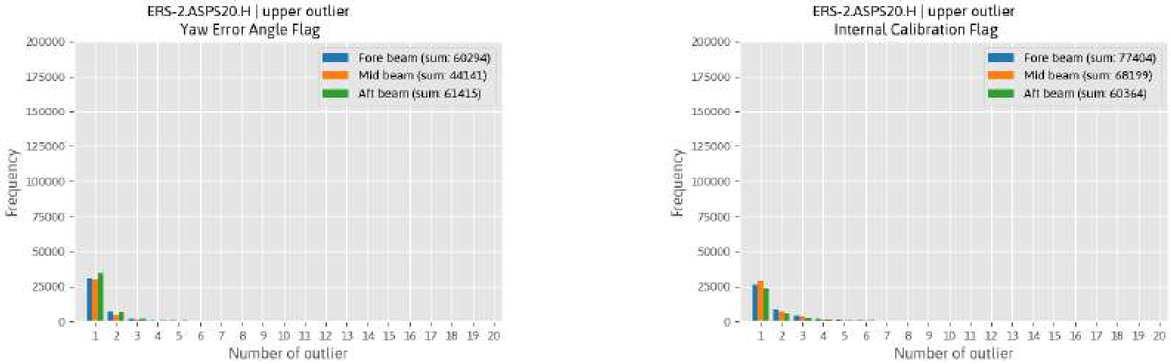

(e) Yaw error angle

(f) Internal calibration flag

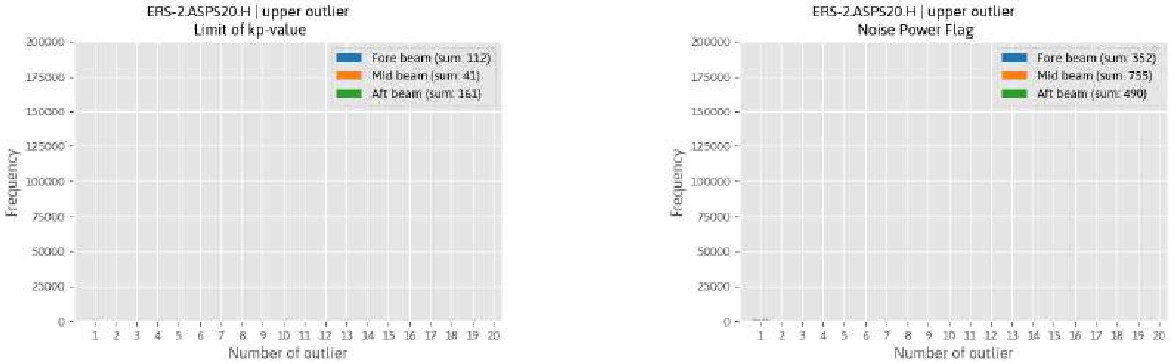

(g) Limit of kp-value

(h) Noise power flag

Figure 1.58: Count of upper outliers flagged by node confidence flag - `ERS-2.ASPS20.H`.

1.6. Summary

The latest version of the Advanced Scatterometer Processing System (ASPS) 10.04 has been used to reprocess ERS-1 and ERS-2 scatterometer Level 2.0 products. These datasets are available in both high-resolution (25 km) and nominal-resolution (50 km) formats.

Product	First File	Last File
`ERS1.ASPS20.H`	`1991-08-01 05:14:57`	`1996-06-02 20:49:04`
`ERS1.ASPS20.N`	`1991-08-01 05:14:57`	`1996-06-02 20:49:04`
`ERS2.ASPS20.H`	`1996-03-26 00:10:11`	`2011-07-04 10:59:02`
`ERS2.ASPS20.N`	`1996-03-26 00:10:11`	`2011-07-04 10:59:04`

Table 1.12: First and Last File Dates for ERS-1 and ERS-2 ASPS20 Level 2.0 products.

All datasets have been analyzed for completeness, missing orbit patterns, and overall data quality by evaluating statistical distributions of node confidence data flags and performing outlier detection. To support the planned inter-calibration of Metop ASCAT with ERS-1 and ERS-2, the high-resolution format has been given priority in the presentation and discussion of the analysis results. Nevertheless, no significant difference in terms of quality or completeness has been found between the high-resolution (25 km) and nominal-resolution (50 km) formats for both, ERS-1 and ERS-2.

There are known periods with missing data due to various mission-related issues, most notably for ERS-2 [2]. A list of gaps found in the ASPS20 datasets is summarized in the Tables 1.5, 1.6, 1.7 and 1.8. Absolute orbit numbers were converted to relative orbit numbers based on mission phase parameters (i.e., orbit repeat cycle) to identify potential patterns in missing orbit files. However, no specific pattern was found.

The ASPS20 swath data has been mapped to a fixed Earth grid using a nearest-neighbor approach, preserving the original data and flags while representing it in a time series format. As a reference grid, the so-called Fibonacci grid was used with two different sampling distances (12.5 km and 25 km). No data integrity issues (e.g., corrupt files) were identified during pre-processing. However, duplicate observations had to be removed at the equator, where resampling two consecutive swaths lead to multiple observations assigned to the same grid point.

The absolute number of observations (including both valid and NaN σ^0 triplets from all available files) for `ERS1.ASPS20.H` (Figure 1.6), `ERS2.ASPS20.H` (Figure 1.7) shows the expected latitude-dependent pattern characteristic of a polar-orbiting satellite instrument, with both the number and frequency of observations increasing towards higher latitudes. When considering only valid σ^0 triplets (i.e., cases where the node confidence data flags 1 and 2 are not set and all three beams contain valid, non-NaN values), specific regions exhibit a reduced number of observations due to critical mission-related issues such as the ERS-2 gyro and tape recorder failures, as well as the accumulation of node confidence flags being set.

A more detailed analysis of the node confidence data 1 and 2 flags (see Table 1.10 and 1.11) revealed that flags associated with power spectrum characteristics (Doppler compensation COG and standard deviation) and Doppler frequency shift were more frequently observed over North America, Greenland,and northeastern Europe for ERS-1 and ERS-2. The arcing flag, in the case of ERS-2, occurred much less frequently and spatially dispersed compared to ERS-1, which again exhibited clustering in the aforementioned regions. The noise power flag displayed a higher frequency of occurrence over parts of Europe, North America, and particularly eastern Asia, whereas the limit of the Kp value flag was rarely set over land, except for sandy deserts in Africa in the case of ERS-2. No distinct spatial distribution has been found in case of the yaw error angle flag, which is generally very low for ERS-1 and due to the gyro failure of ERS-2 much more frequent. Also no specific spatial distribution has been found for the internal calibration flag or any large number of occurrences. Errors detected by the checksum analysis on Low

Rate (LR) frames, as performed by the Frame Synchronizer, are recorded in the frame checksum flag. For ERS-1, this flag shows clustering over northeastern Europe and Greenland, whereas for ERS-2, it displays a more uniform distribution, with certain areas excluded.

Finally, a global outlier detection method using quantile regression was applied to identify σ^0 anomalies. Observations were classified as outliers if their squared difference from the regression estimate exceeded 4 dB, a threshold determined empirically. For `ERS-1.ASPS20.H`, most lower outliers were flagged by node confidence data fields related to Doppler compensation, frame checksum, yaw error angle, and internal calibration issues. Spatial analysis revealed that erroneous data often occurred in specific orbits, while some unflagged lower outliers, particularly in high-latitude regions such as Greenland and northern Russia, were likely caused by natural signal variations. In 1995, an exceptionally warm year in Greenland led to extensive surface melting, which resulted in a significant drop in the backscatter signal. Upper outliers were less frequent and showed no clear orbit patterns, with the Mid beam displaying additional outliers over North America, Eastern Europe, and Australia. Some of these may be explained by natural variations, but others were associated with flagged node confidence data, particularly in the Mid beam.

For `ERS-2.ASPS20.H`, all three beams exhibited similar numbers of lower outliers, with more overall outliers than `ERS-1.ASPS20.H`. The highest number of flagged outliers was associated with Doppler compensation and yaw error angle flags. Spatially, lower outliers clustered around Greenland, northern Russia, and sandy deserts in Africa, likely due to natural variations. Upper outliers were significantly less common and did not show the Mid beam anomaly seen in `ERS-1.ASPS20.H`. Instead, they appeared as isolated instances, likely representing erroneous orbits. A small number of upper outliers clustered in Africa, Australia, and Asia, consistent across all three beams, with Bragg scattering effects in sand dune regions.

Analyzing the spatial distribution and frequency of σ^0 outliers in combination with node confidence data flags for ERS-1 and ERS-2 indicates a good quality of σ^0 data on a global scale. Also, in many cases, it cannot be ruled out that the identified outliers are due to natural signal variations. Therefore, we recommend filtering σ^0 observations using node confidence data flags before processing FDR4LDYN products, while reserving outlier detection for only the most extreme cases. However, mission-related data gaps, particularly for ERS-2, along with gaps introduced by data filtering, may pose challenges for the robust estimation of FDR4LDYN products and should be carefully monitored throughout the processing.

2. Quality control and calibration of ERS-1 and ERS-2 ESCAT data

2.1. Natural calibration targets for ESCAT backscatter

Rainforested regions provide reliable natural calibration targets for scatterometer data [7], [8]. To evaluate ESCAT backscatter calibration globally, we consider three rainforest regions at different longitudes as natural targets (Figures 2.1 and 2.2), examining the stability of backscatter measurements over these regions over time, as well as agreement between the instrument azimuth configurations.

Following [8], we selected natural targets in ESCAT data based on three criteria: azimuthal isotropy, temporal stability, and spatial homogeneity of backscatter measurements (Table 2.2). We analyzed data from the Amazon, Congo, Borneo, Sumatra, and the Malay Peninsula (the latter three considered together as one target – “Southeast Asia”) over each satellite’s complete operational period to find Fibonacci grid points for which observed backscatter measurements fulfill all three criteria.

Data was filtered before analysis. We used only observations which were valid triplet measurements (where all three beams had non-null backscatter and incidence angle values and more than 50 echoes) and which raised no quality flags. For ERS-2, we excluded data from the year 2001 (Zero-Gyro-Mode) and after 2004 due to measurement instabilities that became apparent in the course of analyzing the data. Finally, any grid points with very few (<10) observations were excluded from consideration.

To quantify the selection criteria, we follow the methodology described in [8]. For azimuthal anisotropy, we calculated the mean difference between fore and aft-beam observations for each grid point, orbit direction (ascending/descending), and swath. The maximum of these means was used as the anisotropy measure for each grid point.

An estimate of long-term mean backscatter was calculated by first normalizing the observations to a reference incidence angle of 40°. For each location (grid point) L and azimuth configuration ϕ_j, we modelled the incidence angle dependence as follows:

$$\sigma^0(L, \theta, \phi_j) = B_0(L, 40^\circ, \phi_j) + B_1(L, 40^\circ, \phi_j) \cdot (\theta - 40^\circ) \tag{3}$$

where θ is the incidence angle, B_0 represents the backscatter at the reference angle, and B_1 is the slope parameter. Individual observations were normalized to 40° using:

$$\sigma^0(L, t_i, 40^\circ, \phi_j) = \sigma^0(L, t_i, \theta, \phi_j) - B_1(L, 40^\circ, \phi_j) \cdot (\theta - 40^\circ) \tag{4}$$

The long-term mean backscatter estimate for each grid point was then computed as the average of B_0 across all azimuth configurations:

$$\overline{\sigma^0}(L, 40^\circ) = \frac{1}{n_{\text{azimuth}}} \sum_{j=1}^{n_{\text{azimuth}}} B_0(L, 40^\circ, \phi_j) \tag{5}$$

To assess temporal stability, we calculated the variance of normalized backscatter for each azimuth configuration.

$$\nu^2(L, 40^\circ, \phi_j) = \frac{1}{n} \sum_{i=1}^{n} (\sigma_i^0(L, t_i, 40^\circ, \phi_j) - B_0(L, 40^\circ, \phi_j))^2 \tag{6}$$

The overall temporal variability parameter ν was then determined as the pooled standard deviation across all azimuth configurations:

$$\nu(L, 40^\circ) = \sqrt{\frac{\sum_{j=1}^{n_{\text{azimuth}}} n_j \cdot \nu^2(L, 40^\circ, \phi_j)}{\sum_{j=1}^{n_{\text{azimuth}}} n_j}} \tag{7}$$

where n_j is the number of observations used from azimuth configuration ϕ_j.

Observations for grid points fulfilling the azimuthal anisotropy and temporal variability criteria were kept, and the rest were thrown out. Using the remaining data, spatial variability of grid points within natural targets was evaluated using mean-shift clustering as described in [8, p. 45]. In brief, the most probable mean backscatter coefficient $\overline{\sigma^0}(L, 40°)$ within each target region is estimated from a probability density function, then grid points L with $\overline{\sigma^0}(L, 40°)$ deviating from that mode value by less than the backscatter homogeneity threshold are selected for use in calibration.

Figures 2.1 and 2.2 illustrate the selected grid points and their corresponding selection criteria values for both ERS satellites. In Congo and Southeast Asia, selected points differ slightly but are generally similar, but points selected from the Amazon are notably different. More points from the interior of the region were selected from ERS-2 data, whereas more exterior points were selected for ERS-1. Nevertheless, the total number of selected grid points is comparable for all satellites at the same resolution, including Metop-A, which was processed for comparison (Table 2.1).

Table 2.1: Number of grid points selected by region and satellite

Region	Satellite	Grid Spacing	# Grid Points
Amazon	ERS-1	12.5 km	14986
Amazon	ERS-2	12.5 km	14660
Amazon	Metop-A	12.5 km	13031
Congo	ERS-1	12.5 km	6174
Congo	ERS-2	12.5 km	6115
Congo	Metop-A	12.5 km	6281
SE Asia	ERS-1	12.5 km	2383
SE Asia	ERS-2	12.5 km	1990
SE Asia	Metop-A	12.5 km	2063
Amazon	ERS-1	25 km	4469
Amazon	ERS-2	25 km	4224
Congo	ERS-1	25 km	1690
Congo	ERS-2	25 km	1679
SE Asia	ERS-1	25 km	707
SE Asia	ERS-2	25 km	671

Table 2.2: Criteria for selection of natural targets.

Criterion	**ERS limit**	**Metop limit**
Azimuthal anisotropy	0.3 dB	0.2 dB
Temporal variability	0.4 dB	0.4 dB
Spatial backscatter variability	0.15 dB	0.15 dB

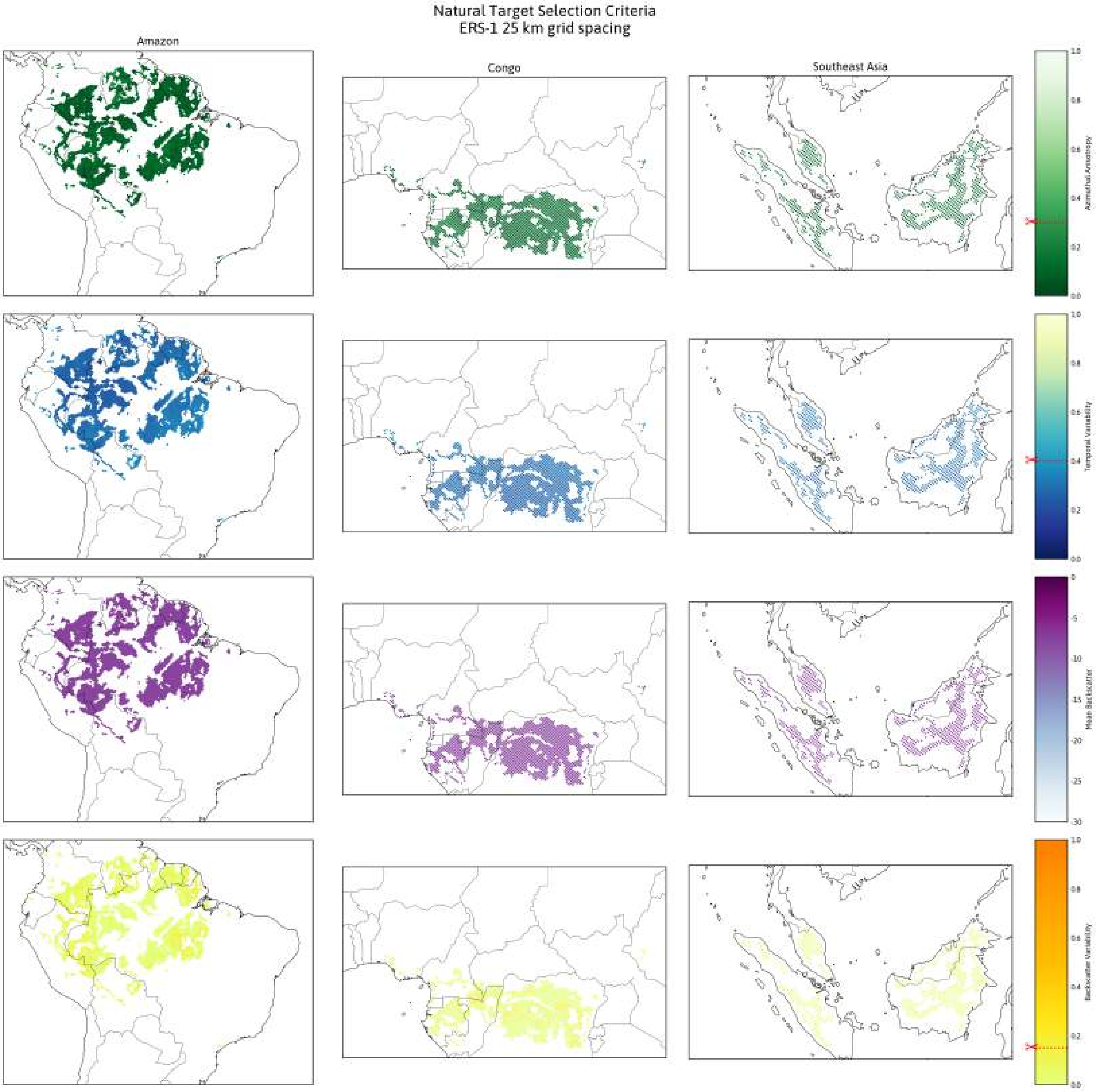

Figure 2.1: Selected natural targets for ERS-1, Nominal resolution, with their respective azimuthal anisotropy, temporal variability, mean long-term backscatter, and spatial backscatter variability.

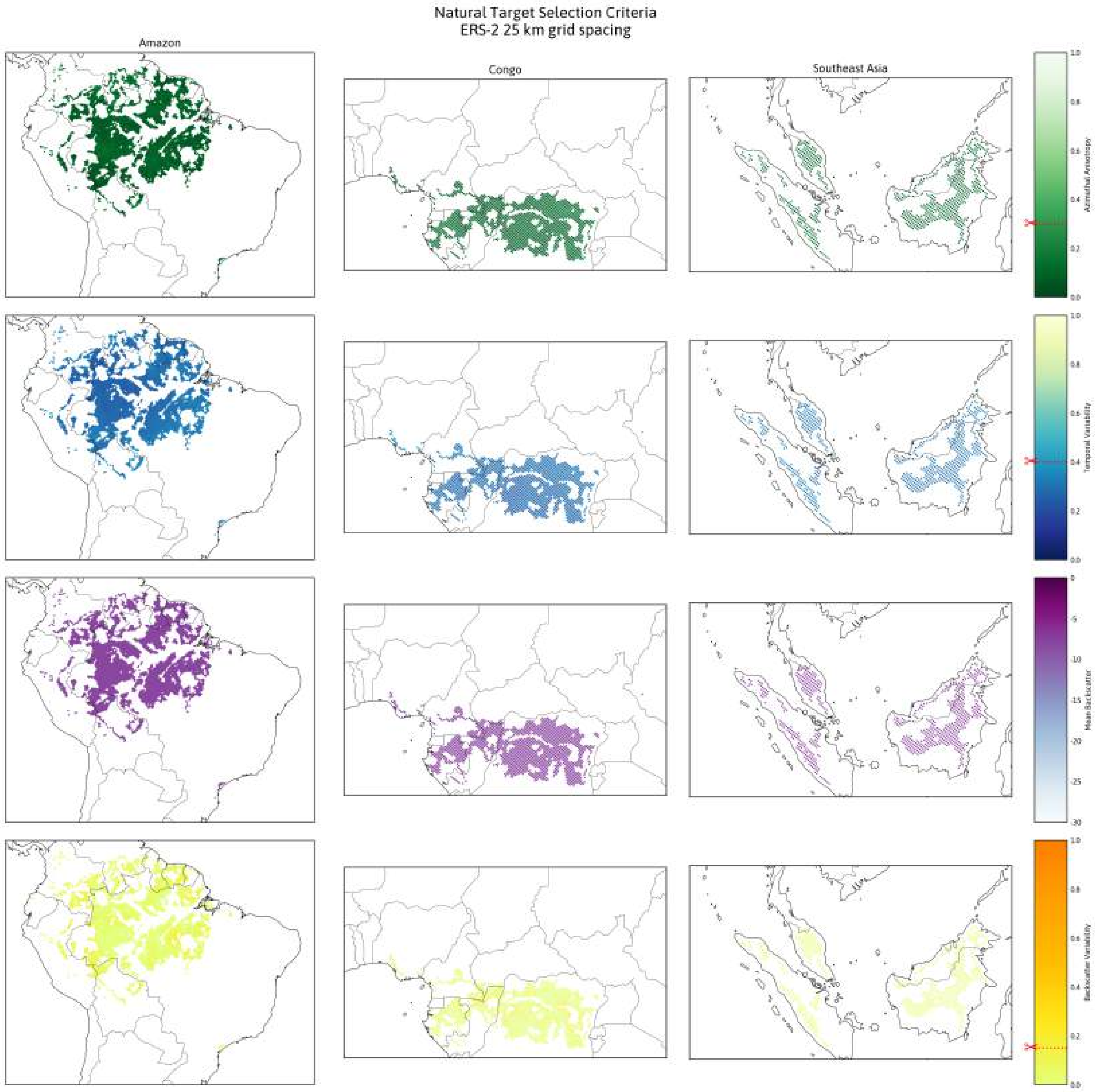

Figure 2.2: Selected natural targets for ERS-2, Nominal resolution, with their respective azimuthal anisotropy, temporal variability, mean long-term backscatter, and spatial backscatter variability.

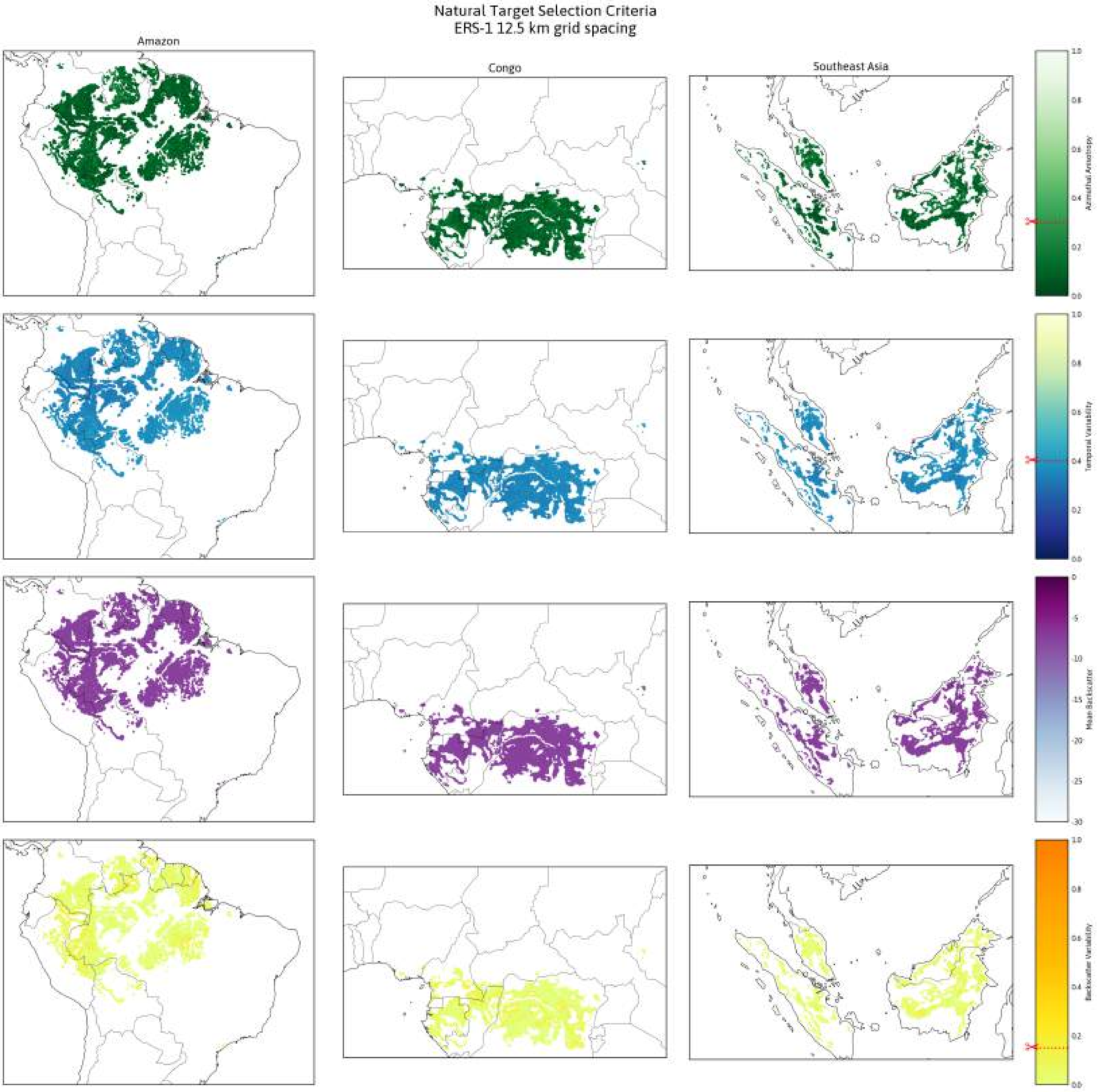

Figure 2.3: Selected natural targets for ERS-1, High resolution, with their respective azimuthal anisotropy, temporal variability, mean long-term backscatter, and spatial backscatter variability.

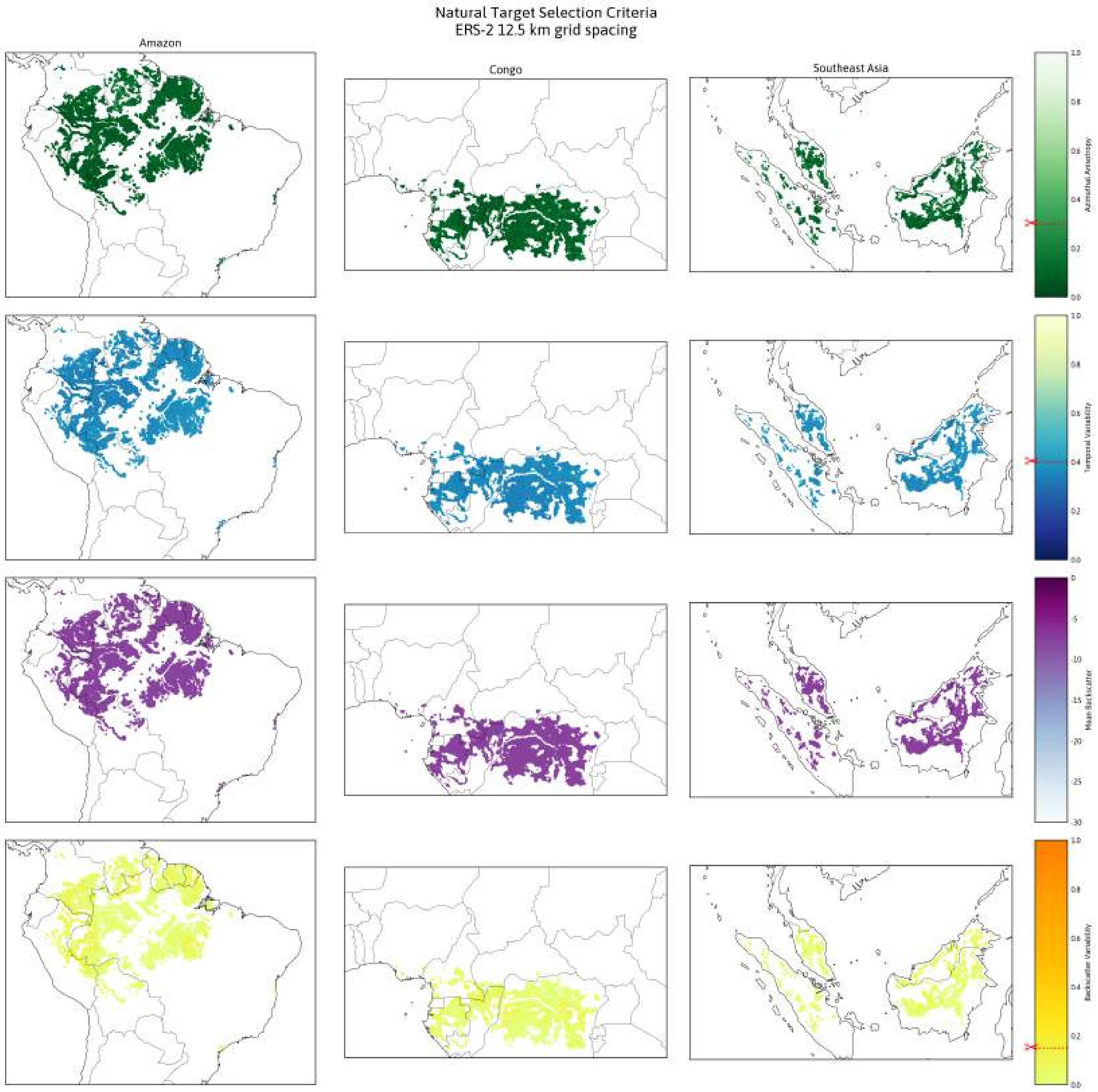

Figure 2.4: Selected natural targets for ERS-2, High resolution, with their respective azimuthal anisotropy, temporal variability, mean long-term backscatter, and spatial backscatter variability.

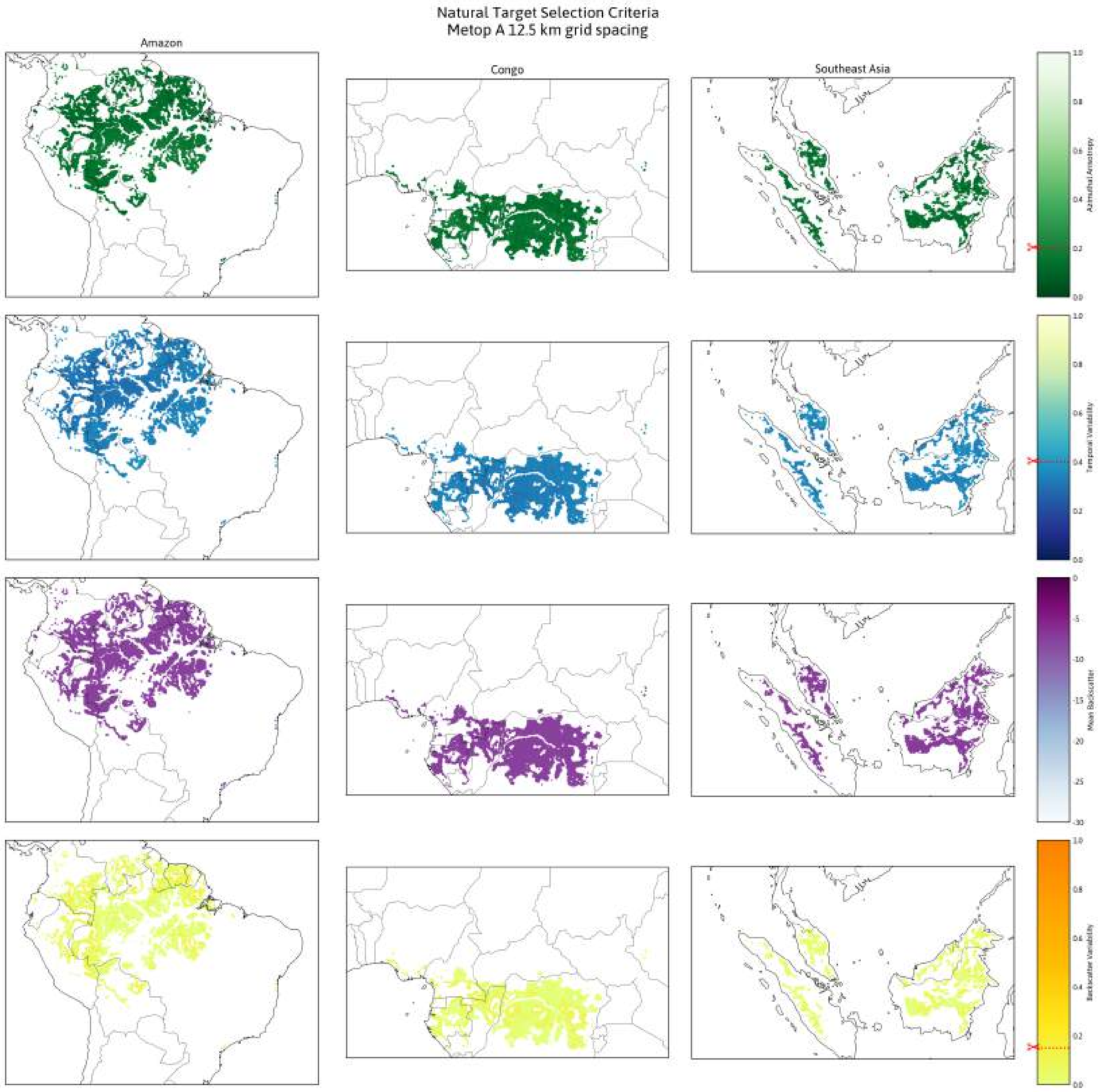

Figure 2.5: Selected natural targets for Metop-A, with their respective azimuthal anisotropy, temporal variability, mean long-term backscatter, and spatial backscatter variability.

2.2. Analysis of breaks and trends

We investigated breaks and trends in the ESCAT backscatter time series over natural targets using a change-point detection approach.

The gamma-nought time series for each beam and orbit was examined for change points using the “ruptures” Python package [9]. This package implements a kernel-based change-point detection algorithm that assumes that the backscatter data is independent and identically distributed, and uses a Gaussian kernel to detect changes in the distribution of the data over time [9]. Whenever a significant break or jump occurs in the time series, it is marked at a single point.

We applied this method to the time series over each natural target for different azimuth configurations and searched for notable events, as well as correspondences between detected breaks and mission events/phases.

2.2.1. Breaks and trends in ERS-1

The ERS-1 mission has minimal levels of long-term drift over the most extensive natural calibration targets (Amazon and Congo). Analysis of the seasonally-corrected gamma-nought time series analysis reveals several breakpoints, often, though not always, occurring near changes of mission phase.

Table 2.3: ERS-1 Mission Phases

Phase	Description	Start Date	End Date
A	Commissioning Phase	1991-07-25	1991-12-10
B	1st Ice Phase	1991-12-28	1992-04-01
R	Roll-tilt Phase	1992-04-02	1992-04-14
C	Multi-disciplinary Phase	1992-04-14	1993-12-23
D	2nd Ice Phase	1993-12-23	1994-04-10
E	Geodetic Phase	1994-04-10	1994-09-28
F	Shifted Geodetic Phase	1994-09-28	1995-03-21
G	2nd Multi-disciplinary	1995-03-21	1996-06-02

First Multidisciplinary Phase (Phase C) Towards the beginning of the first multidisciplinary phase (Phase C - 35 day repeat cycle), some irregularity is apparent in the ascending orbits over the Amazon (Figure 2.6). These are not detected as breakpoints by the kernel-change-detection algorithm, but a less dramatic break in the descending orbits around the same time is.

Second Ice Phase (Phase D) A breakpoint is detected during the transition into the second ice phase (Phase D - 3 day repeat cycle; late 1993) in at least two azimuth configurations over all three regions (Figures 2.6, 2.7, 2.8).

Geodetic Phase (Phase E) An obvious spike is visible (though not detected as a breakpoint) in ascending orbits over the Congo during the geodetic phase (Phase E - 3 day repeat cycle; July 1994; Figure 2.7). An extended dip is visible during this period over Southeast Asia, which lasts until the transition to the Shifted Geodetic Phase (Phase F). Breakpoints are detected at its beginning and end in descending orbits for all three beams.

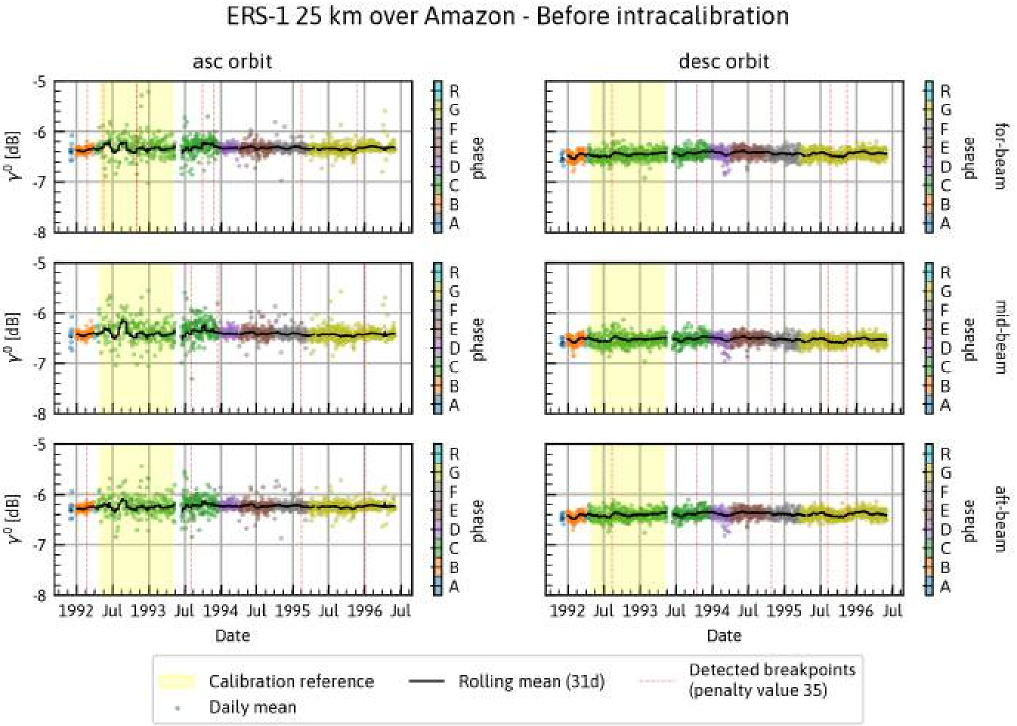

Figure 2.6: Seasonally-corrected γ^0 backscatter over the Amazon and detected timeseries breakpoints prior to calibration (ERS-1, 25 km grid spacing)

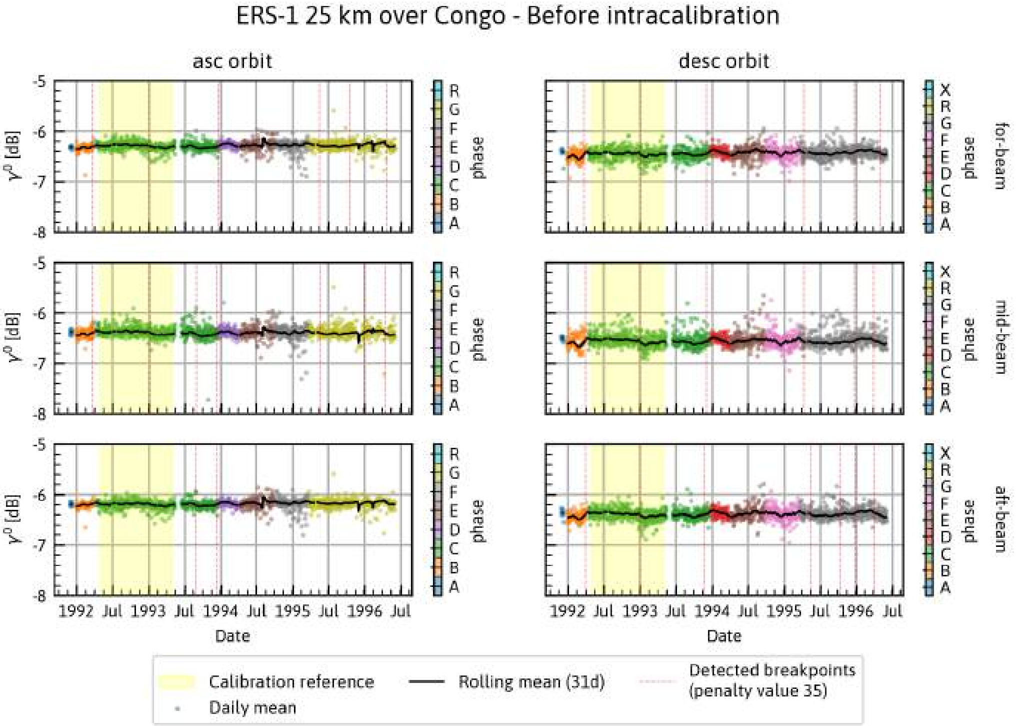

Figure 2.7: Seasonally-corrected γ^0 backscatter over the Congo and detected timeseries breakpoints prior to calibration (ERS-1, 25 km grid spacing)

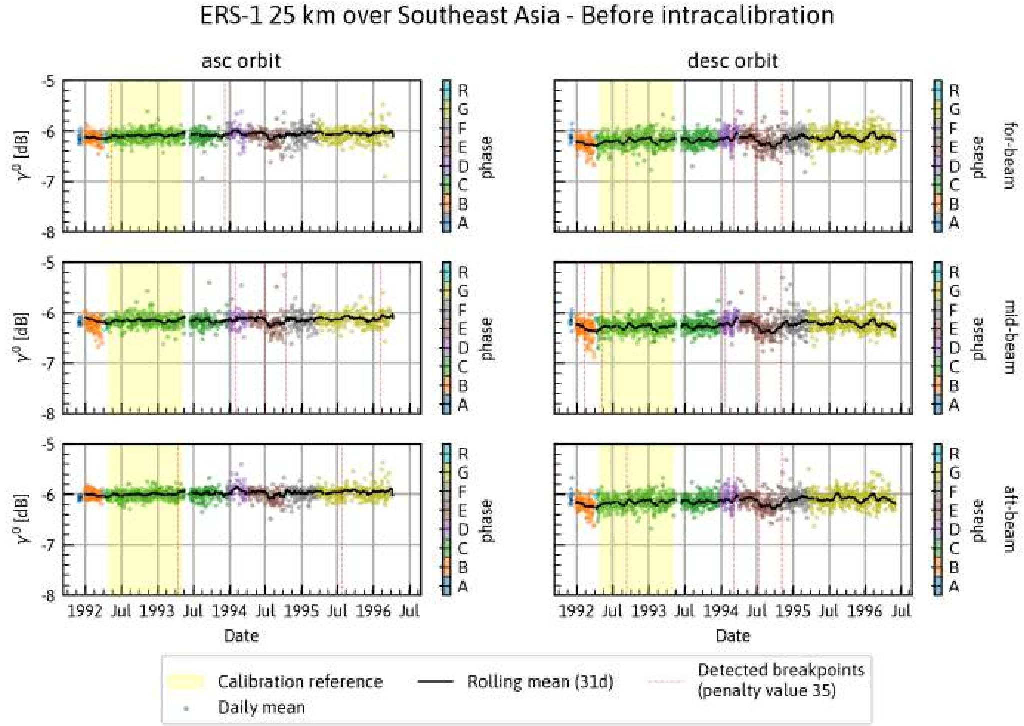

Figure 2.8: Seasonally-corrected γ^0 backscatter over Southeast Asia and detected timeseries breakpoints prior to calibration (ERS-1, 25 km grid spacing)

2.2.2. Breaks and trends in ERS-2

Table 2.4: ERS-2 Mission Phases and Modes

Description	**Start Date**	**End Date**
Commissioning Phase	1995-05-02	1995-08-17
Tandem Phase	1995-08-17	1996-06-02
Multi-disciplinary Phase / LBR recorder	1995-08-17	2003-06-22
Extra Backup Mode	2001-01-01	2001-06-01
Zero Gyro Mode	2001-06-01	2002-03-01
Yaw Control Monitoring	2002-03-01	2003-07-01
YCM-Regional	2003-07-01	2011-07-04
Multi-disciplinary Phase / No LBR Recorder	2003-06-22	2011-02-22
Ice Phase/3-day	2011-03-10	2011-07-04

The ERS-2 data contains significantly more breakpoints than ERS-1, as well as long periods without usable data – particularly over the Congo rainforest (Figures 2.9, 2.10, 2.11).

The period from January 2001 to June 2001, during which ERS-2 was in *Extra Backup Mode*, a gyro-less piloting mode, is already known to contain data of reduced quality [10], a fact which is reflected in the backscatter time series. Between June 2001 and March 2002, ERS-2 was in *Zero Gyro Mode*, which was designed as an improved gyro-less piloting mode. Despite these improvements, the seasonally-corrected gamma-nought timeseries during this period appears more erratic than prior data over the study regions, before dropping out entirely in late 2001.

In March 2002, ERS-2 was put into *Yaw Control Monitoring mode*, and from here until June 2003 data quality resumes essentially as it was prior to gyroscope failure. After this short period, the tape recorder on-board ERS-2 went down and no further valid unflagged triplets exist in the dataset until early 2005 over the Amazon and late 2006 over Southeast Asia. There is only a brief period of valid observations in late 2008 over the Congo after tape recorder failure, and nothing else.

Notably, in this late period from 2005 to the end of the mission, a strong seasonal component is visible in the seasonally-corrected gamma-nought backscatter timeseries derived from descending orbit observations over the Amazon (Figure 2.9). This seasonal component is not as obvious in the (more sparse) ascending orbit observations over the same region, nor is it visible at all over Southeast Asia (Figure 2.11).

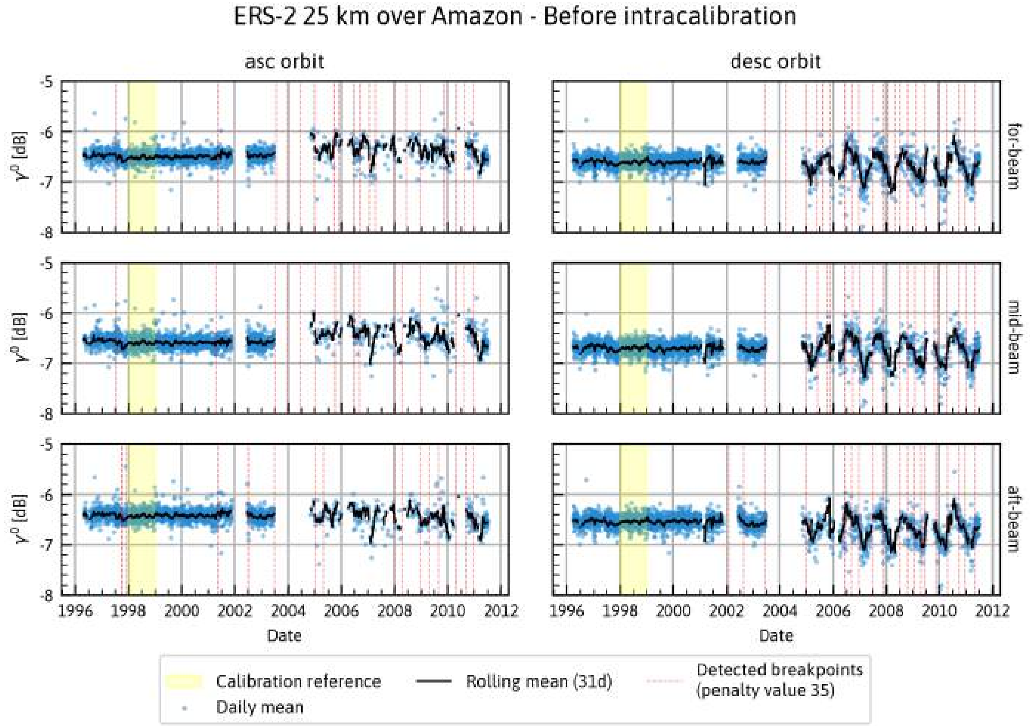

Figure 2.9: Seasonally-corrected γ^0 backscatter over the Amazon and detected timeseries breakpoints prior to calibration (ERS-2, 25 km grid spacing)

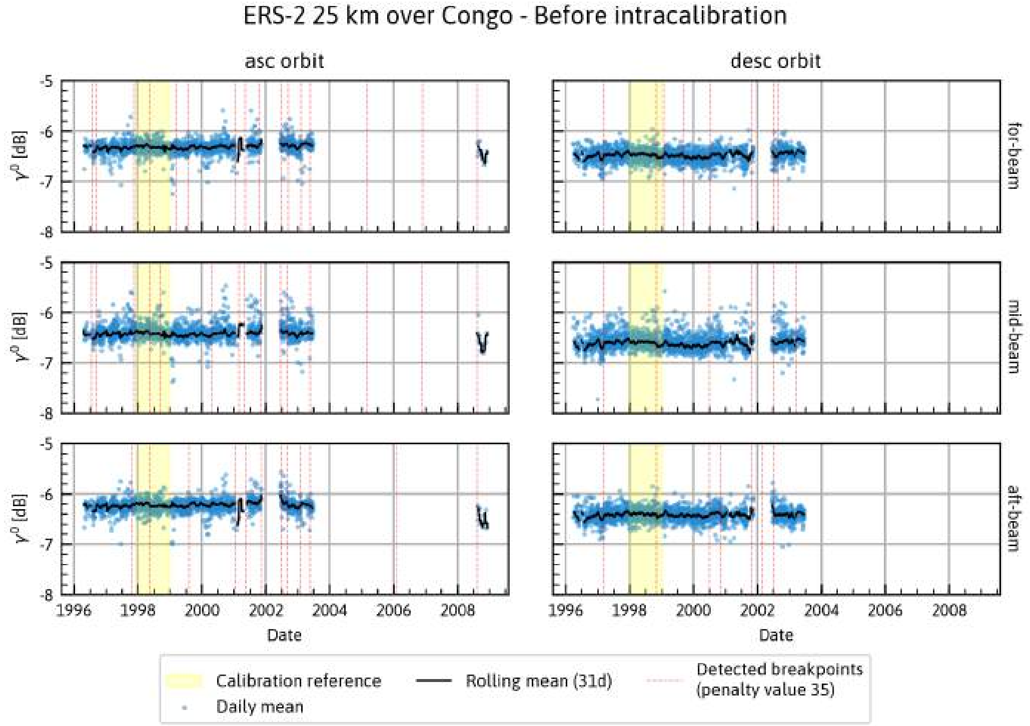

Figure 2.10: Seasonally-corrected γ^0 backscatter over the Congo and detected timeseries breakpoints prior to calibration (ERS-2, 25 km grid spacing)

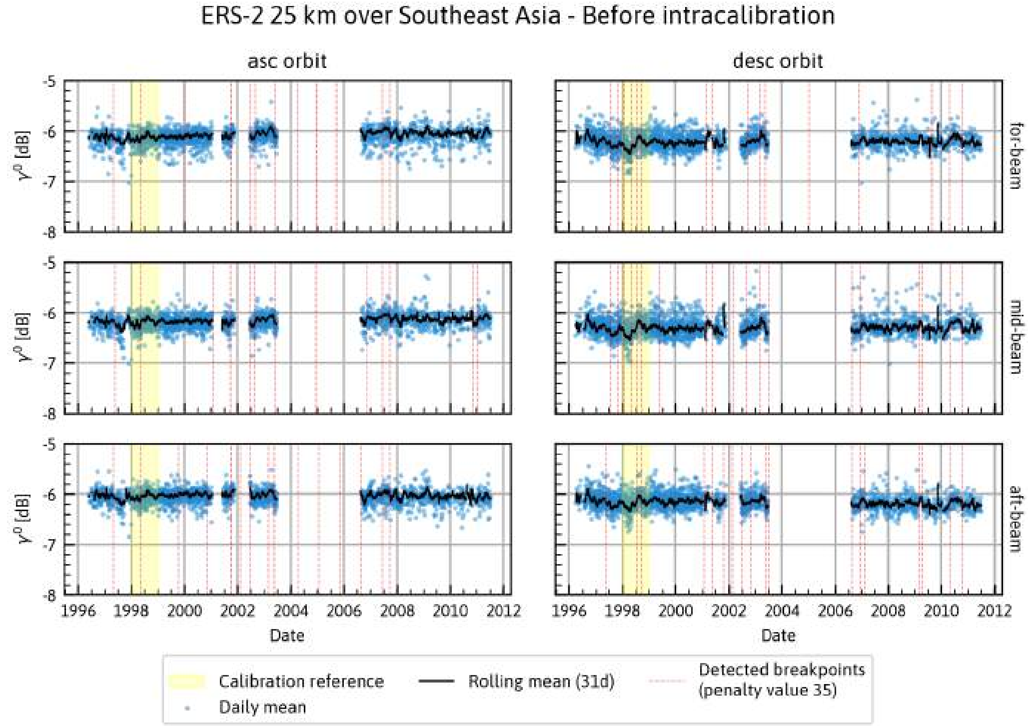

Figure 2.11: Seasonally-corrected γ^0 backscatter over Southeast Asia and detected timeseries breakpoints prior to calibration (ERS-2, 25 km grid spacing)

2.3. Intracalibration of beams per sensor

Despite prior calibration efforts [2], systematic differences between the antenna beams on each satellite remained evident in our analysis. For both ERS-1 and ERS-2, the mid-beam consistently showed lower backscatter response across all incidence angles compared to the fore- and aft-beams, with the fore-beam also exhibiting slightly lower values than the aft-beam (Figures 2.12, 2.13, 2.14, 2.15, 2.16, 2.17,).

To address these discrepancies, we implemented an intracalibration procedure adapting the methodology in [8], using the Amazon and Congo rainforests as reference regions and reserving Southeast Asia for validation. Unlike Reimer's approach, which performs calibration directly on σ^0 values, our method converts measurements to γ^0 before determining correction factors (this modification leverages the more stable response of γ^0 across incidence angles over rainforest targets, potentially improving the consistency of our calibration).

The approach consists of several steps:

First, a stable one-year period was identified for each satellite (Table 2.5) to serve as calibration reference.

Second, for each target region, backscatter measurements were normalized to $40°$ incidence angle on a monthly basis using Equation 4. Seasonal effects were removed by calculating the mean value for each day of year across the entire time series (excluding unstable periods), subtracting this seasonal cycle, and adding back the overall time series mean.

Third, the seasonally-corrected normalized backscatter was converted from σ^0 to γ^0 using:

$$\gamma^0 = 10\log_{10}\left(\frac{10^{\sigma^0/10}}{\cos(\theta)}\right) \tag{8}$$

Assuming rainforests exhibit a relatively flat γ^0 response over incidence angle, we fit a first-degree polynomial to measurements from the reference period for each orbit direction:

$$\overline{\gamma^0}(L_T,\theta) = B_0(L_T,40°) + B_1(L_T,40°)\cdot(\theta-40°) \tag{9}$$

where L_T is the target location, θ is the incidence angle, and $\overline{\gamma^0}$ represents the expected γ^0 over the target for a particular incidence angle.

Fourth, for each observation in the time series, we calculated the deviation between measured and expected backscatter:

$$C_{IAS}(L_T,t_i,\theta,\phi_j) = \gamma^0(L_T,t_i,\theta,\phi_j) - \overline{\gamma^0}(L_T,\theta) \tag{10}$$

These deviations were then modeled as a function of incidence angle for each azimuth configuration and month:

$$\overline{C_{IAS}}(L_T,t_i,\theta,\phi_j) = C_0(L_T,t_i,40°,\phi_j) + C_1(L_T,t_i,40°,\phi_j)\cdot(\theta-40°) \tag{11}$$

In this polynomial model, the correction coefficient C_0 adjusts the vertical offset (y-intercept) between beams in the gamma-nought domain, harmonizing their overall levels at the reference angle of $40°$. The C_1 parameter modifies the slope of each beam's angular response, correcting for differences in sensitivity to incidence angle changes. While higher-order parameters (C_2, C_3, etc.) could be incorporated to adjust curvature and higher-order behavior of the angular response, we limited our model to first-order corrections.

Finally, to account for spatial variability, we computed weighted averages of the correction coefficients from both target regions. Weights were determined based on the mean squared error (MSE) of the models from Equations 11 and 9.

The resulting correction coefficients—one set per month per azimuth configuration—were applied to the entire set of backscatter measurements in the gamma-nought domain to harmonize measurements across different beams. This approach is intended to address both intra-beam variation and temporal variations (through seasonal correction and monthly normalization).

Table 2.5: Reference periods for calibration of ERS-1 and ERS-2.

Satellite	**Reference period**
ERS-1	1992-05-01 to 1993-04-30
ERS-2	1998-01-01 to 1998-12-31

After intracalibration, agreement between satellite beams improves significantly over all reference and validation regions in both satellites (Figures 2.12, 2.13, 2.14, 2.15, 2.16, 2.17).

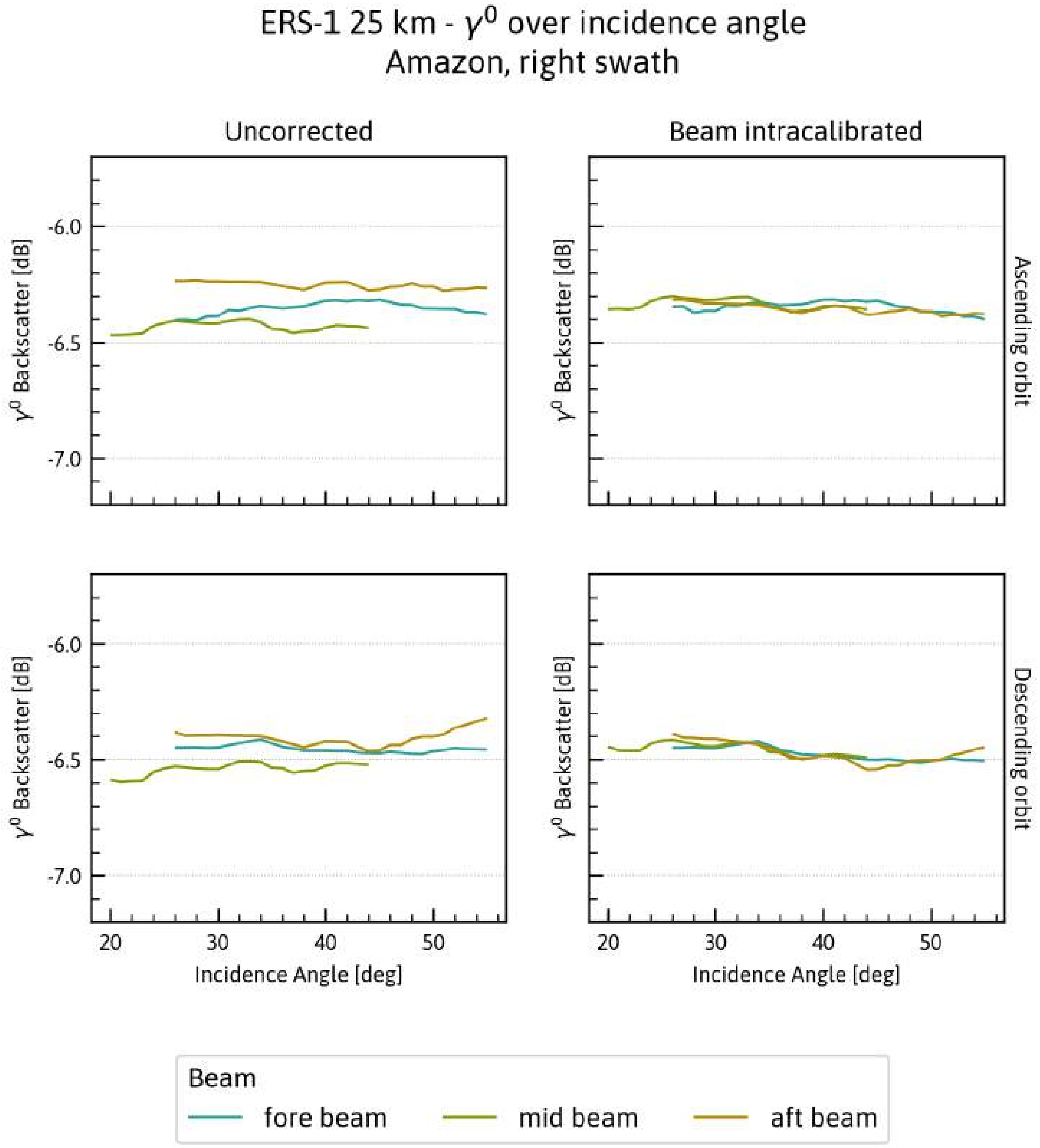

Figure 2.12: Comparison of intra-satellite beam alignment over selected natural targets in the Amazon rainforest before and after intracalibration (ERS-1, Nominal resolution).

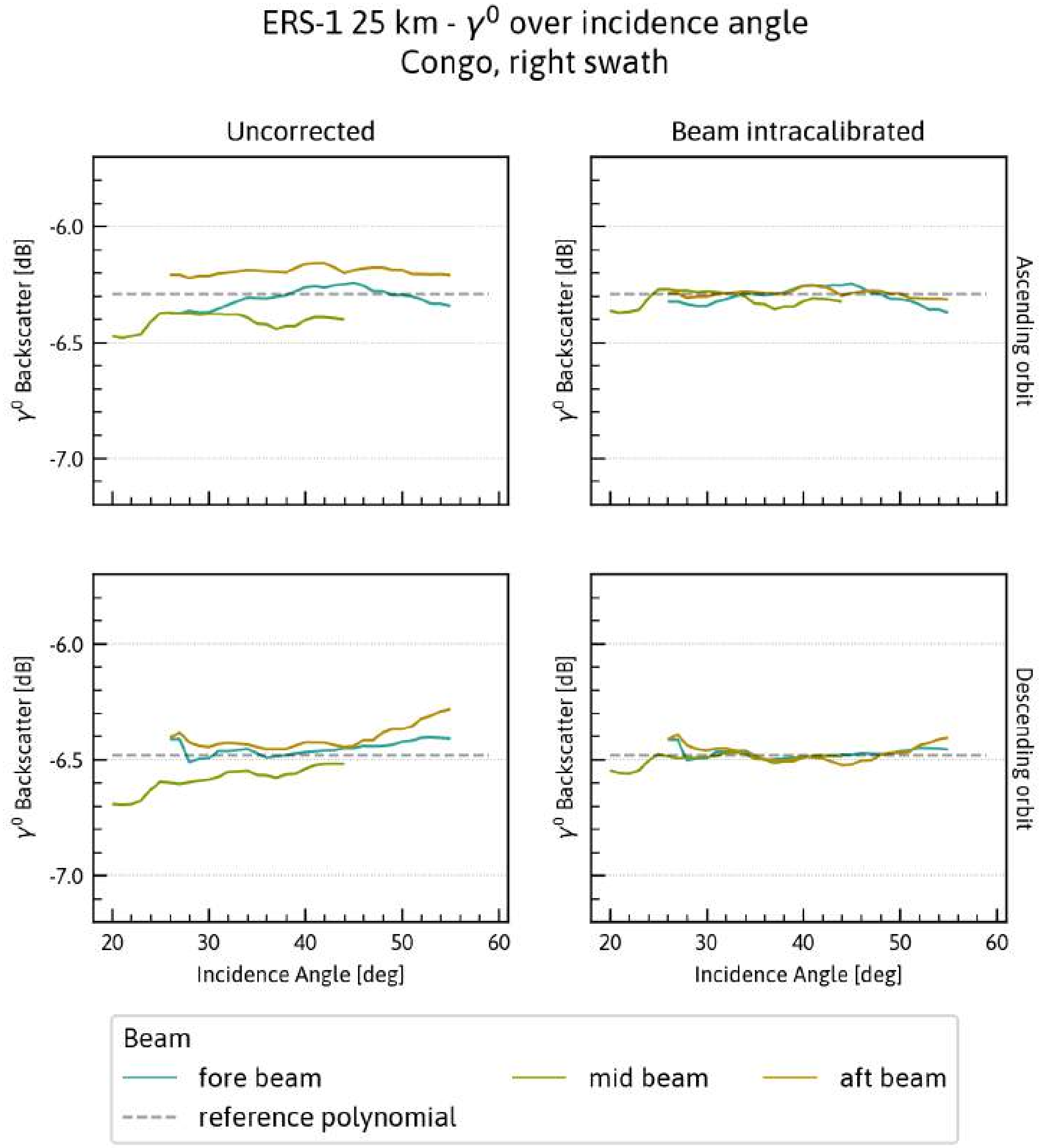

Figure 2.13: Comparison of intra-satellite beam alignment over selected natural targets in the Congo rainforest before and after intracalibration (ERS-1, Nominal resolution).

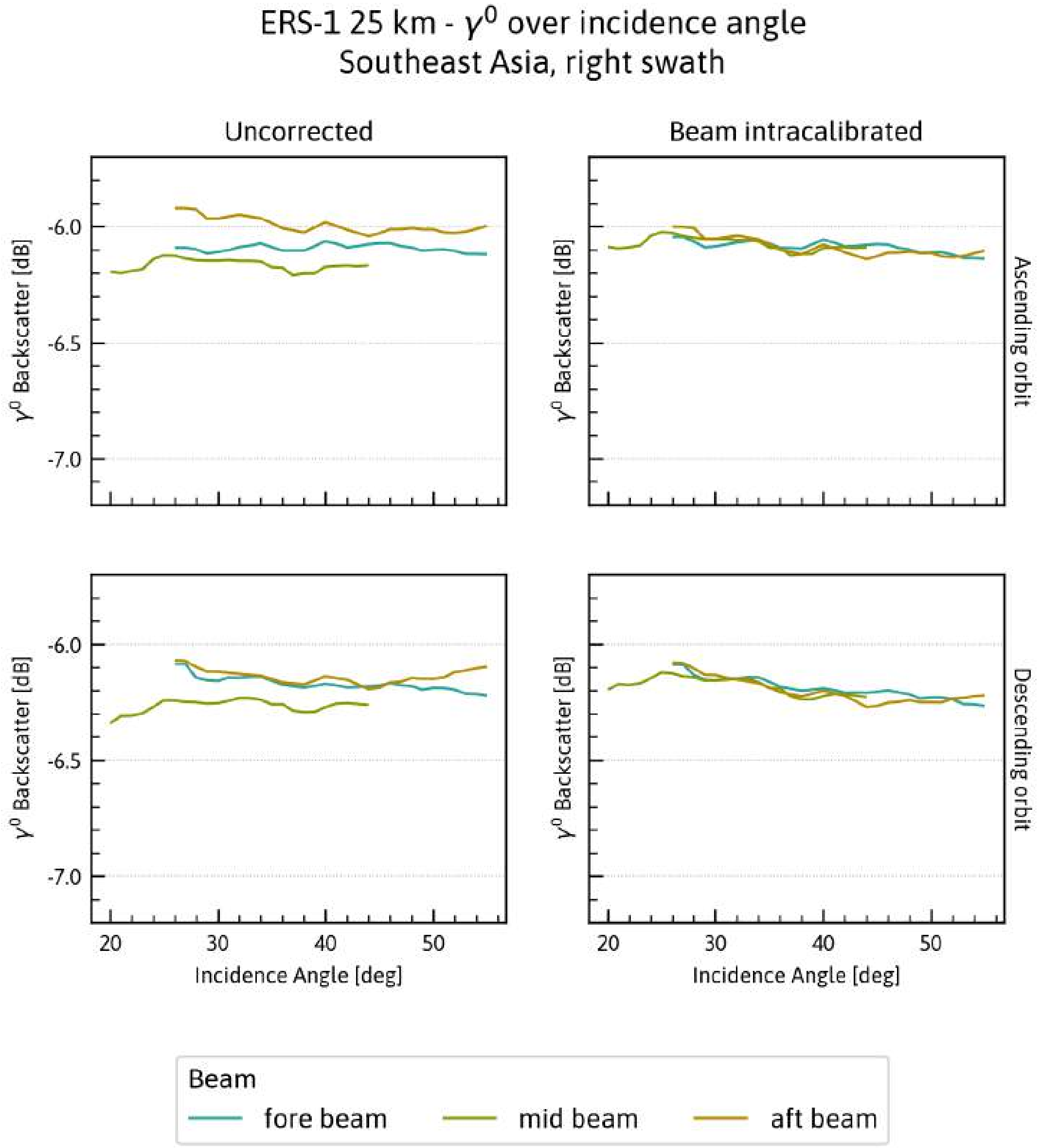

Figure 2.14: Comparison of intra-satellite beam alignment over selected natural targets in Southeast Asian rainforests before and after intracalibration (ERS-1, Nominal resolution).

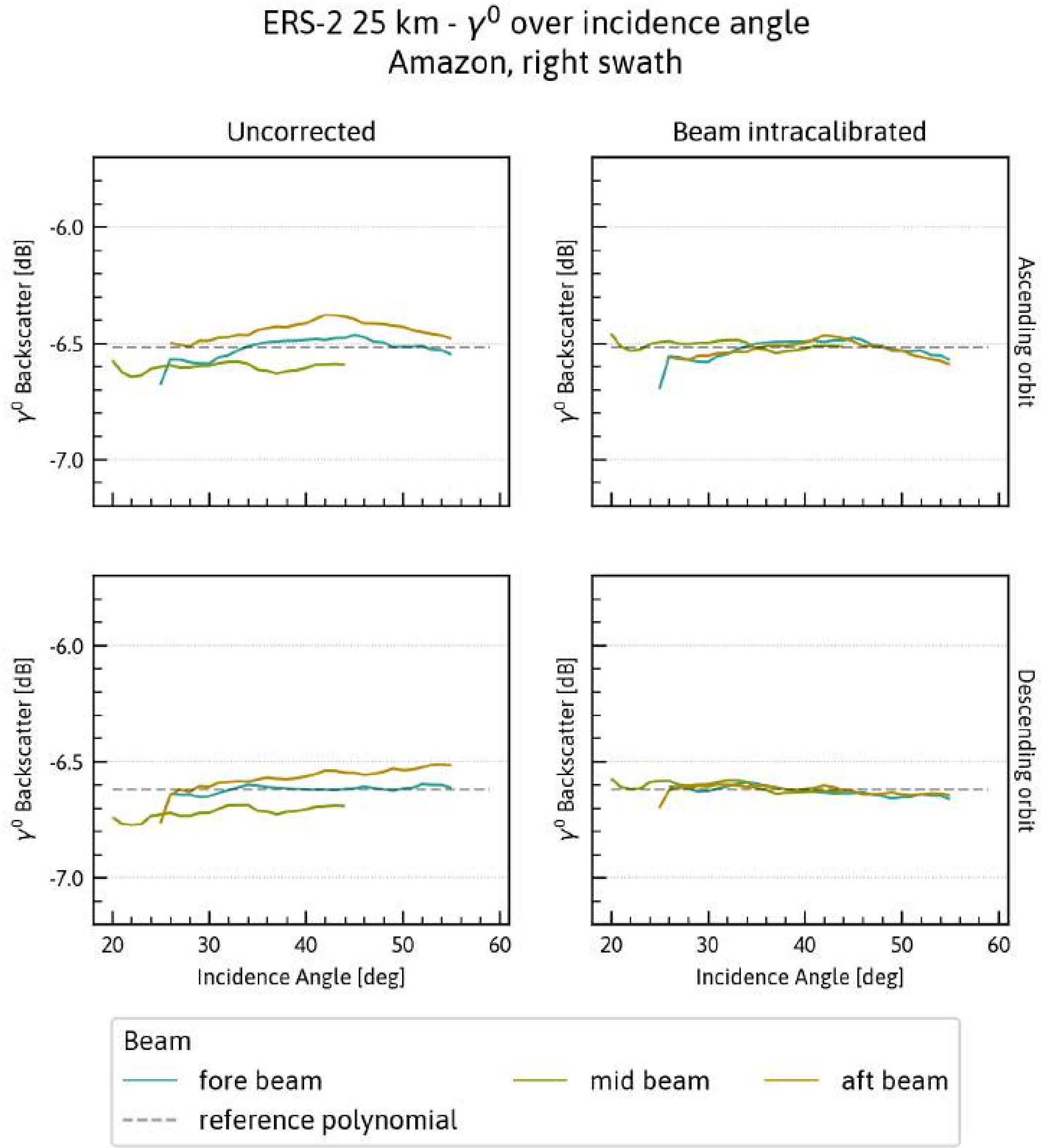

Figure 2.15: Comparison of intra-satellite beam alignment over selected natural targets in the Amazon rainforest before and after intracalibration (ERS-2, Nominal resolution).

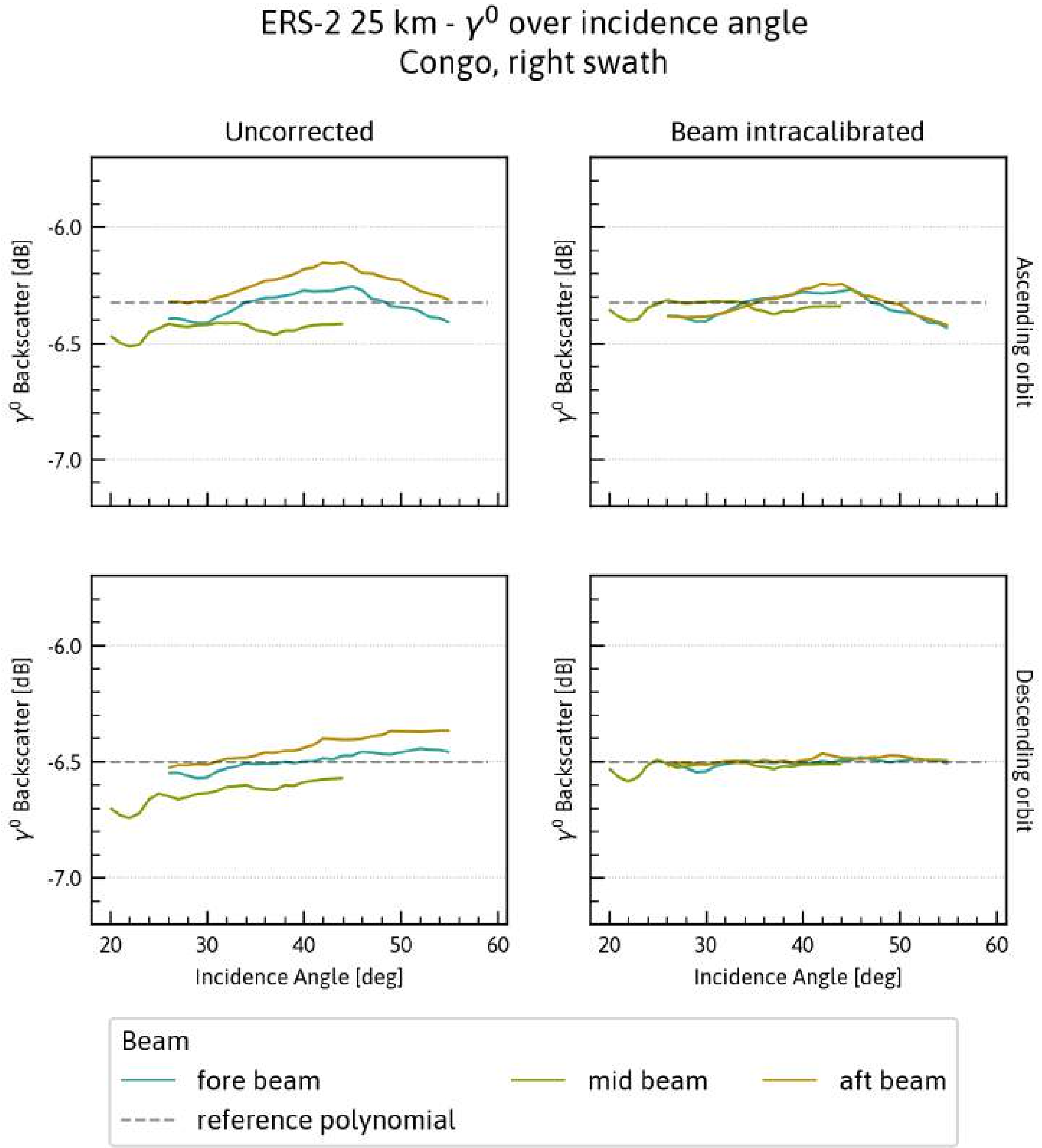

Figure 2.16: Comparison of intra-satellite beam alignment over selected natural targets in the Congo rainforest before and after intracalibration (ERS-2, Nominal resolution).

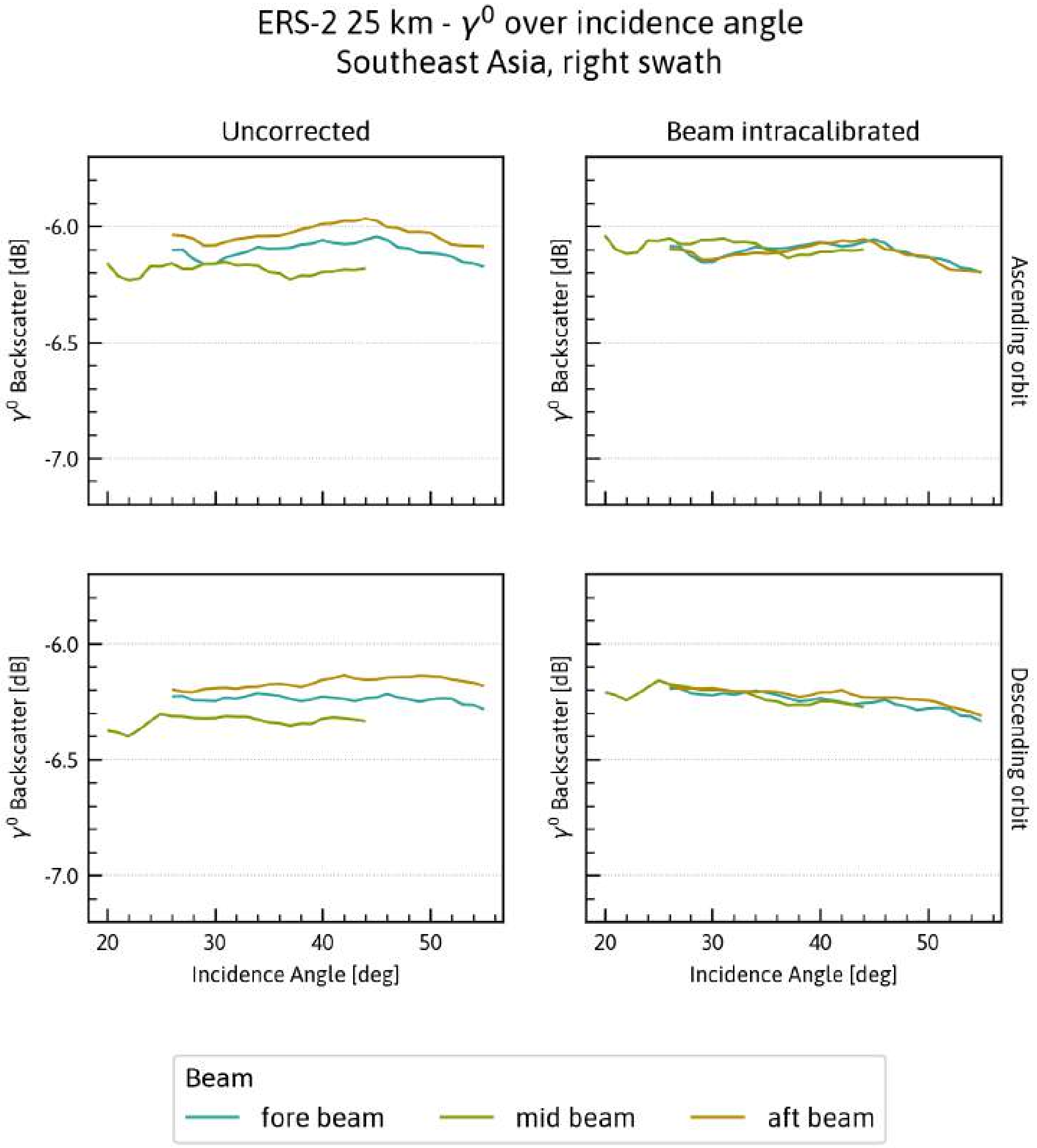

Figure 2.17: Comparison of intra-satellite beam alignment over selected natural targets in Southeast Asian rainforests before and after intracalibration (ERS-2, Nominal resolution).

2.4. Temporal effects of intracalibration

The generation of intracalibration parameters on a monthly basis relative to an overall reference provides for a degree of trend and break correction. Long-term calibration drifts that can be modeled as an incidence-angle dependent bias should be shifted back towards baseline one month at a time, assuming that these drifts exist and are well-captured by the correction coefficients.

Correction coefficients calculated for Metop-A capture the effects caused by the lowering of the satellite's orbit from 2017 to the end of its lifetime, demonstrating the ability of the intracalibration method to capture long-term trends (Figure 2.18). (However, while the calibration method effectively identifies this trend, we would not actually want to remove it from the data since it is caused by changing physical aspects of the satellite's orbit rather than calibration drift in the sensor itself. It is important to understand underlying physical dependencies in the data so they can be properly accounted for before calibration.)

In contrast, no global long-term trends were detected or corrected in ERS-1 data, but the C1 coefficient for the fore-beam in both ascending and descending orbits shows a year-long seasonal pattern with a steady upward trend over the course of the mission (Figure 2.19).

This fore-beam pattern is not present in corrections for ERS-2. The most notable result of calculating correction coefficients for ERS-2 is that, after the failure of the satellite's tape recorder in 2003, the calibration coefficients show a much greater variability than in earlier periods (Figure 2.20). This instability is due in part to a significantly lower volume of data over the calibration areas during this period, making it difficult to make a robust fit to the data during many months - in fact, many months are even missing calibration coefficients altogether because there simply were not enough observations to make a fit.

For months where no correction can be calculated, a decision will need to be made regarding the data product. Options include either setting observations during these months to NaN or using a constant correction value for the entire period, perhaps through interpolation from surrounding months or a mean from the most stable period. This determination will be made in future work.

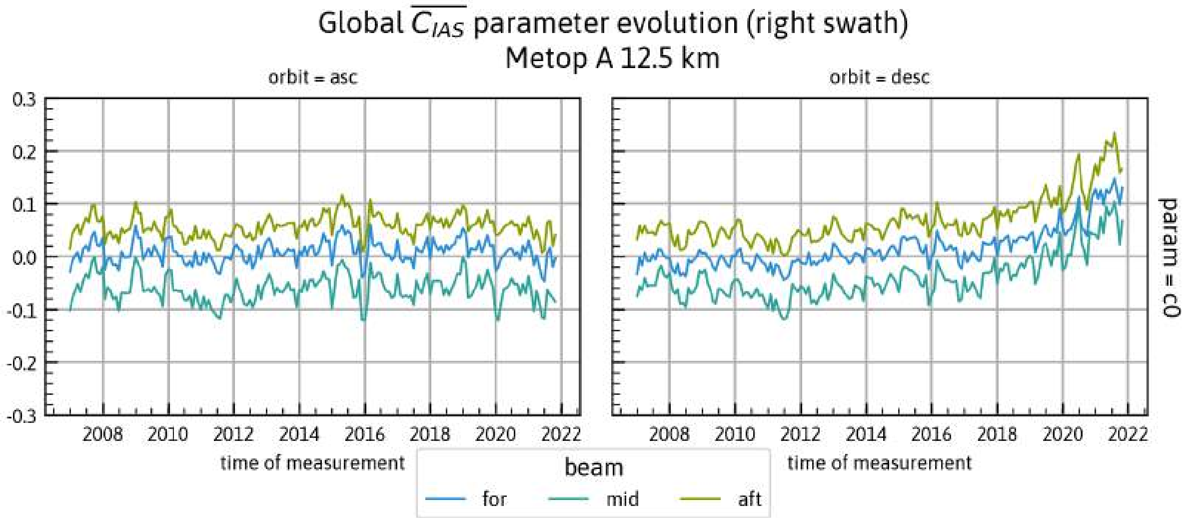

Figure 2.18: Evolution of correction coefficient C_0 calculated for Metop-A (12.5 km grid spacing, right swath) during intracalibration, where $\overline{C_{IAS}}(t_i, \theta, \phi_j) = C_0(t_i, \theta, \phi_j)$

.

While the current intracalibration method is effective at eliminating bias bewteen sensor beams and compensating for long-term trends, its design leaves something to be desired when it comes to compensating for sharp breaks in the data. The fact that compensations are calculated for strictly consecutive monthly periods leads to edge effects at the boundaries between months where breaks and drifts have

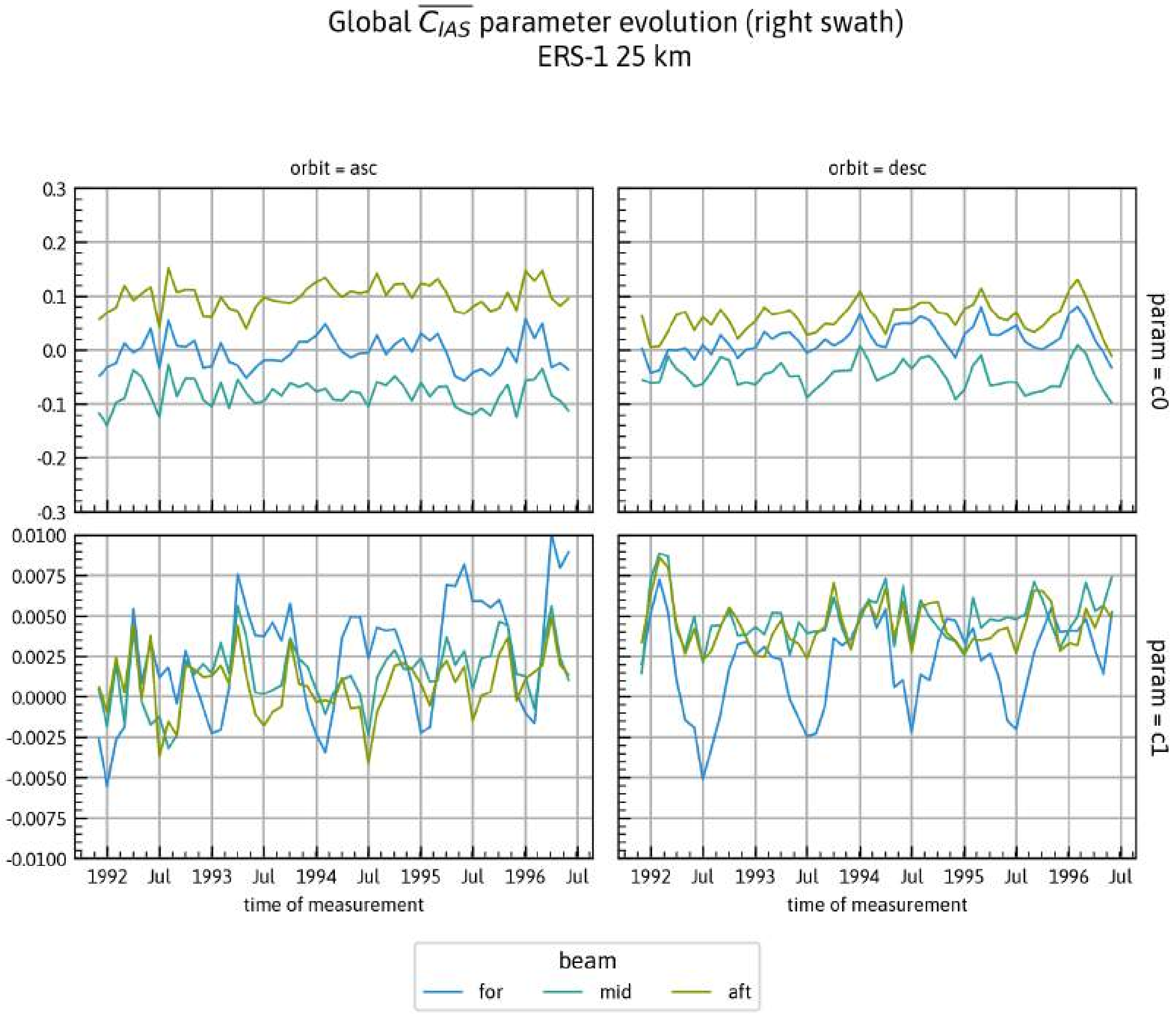

Figure 2.19: Evolution of correction coefficients C_0 and C_1 for calculated for ERS-1 (25 km grid spacing) during intracalibration, where $\overline{C_{IAS}}(t_i, \theta, \phi_j) = C_0(t_i, \theta, \phi_j) + C_1(t_i, \theta, \phi_j) \cdot (\theta - 40°)$
.

been imperfectly captured. Breakpoints detected in seasonally-corrected γ^0 are, at best, moved around rather than remedied when intracalibration is applied to ERS-1, while many new breakpoints appear after intracalibration of ERS-2.

Additionally, a significant side effect of our calibration approach is evident in the seasonal oscillations present in ERS-2 data. These oscillations, which we identified in Section 2.2.2, are incorporated into the correction coefficients. While this successfully removes seasonality over the Amazon region, it unfortunately introduces strong seasonal dependencies into Southeast Asia where none existed before (Fig. 2.26).

This is, in part, a consequence of the limited calibration region coverage during this mission period. Since the Amazon is the primary rainforest calibration region with sufficient data during this period, its unique seasonal characteristics become embedded in the global correction parameters. The Congo rainforest, which might have provided a counterbalance in the weighted average, lacks adequate data coverage for ERS-2. We might consider including other rainforests in the set of calibration regions to mitigate this problem, but this is unlikely to improve the situation significantly: none of them are nearly

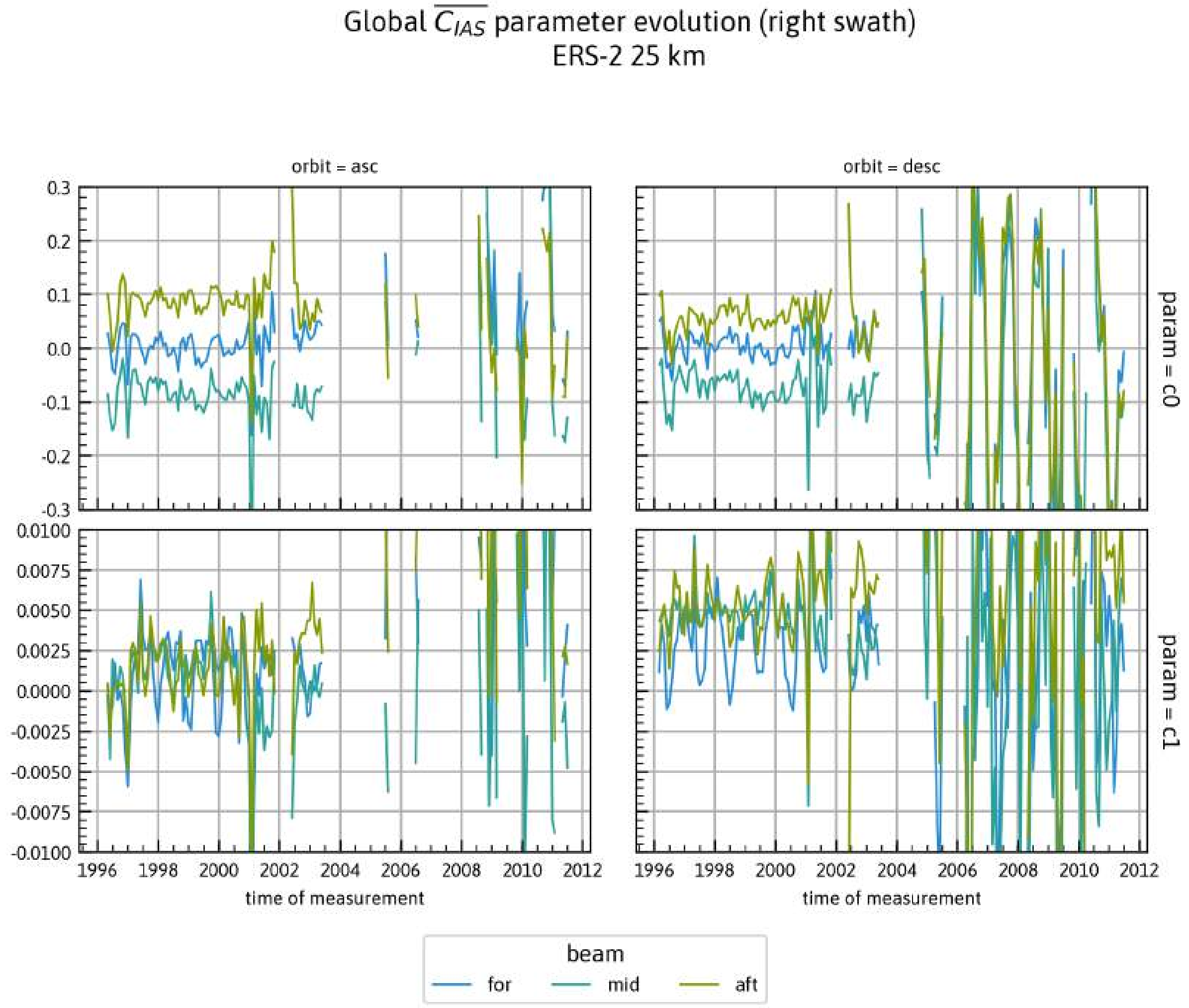

Figure 2.20: Evolution of correction coefficients C_0 and C_1 for calculated for ERS-2 (25 km grid spacing) during intracalibration, where $\overline{C_{IAS}}(t_i, \theta, \phi_j) = C_0(t_i, \theta, \phi_j) + C_1(t_i, \theta, \phi_j) \cdot (\theta - 40°)$.

as large as the Amazon and Congo, and all would be subject to the same issues of data scarcity.

Of course, the real underlying issue is that the seasonal oscillations in the Amazon data were not captured well enough in the seasonal correction step before calibration. The design of this step will have to be reconsidered in future work. Nevertheless, this issue demonstrates the broader difficulties we encounter when working with late-period ERS-2 data, which is characterized by such sparse temporal sampling that inferring robust, generalizable bias corrections from data over natural targets becomes a significant challenge.

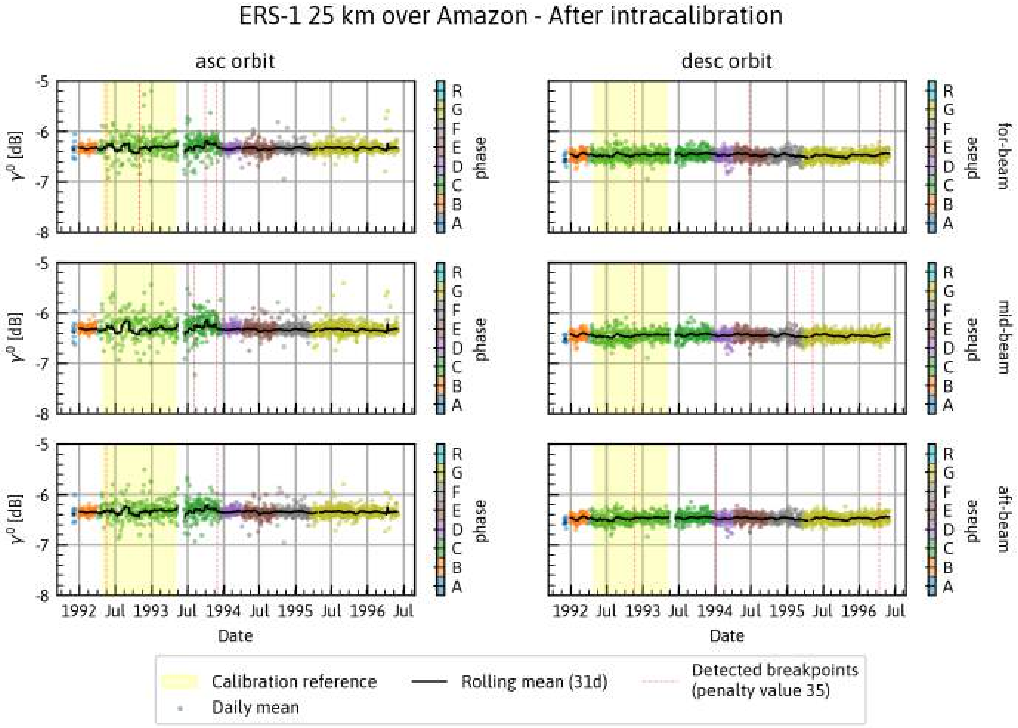

Figure 2.21: Seasonally-corrected γ^0 backscatter over the Amazon and detected timeseries breakpoints after calibration (ERS-1, 25 km grid spacing)

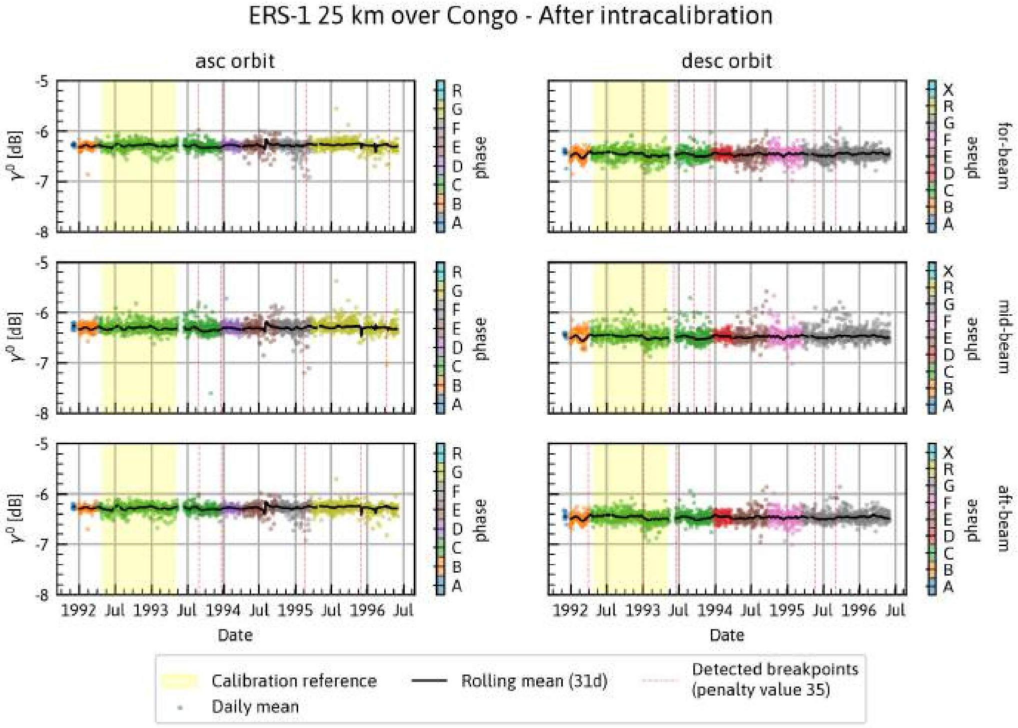

Figure 2.22: Seasonally-corrected γ^0 backscatter over the Congo and detected timeseries breakpoints after calibration (ERS-1, 25 km grid spacing)

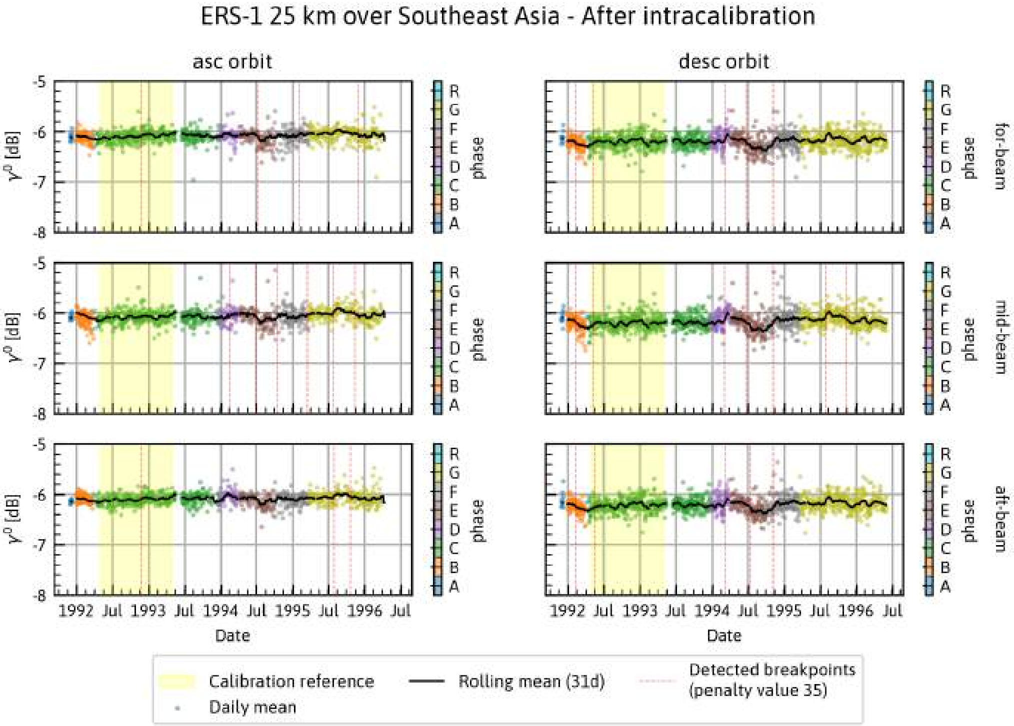

Figure 2.23: Seasonally-corrected γ^0 backscatter over Southeast Asia and detected timeseries breakpoints after calibration (ERS-1, 25 km grid spacing)

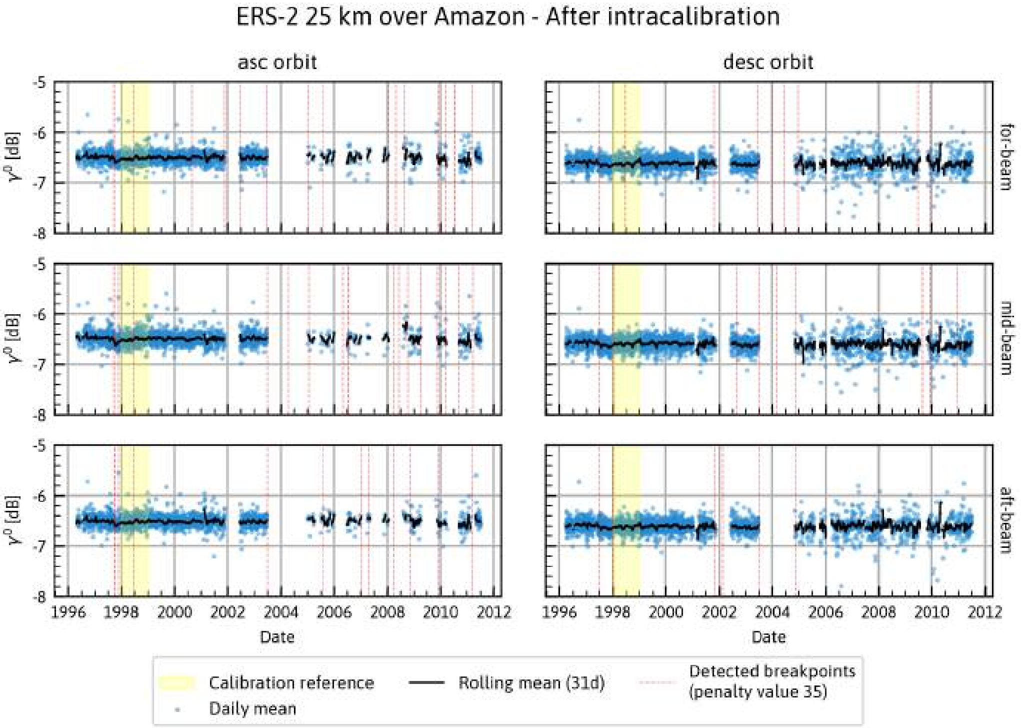

Figure 2.24: Seasonally-corrected γ^0 backscatter over the Amazon and detected timeseries breakpoints after calibration (ERS-2, 25 km grid spacing)

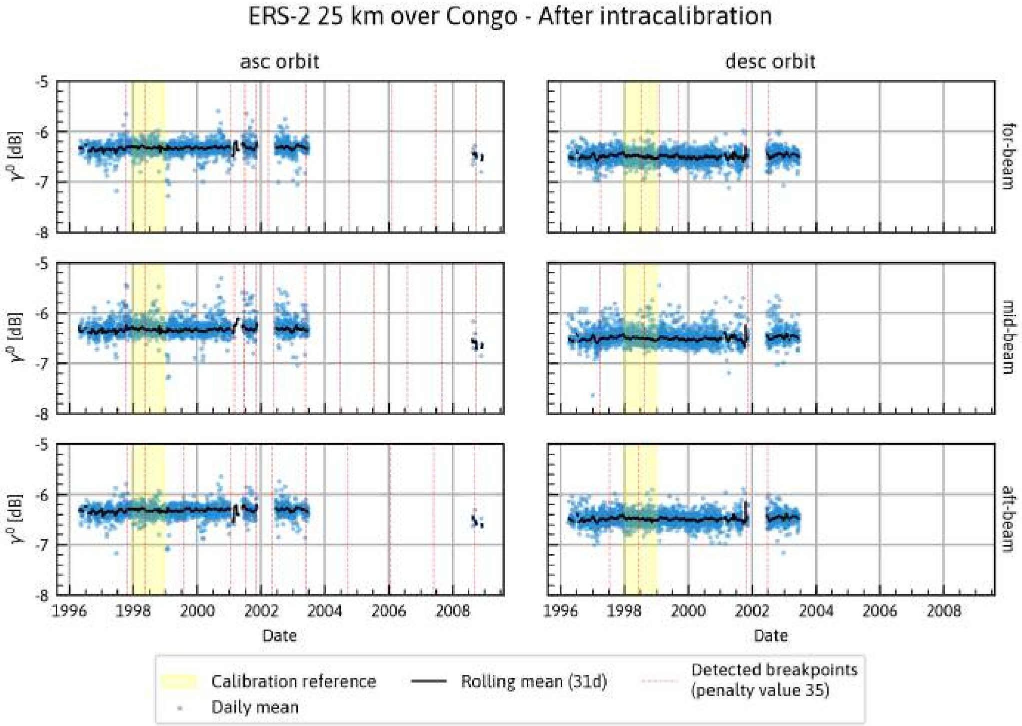

Figure 2.25: Seasonally-corrected γ^0 backscatter over the Congo and detected timeseries breakpoints after calibration (ERS-2, 25 km grid spacing)

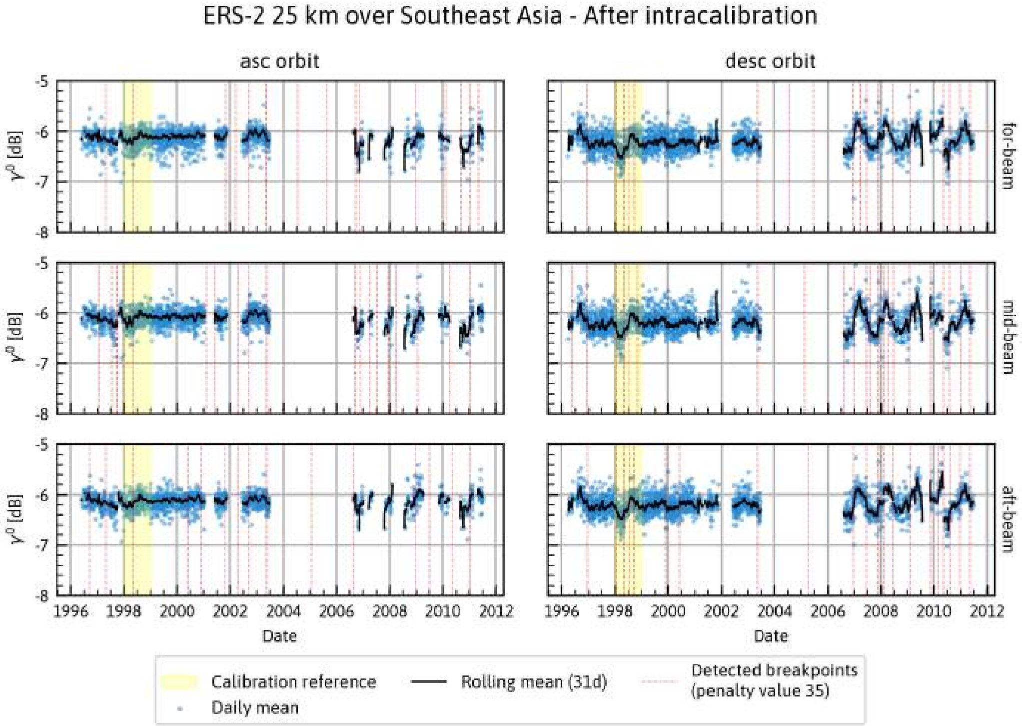

Figure 2.26: Seasonally-corrected γ^0 backscatter over Southeast Asia and detected timeseries breakpoints after calibration (ERS-2, 25 km grid spacing)

2.5. Intercalibration between ESCAT and ASCAT

To assess the existing calibration differences between ERS and Metop, we examined the average gamma-nought bias between intracalibrated measurements from both families of satellites for each beam over the range of incidence angles (Figures 2.27). Specifically, we compared both ERS-1 and ERS-2, separately, to Metop-A.

While ESCAT gamma-nought measurements tend to have a flat incidence-angle relationship, ASCAT measurements have a negative relationship (a finding consistent with prior work, e.g. [11]). This means the bias between corresponding beams from the two satellites decreases as incidence angle increases.

We found that the existing gamma-nought bias between ESCAT measurements and ASCAT measurements decreases from approximately 0.4 dB to 0.1 dB in descending orbits, and from about 0.3 dB to around 0 dB in ascending orbits. These ranges are more-or-less consistent across the fore-, mid-, and aft-beams of both satellites for all studied natural targets.

To see if the satellites' calibration could be improved, we applied the intercalibration methodology from [8] to calibrate ERS (Tar) using Metop-A (Ref) as a reference.

For each calibration region L_T, we calculated the difference $C_{IES}(L_T, t_i, \theta, \phi_j)$ between each backscatter observation $\gamma^0_{Tar}(L_T, t_i, \theta, \phi_j)$ and the expected backscatter for that observation according to $\overline{\gamma^0_{Ref}}$, which we already determined in Section 2.3.

$$C_{IES}(L_T, t_i, \theta, \phi_j) = \overline{\gamma^0_{Ref}}(L_T, t_i, \theta, \phi_j) - \gamma^0_{Tar}(L_T, t_i, \theta, \phi_j) \tag{12}$$

Then we fit a linear model to the differences C_{IES} versus the incidence angle θ for each azimuth configuration ϕ_j, including observations from *all* calibration regions.

$$\overline{C_{IES}}(\theta, \phi_j) = C_0(40) + C_1(40) \cdot (\theta - 40) \tag{13}$$

This model was then evaluated for every backscatter observation in ERS-1/2 to provide a correction factor that was applied to bring the observation in line with Metop-A.

After intercalibration, the bias between the satellites over both the calibration regions and the validation region was reduced across the entire incidence angle range. Because the correction model is a first-degree polynomial, the negative incidence-angle dependency of Metop gamma-nought backscatter measurements has now been introduced into ERS. Thus, the measurements from the two satellites are better aligned, but more study is needed to determine whether this has any benificial (or detrimental) effects on the use of derived slope and curvature parameters, especially outside the calibration regions. A first analysis of the global ramifications of intercalibration is consequently provided in Section 3.3.

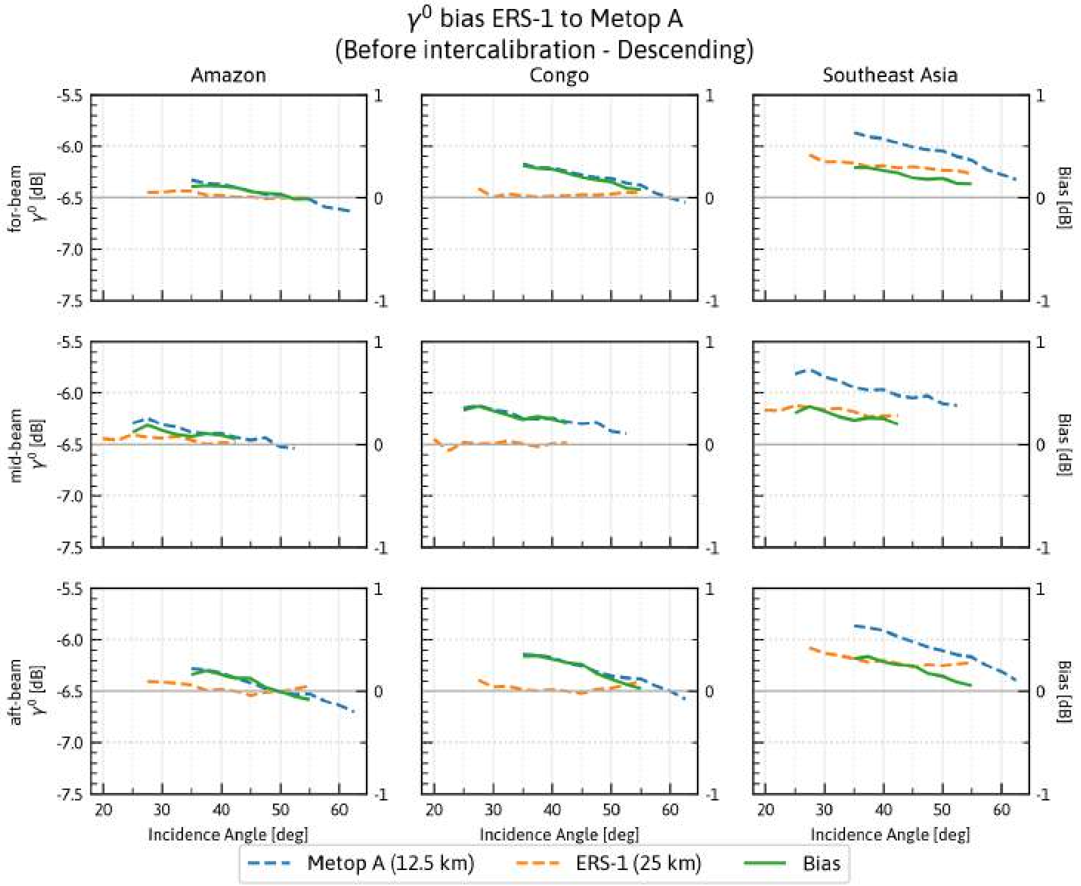

Figure 2.27: Comparison of γ^0 backscatter measurements from ERS-1 and Metop-A over incidence angle θ, prior to intercalibration.

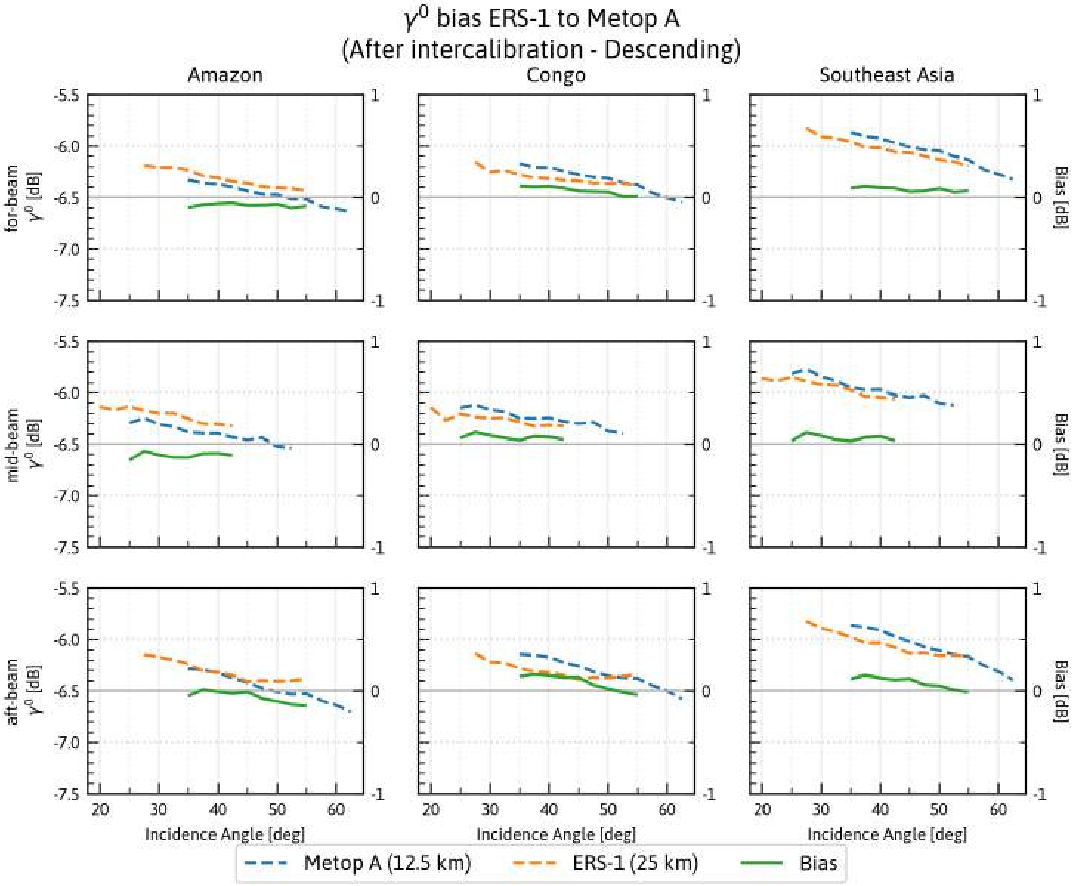

Figure 2.28: Comparison of γ^0 backscatter measurements from ERS-1 and Metop-A over incidence angle θ, after intercalibration.

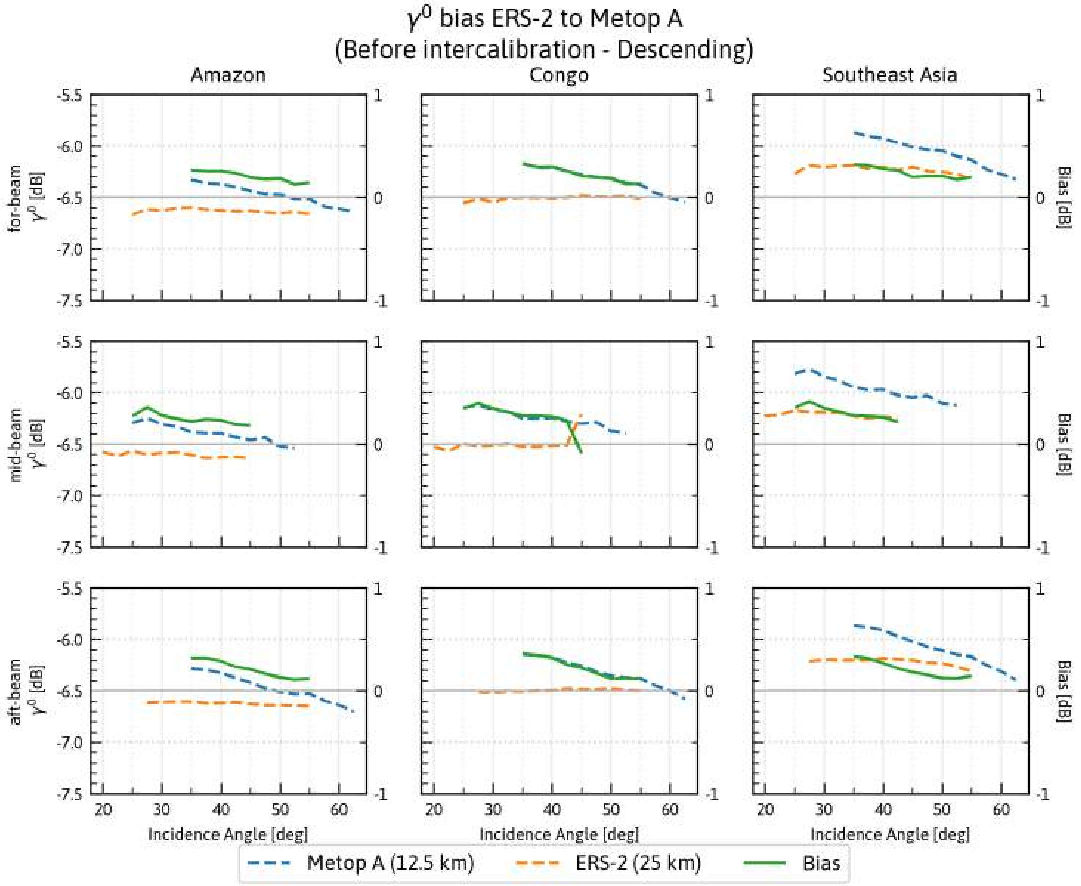

Figure 2.29: Comparison of γ^0 backscatter measurements from ERS-2 and Metop-A over incidence angle θ, prior to intercalibration.

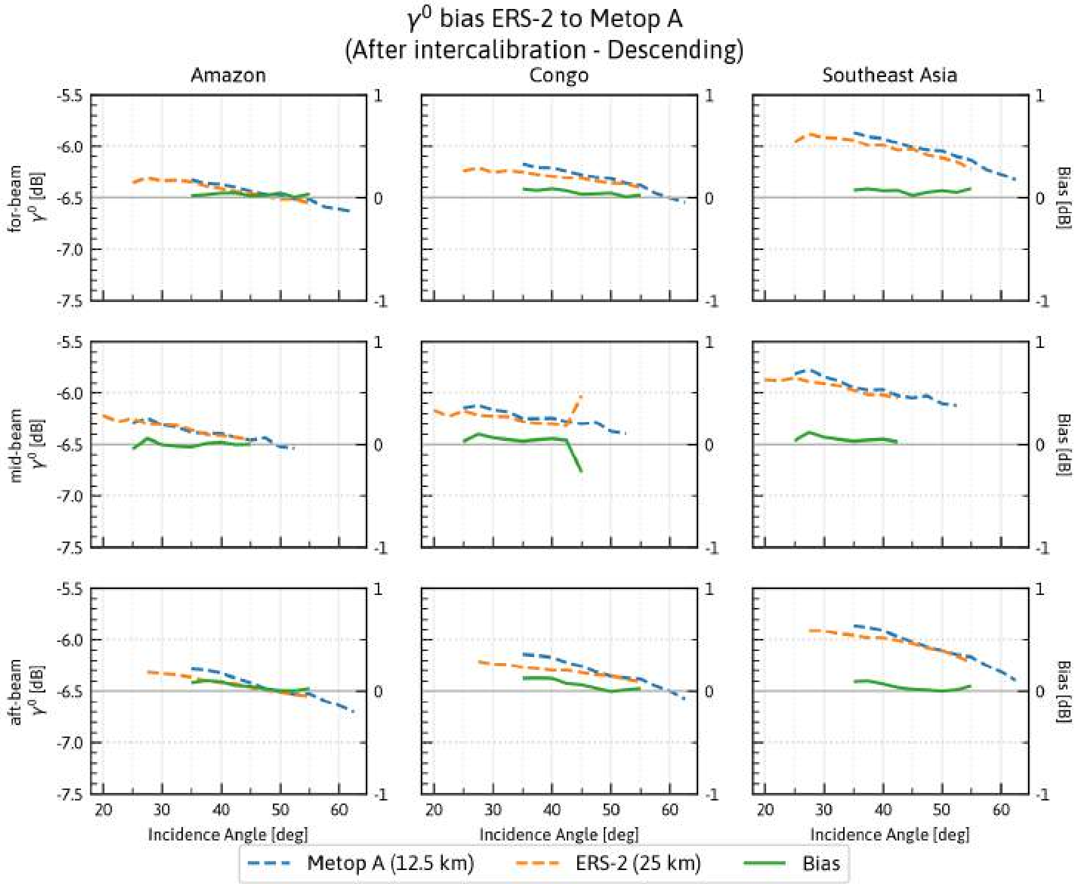

Figure 2.30: Comparison of γ^0 backscatter measurements from ERS-2 and Metop-A over incidence angle θ, after intercalibration.

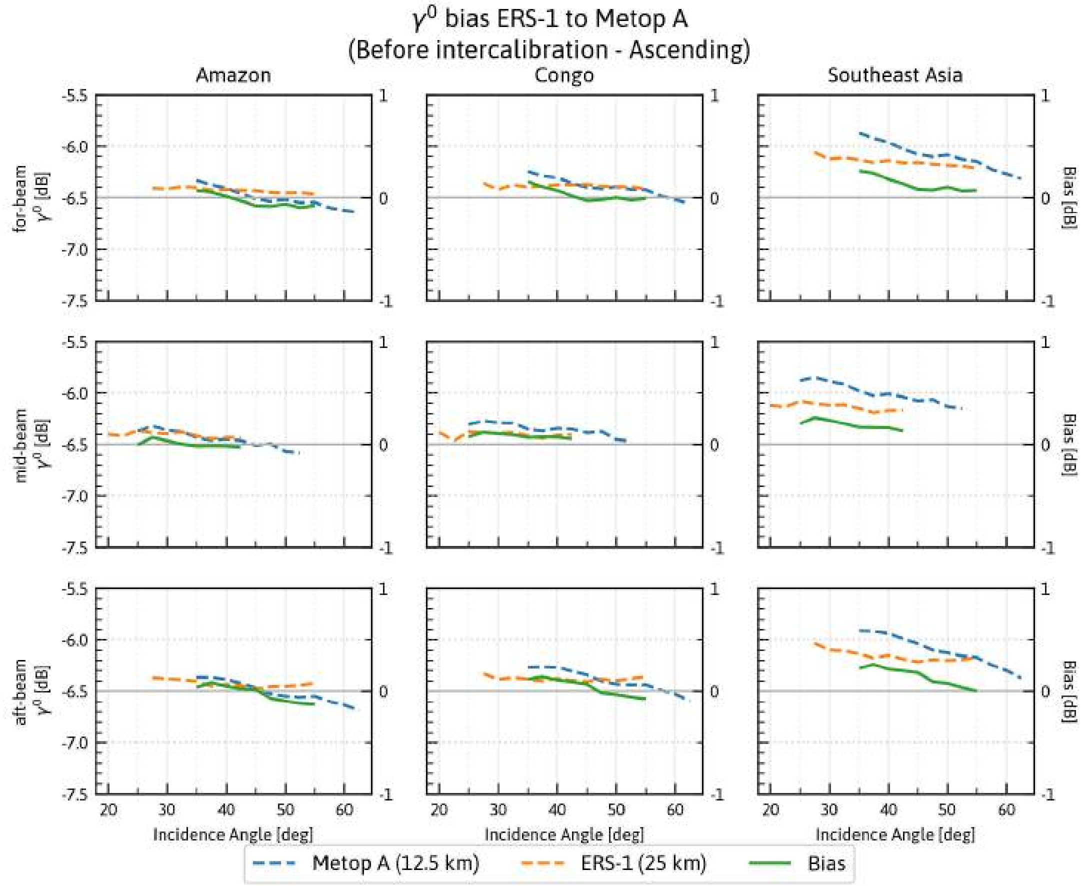

Figure 2.31: Comparison of γ^0 backscatter measurements from ERS-1 and Metop-A over incidence angle θ, prior to intercalibration.

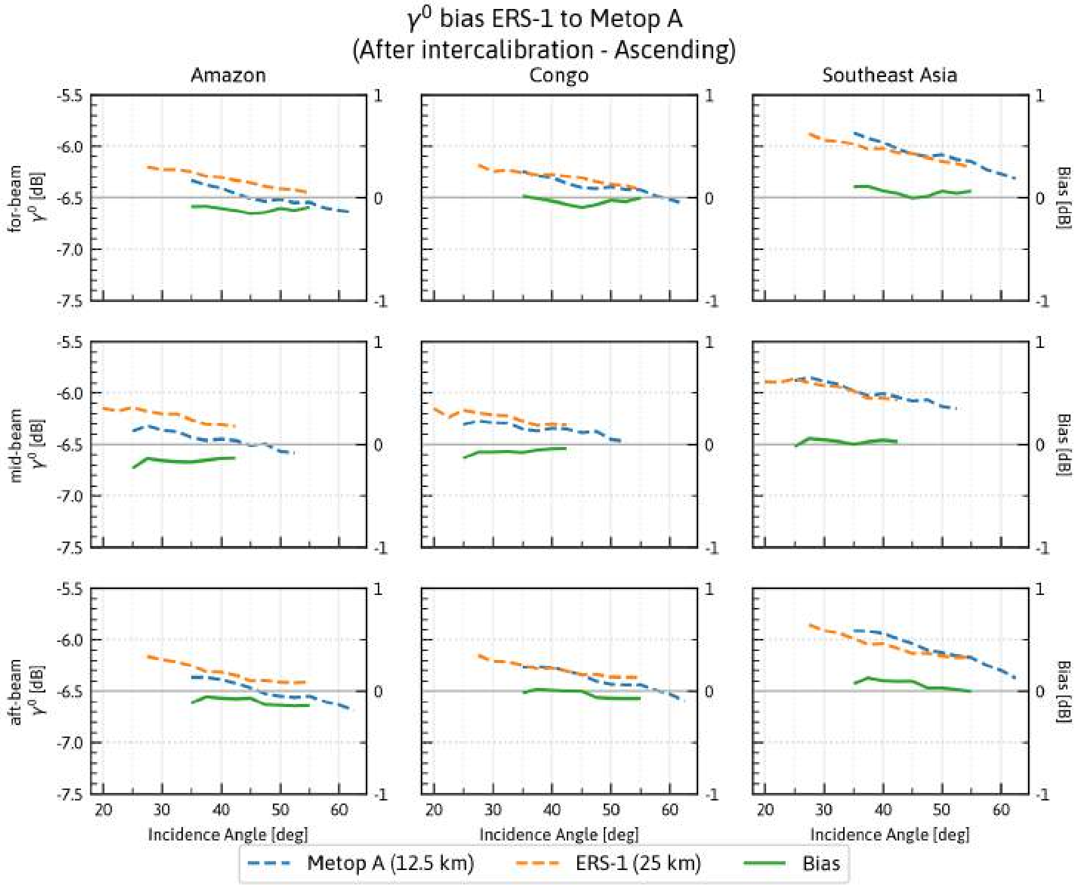

Figure 2.32: Comparison of γ^0 backscatter measurements from ERS-1 and Metop-A over incidence angle θ, after intercalibration.

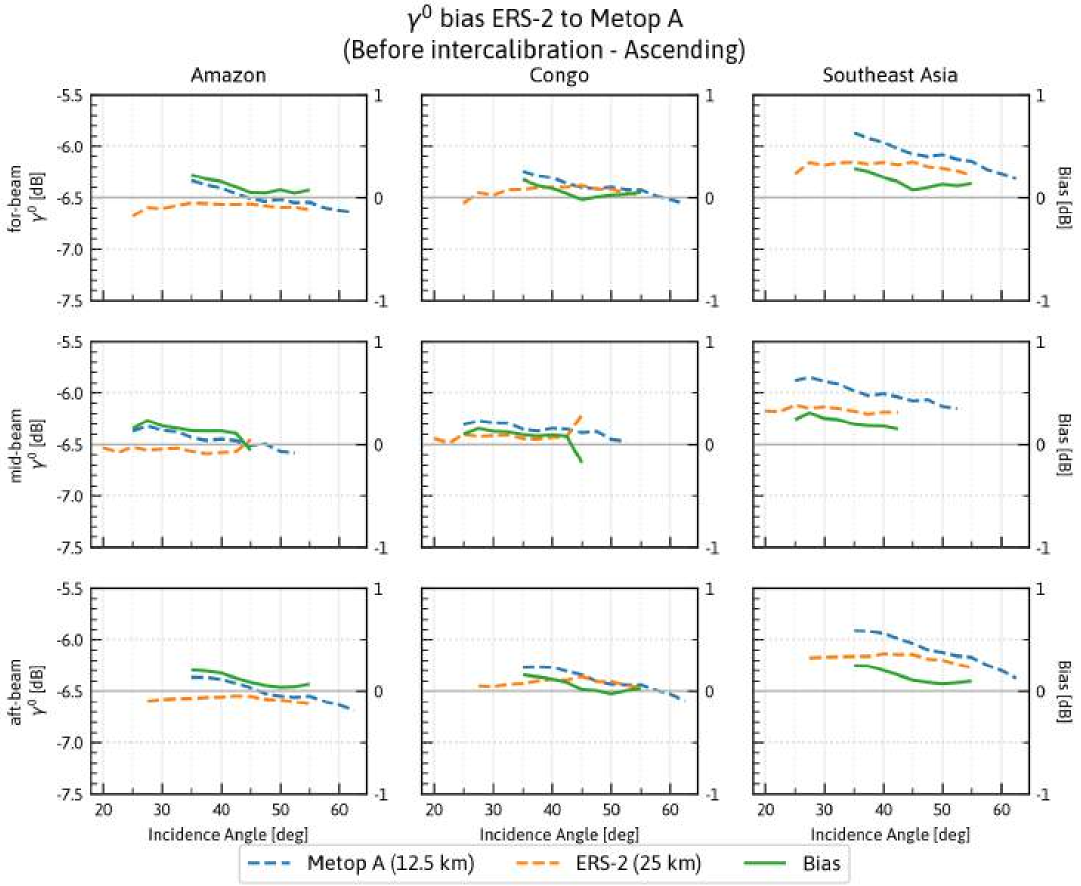

Figure 2.33: Comparison of γ^0 backscatter measurements from ERS-2 and Metop-A over incidence angle θ, prior to intercalibration.

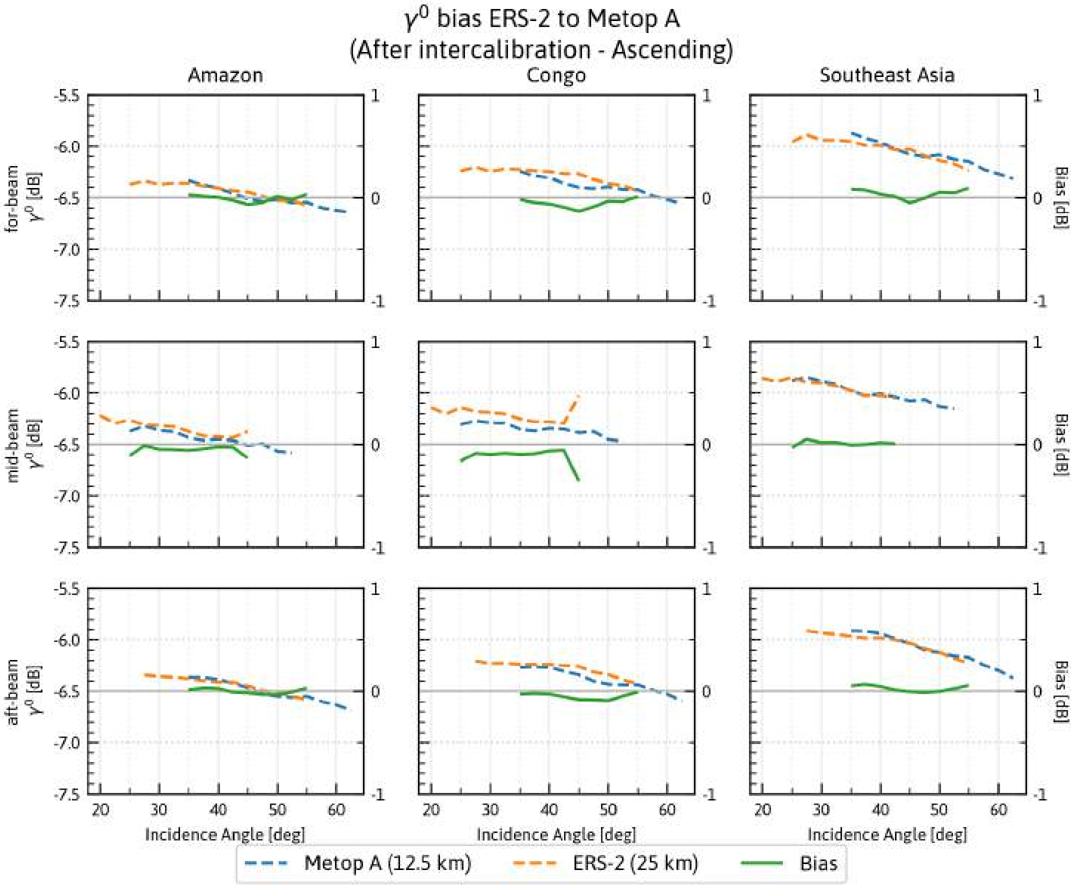

Figure 2.34: Comparison of γ^0 backscatter measurements from ERS-2 and Metop-A over incidence angle θ, after intercalibration.

2.6. Summary

We assessed the calibration quality of ERS-1 and ERS-2 scatterometer data using tropical rainforests as natural calibration targets. Our analysis provides several key findings relevant to creating a homogeneous climate data record from these instruments.

We successfully identified stable natural targets in the Amazon, Congo, and Southeast Asian rainforests, with comparable numbers of grid points selected for both satellites. These regions exhibited the expected characteristics of azimuthal isotropy, temporal stability, and spatial homogeneity necessary for reliable calibration references.

Time series analysis revealed systematic differences between the three antenna beams on both ERS satellites, with the mid-beam consistently showing lower backscatter response than fore- and aft-beams before calibration. The analysis also detected several breakpoints corresponding to mission phase transitions, particularly during ERS-1's second ice phase and geodetic phase.

ERS-2 data presented more complex challenges, with extensive data gaps and quality issues after gyroscope failures in 2001 and tape recorder problems in 2003. Late-period ERS-2 data (2005-2011) over the Amazon exhibited pronounced seasonal patterns that were not adequately removed by seasonality correction, further complicating calibration efforts.

Our intracalibration procedure, which adapted the methodology of [8] to operate in the gamma-nought domain, successfully harmonized measurements across the three beams of each satellite. The monthly calibration parameter approach effectively addresses beam biases and can track long-term trends, as demonstrated with Metop-A data. However, this approach has limitations in handling sharp breaks in the data, which are more present in ERS data than long-term trends, and transferred previously uncorrected region-specific seasonal patterns to other areas.

Analysis of calibration between ERS and Metop-A satellites revealed systematic biases of 0.1-0.4 dB in gamma-nought measurements, with a distinctive difference in incidence angle dependence between the instrument families. After applying the intercalibration procedure from [8], these biases were substantially reduced across all incidence angles and azimuth configurations.

These findings demonstrate that while ERS-1 data is generally robust and can be effectively calibrated, late-period ERS-2 data requires careful handling due to sparse coverage and technical issues. The procedures developed here provide a solid foundation for creating a consistent scatterometer climate data record spanning the ERS and Metop missions, though additional refinements to the seasonality correction approach and special handling of data gaps will be necessary for optimal results.

3. Interoperability between ERS-1 and ERS-2 ESCAT and Metop ASCAT data

3.1. Synthetic ESCAT dataset experiment

To evaluate whether ASCAT-specific processing procedures can be effectively applied to ESCAT, we analyzed how ESCAT's coarser temporal resolution might affect the retrieval quality of backscatter, slope, and curvature – key components of the FDR4LDYN data record. An experiment was conducted where several synthetic ESCAT datasets were generated from original ASCAT data, each trying to replicate the temporal sampling rate of ESCAT. For both original ASCAT measurements and synthetic datasets, backscatter (normalized to 40°), slope, and curvature were calculated and compared using metrics such as the root mean squared difference (RMSD) and Spearman rank correlation. The WAter Retrieval Package (WARP), used by TU Wien for deriving soil moisture from Level 1b backscatter data, facilitated these calculations. Interactive widgets were created to visualize time series and temporal sampling characteristics for selected grid points, including globally distributed points to capture diverse environmental and surface conditions. The widgets for the selected 38 grid points display:

- Time series of normalized backscatter at 40° for valid original ASCAT backscatter triplets, unmasked ESCAT valid backscatter triplets (no flags applied), and various synthetic ESCAT datasets
- Slope and curvature time series at 40°
- Histograms of temporal sampling characteristics for ESCAT and synthetic ESCAT datasets, including:
  - Distribution of time deltas between consecutive measurements
  - Distribution of measurements per day

The differences between synthetic datasets arise from the following subsampling methods:

- **3 satellite, 1 swath subsampling**: Uses data from all 3 Metop satellites but is limited to the right swath.
- **1 satellite, 1 swath subsampling**: Uses only Metop-B data from the right swath.
- **Random subsampling**: Randomly selects time intervals based on the distribution of ESCAT measurement intervals. First, the statistical distribution of time deltas between consecutive ESCAT measurements is captured. Then, these time deltas are randomly sampled to construct the synthetic ESCAT time series, mimicking ESCAT's temporal sampling behavior.
- **ESCAT-shift subsampling**: Shifts ESCAT time deltas to create the synthetic ESCAT time series. The time delta between the first two ESCAT measurements is added to the first measurement of ASCAT, and the nearest ASCAT measurement in time is selected as the next point. Since the combined ESCAT dataset (ERS-1 and ERS-2) spans from 1991 to 2011, this method can be applied to the entire ASCAT time series (2007–2023). To account for seasonal differences due to the differing start dates of ESCAT and ASCAT, ASCAT data from 2007 is excluded until its day of the year aligns with the first available ESCAT measurement.
- **Measurements-per-day subsampling**: Matches the number of daily measurements to ESCAT by adjusting the ASCAT time series accordingly. Instead of analyzing time deltas, this method focuses on matching the number of measurements per day. Extra ASCAT measurements are discarded, and when ASCAT has fewer measurements than ESCAT, data from adjacent days are included to maintain temporal proximity and better align with ESCAT's resolution.

As shown in Fig. 3.1, subsampling by excluding certain satellites and swaths still leaves too many measurements in the synthetic ESCAT dataset. Even with data from just Metop-B's right swath, the alignment with ESCAT's sampling distribution is poor. The median and mean time deltas for ESCAT at the Castelporziano station near Rome, Italy are 7 and 12.4 days, respectively, whereas subsampled ASCAT data from Metop-B's right swath show significantly shorter median and mean intervals of 1 and 1.7 days. However, more complex methods like random, ESCAT shift, and measurements per day (Fig. 3.2) achieve much better alignment with ESCAT's temporal sampling. The median and mean time deltas here are comparable to those of ESCAT, with median values ranging from 6.5 to 7 days and mean values between 11.7 and 11.9 days in this example.

A key limitation of the random subsampling method is the regional mission data gaps during ERS-2's operation, which cause large time deltas that skew the distribution. Random sampling fails to reflect the deterministic nature of these gaps. The measurements-per-day method also has drawbacks; due to differences in orbital characteristics, matching measurements per day can miss nearby timestamps, though this can be mitigated by including surrounding days. The ESCAT-shift method, which directly applies ESCAT time deltas to ASCAT, avoids these issues. ASCAT's regular intervals and lack of large data gaps make it a more consistent representation of ESCAT, with fewer assumptions or adjustments. Therefore, for fine-tuning slope/curvature calculation parameters, the ESCAT-shift subsampling method was chosen for further adaptation.

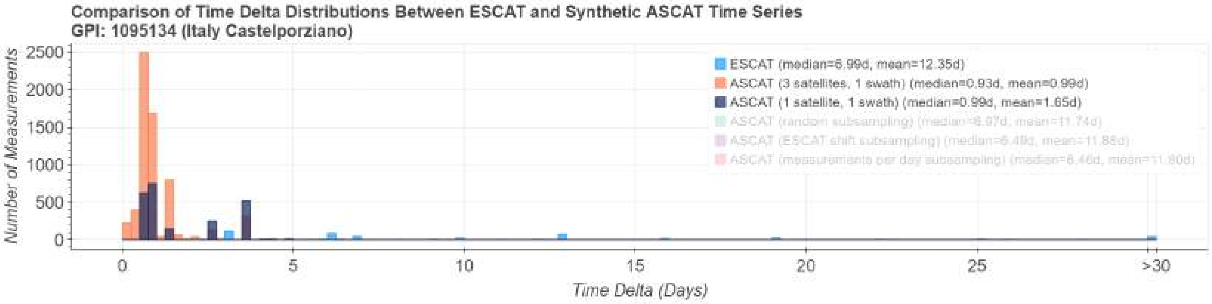

Figure 3.1: Distribution of time deltas between consecutive measurements at the Castelporziano station near Rome, Italy, displayed in 6-hour interval histograms. ESCAT's sampling distribution is represented in blue, while the synthetic ESCAT distributions are shown in orange (3 satellites, 1 swath) and gray (1 satellite, 1 swath).

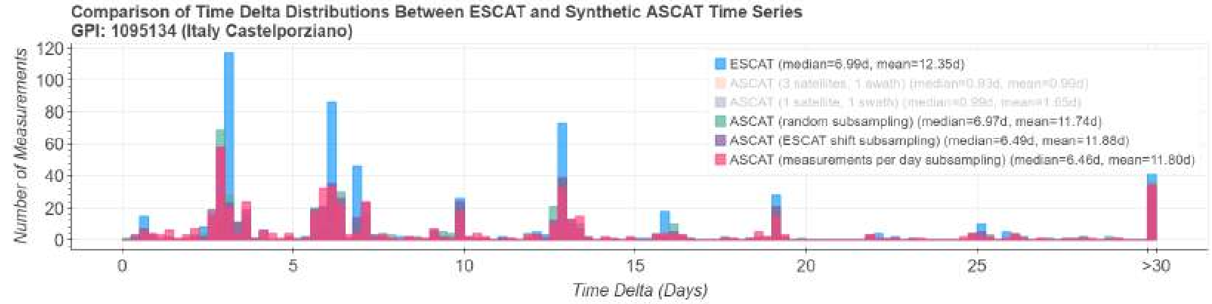

Figure 3.2: Distribution of time deltas between consecutive measurements at the Castelporziano station, shown in 6-hour interval histograms. ESCAT's sampling distribution is depicted in blue, while the synthetic ESCAT distributions for more advanced subsampling methods are represented in green (random), purple (ESCAT shift), and pink (measurements per day).

3.2. Slope and curvature calculation based on synthetic ESCAT data

Each subsampling variant employs two different methods for calculating slope and curvature:

- **clim**: Based on climatology, with equal values across years.
- **ts**: Time-series-based, with values changing year-to-year.

3.2.1. Climatology-based slope and curvature

Climatology-based slope and curvature are generally more robust due to their derivation from long-term datasets spanning multiple years. However, they lack information on both inter-annual and short-term variations, which can be valuable for studies like vegetation dynamics. In contrast, time-series-based slope and curvature are typically calculated from a 42-day window of data (21 days before and after the target date), with a function fitted to the data points within this period. This method yields daily varying slope and curvature values that do not repeat annually. A key objective of the synthetic ESCAT experiment is to assess the impact of ESCAT's coarser temporal resolution and to evaluate the feasibility of calculating time-series-based slope and curvature. Nevertheless, also the quality of climatology-based metrics is crucial, especially in the context of fusing data from ESCAT and ASCAT, where sparser data points and biases could also affect data quality.

Analysis of the climatology-based slope time series for the three subsampling variants, shown in Fig. 3.3, demonstrates strong alignment with the climatology derived from the original ASCAT data (thick magenta line) for the ARM soil moisture station in Oklahoma, USA. While the subsampled data show increased noise, rank correlations remain high, often approaching 1 across many grid points. In cases where the temporal variation's amplitude is small, noise becomes more noticeable, occasionally lowering correlations to around 0.5. This is illustrated in Fig. 3.4, which depicts the climatology-derived slope for a grid point in the Borneo rainforest. The various subsampling methods significantly affect which parts of the curve are emphasized, depending on the specific measurements selected. However, despite these variations, the overall shape of the temporal pattern is reasonably preserved both in the Borneo example and across all 38 grid points analyzed.

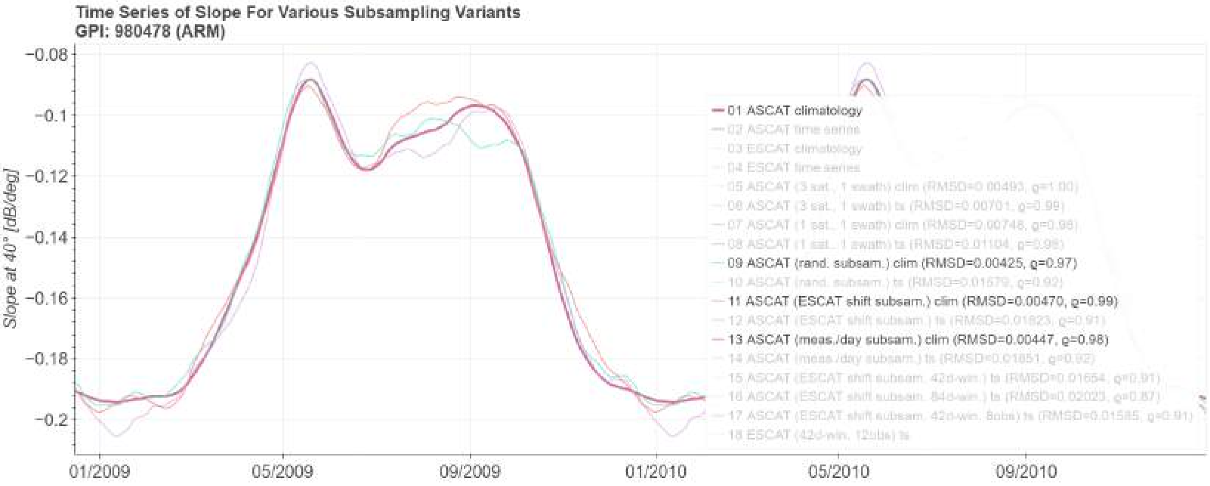

Figure 3.3: Time series of climatology-based slope for 2009 at the ARM station in Oklahoma, USA, comparing the original ASCAT data (thick magenta line) with the subsampled versions (mint, violet, and orange lines).

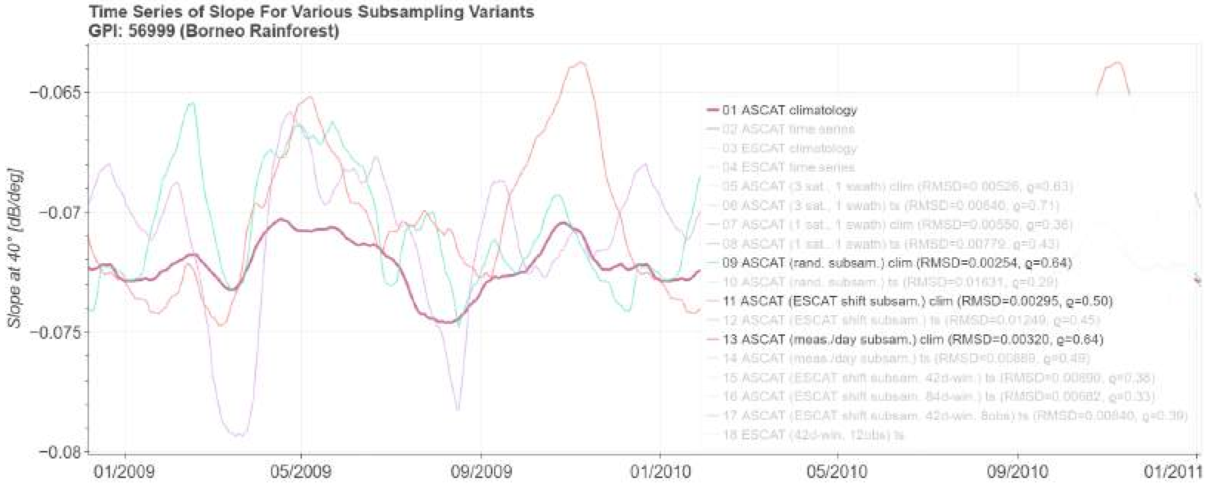

Figure 3.4: Time series of climatology-based slope for 2009 at a Borneo rainforest grid point, comparing the original ASCAT data (thick magenta line) with the subsampled versions (mint, violet, and orange lines).

The higher-order term, climatology-based curvature from subsampled ASCAT data, tends to exhibit slightly more noise than slope compared to the original ASCAT data. Despite this, Spearman correlations generally remain high, exceeding 0.9 for the analyzed grid point at the Park Hills soil moisture station in Wisconsin, USA, as shown in Fig. 3.5. A visual analysis confirms that the overall behavior of curvature is reasonably well captured. However, correlations vary at other grid points, with some dropping to around 0.3. An extreme case is the grid point in San Rossore, Pisa, Italy, where the correlation between subsampled climatology-based curvature and original ASCAT data is slightly negative at –0.2 (Fig. 3.6). Notably, the time-series-based curvature from original ASCAT data also shows deviations from climatology, often displaying behavior contrary to climatological expectations. This suggests that curvature variations may not follow a clear seasonal pattern but are influenced by current environmental conditions. Additionally, the small amplitude of variation reduces the impact of low correlations. Given that climatology provides the most robust estimate of slope and curvature available, computing climatologies for ESCAT data is still recommended and planned. For users focused on inter-annual and short-term variations, time-series-based values will be particularly relevant, which will be discussed in the following section.

3.2.2. Time-series-based slope and curvature

At the ARM station, Fig. 3.7 shows that for time-series-derived slope, there is still a strong alignment between the original and subsampled ASCAT data. While RMSD values are notably higher compared to the climatology-based time series, Spearman correlations remain above 0.9 for all subsampling variants. This increase in RMSD is unsurprising, as the climatology-based slopes use data spanning 17 years, offering much more robust fits than the 42-day window used in the time-series analysis. What stands out, however, is how notably the subsampling method – and therefore the specific choice of limited data points used in the fit – impacts short-term variability. This is especially evident at the beginning of 2020, where the different subsampled variants diverge significantly from each other for several days. A second issue to observe is the presence of data gaps. For subsampling variant 10 (random subsampling), there is a brief gap in mid-2019. Although short, this leads to pronounced edge effects, particularly immediately after the gap – a consequence of the sparse data, as is the case with ESCAT.

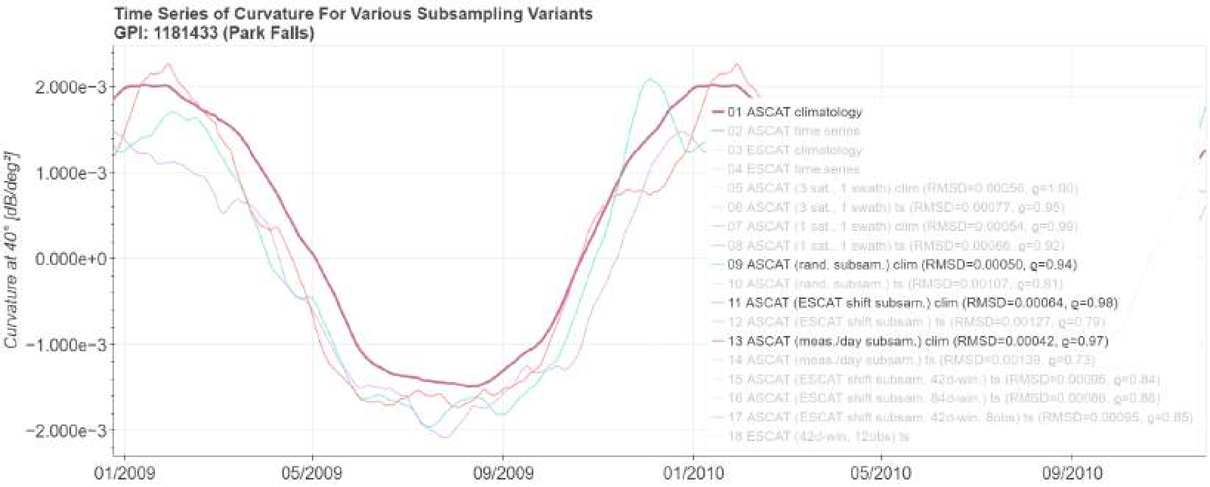

Figure 3.5: Time series of climatology-based curvature for 2009 at the Park Falls station in Wisconsin, USA, comparing the original ASCAT data (thick magenta line) with the subsampled versions (mint, violet, and orange lines).

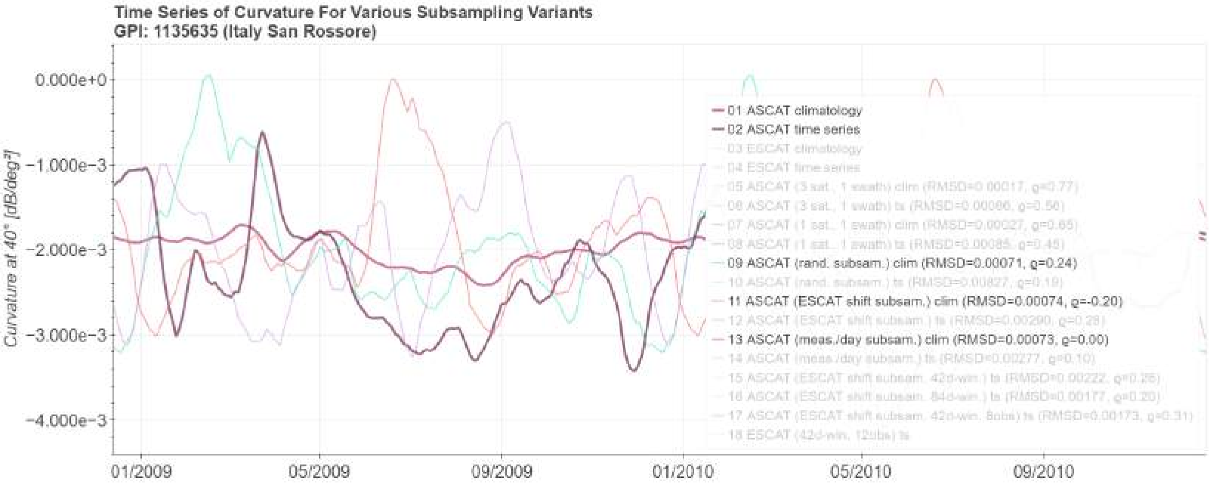

Figure 3.6: Time series of climatology-based curvature for 2009 at the San Rossore station near Pisa, Italy, comparing the original ASCAT data (thick light magenta line) with the subsampled versions (mint, violet, and orange lines) and time-series-based curvature (thick dark magenta line).

Both effects become significantly more pronounced in other regions, as demonstrated by the Loobos (Netherlands) example in Fig. 3.8 for curvature. In this case, all subsampling variants exhibit strong edge effects and numerous gaps, some lasting for weeks. When sufficient data is available, the general curvature pattern is however reasonably captured, yielding weak but positive correlations between 0.2 and 0.4.

Before time-series-based slope and curvature can be included in the FDR4LDYN data record, processing parameters must thus be adjusted to ensure more robust fits by incorporating additional data points and tightening criteria to minimize edge effects. These adjustments will be discussed in the next section.

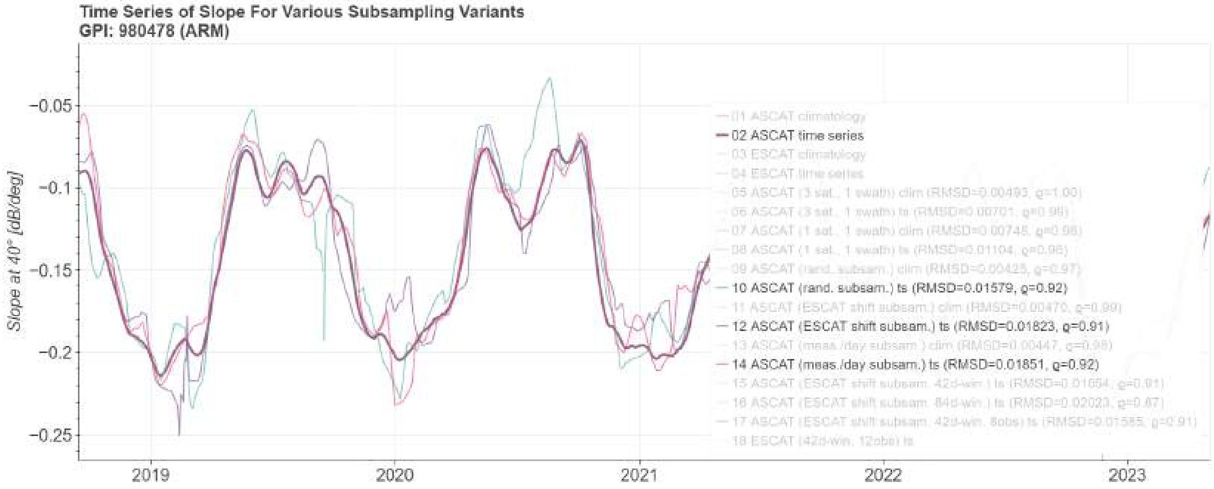

Figure 3.7: Time series of time-series-based slope from 2019 to 2021 at the ARM station in Oklahoma, USA, comparing the original ASCAT data (thick magenta line) with the subsampled versions (mint, violet, and orange lines).

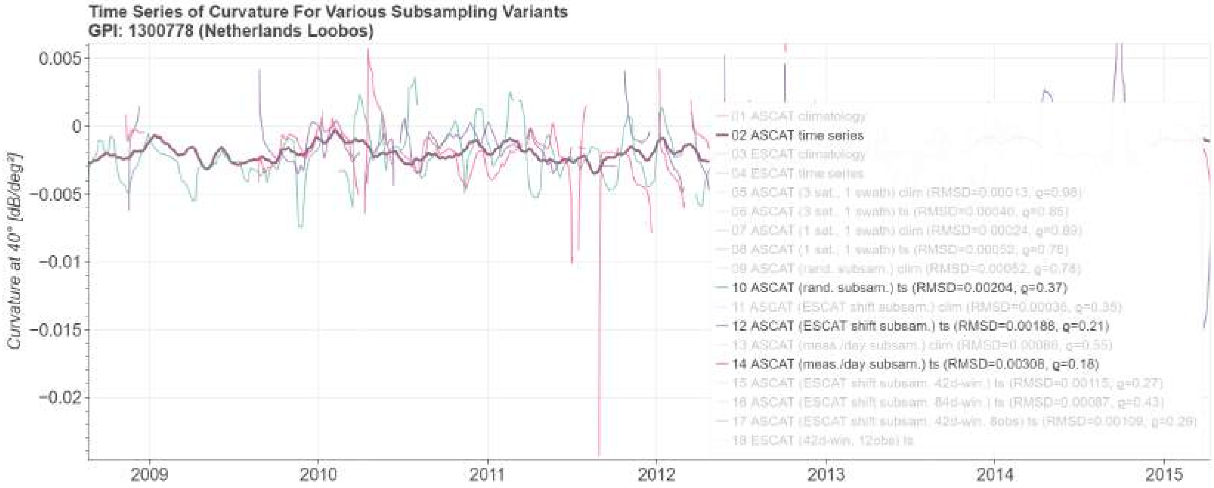

Figure 3.8: Time series of time-series-based curvature from 2009 to 2012 at the Loobos site near Kootwijk, the Netherlands, comparing the original ASCAT data (thick light magenta line) with the subsampled versions (mint, violet, and orange lines).

3.2.3. Parameter adaptations for time-series-based slope and curvature

As noted earlier, we have chosen to focus on the ESCAT-shift subsampling method due to its advantages. All following parameter adaptations will therefore be applied using this specific subsampling approach. To adjust the number of measurements used in slope and curvature fitting, we can modify the window half-width in the WARP processing. The following options have been explored:

- **21 days**: Standard window size used in ASCAT processing.
- **42 days**: A balance between noise reduction and robustness for ESCAT-based temporal resolution.
- **84 days**: Provides robust results but smooths out time dynamics.

To reduce edge effects and avoid unreliable results caused by too few data points, we can tighten the criteria for the minimum number of measurements required to compute a result for a given date. The following initial options have been tested:

- **4 observations**: Standard setting for ASCAT processing.
- **8 observations**: Increases robustness and reduces edge effects near data gaps for time-series-based slope/curvature.

In the Netherlands example, Fig. 3.10 illustrates significant improvements achieved through parameter adjustments. Doubling the required number of measurements per fit from four to eight substantially reduces edge effects, as shown by the gray line. In contrast, the yellow line, which represents the standard method with only four measurements per fit, exhibits more pronounced edge effects. Additionally, increasing the window half-width from 21 to 84 days (resulting in a total window size of 168 days) enhances the Spearman correlation with original ASCAT data from 0.21 to 0.43.

However, these improvements must be balanced against potential drawbacks related to smoothing and data availability. A broader window size or stricter fit conditions may either overly smooth the time series or introduce more gaps. This smoothing effect is evident in the ARM station example, where a 84-day window (olive line) even reduces the Spearman correlation with original ASCAT data from 0.91 to 0.87. This decrease occurs because subtle short-term fluctuations are lost in the more smoothed data. Conversely, shorter windows, such as 42 days (e.g., gray line), capture more of these short-term variations, highlighting that a longer time window is not always beneficial. The issue of data gaps can be observed in the Loobos example, again. While tightening fit conditions reduces edge effects, it results in more data gaps, as values are only computed if the stricter criteria are met.

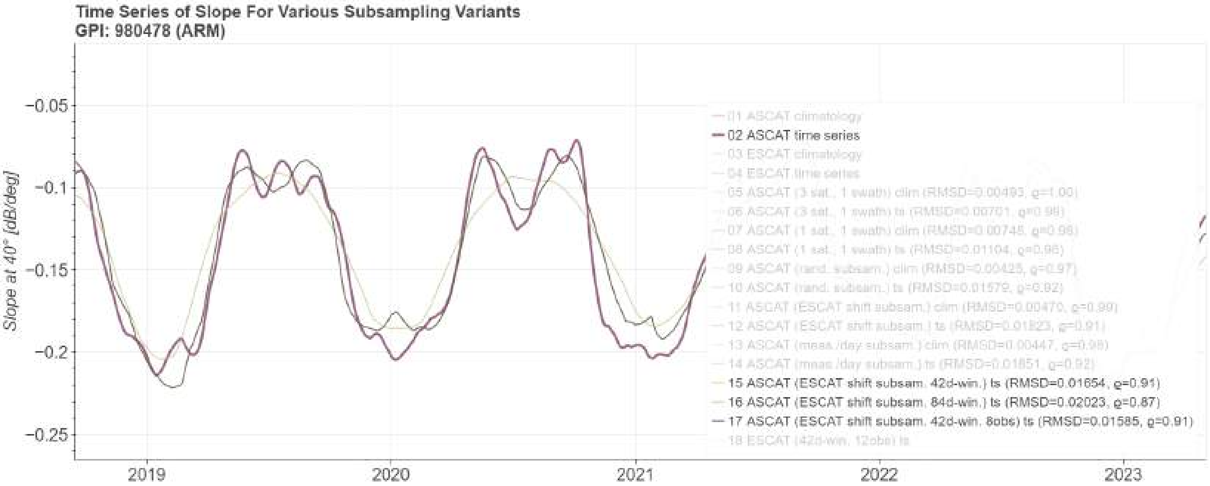

Figure 3.9: Time series of slope from 2019 to 2021 at the ARM station in Oklahoma, USA, based on time-series data, comparing the original ASCAT data (thick magenta line) with the ESCAT-shift-subsampled versions using different parameter adaptations (yellow, olive, and gray lines).

However, it should be noted that these parameter adaptations represent only an initial test to assess how different parameter settings influence the slope and curvature derived from the synthetic ESCAT dataset as part of this experiment. In the actual FDR4LDYN data record based on actual ESCAT data, we will likely include various versions of time-series-derived slope and curvature alongside climatologies. To meet diverse user needs, we will test options that focus on capturing short-term variability – although these may result in more data gaps – as well as more robust, readily available data that retains a useful

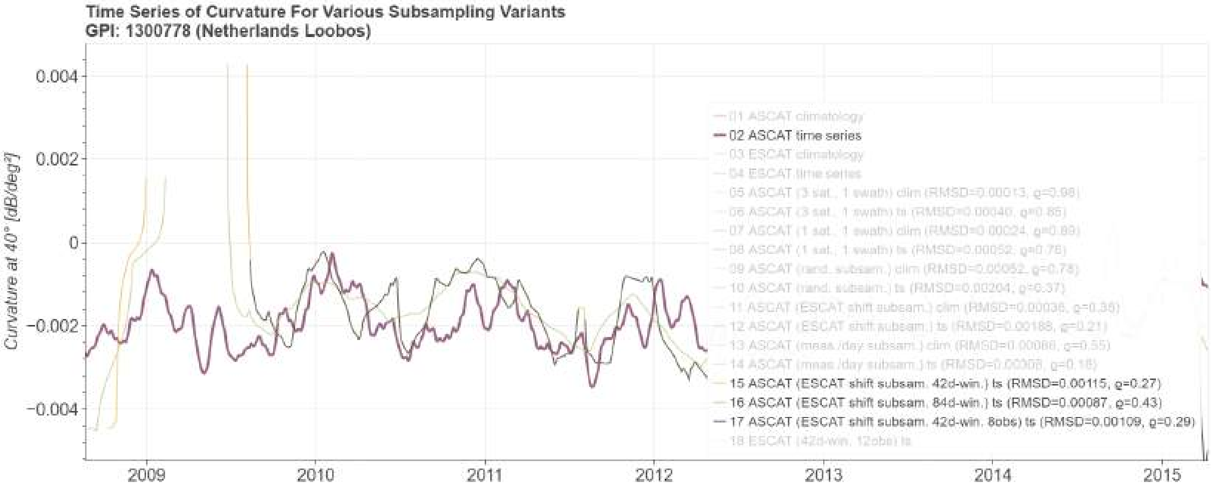

Figure 3.10: Time series of curvature from 2009 to 2012 at the Loobos site near Kootwijk, the Netherlands, based on time-series data, comparing the original ASCAT data (thick magenta line) with the ESCAT-shift-subsampled versions using different parameter adaptations (yellow, olive, and gray lines).

degree of time-series information by applying the existing two-time-window approach. One time window determines the extent to which recent local slope information is incorporated into the slope and curvature fit. The second window controls whether the calculation is based solely on the current year or also includes data from the same short-term window in adjacent years to enhance robustness. Incorporating data from all years effectively produces a climatology. Additionally, we will explore a new Bayesian approach in which observations closer to a given measurement date are assigned higher weights, while more distant observations receive lower weights. Furthermore, we will experiment with alternative statistical methods for estimating slope and curvature without relying on fixed time windows. These approaches are envisioned to enhance robustness, produce gap-free slope and curvature time series, and provide valuable insights for applications such as vegetation studies.

3.3. Preliminary processing of ESCAT data

3.3.1. Time series analysis

Building on insights from the synthetic ESCAT experiment, we proceeded to process both the original and inter-calibrated ESCAT data, which was derived as described in the previous section. After assessing input data quality and ensuring proper calibration to Metop ASCAT for quality control, we now focus on evaluating the quality and robustness of the first set of resulting FDR4LDYN variables. These currently include normalized backscatter as well as slope and curvature climatologies. In this preliminary analysis, these variables were processed using real ESCAT data from 1991 to 2000, as calibration correction coefficients are occasionally missing for some regions beyond this period due to ERS-2 mission challenges, including the zero-gyro mode and the tape recorder failure after 2003. Despite these limitations, this 10-year period is expected to provide a comprehensive assessment of inter-calibration impacts.

Fig. 3.11 presents a comparison of normalized backscatter at a reference incidence angle of 40° for the ARM station during the first half of 2009, when ESCAT and ASCAT data overlap. The variants shown include original ASCAT data (bold orange, variant 99), synthetic ESCAT data from the ASCAT subsampling experiment described above (brown, v96), original ESCAT data (red, v01), and inter-calibrated ESCAT data (dark blue, v06). Overall, both the synthetic and real ESCAT data capture backscatter dynamics well despite their lower temporal resolution. The absolute magnitude and dynamic range visibly align well with ASCAT data, and also short-term variations are represented to some extent. However, due to the individual sampling points of the ESCAT variants, it is evident that ESCAT cannot capture short-term fluctuations with the same precision as ASCAT – an expected limitation. Moreover, especially in earlier years, the time series becomes increasingly sparse, with extended data gaps limiting the ability to capture events critical for applications such as soil moisture, vegetation dynamics, and flood monitoring in some cases.

Comparing the synthetic ESCAT time series with actual ESCAT data, we observe that for the ARM station, RMSD values are significantly lower, and Spearman correlations are higher for the synthetic variant. Additionally, biases in average backscatter across the full time series are noticeably larger for actual ESCAT data, while its standard deviation slightly exceeds expectations based on the synthetic experiment. This suggests that insights from the synthetic experiment should be interpreted with caution, as the subsampling procedure alone may not fully account for all measurement differences between the ERS and Metop instruments. To further investigate these discrepancies, we will extend the statistical analysis to a global scale. One encouraging result is that the inter-calibration procedure effectively reduces the bias for the ARM station from –0.22 to –0.14. However, the remaining bias remains notably stronger than the positive bias of 0.033 observed for the synthetic ESCAT dataset. Despite these differences, the overall alignment between ESCAT and ASCAT normalized backscatter at the ARM station is reasonable.

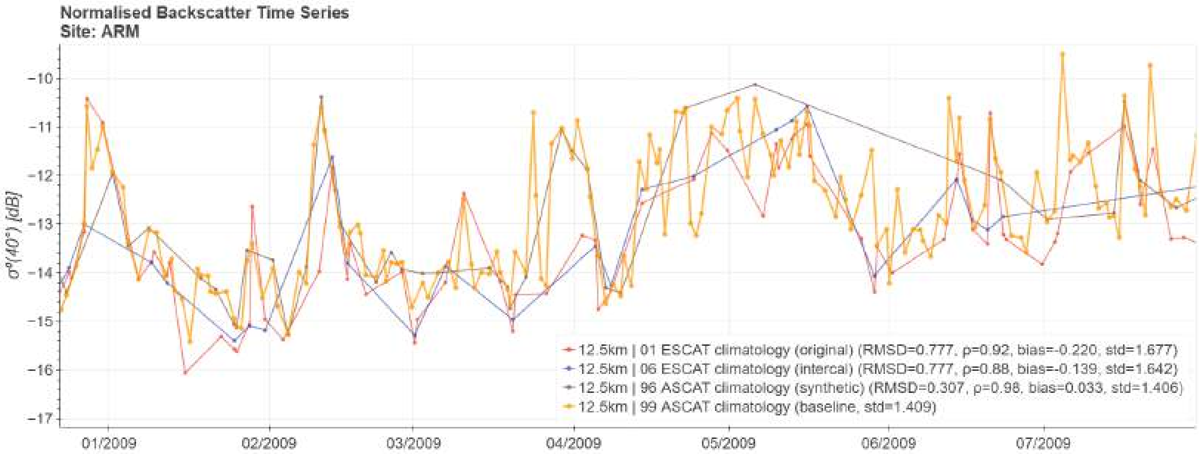

Figure 3.11: Time series of normalized backscatter based on slope and curvature climatologies for the first half of 2009 at the ARM station in Oklahoma, USA. Comparison between original ASCAT (bold orange, v99), synthetic ESCAT (brown, v96), original ESCAT (red, v01), and inter-calibrated ESCAT data (dark blue, v06).

In the initial processing of ESCAT FDR4LDYN variables, we focused on analyzing climatologies for slope and curvature, which provide values for each day of the year that repeat annually. These climatologies are derived from the entire available time series. For the ARM station, shown in Fig. 3.12, the slope results are promising. While slopes based on actual ESCAT data exhibit a slight overshoot in early spring, leading to higher maximum values, the overall temporal pattern closely aligns with ASCAT results. RMSD values are minimal, and Spearman correlations exceed 0.95, indicating a very strong agreement. Encouragingly, the inter-calibration procedure effectively eliminates the small bias observed in the original ESCAT data.

The corresponding curvature data for the ARM station is shown in Fig. 3.13. While the overall shape of the time series aligns reasonably well again, there are substantial biases between original ASCAT curvatures and those derived from ESCAT data. ESCAT-based values are approximately twice as large

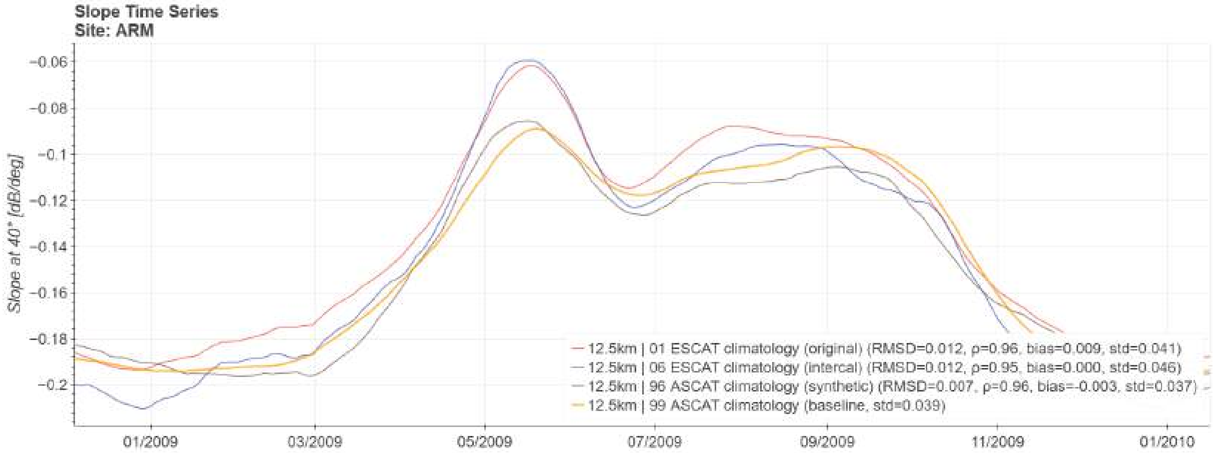

Figure 3.12: Time series of slope for 2009 at the ARM station in Oklahoma, USA. Comparison between original ASCAT (bold orange, v99), synthetic ESCAT (brown, v96), original ESCAT (red, v01), and inter-calibrated ESCAT data (dark blue, v06).

as both the climatology and time-series-based curvature results. Interestingly, the curvature time series derived from synthetic ESCAT data do not exhibit this strong bias, suggesting that the sparser temporal sampling alone is not the primary cause of the observed discrepancies. We expect curvature results to be less robust due to their greater sensitivity as a higher-order term. However, the significant discrepancies observed in this example warrant further investigation into these biases.

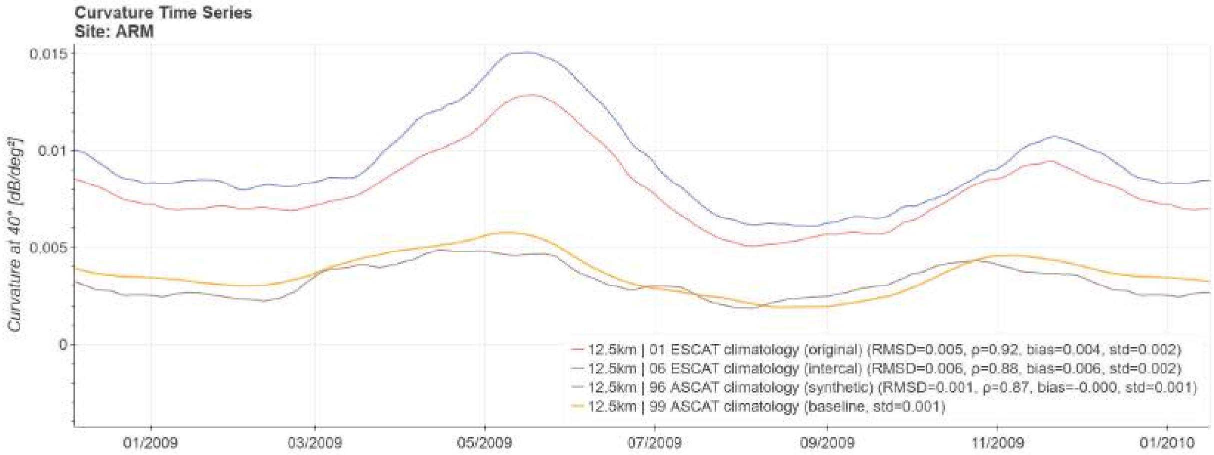

Figure 3.13: Time series of curvature for 2009 at the ARM station in Oklahoma, USA. Comparison between original ASCAT (bold orange, v99), synthetic ESCAT (brown, v96), original ESCAT (red, v01), and inter-calibrated ESCAT data (dark blue, v06).

From the previous analysis, we recall that the ARM station in the US represents a case with relatively good ESCAT data coverage. For comparison, we also examine preliminary ESCAT FDR4LDYN results in more challenging conditions, such as during the zero-gyro mode and the ERS-2 tape recorder failure after 2003 in Europe. Figures 3.14–3.16 present backscatter, slope, and curvature results for the Collelongo station in the Abruzzo region of Italy.

In the time series of normalized backscatter, we observe extended data gaps, particularly in the inter-calibrated ESCAT version, where most of 2009 lacks data. The longest gap spans approximately eight months, as the inter-calibration procedure requires a minimum number of measurements to provide corrected sigma values. Even in the original ESCAT data, a five-month gap is present, preventing the reliable capture of short-term backscatter dynamics during these periods.

The ESCAT-derived slope climatology shows reasonable agreement with ASCAT data. While the ESCAT signal exhibits greater variability – amounting to twice the standard deviation of ASCAT – the general seasonal pattern aligns well. However, a notable issue arises: applying inter-calibration appears to introduce a slope bias that was not present in the original ESCAT data. We will revisit this issue when analyzing slope biases at a global scale in the following subsection.

For curvature, the ESCAT data exhibit even greater noise compared to the relatively smooth ASCAT time series. This increased noise is a direct consequence of large data gaps and the limited data availability, which strongly affect the highly sensitive curvature parameter. The synthetic ESCAT time series also reflects these challenges. However, we again observe a significant bias between synthetic and actual ESCAT data: Although curvature values remain small, actual ESCAT-derived curvatures turn positive for large portions of autumn, winter, and spring, whereas ASCAT curvatures remain consistently negative throughout the year.

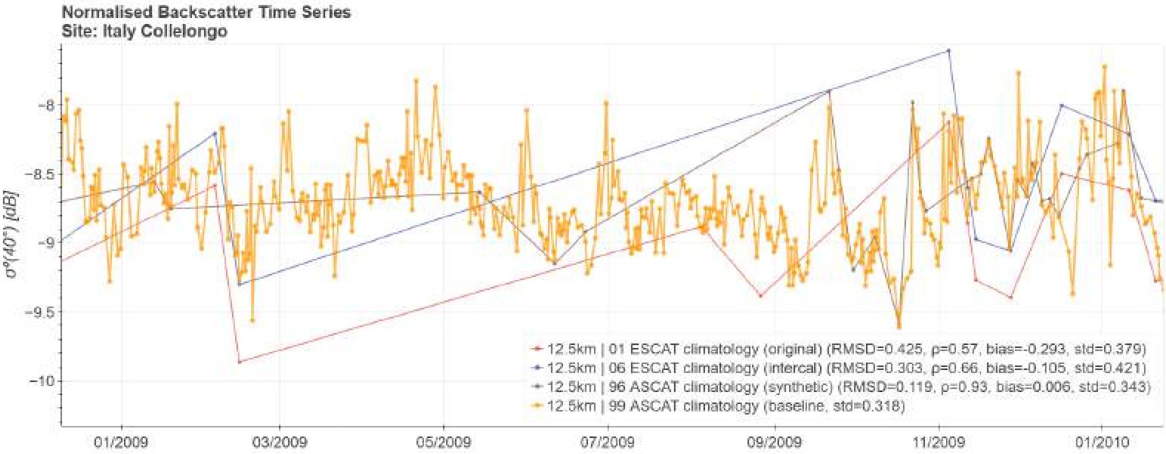

Figure 3.14: Time series of normalized backscatter based on slope and curvature climatologies for the first half of 2009 at the Collelongo station in Abruzzo, Italy. Comparison between original ASCAT (bold orange, v99), synthetic ESCAT (brown, v96), original ESCAT (red, v01), and inter-calibrated ESCAT data (dark blue, v06).

Two key factors have been identified as potential contributors to the biases observed in these examples. First, as discussed in Section 2.5, the differing calibration approaches for ERS (based on natural stable targets over the rainforest) and Metop (using active transponders) result in distinct incidence angle–backscatter relationships over the rainforest. We expect this discrepancy to particularly affect slope behavior on a global scale. Second, the different incidence angle ranges of ESCAT (18°–57°, [12]) and ASCAT (25°–65°, [13]) are expected to influence both slope and curvature, as their absolute values strongly depend on the incidence angle. To further examine the impact of these factors, we analyze the time series of a pixel in the Amazon rainforest, a region expected to exhibit stable scattering, assuming near-ideal volume scattering conditions.

Since the grid point in the Amazon rainforest represents an area that serves as a reference for the inter-calibration process, it provides a strong example of how inter-calibration effectively reduces slope biases in these regions. Comparing original ESCAT and ASCAT slope climatologies in Fig. 3.17, we observe a clear bias of 0.013 dB/deg, with ESCAT consistently exhibiting higher slope values throughout the year – a pattern typical for most locations. In this plot, an additional magenta line represents slopes derived from

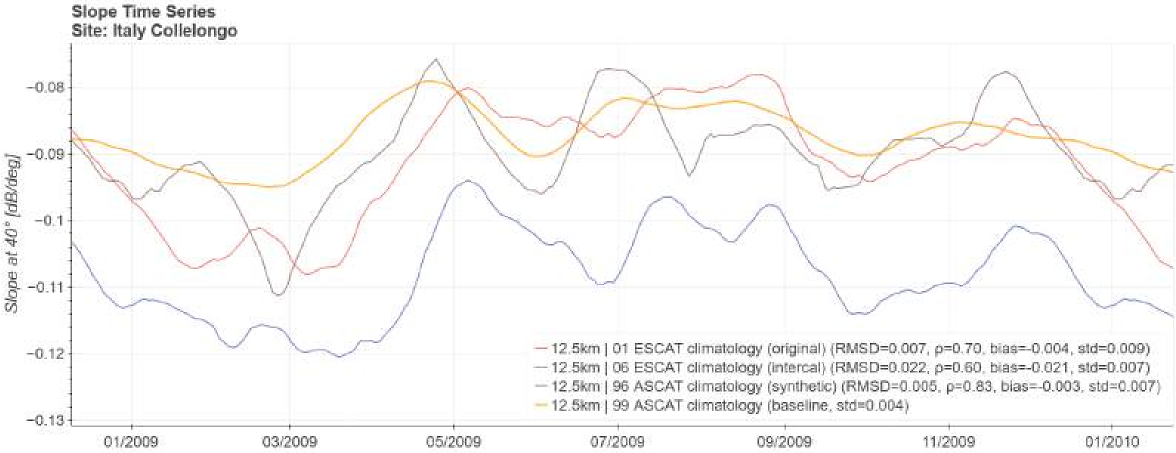

Figure 3.15: Time series of slope for 2009 at the Collelongo station in Abruzzo, Italy. Comparison between original ASCAT (bold orange, v99), synthetic ESCAT (brown, v96), original ESCAT (red, v01), and inter-calibrated ESCAT data (dark blue, v06).

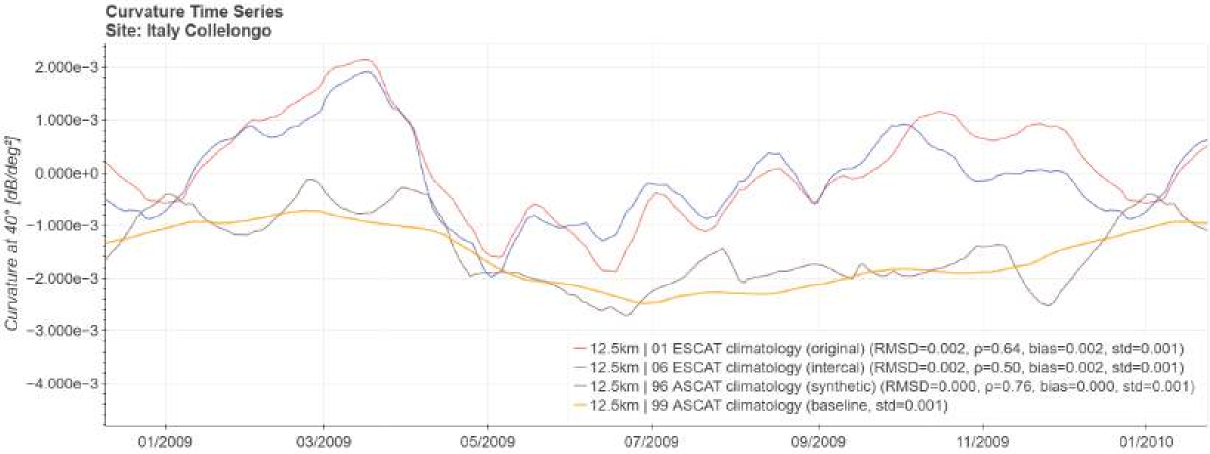

Figure 3.16: Time series of curvature for 2009 at the Collelongo station in Abruzzo, Italy. Comparison between original ASCAT (bold orange, v99), synthetic ESCAT (brown, v96), original ESCAT (red, v01), and inter-calibrated ESCAT data (dark blue, v06).

original ESCAT data restricted to the overlapping incidence angle range between ESCAT and ASCAT in the processing procedure. Similarly, variant 98, shown in turquoise, represents the same adaptation for ASCAT slopes. Since these adapted time series exhibit nearly the same bias as before, we conclude that differences in the incidence angle ranges of the ERS and Metop instruments have a limited impact in this case. This is expected as slope values in the rainforest tend to be small. After applying the inter-calibration procedure, however, this bias is nearly eliminated. One notable feature that remains is the more pronounced seasonal pattern in ESCAT data compared to ASCAT, which leads to low correlation values between the two. This discrepancy warrants further investigation.

In stark contrast, the time series in Fig. 3.18 represents a grid point in a sand dune desert in Libya. Here, the red and dark blue lines, representing the original and inter-calibrated ESCAT-based slope climatologies, respectively, exhibit nearly identical biases compared to ASCAT slopes. However, when considering slopes derived from time series limited to the common incidence angle range, the bias is significantly re-

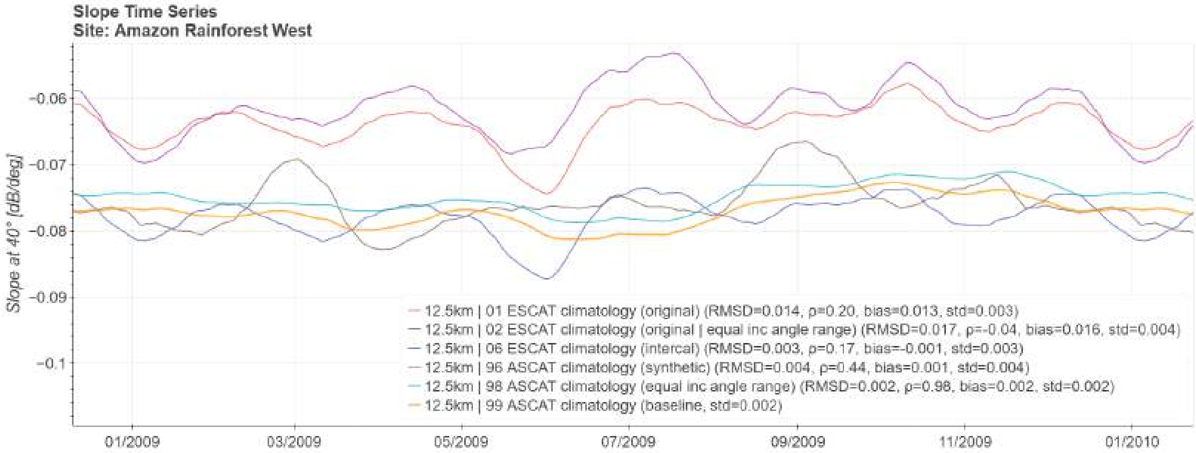

Figure 3.17: Time series of slope for 2009 at a grid point in the Amazon rainforest in Brazil (5.25°S, 66.045°W. Comparison between original ASCAT (bold orange, v99), original ASCAT filtered by common incidence-angle-range (turquoise, v98), synthetic ESCAT (brown, v96), original ESCAT (red, v01), original ESCAT filtered by common incidence-angle-range (magenta, v02), and inter-calibrated ESCAT data (dark blue, v06).

duced. This is likely due to the steep slopes characteristic of desert regions, where backscatter exhibits a strong dependence on incidence angle.

Another contributing factor may be the dominance of Bragg scattering in sand seas at incidence angles between 32°–34°, as discussed in Section 1.5. While ASCAT's fore and aft beams, with an incidence angle range of 35°–63°, largely miss this effect, ESCAT's beams, covering 24°–57°, fully capture the active range of Bragg scattering. A more detailed analysis of azimuthal effects in ESCAT data will help determine whether this phenomenon contributes to slope biases relative to ASCAT. If so, part of this bias would be geophysical in nature and should not be removed in the processing.

More broadly, restricting ESCAT data to the common incidence angle range shared with ASCAT does not appear to be a viable approach, given the already limited data availability in ESCAT. Further reducing the number of valid data points for slope and curvature calculations is unlikely to improve data quality. Instead, we will focus on refining the inter-calibration strategy and assess remaining biases at a global scale to determine whether additional adjustments are necessary to ensure good interoperability between the sensors, despite differences in their respective incidence angle ranges.

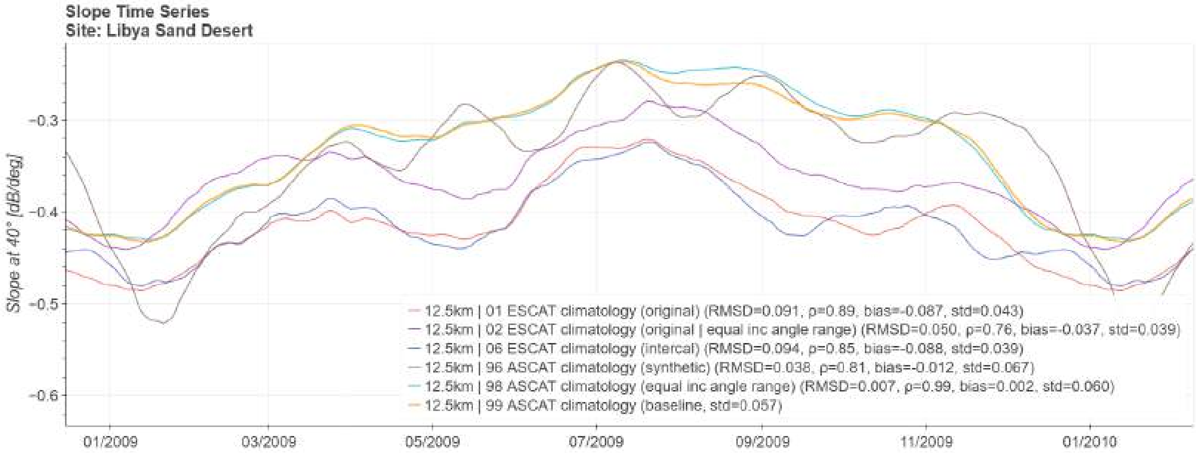

Figure 3.18: Time series of slope for 2009 at a grid point in a sand dune desert in Libya (24.89°N, 20.83°E. Comparison between original ASCAT (bold orange, v99), original ASCAT filtered by common incidence-angle-range (turquoise, v98), synthetic ESCAT (brown, v96), original ESCAT (red, v01), original ESCAT filtered by common incidence-angle-range (magenta, v02), and inter-calibrated ESCAT data (dark blue, v06).

3.3.2. Spatial analysis of slope

Having examined time series at individual grid points, we now extend the analysis of the initial FDR4LDYN variable results to a global scale. Specifically, we aim to investigate the biases observed when comparing ESCAT and ASCAT slope and curvature climatologies. The following figures illustrate the differences in these variables, first by comparing results derived from original ESCAT data with ASCAT slopes and curvatures, and then by assessing how these biases evolve when inter-calibrated ESCAT data is used instead.

Figures 3.19 and 3.20 show the biases between the mean slope climatologies of ESCAT and ASCAT, for original and inter-calibrated ESCAT data respectively. On a global scale, the distribution of bias values follows a slightly skewed normal distribution, with a small positive bias. This indicates that, in general, ESCAT slopes tend to be slightly higher than ASCAT slopes. Since slope values are typically negative – reflecting the decrease in backscatter with increasing incidence angle – "higher" here refers to a less steep slope in most cases. Extreme bias values are primarily found in desert regions, including the Sahara and Sahel in northern Africa, the sand deserts of the Arabian Peninsula, the Taklamakan Desert in China, Greenland, and eastern China, while biases are slightly elevated in parts of South Africa and Australia.

Notably, this spatial pattern closely resembles the distribution of the estimated standard deviation of backscatter (ESD) observed for both ESCAT [12] and ASCAT [14]. [12] and [14] investigated azimuthal anisotropy in ESCAT and ASCAT backscatter signals and found that the estimated standard deviation (ESD), derived from differences between fore- and aft-beam backscatter measurements within a measurement triplet (instantaneous fore, mid, and aft beam measurements), serves as a reliable indicator of azimuthal anisotropy. This anisotropy primarily arises from the interaction between incident microwaves and regularly aligned surface or subsurface roughness within the sensor's penetration depth, particularly when the roughness scale approaches or exceeds the Rayleigh roughness criterion. Such interactions are common in wind-induced small-scale terrain features [15]. When microwaves encounter structured roughness perpendicularly, backscatter increases, a pattern frequently observed in environments such as sand dune systems, croplands, and the Greenland and Antarctic ice sheets, where wind-formed sastrugi (surface microrelief features) contribute to anisotropic scattering [16]. The spatial patterns of sand seas and sastrugi shown in Fig. 3 of [12] and Fig. 5.1 of [14] closely align with the regions exhibiting strong biases between original ESCAT and ASCAT slopes.

Although anisotropic effects are present in both ESCAT and ASCAT data, their influence on slope and curvature values likely varies due to differences in incidence angle ranges – as observed in the time series analysis of a grid point in Libya (Fig. 3.18) – as well as other measurement characteristics. To better understand the biases associated with anisotropic backscatter behavior, we will further investigate example grid points in these regions.

Nevertheless, this still leaves the regions in eastern China and the southern Sahel, which do not prominently exhibit anisotropic behavior characterized by high ESD values. [14], however, also analyzed the temporal variability of anisotropy indicators and found that these regions stand out in that context. As shown in Fig. 5.14 of [14], urban sprawl in eastern China, for example, leads to a gradual change in backscatter over time. Such land cover changes may also alter slope and curvature signatures. Similarly, the Sahel has experienced a greening effect in recent decades, resulting in significant land cover changes. When computing climatologies, observations from both before and after the land cover change contribute to a single slope and curvature time series. This could introduce a bias between ESCAT- and ASCAT-derived results, as the datasets cover different time periods, for instance including highly active construction phases in China. To better understand these effects, we will conduct further analyses, particularly in the context of azimuthal corrections, which are part of the FDR4LDYN processing procedure.

Importantly, after applying the inter-calibration to ESCAT data, we observe a significant shift in bias values at the global scale. While positive biases previously recorded in rainforest calibration regions are effectively eliminated, other areas tend to be over-corrected, resulting in slightly negative biases. The distribution remains similar in shape, but its mode has shifted from a positive to an equally negative value, instead of converging toward zero. To address this, we will revisit the inter-calibration approach and explore refinements that maintain good agreement in calibration regions while preventing over-corrections elsewhere. Additionally, we will incorporate a global bias map derived from the synthetic ESCAT experiment and examine maps illustrating the impact of inter-calibration on slope and curvature noise levels to better understand this shift.

Another consideration regarding bias values is their susceptibility to the absolute magnitudes of slope and curvature, potentially leading to higher values in regions where slopes are exceptionally steep, such as hyperarid desert areas. To mitigate this drawback, we will carry out a normalization by dividing absolute slope and curvature values by the mean over the entire period, resulting in coefficients of variation.

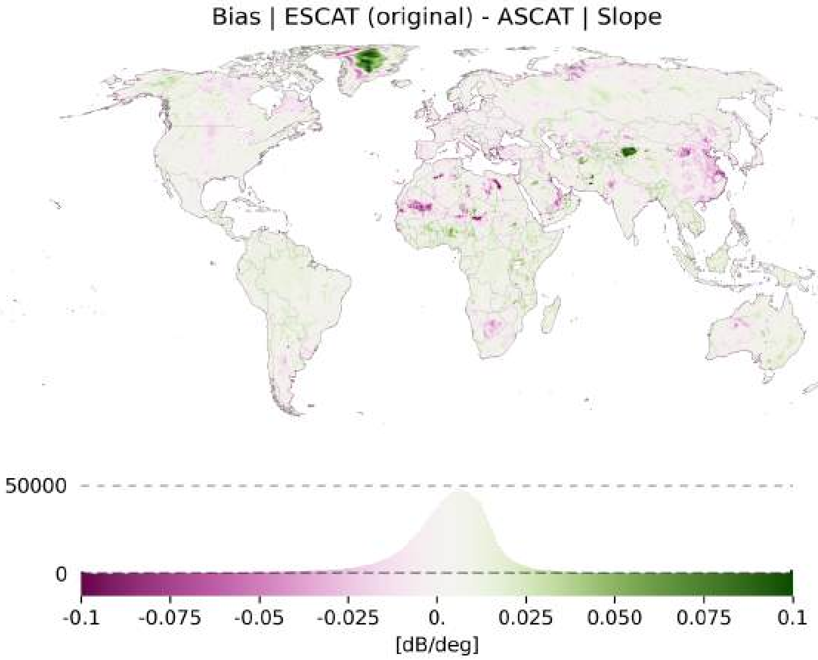

Figure 3.19: Global map of biases between the mean slope climatologies of original ESCAT and ASCAT data. Positive (green) values indicate greater mean slopes in the original ESCAT data compared to ASCAT.

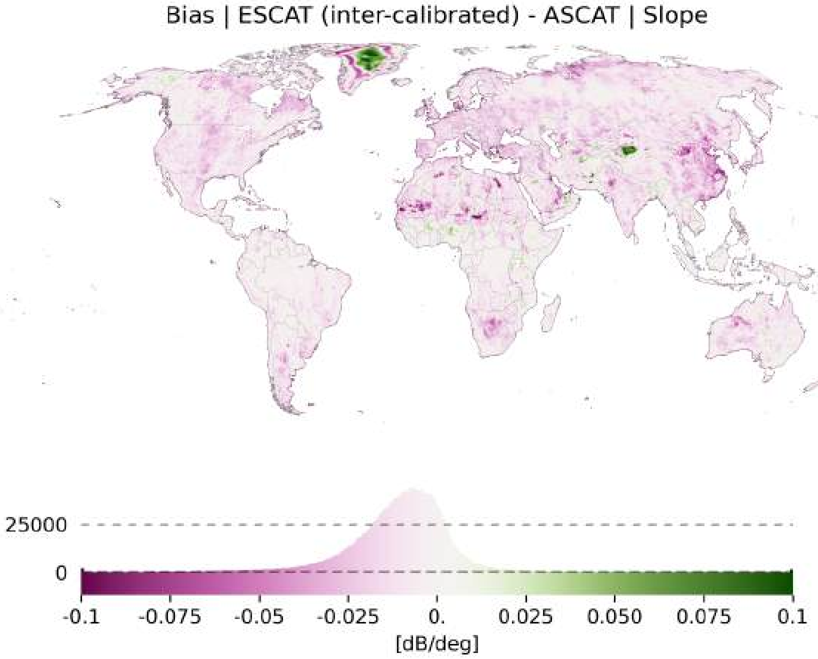

Figure 3.20: Global map of biases between the mean slope climatologies of inter-calibrated ESCAT and ASCAT data. Positive (green) values indicate greater mean slopes in the original ESCAT data compared to ASCAT.

Examining the correlations between ESCAT and ASCAT slopes in Figures 3.21 and 3.22, we observe strong global agreement. Exceptions include hyper-arid regions such as the Sahara, the Arabian Peninsula, and Australia, as well as Antarctica and China, which align with the previously discussed factors. A notable new effect is the lower correlation in parts of the rainforest regions, potentially linked to the stronger seasonal signal observed in ESCAT compared to ASCAT (as evident in Fig. 3.17). Following inter-calibration, correlations decrease slightly at a global scale, as seen in the histograms, yet remain consistently high without introducing new problematic regions. Future efforts will thus rather focus on optimizing residual biases while maintaining these high correlation levels.

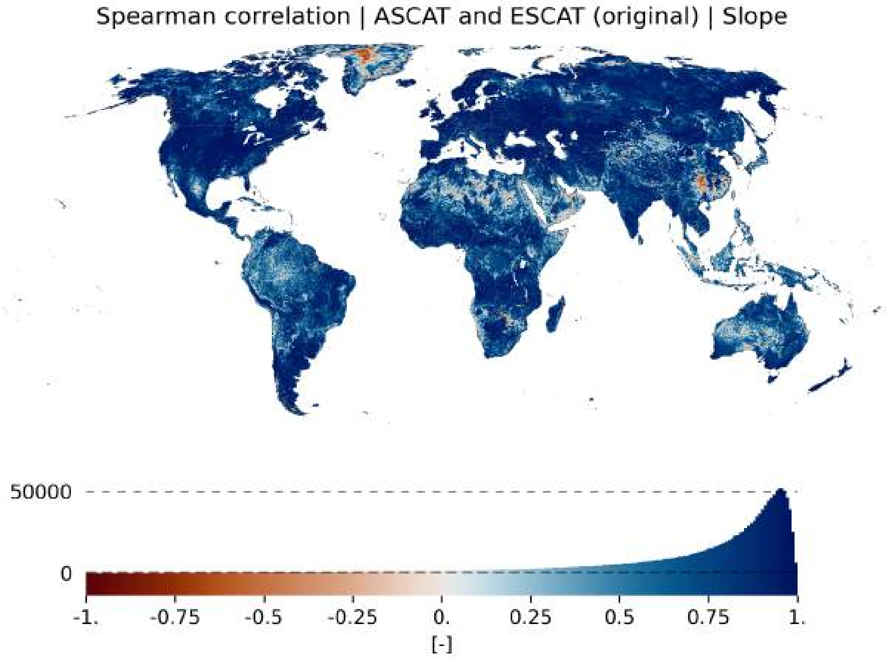

Figure 3.21: Global map of Spearman correlations between the mean slope climatologies of original ESCAT and ASCAT data.

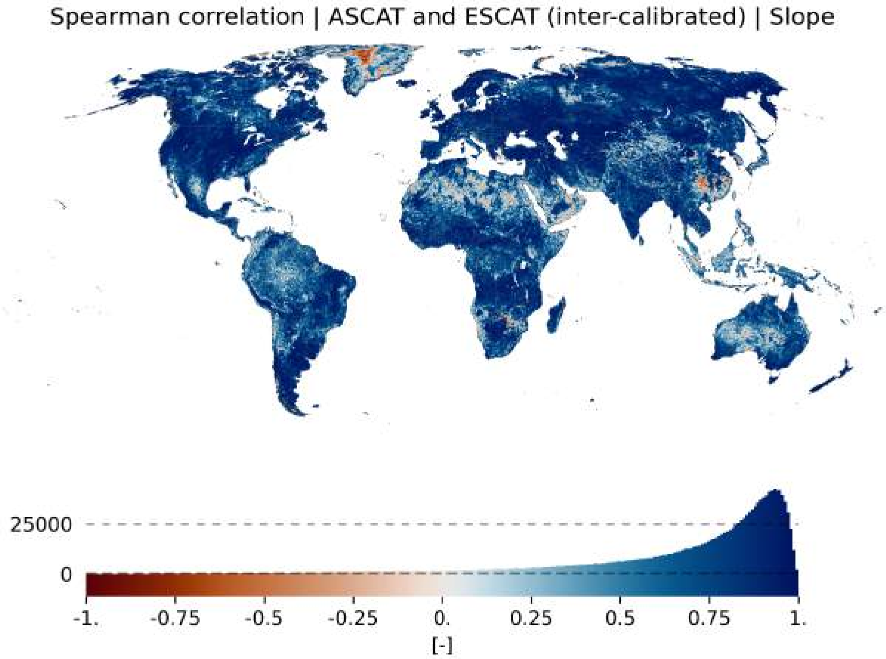

Figure 3.22: Global map of Spearman correlations between the slope climatologies of inter-calibrated ESCAT and ASCAT data.

A similar pattern emerges in Figures 3.23 and 3.24, which illustrate the root mean squared differences (RMSD) between ESCAT and ASCAT slope climatologies. Regions with pronounced azimuthal anisotropy or strong temporal variability in anisotropy exhibit the largest discrepancies again. However, after inter-calibration, RMSD values increase at a global scale, with particularly noticeable rises in Europe and the US Midwest. Further investigation is needed to determine whether bias over-correction contributes to these higher-than-expected RMSD values in these regions.

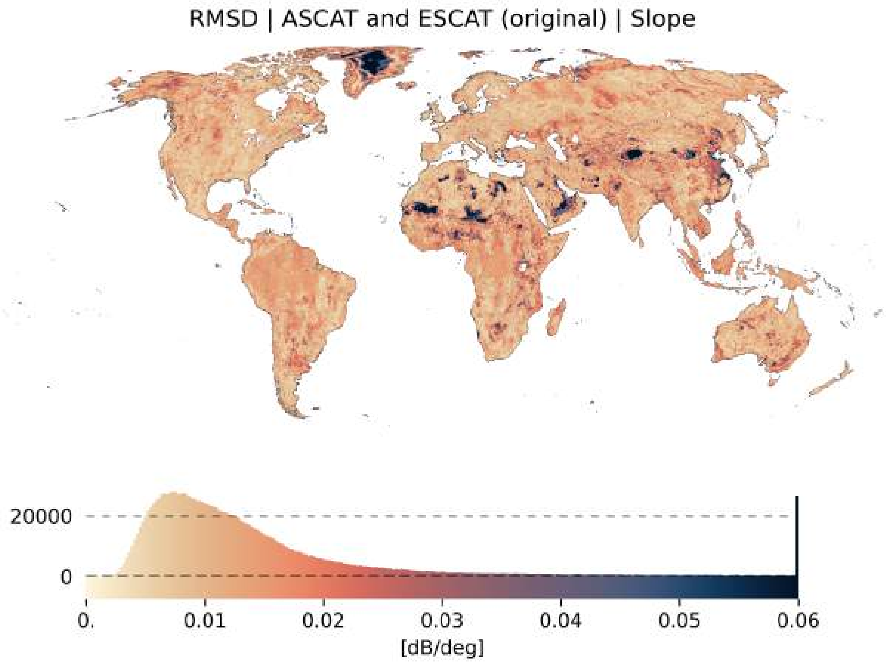

Figure 3.23: Global map of root mean squared differences (RMSD) between the mean slope climatologies of original ESCAT and ASCAT data.

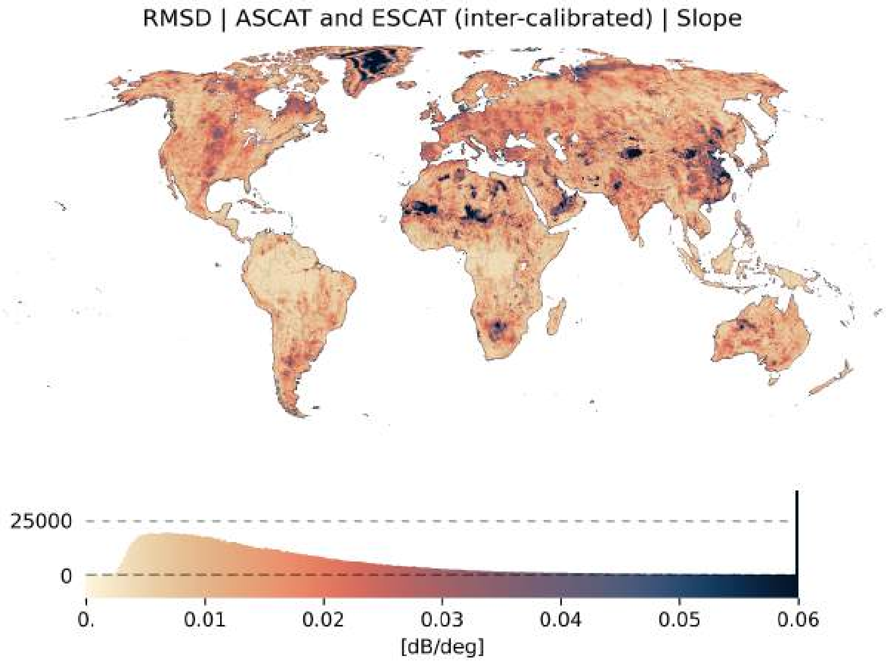

Figure 3.24: Global map of root mean squared differences (RMSD) between the slope climatologies of inter-calibrated ESCAT and ASCAT data.

As a final step in the slope analysis, we examined the standard deviations of ASCAT, as well as original and inter-calibrated ESCAT slopes, to assess potential differences in the overall variability of slope climatologies. The maps in Figures 3.25–3.27 show strong agreement between ASCAT and both ESCAT slope variants. Once again, we observe the characteristic patterns of sand dunes, where alignment with the sensor look direction leads to high variability. Additionally, the steppes and grasslands of the Great Plains and the Great Dala stand out, highlighting how variations in grass vegetation influence slope standard deviations. Overall, the two sensors exhibit very good agreement, both in the spatial distribution and in the magnitude of recorded standard deviation values.

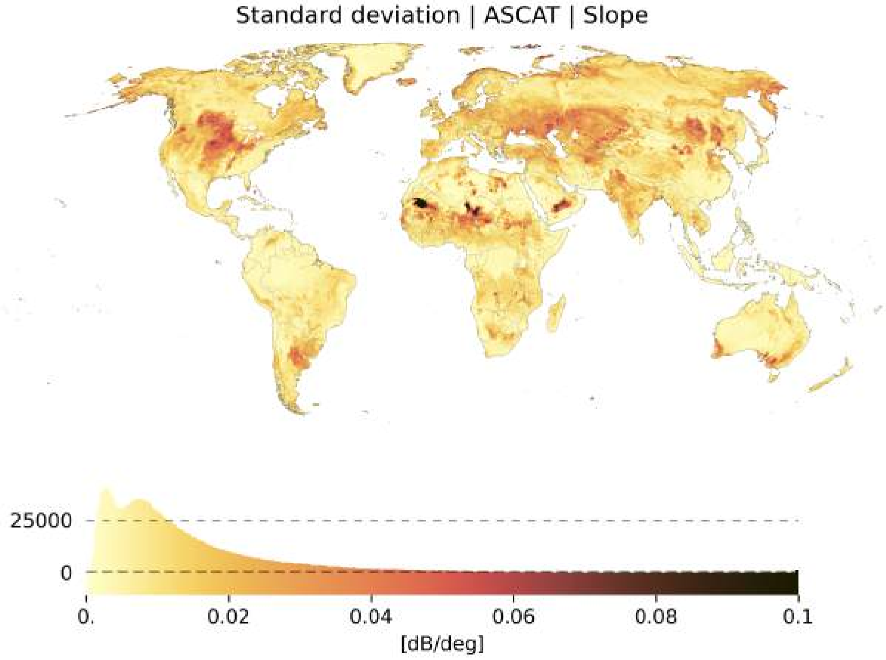

Figure 3.25: Global map of standard deviations (std) of the slope climatologies of ASCAT data.

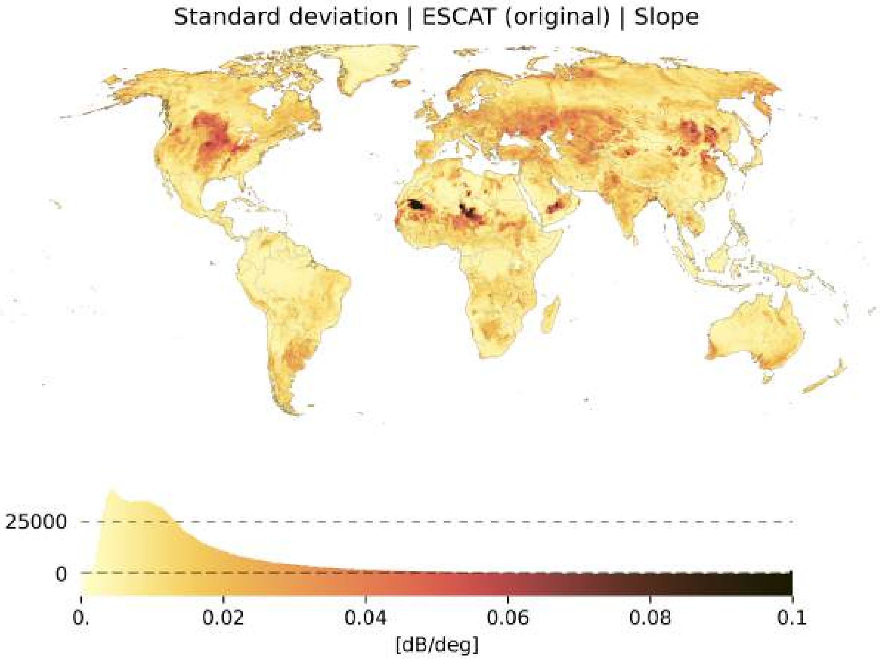

Figure 3.26: Global map of standard deviations (std) of the slope climatologies of original ESCAT data.

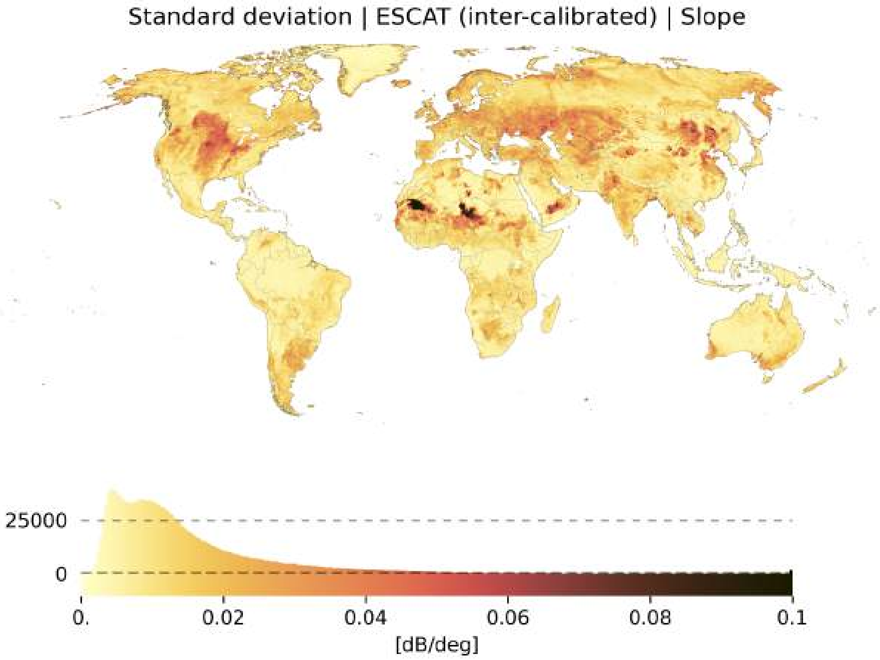

Figure 3.27: Global map of standard deviations (std) of the slope climatologies of inter-calibrated ESCAT data.

3.3.3. Spatial analysis of curvature

Many of the patterns observed in the comparison of ESCAT and ASCAT slope climatologies also apply to curvature values. Therefore, we highlight only the most notable differences here. The extreme bias patterns seen in the slope analysis partially show up in the original-ESCAT-minus-ASCAT curvature bias map (Fig. 3.28); however, the sign of the bias is often reversed. For example, while slopes exhibited strong positive biases in the Taklamakan Desert, curvature biases in this region are now strongly negative. Additionally, more regions globally show slightly elevated curvature biases, including the Arabian Peninsula, Australia, southern South America, northern China, and the Great Dala grasslands. However, fewer regions exhibit extreme biases compared to slopes. The skewed nature of the bias distribution also closely resembles that of slope biases, but interestingly it is mirrored. Given that curvature is a higher-order term and inherently more sensitive, larger discrepancies are expected. Encouragingly, no new problematic areas emerge in the curvature analysis. Another positive finding is that inter-calibration has only a minimal effect on curvature biases, which aligns with the fact that the calibration approach is based on linear correction terms. We will further investigate whether refinements in inter-calibration aimed at fine-tuning slope differences could also help reduce the generally slightly positive curvature biases.

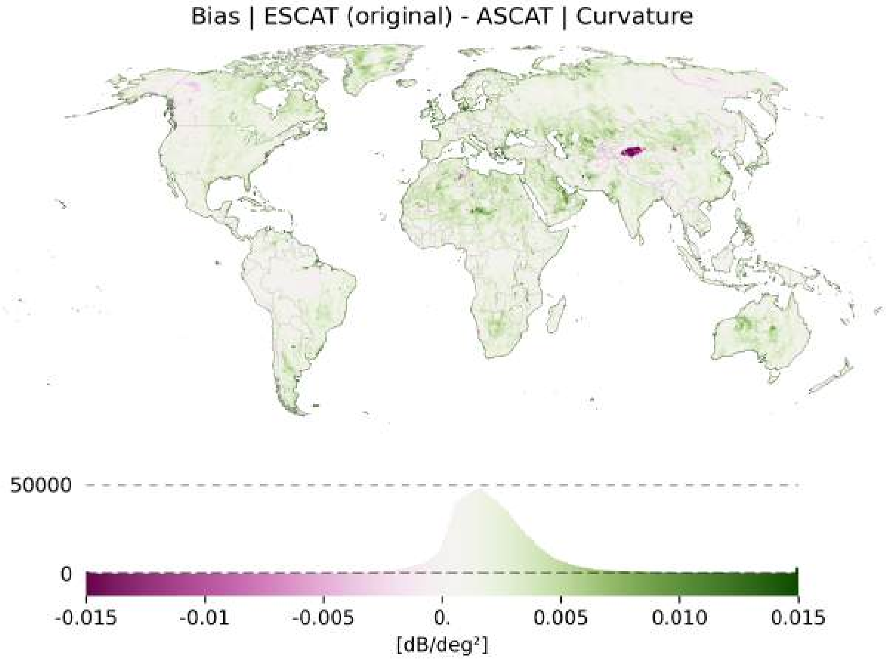

Figure 3.28: Global map of biases between the mean curvature climatologies of original ESCAT and ASCAT data. Positive (green) values indicate higher mean curvatures in the original ESCAT data compared to ASCAT.

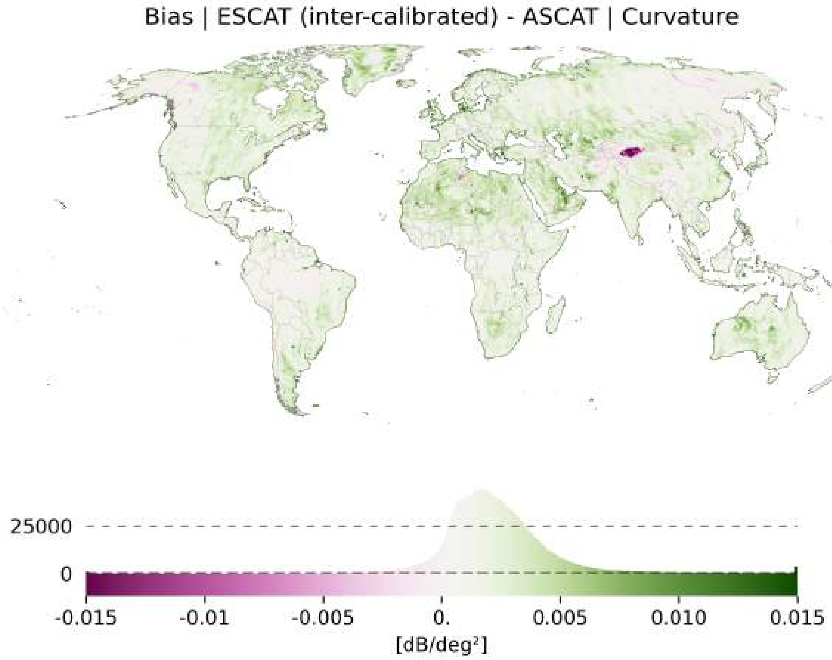

Figure 3.29: Global map of biases between the mean curvature climatologies of inter-calibrated ESCAT and ASCAT data. Positive (green) values indicate higher mean curvatures in the original ESCAT data compared to ASCAT.

As expected, correlations between ESCAT and ASCAT curvatures – shown in Figures 3.30 and 3.31 – are lower than those observed for slopes. In particular, arid regions, high-latitude areas, and mountainous terrain exhibit notable differences in curvature behavior between ESCAT and ASCAT. An especially interesting observation is that correlations are unexpectedly low in rainforest regions, even more so than for slopes. This is likely linked to differences in the seasonal variability captured by ESCAT compared to ASCAT, as previously seen in Fig. 3.17. Further analysis of the incidence angle–backscatter relationship across different viewing geometries is expected to provide deeper insights into the underlying causes of this behavior.

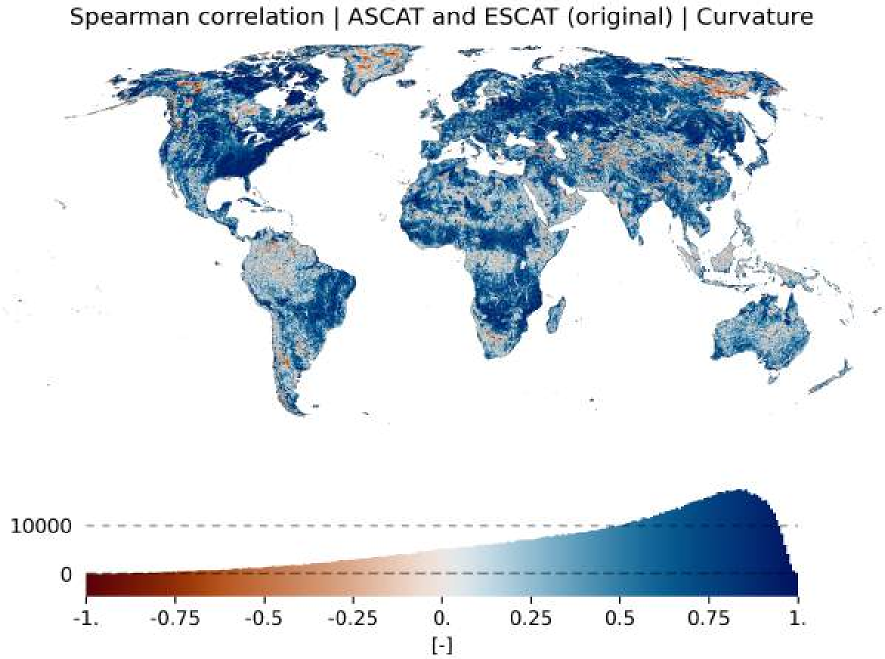

Figure 3.30: Global map of Spearman correlations between the mean curvature climatologies of original ESCAT and ASCAT data.

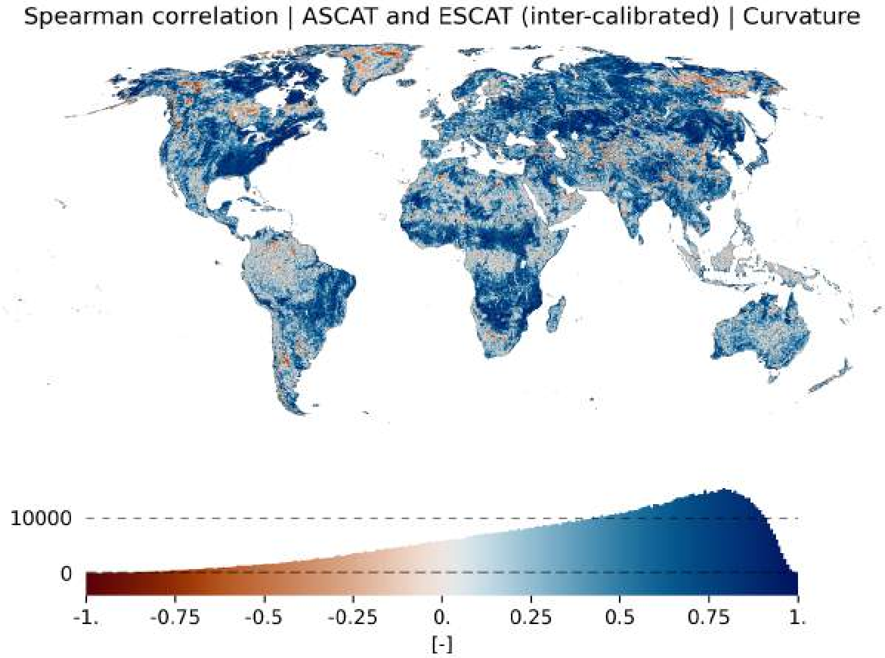

Figure 3.31: Global map of Spearman correlations between the curvature climatologies of inter-calibrated ESCAT and ASCAT data.

The RMSD patterns observed for curvatures, which are shown in Figures 3.32 and 3.33, closely resemble those of slopes. The main difference is that regions with very high RMSD values are less pronounced while surrounding areas, particularly in the Sahara desert, exhibit slightly elevated RMSD values. The inter-calibration process has minimal impact on RMSD but does lead to a slight overall increase.

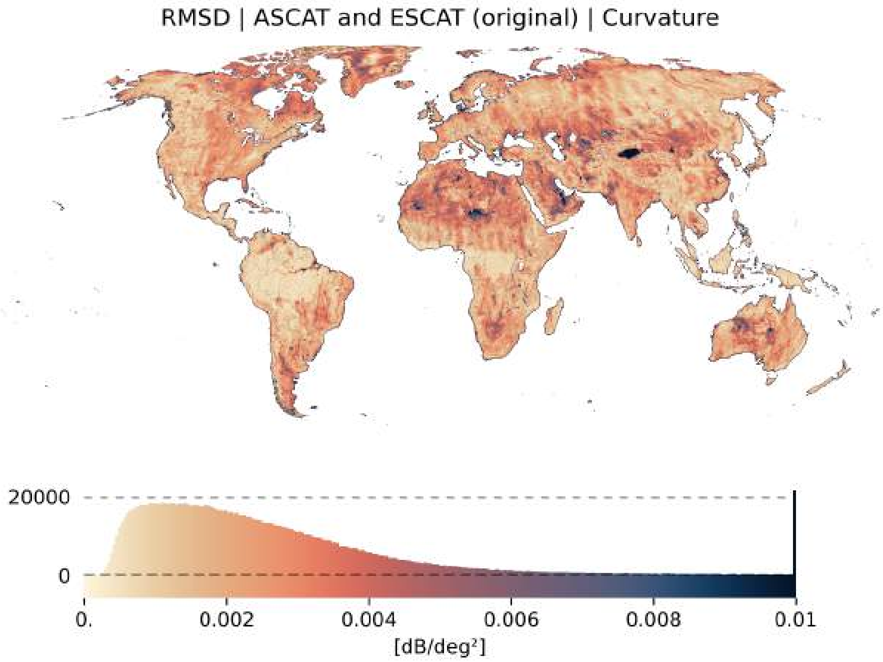

Figure 3.32: Global map of root mean squared differences (RMSD) between the mean curvature climatologies of original ESCAT and ASCAT data.

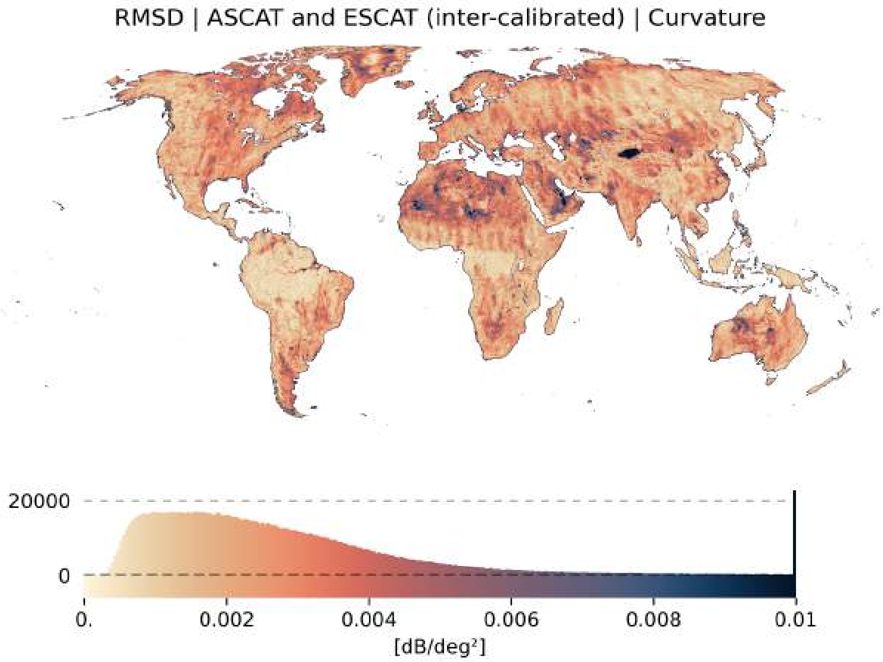

Figure 3.33: Global map of root mean squared differences (RMSD) between the curvature climatologies of inter-calibrated ESCAT and ASCAT data.

The standard deviations of curvature climatologies – shown in Figures 3.34–3.36 – closely resemble the patterns observed for slope standard deviations. One notable difference is the high standard deviation values recorded in the southern Sahel, a region characterized by intermittent rainfall followed by pronounced dry seasons. These sharp environmental transitions appear to drive increased variability in recorded curvature values. While the overall spatial patterns are also similar between ESCAT and ASCAT, the standard deviations are significantly larger for ESCAT, which contrasts with slope results. A possible explanation is that improved data availability in ASCAT leads to more stable estimates of the sensitive higher-order curvature term, thereby reducing its variability.

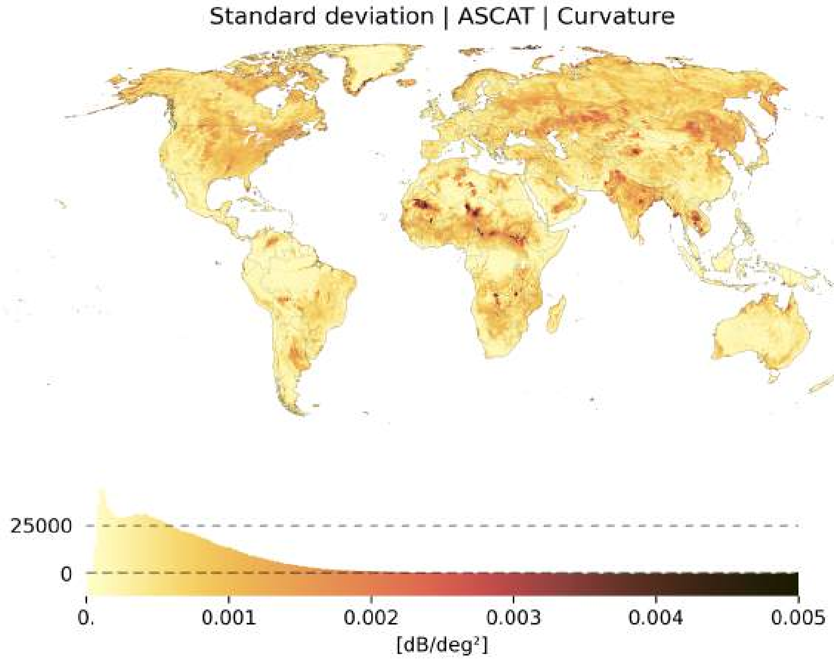

Figure 3.34: Global map of standard deviations (std) of the curvature climatologies of ASCAT data.

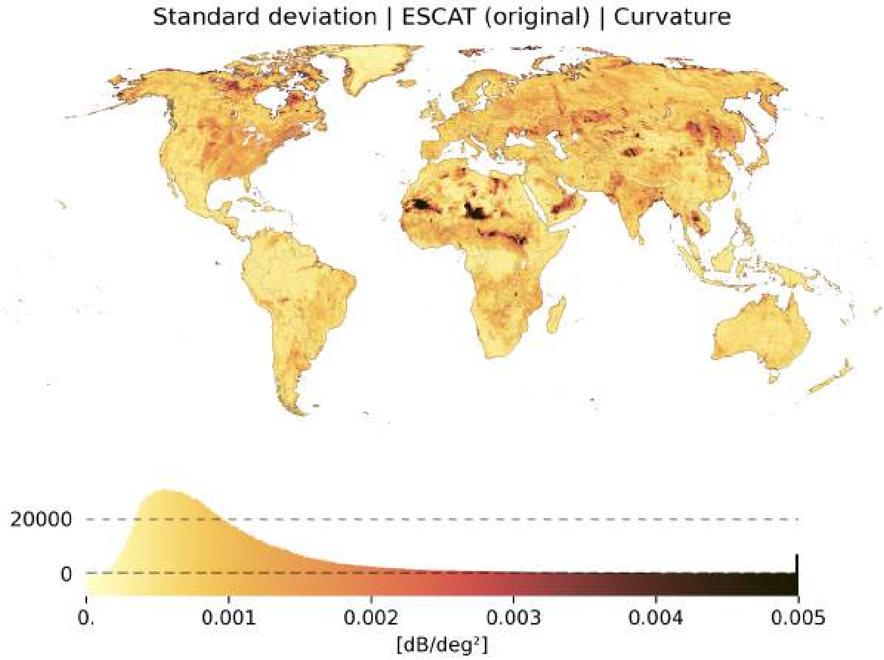

Figure 3.35: Global map of standard deviations (std) of the curvature climatologies of original ESCAT data.

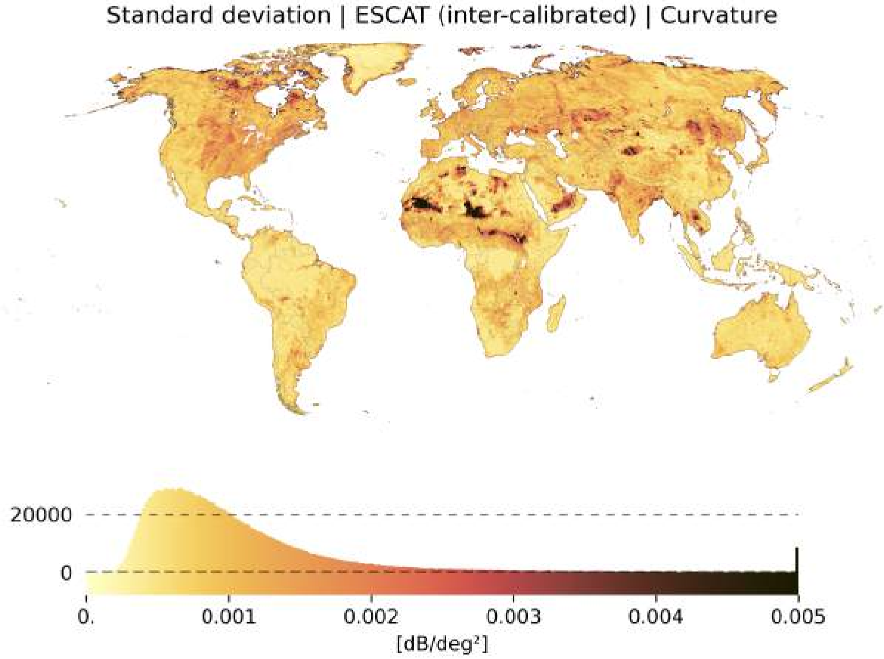

Figure 3.36: Global map of standard deviations (std) of the curvature climatologies of inter-calibrated ESCAT data.

3.4. Summary

We evaluated the feasibility of applying ASCAT-based processing methods to ESCAT data, focusing on the retrieval quality of backscatter, slope, and curvature for the FDR4LDYN dataset. To account for ESCAT's coarser temporal resolution, we conducted an experiment in which ASCAT data was subsampled to create a synthetic ESCAT dataset, allowing direct comparison with original ASCAT data. Among the various subsampling approaches tested, the ESCAT-shift method proved to be the most suitable for analyzing slope and curvature, as it most accurately replicated ESCAT's sampling characteristics while minimizing artificial distortions.

The analysis showed that slope and curvature climatologies from synthetic ESCAT data generally align well with original ASCAT data, although increased noise – particularly for curvature – was observed depending on local data availability. Time-series-based slope and curvature calculations exhibited higher RMSD values and lower correlations than climatologies, highlighting the challenge of capturing short-term variations with sparse data. Refining processing parameters, such as increasing the fit window size or tightening the minimum observation criteria, allowed for improved robustness but introduced the trade-off between smoothing fine-scale variations and increasing data gaps.

Building on these insights, we processed actual original and inter-calibrated ESCAT data to evaluate biases and overall consistency with ASCAT. The analysis of normalized backscatter, slope, and curvature climatologies provided a first assessment of ESCAT-ASCAT interoperability. Inter-calibration significantly reduced biases in rainforest regions used as calibration references, but in other areas, it led to over-corrections, introducing slight negative biases. Time series analysis at individual stations such as the ARM (US) and Collelongo (Italy) soil moisture stations, the Amazon rainforest, and a Libyan sand desert highlighted the impact of limited data availability and varying environmental conditions on the agreement between ESCAT and ASCAT slopes and curvatures.

Regions exhibiting anisotropic backscatter behavior, such as sand dune deserts and ice sheets, showed the largest ESCAT-ASCAT differences in both slope and curvature climatologies. Additionally, areas undergoing rapid land cover changes, such as urban expansion in China and Sahel greening, displayed inconsistencies between ESCAT- and ASCAT-derived climatologies. However, these strong biases seem to be linked to actual geophysical phenomena rather than compromised ESCAT data quality. Nevertheless, further detailed analyses of viewing-geometry-related impacts on backscatter, slope, and curvature will be conducted to determine whether additional processing refinements are needed.

To enhance interoperability and data quality, our next steps include refining the inter-calibration strategy to improve consistency across regions while avoiding over-correction and artificial trends. We will expand the global statistical analysis of biases by including maps of normalized backscatter, relative slope and curvature measures, and noise levels to better quantify persisting discrepancies. A further investigation into the incidence angle–backscatter relationship across different viewing geometries will help assess its impact on slope and curvature retrievals. To improve robustness in data-sparse conditions, we plan to develop a Bayesian approach for time-series-based slope and curvature retrieval, incorporating weighted observations. We will also explore alternative methods, such as regularization techniques, to achieve robust slope and curvature estimation.

Overall, the analysis demonstrates that ESCAT and ASCAT exhibit good general agreement in backscatter, slope ,and curvature retrievals, but regional biases and slope and curvature variability must be addressed to ensure high-quality interoperability in the FDR4LDYN dataset.

4. References

[1] Telespazio, *ERS-1 Scatterometer Full Mission Reprocessing Verification Report (IDEAS+-SER-IPF-REP-2992)*, v1.0, 2018.

[2] Crapolicchio, R., De Chiara, G., Elyouncha, A., Lecomte, P., Neyt, X., Paciucci, A., and Talone, M., "Ers-2 scatterometer: Mission performances and current reprocessing achievements," *IEEE Transactions on Geoscience and Remote Sensing*, vol. 50, no. 7, pp. 2427–2448, Jul. 2012. DOI: 10.1109/tgrs.2011.2179808. [Online]. Available: http://dx.doi.org/10.1109/TGRS.2011.2179808.

[3] ESS Team, "EO-SIP Specialisation for ERS-1/2 Wind Scatterometer L1.5/L2," ESA, Tech. Rep. EMSS-EOPG-TN-16-028, Sep. 2023.

[4] Álvaro González, "Measurement of areas on a sphere using fibonacci and latitude–longitude lattices," *Mathematical Geosciences*, vol. 42, no. 1, pp. 49–64, Nov. 2009. DOI: 10.1007/s11004-009-9257-x.

[5] Seabold, S. and Perktold, J., "Statsmodels: Econometric and statistical modeling with python," in *Proceedings of the 9th Python in Science Conference*, 2010, pp. 92–96.

[6] Koenker, R., *Quantile Regression*. Cambridge University Press, 2005. DOI: 10.1017/CBO9780511754098.

[7] Hawkins, R., Attema, E., Crapolicchio, R., Lecomte, P., Closa, J., Meadows, P., and Srivastava, S., "Stability of amazon backscatter at c-band: Spaceborne results from ers-1/2 and radarsat-1.," vol. 450, p. 99, Feb. 2000.

[8] Reimer, C., "Calibration of space-borne Scatterometers: Towards a consistent climate data record for Soil Moisture Retrieval," Vienna University of Technology, Department of Geodesy and Geoinformation, Austria, 2014. [Online]. Available: http://repositum.tuwien.ac.at/urn:nbn:at:at-ubtuw:1-70509.

[9] Truong, C., Oudre, L., and Vayatis, N., "Selective review of offline change point detection methods," *Signal Processing*, vol. 167, p. 107 299, Feb. 2020. DOI: 10.1016/j.sigpro.2019.107299. [Online]. Available: http://dx.doi.org/10.1016/j.sigpro.2019.107299.

[10] Miranda, N., Rosich, B., Santella, C., and Grion, M., "Review of the impact of ers-2 piloting modes on the sar doppler stability," pp. 4–, Apr. 2005.

[11] Anderson, C., Figa, J., Bonekamp, H., Wilson, J. J. W., Verspeek, J., Stoffelen, A., and Portabella, M., "Validation of backscatter measurements from the advanced scatterometer on metop-a," *Journal of Atmospheric and Oceanic Technology*, vol. 29, no. 1, pp. 77–88, Jan. 2011. DOI: 10.1175/jtech-d-11-00020.1. [Online]. Available: http://dx.doi.org/10.1175/JTECH-D-11-00020.1.

[12] Bartalis, Z., Scipal, K., and Wagner, W., "Azimuthal anisotropy of scatterometer measurements over land," *IEEE Transactions on Geoscience and Remote Sensing*, vol. 44, no. 8, pp. 2083–2092, 2006. DOI: 10.1109/TGRS.2006.872084.

[13] Figa-Saldaña, J., Wilson, J. J., Attema, E., Gelsthorpe, R., Drinkwater, M. R., and Stoffelen, A., "The advanced scatterometer (ascat) on the meteorological operational (metop) platform: A follow on for european wind scatterometers," *Canadian Journal of Remote Sensing*, vol. 28, no. 3, pp. 404–412, 2002. DOI: 10.5589/m02-035.

[14] Lindorfer, R., "Azimuthal anisotropy in ASCAT backscatter measurements," Technische Universität Wien, Vienna, Austria, 2024. [Online]. Available: https://doi.org/10.34726/hss.2024.120220.

[15] Fraser, A. D., Young, N. W., and Adams, N., "Comparison of microwave backscatter anisotropy parameterizations of the antarctic ice sheet using ascat," *IEEE Transactions on Geoscience and Remote Sensing*, vol. 52, no. 3, pp. 1583–1595, 2014. DOI: 10.1109/TGRS.2013.2252621.

[16] Long, D. G. and Drinkwater, M. R., “Azimuth variation in microwave scatterometer and radiometer data over antarctica,” *IEEE Transactions on Geoscience and Remote Sensing*, vol. 38, no. 4, pp. 1857–1870, 2000. DOI: 10.1109/36.851769.

List of Tables

1.1. Operating Characteristics of ERS-1 and ERS-2 AMI in Wind Scatterometer mode 4
1.2. Dataset specification of `ERS.ASPS20.H` and `ERS.ASPS20.N`. 5
1.3. Dataset size and number of files for `ERS.ASPS20.H` and `ERS.ASPS20.N`. 5
1.4. First and Last File Dates for ERS-1 and ERS-2 ASPS20 Level 2.0 products. 5
1.5. Gaps in ERS1.ASPS20.H products. 6
1.6. Gaps in ERS1.ASPS20.N products. 6
1.7. Gaps in ERS2.ASPS20.H products. 6
1.8. Summary of gaps in ERS2.ASPS20.N products. 7
1.9. ERS-1 and ERS-2 mission phases parameters [3]. 9
1.10. Node Confidence Data 1 flags. 10
1.11. Node Confidence Data 2 flags. 10
1.12. First and Last File Dates for ERS-1 and ERS-2 ASPS20 Level 2.0 products. 43
2.1. Number of grid points selected by region and satellite 46
2.2. Criteria for selection of natural targets. 46
2.3. ERS-1 Mission Phases 52
2.4. ERS-2 Mission Phases and Modes 55
2.5. Reference periods for calibration of ERS-1 and ERS-2. 59

List of Figures

1.1. Number of missing orbit files per relative orbit number for dataset `ERS-1.ASPS20.H`. . . 7
1.2. Number of missing orbit files per relative orbit number for dataset `ERS-1.ASPS20.N`. . . 8
1.3. Number of missing orbit files per relative orbit number for dataset `ERS-2.ASPS20.H`. . . 8
1.4. Number of missing orbit files per relative orbit number for dataset `ERS-2.ASPS20.N`. . . 8
1.5. Fibonacci grid with 12.5 km sampling (N=1,650,000) showcasing 3 different areas: Equator (left), North Pole (center), and 180° meridian. 9
1.6. Absolute number of observations for dataset `ERS-1.ASPS20.H` (including NaN). 11
1.7. Absolute number of observations for dataset `ERS-2.ASPS20.H` (including NaN). 11
1.8. Number of valid backscatter triplet observations for dataset `ERS-1.ASPS20.H`. 12
1.9. Number of valid backscatter triplet observations for dataset `ERS-2.ASPS20.H`. 12
1.10. Percent valid backscatter triplet observations for dataset `ERS-1.ASPS20.H`. 13
1.11. Percent valid backscatter triplet observations for dataset `ERS-2.ASPS20.H`. 13
1.12. Fore beam doppler compensation center of gravity flag for dataset `ERS-1.ASPS20.H`. . . 14
1.13. Fore beam doppler compensation center of gravity flag for dataset `ERS-2.ASPS20.H`. . . 14
1.14. Fore beam doppler compensation standard deviation flag for dataset `ERS-1.ASPS20.H`. . 15
1.15. Fore beam doppler compensation standard deviation flag for dataset `ERS-2.ASPS20.H`. . 15
1.16. Fore beam doppler frequency shift flag for dataset `ERS-1.ASPS20.H`. 16
1.17. Fore beam doppler frequency shift flag for dataset `ERS-2.ASPS20.H`. 16
1.18. Fore beam arcing flag for dataset `ERS-1.ASPS20.H`. 17
1.19. Fore beam arcing flag for dataset `ERS-2.ASPS20.H`. 17
1.20. Mid beam doppler compensation center of gravity flag for dataset `ERS-1.ASPS20.H`. . . 18
1.21. Mid beam doppler compensation center of gravity flag for dataset `ERS-2.ASPS20.H`. . . 18
1.22. Mid beam doppler compensation standard deviation flag for dataset `ERS-1.ASPS20.H`. . 19
1.23. Mid beam doppler compensation standard deviation flag for dataset `ERS-2.ASPS20.H`. . 19
1.24. Mid beam doppler frequency shift flag for dataset `ERS-1.ASPS20.H`. 20
1.25. Mid beam doppler frequency shift flag for dataset `ERS-2.ASPS20.H`. 20

1.26. Mid beam arcing flag for dataset `ERS-1.ASPS20.H`. 21
1.27. Mid beam arcing flag for dataset `ERS-2.ASPS20.H`. 21
1.28. Aft beam doppler compensation center of gravity flag for dataset `ERS-1.ASPS20.H`. . . 22
1.29. Aft beam doppler compensation center of gravity flag for dataset `ERS-2.ASPS20.H`. . . 22
1.30. Aft beam doppler compensation standard deviation flag for dataset `ERS-1.ASPS20.H`. . 23
1.31. Aft beam doppler compensation standard deviation flag for dataset `ERS-2.ASPS20.H`. . 23
1.32. Aft beam doppler frequency shift flag for dataset `ERS-1.ASPS20.H`. 24
1.33. Aft beam doppler frequency shift flag for dataset `ERS-2.ASPS20.H`. 24
1.34. Aft beam arcing flag for dataset `ERS-1.ASPS20.H`. 25
1.35. Aft beam arcing flag for dataset `ERS-2.ASPS20.H`. 25
1.36. Yaw error flag for dataset `ERS-1.ASPS20.H`. 26
1.37. Yaw error flag for dataset `ERS-2.ASPS20.H`. 26
1.38. Frame checksum flag for dataset `ERS-1.ASPS20.H`. 27
1.39. Frame checksum flag for dataset `ERS-2.ASPS20.H`. 27
1.40. Internal calibration flag for dataset `ERS-1.ASPS20.H`. 28
1.41. Internal calibration flag for dataset `ERS-2.ASPS20.H`. 28
1.42. Noise power flag for dataset `ERS-1.ASPS20.H`. 29
1.43. Noise power flag for dataset `ERS-2.ASPS20.H`. 29
1.44. Kp flag for dataset `ERS-1.ASPS20.H`. 30
1.45. Kp flag for dataset `ERS-2.ASPS20.H`. 30
1.46. Relative number of observations with a time difference between 0 and 3 days for the dataset `ERS-1.ASPS20.H`. 31
1.47. Relative number of observations with a time difference between 0 and 10 days for the dataset `ERS-1.ASPS20.H`. 31
1.48. Relative number of observations with a time difference between 0 and 3 days for the dataset `ERS-2.ASPS20.H`. 32
1.49. Relative number of observations with a time difference between 0 and 10 days for the dataset `ERS-2.ASPS20.H`. 32
1.50. `ERS-1-2.ASPS20.H` time series example for a location in Colombia 5.53° N -69.15° W. 33
1.51. `ERS-1.ASPS20.H` σ^0 time series and incidence angle relationship for a grid point in Greenland (GPI: 1548735, FibGrid 12.5 km) 35
1.52. Count of lower outliers flagged by node confidence flag - `ERS-1.ASPS20.H`. 36
1.53. `ERS-1.ASPS20.H` σ^0 time series and incidence angle relationship for a grid point in northern Russia (GPI: 1541998, FibGrid 12.5 km) 37
1.54. Count of upper outliers flagged by node confidence flag - `ERS-1.ASPS20.H`. 38
1.55. `ERS-2.ASPS20.H` σ^0 time series and incidence angle relationship for a grid point in northern Africa (GPI: 622058, FibGrid 12.5 km) 39
1.56. Count of lower outliers flagged by node confidence flag - `ERS-2.ASPS20.H`. 40
1.57. `ERS-2.ASPS20.H` σ^0 time series and incidence angle relationship for a grid point in northern Africa (GPI: 505299, FibGrid 12.5 km) 41
1.58. Count of upper outliers flagged by node confidence flag - `ERS-2.ASPS20.H`. 42
2.1. Selected natural targets for ERS-1, Nominal resolution 47
2.2. Selected natural targets for ERS-2, Nominal resolution 48
2.3. Selected natural targets for ERS-1, High resolution 49
2.4. Selected natural targets for ERS-2, High resolution 50
2.5. Selected natural targets for Metop-A 51
2.6. Seasonally-corrected γ^0 backscatter over the Amazon and detected timeseries breakpoints prior to calibration (ERS-1, 25 km grid spacing) 53

2.7. Seasonally-corrected γ^0 backscatter over the Congo and detected timeseries breakpoints prior to calibration (ERS-1, 25 km grid spacing) 53
2.8. Seasonally-corrected γ^0 backscatter over Southeast Asia and detected timeseries breakpoints prior to calibration (ERS-1, 25 km grid spacing) 54
2.9. Seasonally-corrected γ^0 backscatter over the Amazon and detected timeseries breakpoints prior to calibration (ERS-2, 25 km grid spacing) 56
2.10. Seasonally-corrected γ^0 backscatter over the Congo and detected timeseries breakpoints prior to calibration (ERS-2, 25 km grid spacing) 56
2.11. Seasonally-corrected γ^0 backscatter over Southeast Asia and detected timeseries breakpoints prior to calibration (ERS-2, 25 km grid spacing) 57
2.12. Comparison of intra-satellite beam alignment over selected natural targets in the Amazon rainforest before and after intracalibration (ERS-1, Nominal resolution). 60
2.13. Comparison of intra-satellite beam alignment over selected natural targets in the Congo rainforest before and after intracalibration (ERS-1, Nominal resolution). 61
2.14. Comparison of intra-satellite beam alignment over selected natural targets in Southeast Asian rainforests before and after intracalibration (ERS-1, Nominal resolution). 62
2.15. Comparison of intra-satellite beam alignment over selected natural targets in the Amazon rainforest before and after intracalibration (ERS-2, Nominal resolution). 63
2.16. Comparison of intra-satellite beam alignment over selected natural targets in the Congo rainforest before and after intracalibration (ERS-2, Nominal resolution). 64
2.17. Comparison of intra-satellite beam alignment over selected natural targets in Southeast Asian rainforests before and after intracalibration (ERS-2, Nominal resolution). 65
2.18. Evolution of correction coefficient C_0 calculated for Metop-A (12.5 km grid spacing, right swath) during intracalibration, where $\overline{C_{IAS}}(t_i, \theta, \phi_j) = C_0(t_i, \theta, \phi_j)$ 66
2.19. Evolution of correction coefficients C_0 and C_1 for calculated for ERS-1 (25 km grid spacing) during intracalibration, where $\overline{C_{IAS}}(t_i, \theta, \phi_j) = C_0(t_i, \theta, \phi_j) + C_1(t_i, \theta, \phi_j) \cdot (\theta - 40°)$ 67
2.20. Evolution of correction coefficients C_0 and C_1 for calculated for ERS-2 (25 km grid spacing) during intracalibration, where $\overline{C_{IAS}}(t_i, \theta, \phi_j) = C_0(t_i, \theta, \phi_j) + C_1(t_i, \theta, \phi_j) \cdot (\theta - 40°)$ 68
2.21. Seasonally-corrected γ^0 backscatter over the Amazon and detected timeseries breakpoints after calibration (ERS-1, 25 km grid spacing) 69
2.22. Seasonally-corrected γ^0 backscatter over the Congo and detected timeseries breakpoints after calibration (ERS-1, 25 km grid spacing) 69
2.23. Seasonally-corrected γ^0 backscatter over Southeast Asia and detected timeseries breakpoints after calibration (ERS-1, 25 km grid spacing) 70
2.24. Seasonally-corrected γ^0 backscatter over the Amazon and detected timeseries breakpoints after calibration (ERS-2, 25 km grid spacing) 70
2.25. Seasonally-corrected γ^0 backscatter over the Congo and detected timeseries breakpoints after calibration (ERS-2, 25 km grid spacing) 71
2.26. Seasonally-corrected γ^0 backscatter over Southeast Asia and detected timeseries breakpoints after calibration (ERS-2, 25 km grid spacing) 71
2.27. Comparison of γ^0 backscatter measurements from ERS-1 and Metop-A over incidence angle θ, prior to intercalibration. 73
2.28. Comparison of γ^0 backscatter measurements from ERS-1 and Metop-A over incidence angle θ, after intercalibration. 74
2.29. Comparison of γ^0 backscatter measurements from ERS-2 and Metop-A over incidence angle θ, prior to intercalibration. 75
2.30. Comparison of γ^0 backscatter measurements from ERS-2 and Metop-A over incidence angle θ, after intercalibration. 76

2.31. Comparison of γ^0 backscatter measurements from ERS-1 and Metop-A over incidence angle θ, prior to intercalibration. . . . 77
2.32. Comparison of γ^0 backscatter measurements from ERS-1 and Metop-A over incidence angle θ, after intercalibration. . . . 78
2.33. Comparison of γ^0 backscatter measurements from ERS-2 and Metop-A over incidence angle θ, prior to intercalibration. . . . 79
2.34. Comparison of γ^0 backscatter measurements from ERS-2 and Metop-A over incidence angle θ, after intercalibration. . . . 80
3.1. Histogram Castelporziano station: satellites/swaths . . . 83
3.2. Histogram Castelporziano station: subsampling methods . . . 83
3.3. Slope time series ARM station: climatology . . . 84
3.4. Slope time series Borneo: climatology . . . 85
3.5. Curvature time series Park Falls station: climatology . . . 86
3.6. Curvature time series San Rossore station: climatology . . . 86
3.7. Slope time series ARM station: time series . . . 87
3.8. Curvature time series Loobos station: time series . . . 87
3.9. Slope time series ARM station: time series, parameter adaptations . . . 88
3.10. Curvature time series Loobos station: time series, parameter adaptations . . . 89
3.11. Normalized backscatter time series ARM station: ESCAT and ASCAT . . . 90
3.12. Slope time series ARM station: ESCAT and ASCAT . . . 91
3.13. Curvature time series ARM station: ESCAT and ASCAT . . . 91
3.14. Normalized backscatter time series Collelongo station: ESCAT and ASCAT . . . 92
3.15. Slope time series Collelongo station: ESCAT and ASCAT . . . 93
3.16. Curvature time series Collelongo station: ESCAT and ASCAT . . . 93
3.17. Slope time series Amazon rainforest: ESCAT and ASCAT . . . 94
3.18. Slope time series Libya sand desert: ESCAT and ASCAT . . . 95
3.19. Global map of biases between mean original ESCAT and ASCAT slope climatologies . . 97
3.20. Global map of biases between mean inter-calibrated ESCAT and ASCAT slope climatologies . . . 97
3.21. Global map of Spearman correlations between original ESCAT and ASCAT slope climatologies . . . 98
3.22. Global map of Spearman correlations between inter-calibrated ESCAT and ASCAT slope climatologies . . . 99
3.23. Global map of RMSD between original ESCAT and ASCAT slope climatologies 100
3.24. Global map of RMSD between inter-calibrated ESCAT and ASCAT slope climatologies 100
3.25. Global map of std of ASCAT slope climatologies . . . 101
3.26. Global map of std of original ESCAT slope climatologies . . . 102
3.27. Global map of std of inter-calibrated ESCAT slope climatologies . . . 102
3.28. Global map of biases between mean original ESCAT and ASCAT curvature climatologies 103
3.29. Global map of biases between mean inter-calibrated ESCAT and ASCAT curvature climatologies . . . 104
3.30. Global map of Spearman correlations between original ESCAT and ASCAT curvature climatologies . . . 105
3.31. Global map of Spearman correlations between inter-calibrated ESCAT and ASCAT curvature climatologies . . . 105
3.32. Global map of RMSD between original ESCAT and ASCAT curvature climatologies . . 106
3.33. Global map of RMSD between inter-calibrated ESCAT and ASCAT curvature climatologies 106
3.34. Global map of std of ASCAT curvature climatologies . . . 107

3.35. Global map of std of original ESCAT curvature climatologies 108
3.36. Global map of std of inter-calibrated ESCAT curvature climatologies 108
A.1. Lower outliers (in percent) that have been flagged by the node confidence data field “Doppler Compensation Center of Gravity (CoG) flag” for the Fore beam in `ERS-1.ASPS20.H`.120
A.2. Upper outliers (in percent) that have been flagged by the node confidence data field “Doppler Compensation Center of Gravity (CoG) flag” for the Fore beam in `ERS-1.ASPS20.H`. . . 120
A.3. Lower outliers (in percent) that have been flagged by the node confidence data field “Doppler Compensation Center of Gravity (CoG) flag” for the Mid beam in `ERS-1.ASPS20.H`.121
A.4. Upper outliers (in percent) that have been flagged by the node confidence data field “Doppler Compensation Center of Gravity (CoG) flag” for the Mid beam in `ERS-1.ASPS20.H`. . . 121
A.5. Lower outliers (in percent) that have been flagged by the node confidence data field “Doppler Compensation Center of Gravity (CoG) flag” for the Aft beam in `ERS-1.ASPS20.H`.122
A.6. Upper outliers (in percent) that have been flagged by the node confidence data field “Doppler Compensation Center of Gravity (CoG) flag” for the Aft beam in `ERS-1.ASPS20.H`. . . 122
A.7. Lower outliers (in percent) that have been flagged by the node confidence data field “Doppler Compensation Stdev flag” for the Fore beam in `ERS-1.ASPS20.H`. 123
A.8. Upper outliers (in percent) that have been flagged by the node confidence data field “Doppler Compensation Stdev flag” for the Fore beam in `ERS-1.ASPS20.H`. 123
A.9. Lower outliers (in percent) that have been flagged by the node confidence data field “Doppler Compensation Stdev flag” for the Mid beam in `ERS-1.ASPS20.H`. 124
A.10. Upper outliers (in percent) that have been flagged by the node confidence data field “Doppler Compensation Stdev flag” for the Mid beam in `ERS-1.ASPS20.H`. 124
A.11. Lower outliers (in percent) that have been flagged by the node confidence data field “Doppler Compensation Stdev flag” for the Aft beam in `ERS-1.ASPS20.H`. 125
A.12. Upper outliers (in percent) that have been flagged by the node confidence data field “Doppler Compensation Stdev flag” for the Aft beam in `ERS-1.ASPS20.H`. 125
A.13. Lower outliers (in percent) that have been flagged by the node confidence data field “Doppler Frequency Shift flag” for the Fore beam in `ERS-1.ASPS20.H`. 126
A.14. Upper outliers (in percent) that have been flagged by the node confidence data field “Doppler Frequency Shift flag” for the Fore beam in `ERS-1.ASPS20.H`. 126
A.15. Lower outliers (in percent) that have been flagged by the node confidence data field “Doppler Frequency Shift flag” for the Mid beam in `ERS-1.ASPS20.H`. 127
A.16. Upper outliers (in percent) that have been flagged by the node confidence data field “Doppler Frequency Shift flag” for the Mid beam in `ERS-1.ASPS20.H`. 127
A.17. Lower outliers (in percent) that have been flagged by the node confidence data field “Doppler Frequency Shift flag” for the Aft beam in `ERS-1.ASPS20.H`. 128
A.18. Upper outliers (in percent) that have been flagged by the node confidence data field “Doppler Frequency Shift flag” for the Aft beam in `ERS-1.ASPS20.H`. 128
A.19. Lower outliers (in percent) that have been flagged by the node confidence data field “Frame Checksum flag” for the Fore beam in `ERS-1.ASPS20.H`. 129
A.20. Upper outliers (in percent) that have been flagged by the node confidence data field “Frame Checksum flag” for the Fore beam in `ERS-1.ASPS20.H`. 129
A.21. Lower outliers (in percent) that have been flagged by the node confidence data field “Frame Checksum flag” for the Mid beam in `ERS-1.ASPS20.H`. 130
A.22. Upper outliers (in percent) that have been flagged by the node confidence data field “Frame Checksum flag” for the Mid beam in `ERS-1.ASPS20.H`. 130
A.23. Lower outliers (in percent) that have been flagged by the node confidence data field “Frame Checksum flag” for the Aft beam in `ERS-1.ASPS20.H`. 131

A.24. Upper outliers (in percent) that have been flagged by the node confidence data field “Frame Checksum flag” for the Aft beam in `ERS-1.ASPS20.H`. 131
A.25. Lower outliers (in percent) that have been flagged by the node confidence data field “Yaw Error Angle flag” for the Fore beam in `ERS-1.ASPS20.H`. 132
A.26. Upper outliers (in percent) that have been flagged by the node confidence data field “Yaw Error Angle flag” for the Fore beam in `ERS-1.ASPS20.H`. 132
A.27. Lower outliers (in percent) that have been flagged by the node confidence data field “Yaw Error Angle flag” for the Mid beam in `ERS-1.ASPS20.H`. 133
A.28. Upper outliers (in percent) that have been flagged by the node confidence data field “Yaw Error Angle flag” for the Mid beam in `ERS-1.ASPS20.H`. 133
A.29. Lower outliers (in percent) that have been flagged by the node confidence data field “Yaw Error Angle flag” for the Aft beam in `ERS-1.ASPS20.H`. 134
A.30. Upper outliers (in percent) that have been flagged by the node confidence data field “Yaw Error Angle flag” for the Aft beam in `ERS-1.ASPS20.H`. 134
A.31. Lower outliers (in percent) that have been flagged by the node confidence data field “Arcing flag” for the Fore beam in `ERS-1.ASPS20.H`. 135
A.32. Upper outliers (in percent) that have been flagged by the node confidence data field “Arcing flag” for the Fore beam in `ERS-1.ASPS20.H`. 135
A.33. Lower outliers (in percent) that have been flagged by the node confidence data field “Arcing flag” for the Mid beam in `ERS-1.ASPS20.H`. 136
A.34. Upper outliers (in percent) that have been flagged by the node confidence data field “Arcing flag” for the Mid beam in `ERS-1.ASPS20.H`. 136
A.35. Lower outliers (in percent) that have been flagged by the node confidence data field “Arcing flag” for the Aft beam in `ERS-1.ASPS20.H`. 137
A.36. Upper outliers (in percent) that have been flagged by the node confidence data field “Arcing flag” for the Aft beam in `ERS-1.ASPS20.H`. 137
A.37. Lower outliers (in percent) that have been flagged by the node confidence data field “Internal calibration flag” for the Fore beam in `ERS-1.ASPS20.H`. 138
A.38. Upper outliers (in percent) that have been flagged by the node confidence data field “Internal calibration flag” for the Fore beam in `ERS-1.ASPS20.H`. 138
A.39. Lower outliers (in percent) that have been flagged by the node confidence data field “Internal calibration flag” for the Mid beam in `ERS-1.ASPS20.H`. 139
A.40. Upper outliers (in percent) that have been flagged by the node confidence data field “Internal calibration flag” for the Mid beam in `ERS-1.ASPS20.H`. 139
A.41. Lower outliers (in percent) that have been flagged by the node confidence data field “Internal calibration flag” for the Aft beam in `ERS-1.ASPS20.H`. 140
A.42. Upper outliers (in percent) that have been flagged by the node confidence data field “Internal calibration flag” for the Aft beam in `ERS-1.ASPS20.H`. 140
A.43. Lower outliers (in percent) that have been flagged by the node confidence data field “Doppler Compensation Center of Gravity (CoG) flag” for the Fore beam in `ERS-2.ASPS20.H`.141
A.44. Upper outliers (in percent) that have been flagged by the node confidence data field “Doppler Compensation Center of Gravity (CoG) flag” for the Fore beam in `ERS-2.ASPS20.H`. . . 141
A.45. Lower outliers (in percent) that have been flagged by the node confidence data field “Doppler Compensation Center of Gravity (CoG) flag” for the Mid beam in `ERS-2.ASPS20.H`.142
A.46. Upper outliers (in percent) that have been flagged by the node confidence data field “Doppler Compensation Center of Gravity (CoG) flag” for the Mid beam in `ERS-2.ASPS20.H`. . . 142
A.47. Lower outliers (in percent) that have been flagged by the node confidence data field “Doppler Compensation Center of Gravity (CoG) flag” for the Aft beam in `ERS-2.ASPS20.H`.143

A.48. Upper outliers (in percent) that have been flagged by the node confidence data field "Doppler Compensation Center of Gravity (CoG) flag" for the Aft beam in `ERS-2.ASPS20.H`. . . 143
A.49. Lower outliers (in percent) that have been flagged by the node confidence data field "Doppler Compensation Stdev flag" for the Fore beam in `ERS-2.ASPS20.H`. 144
A.50. Upper outliers (in percent) that have been flagged by the node confidence data field "Doppler Compensation Stdev flag" for the Fore beam in `ERS-2.ASPS20.H`. 144
A.51. Lower outliers (in percent) that have been flagged by the node confidence data field "Doppler Compensation Stdev flag" for the Mid beam in `ERS-2.ASPS20.H`. 145
A.52. Upper outliers (in percent) that have been flagged by the node confidence data field "Doppler Compensation Stdev flag" for the Mid beam in `ERS-2.ASPS20.H`. 145
A.53. Lower outliers (in percent) that have been flagged by the node confidence data field "Doppler Compensation Stdev flag" for the Aft beam in `ERS-2.ASPS20.H`. 146
A.54. Upper outliers (in percent) that have been flagged by the node confidence data field "Doppler Compensation Stdev flag" for the Aft beam in `ERS-2.ASPS20.H`. 146
A.55. Lower outliers (in percent) that have been flagged by the node confidence data field "Doppler Frequency Shift flag" for the Fore beam in `ERS-2.ASPS20.H`. 147
A.56. Upper outliers (in percent) that have been flagged by the node confidence data field "Doppler Frequency Shift flag" for the Fore beam in `ERS-2.ASPS20.H`. 147
A.57. Lower outliers (in percent) that have been flagged by the node confidence data field "Doppler Frequency Shift flag" for the Mid beam in `ERS-2.ASPS20.H`. 148
A.58. Upper outliers (in percent) that have been flagged by the node confidence data field "Doppler Frequency Shift flag" for the Mid beam in `ERS-2.ASPS20.H`. 148
A.59. Lower outliers (in percent) that have been flagged by the node confidence data field "Doppler Frequency Shift flag" for the Aft beam in `ERS-2.ASPS20.H`. 149
A.60. Upper outliers (in percent) that have been flagged by the node confidence data field "Doppler Frequency Shift flag" for the Aft beam in `ERS-2.ASPS20.H`. 149
A.61. Lower outliers (in percent) that have been flagged by the node confidence data field "Frame Checksum flag" for the Fore beam in `ERS-2.ASPS20.H`. 150
A.62. Upper outliers (in percent) that have been flagged by the node confidence data field "Frame Checksum flag" for the Fore beam in `ERS-2.ASPS20.H`. 150
A.63. Lower outliers (in percent) that have been flagged by the node confidence data field "Frame Checksum flag" for the Mid beam in `ERS-2.ASPS20.H`. 151
A.64. Upper outliers (in percent) that have been flagged by the node confidence data field "Frame Checksum flag" for the Mid beam in `ERS-2.ASPS20.H`. 151
A.65. Lower outliers (in percent) that have been flagged by the node confidence data field "Frame Checksum flag" for the Aft beam in `ERS-2.ASPS20.H`. 152
A.66. Upper outliers (in percent) that have been flagged by the node confidence data field "Frame Checksum flag" for the Aft beam in `ERS-2.ASPS20.H`. 152
A.67. Lower outliers (in percent) that have been flagged by the node confidence data field "Yaw Error Angle flag" for the Fore beam in `ERS-2.ASPS20.H`. 153
A.68. Upper outliers (in percent) that have been flagged by the node confidence data field "Yaw Error Angle flag" for the Fore beam in `ERS-2.ASPS20.H`. 153
A.69. Lower outliers (in percent) that have been flagged by the node confidence data field "Yaw Error Angle flag" for the Mid beam in `ERS-2.ASPS20.H`. 154
A.70. Upper outliers (in percent) that have been flagged by the node confidence data field "Yaw Error Angle flag" for the Mid beam in `ERS-2.ASPS20.H`. 154
A.71. Lower outliers (in percent) that have been flagged by the node confidence data field "Yaw Error Angle flag" for the Aft beam in `ERS-2.ASPS20.H`. 155

A.72. Upper outliers (in percent) that have been flagged by the node confidence data field “Yaw Error Angle flag” for the Aft beam in `ERS-2.ASPS20.H`. 155
A.73. Lower outliers (in percent) that have been flagged by the node confidence data field “Arcing flag” for the Fore beam in `ERS-2.ASPS20.H`. 156
A.74. Upper outliers (in percent) that have been flagged by the node confidence data field “Arcing flag” for the Fore beam in `ERS-2.ASPS20.H`. 156
A.75. Lower outliers (in percent) that have been flagged by the node confidence data field “Arcing flag” for the Mid beam in `ERS-2.ASPS20.H`. 157
A.76. Upper outliers (in percent) that have been flagged by the node confidence data field “Arcing flag” for the Mid beam in `ERS-2.ASPS20.H`. 157
A.77. Lower outliers (in percent) that have been flagged by the node confidence data field “Arcing flag” for the Aft beam in `ERS-2.ASPS20.H`. 158
A.78. Upper outliers (in percent) that have been flagged by the node confidence data field “Arcing flag” for the Aft beam in `ERS-2.ASPS20.H`. 158
A.79. Lower outliers (in percent) that have been flagged by the node confidence data field “Internal calibration flag” for the Fore beam in `ERS-2.ASPS20.H`. 159
A.80. Upper outliers (in percent) that have been flagged by the node confidence data field “Internal calibration flag” for the Fore beam in `ERS-2.ASPS20.H`. 159
A.81. Lower outliers (in percent) that have been flagged by the node confidence data field “Internal calibration flag” for the Mid beam in `ERS-2.ASPS20.H`. 160
A.82. Upper outliers (in percent) that have been flagged by the node confidence data field “Internal calibration flag” for the Mid beam in `ERS-2.ASPS20.H`. 160
A.83. Lower outliers (in percent) that have been flagged by the node confidence data field “Internal calibration flag” for the Aft beam in `ERS-2.ASPS20.H`. 161
A.84. Upper outliers (in percent) that have been flagged by the node confidence data field “Internal calibration flag” for the Aft beam in `ERS-2.ASPS20.H`. 161

Appendices

A. Supplementary figures

A.1. ERS-1 outlier detection

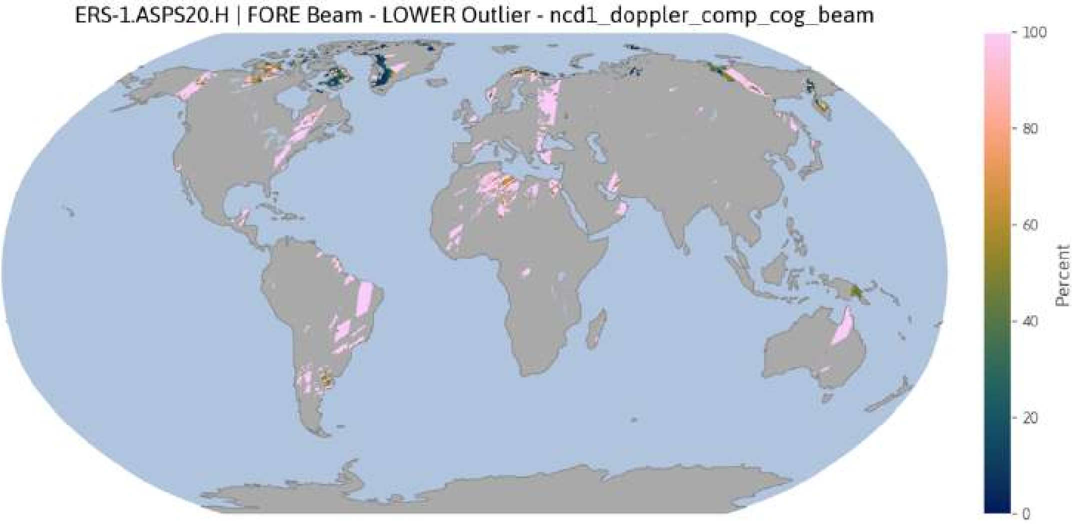

Figure A.1: Lower outliers (in percent) that have been flagged by the node confidence data field “Doppler Compensation Center of Gravity (CoG) flag” for the Fore beam in `ERS-1.ASPS20.H`.

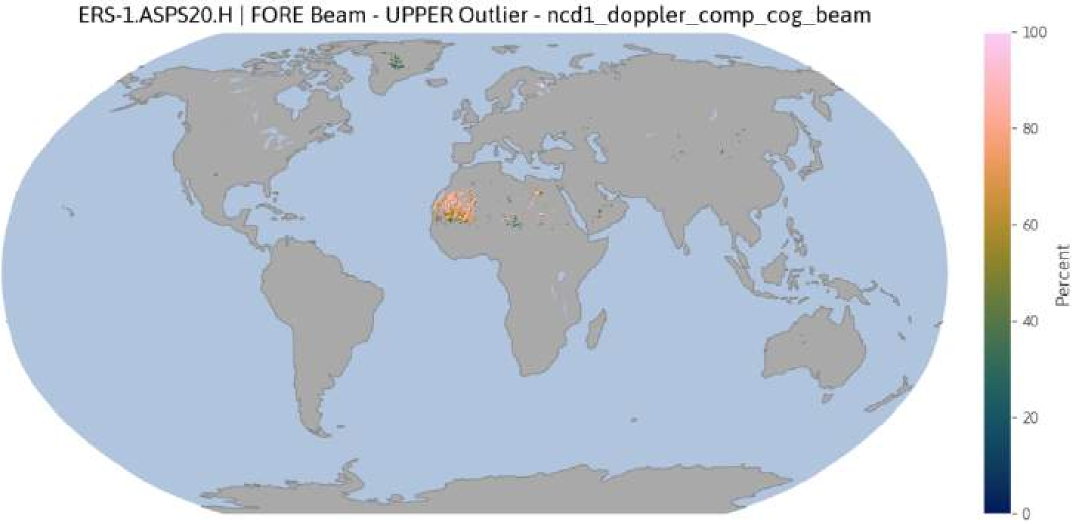

Figure A.2: Upper outliers (in percent) that have been flagged by the node confidence data field “Doppler Compensation Center of Gravity (CoG) flag” for the Fore beam in `ERS-1.ASPS20.H`.

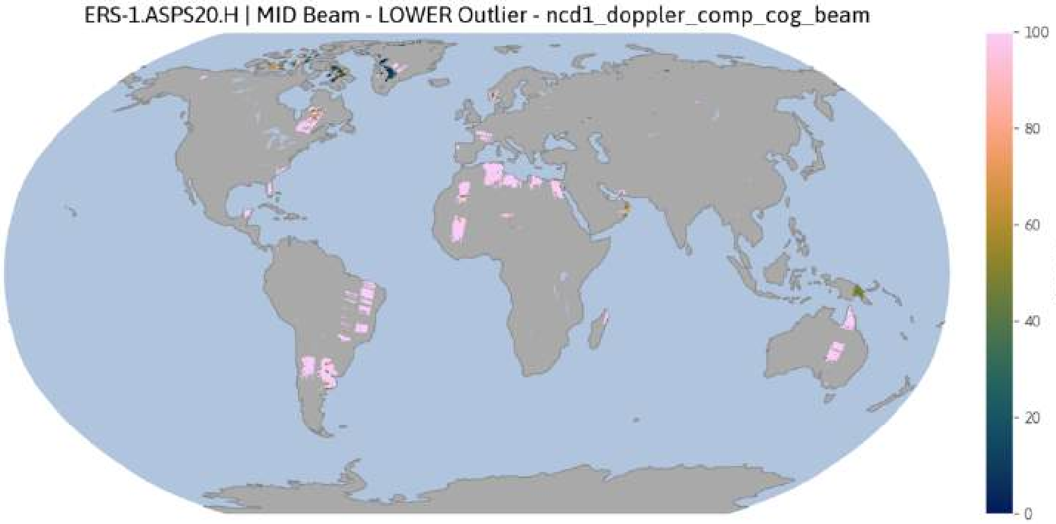

Figure A.3: Lower outliers (in percent) that have been flagged by the node confidence data field “Doppler Compensation Center of Gravity (CoG) flag” for the Mid beam in `ERS-1.ASPS20.H`.

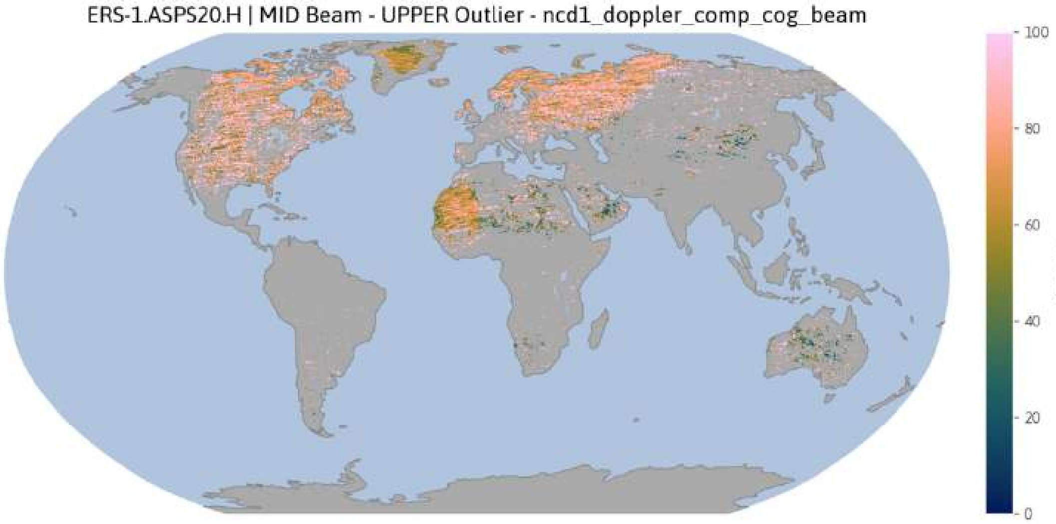

Figure A.4: Upper outliers (in percent) that have been flagged by the node confidence data field “Doppler Compensation Center of Gravity (CoG) flag” for the Mid beam in `ERS-1.ASPS20.H`.

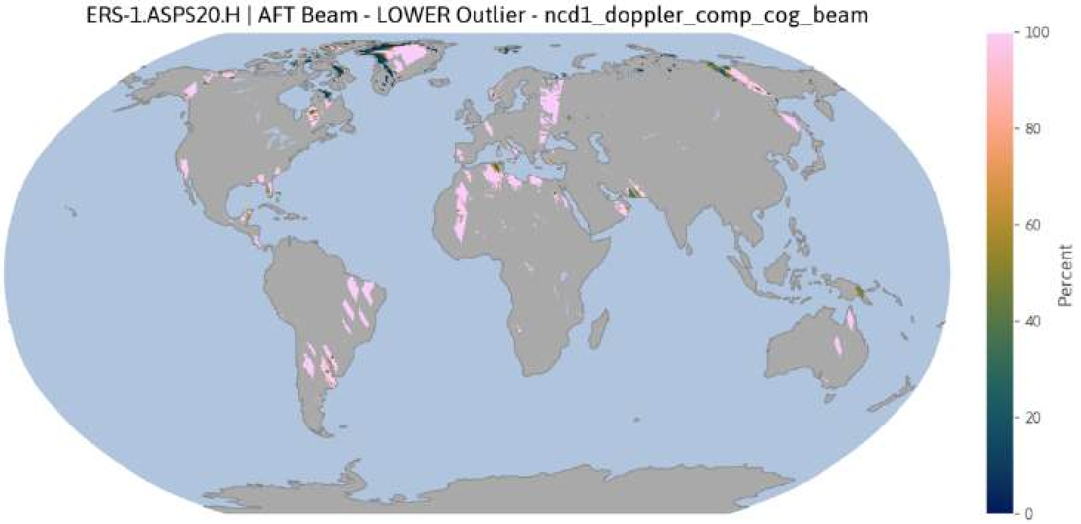

Figure A.5: Lower outliers (in percent) that have been flagged by the node confidence data field “Doppler Compensation Center of Gravity (CoG) flag” for the Aft beam in `ERS-1.ASPS20.H`.

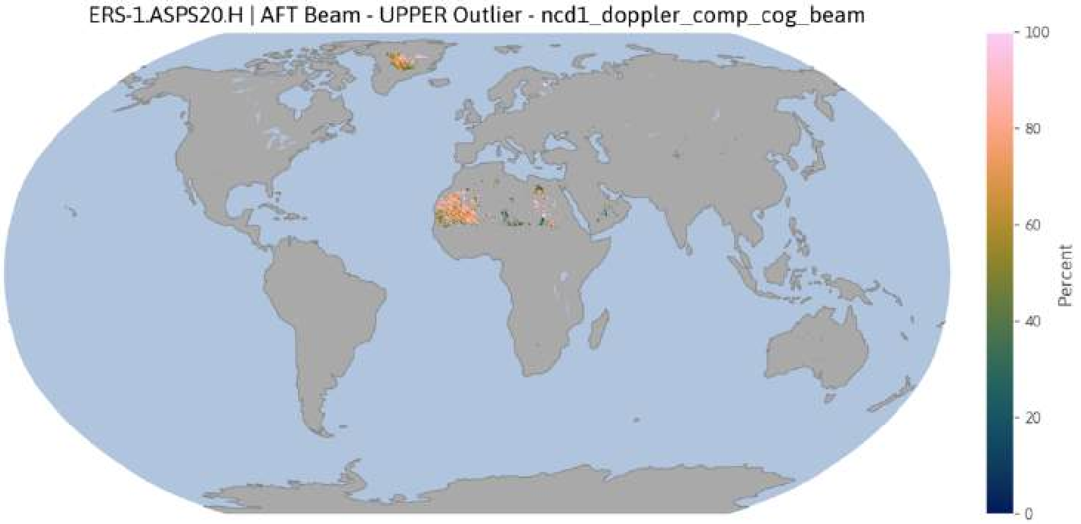

Figure A.6: Upper outliers (in percent) that have been flagged by the node confidence data field “Doppler Compensation Center of Gravity (CoG) flag” for the Aft beam in `ERS-1.ASPS20.H`.

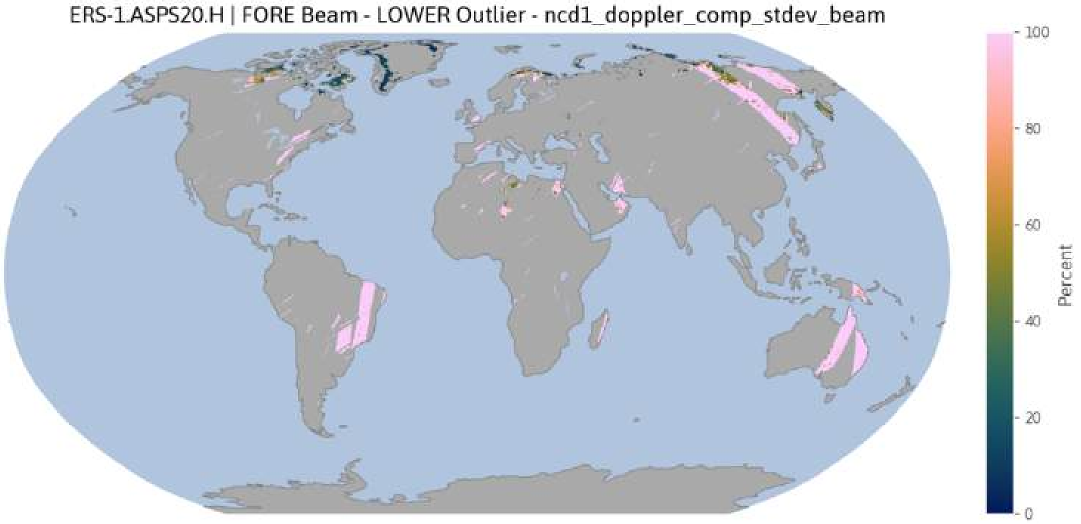

Figure A.7: Lower outliers (in percent) that have been flagged by the node confidence data field "Doppler Compensation Stdev flag" for the Fore beam in `ERS-1.ASPS20.H`.

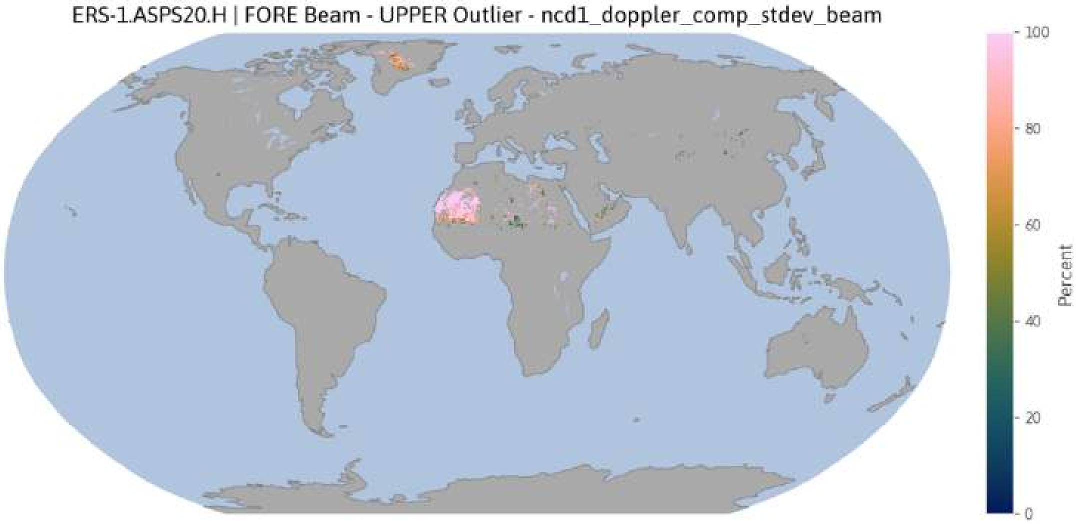

Figure A.8: Upper outliers (in percent) that have been flagged by the node confidence data field "Doppler Compensation Stdev flag" for the Fore beam in `ERS-1.ASPS20.H`.

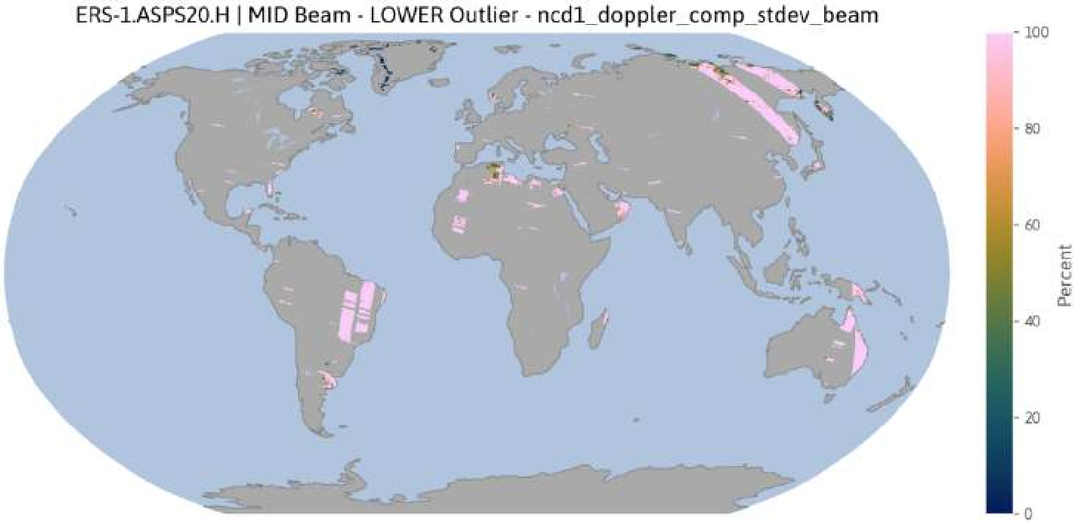

Figure A.9: Lower outliers (in percent) that have been flagged by the node confidence data field "Doppler Compensation Stdev flag" for the Mid beam in `ERS-1.ASPS20.H`.

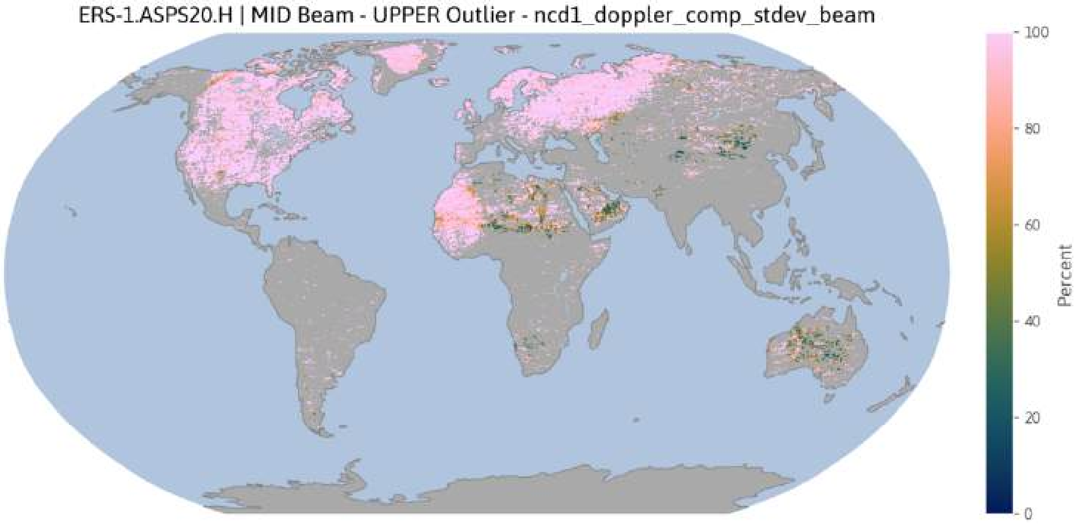

Figure A.10: Upper outliers (in percent) that have been flagged by the node confidence data field "Doppler Compensation Stdev flag" for the Mid beam in `ERS-1.ASPS20.H`.

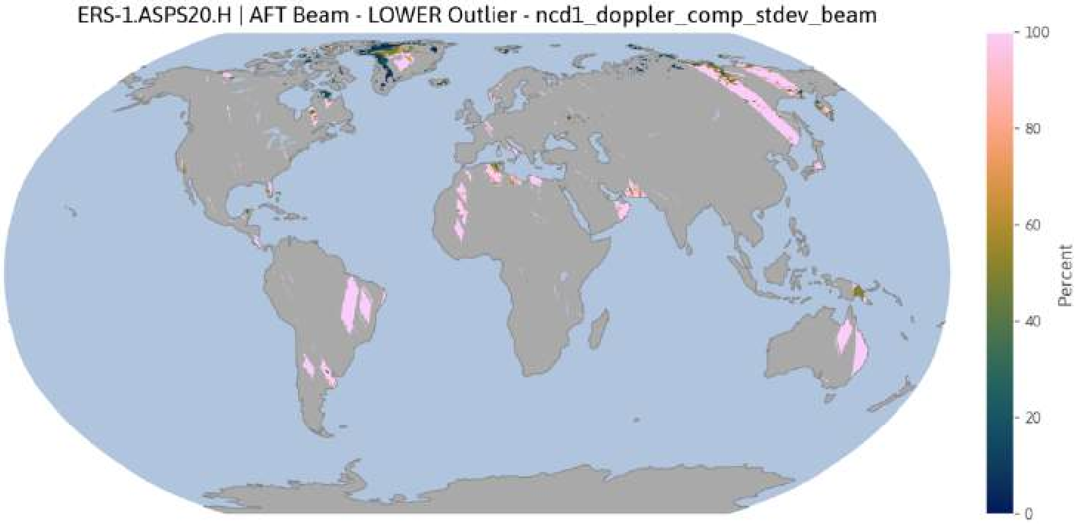

Figure A.11: Lower outliers (in percent) that have been flagged by the node confidence data field “Doppler Compensation Stdev flag” for the Aft beam in `ERS-1.ASPS20.H`.

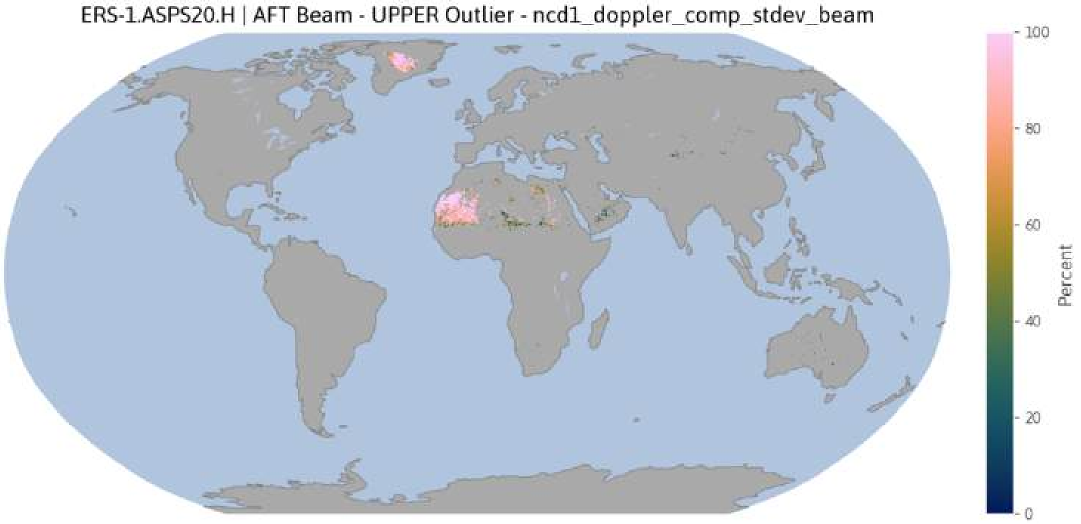

Figure A.12: Upper outliers (in percent) that have been flagged by the node confidence data field “Doppler Compensation Stdev flag” for the Aft beam in `ERS-1.ASPS20.H`.

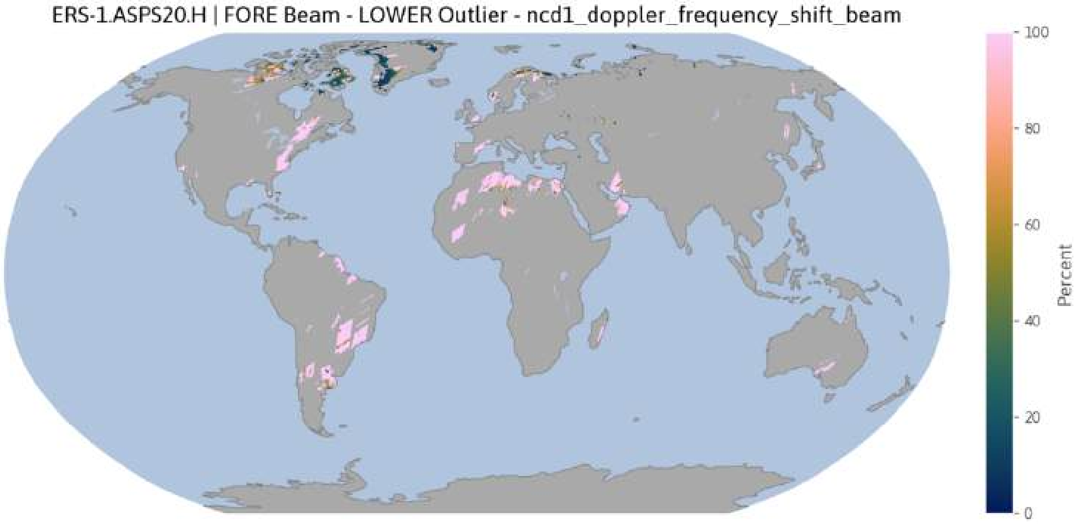

Figure A.13: Lower outliers (in percent) that have been flagged by the node confidence data field “Doppler Frequency Shift flag” for the Fore beam in `ERS-1.ASPS20.H`.

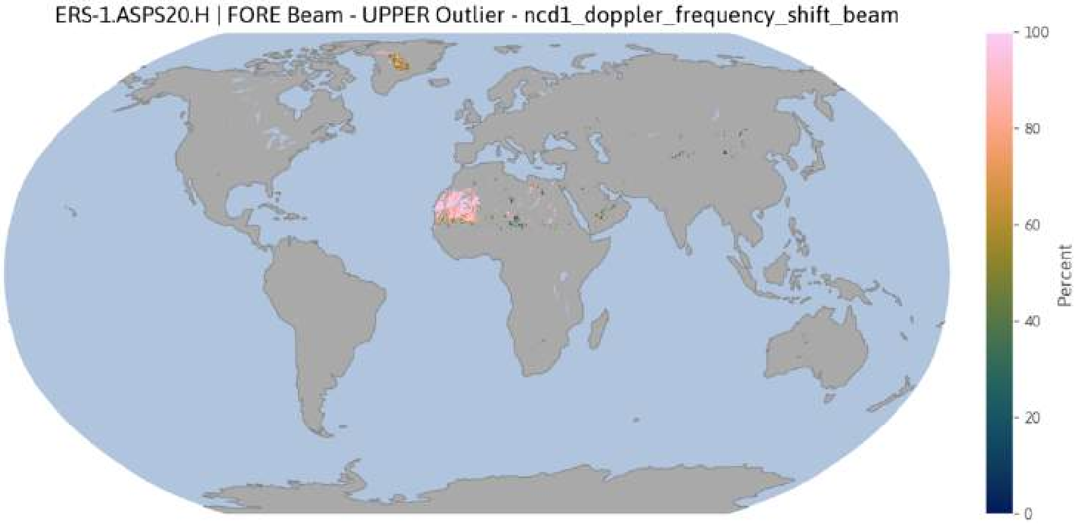

Figure A.14: Upper outliers (in percent) that have been flagged by the node confidence data field “Doppler Frequency Shift flag” for the Fore beam in `ERS-1.ASPS20.H`.

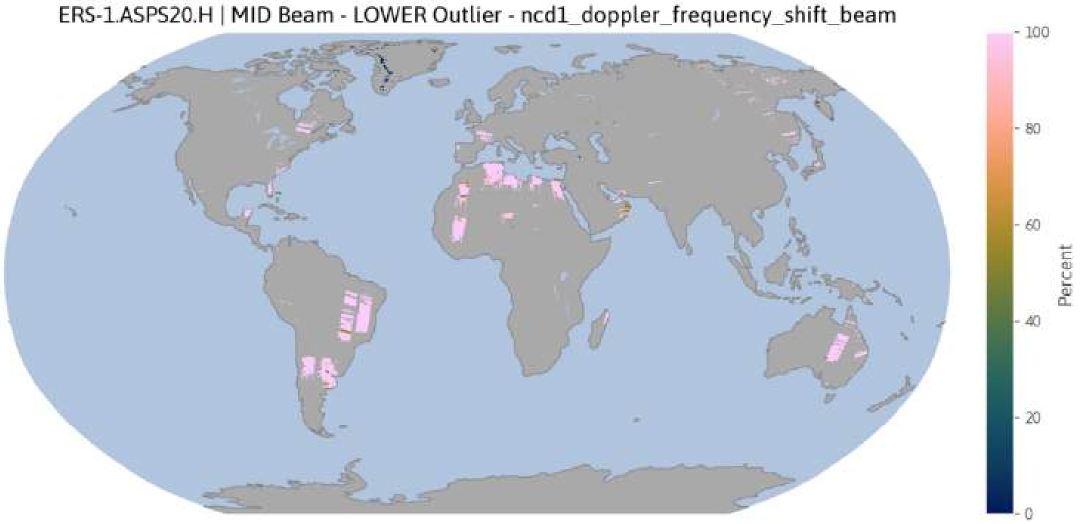

Figure A.15: Lower outliers (in percent) that have been flagged by the node confidence data field “Doppler Frequency Shift flag” for the Mid beam in `ERS-1.ASPS20.H`.

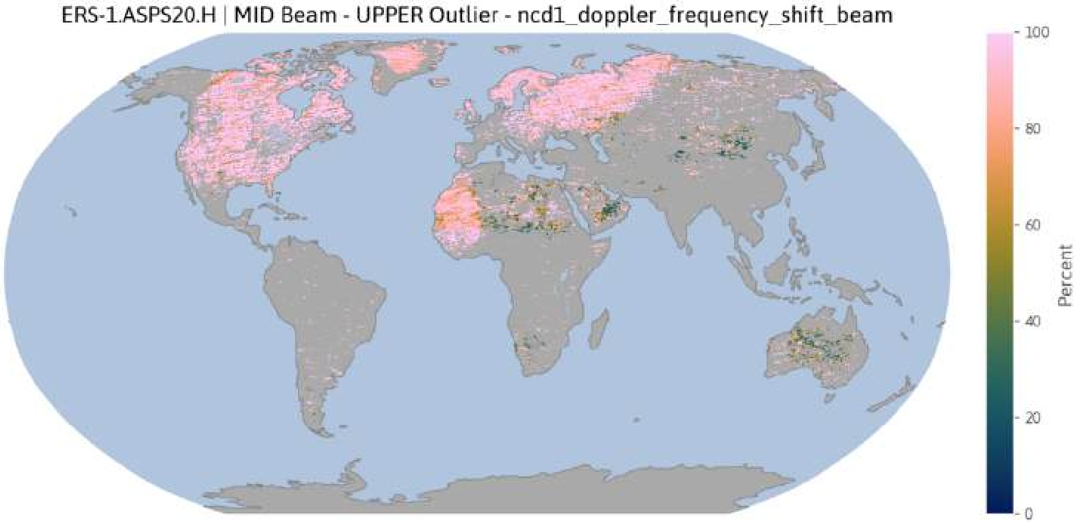

Figure A.16: Upper outliers (in percent) that have been flagged by the node confidence data field “Doppler Frequency Shift flag” for the Mid beam in `ERS-1.ASPS20.H`.

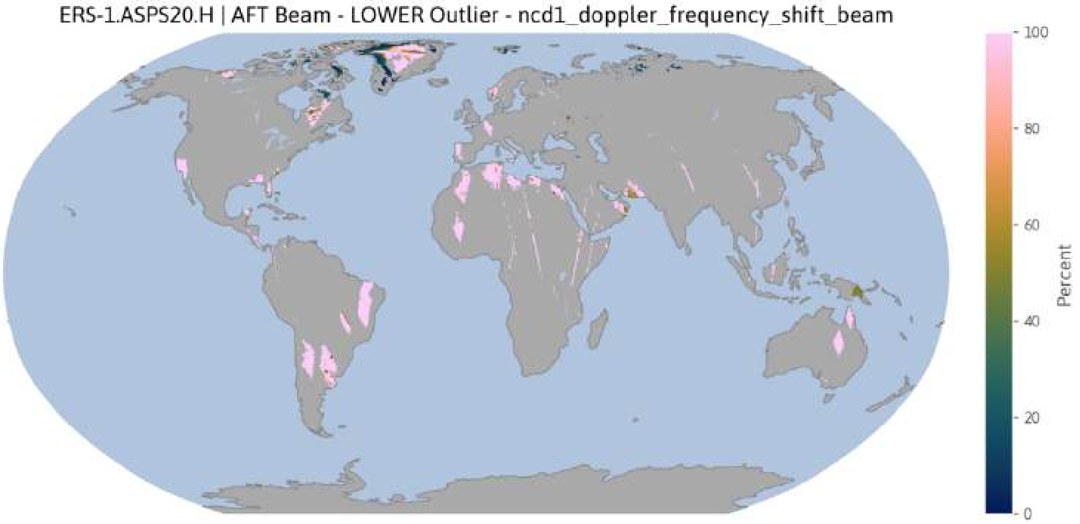

Figure A.17: Lower outliers (in percent) that have been flagged by the node confidence data field “Doppler Frequency Shift flag” for the Aft beam in `ERS-1.ASPS20.H`.

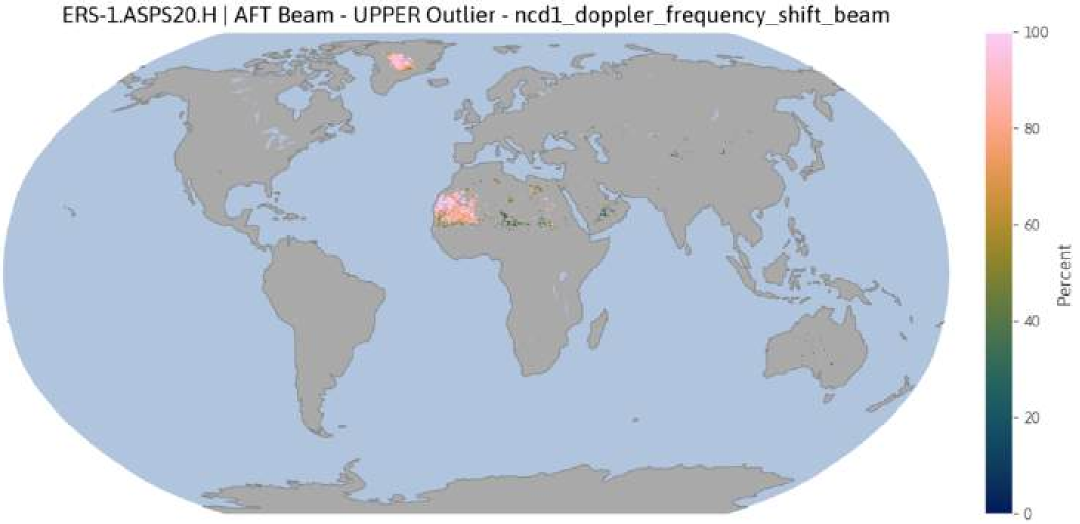

Figure A.18: Upper outliers (in percent) that have been flagged by the node confidence data field “Doppler Frequency Shift flag” for the Aft beam in `ERS-1.ASPS20.H`.

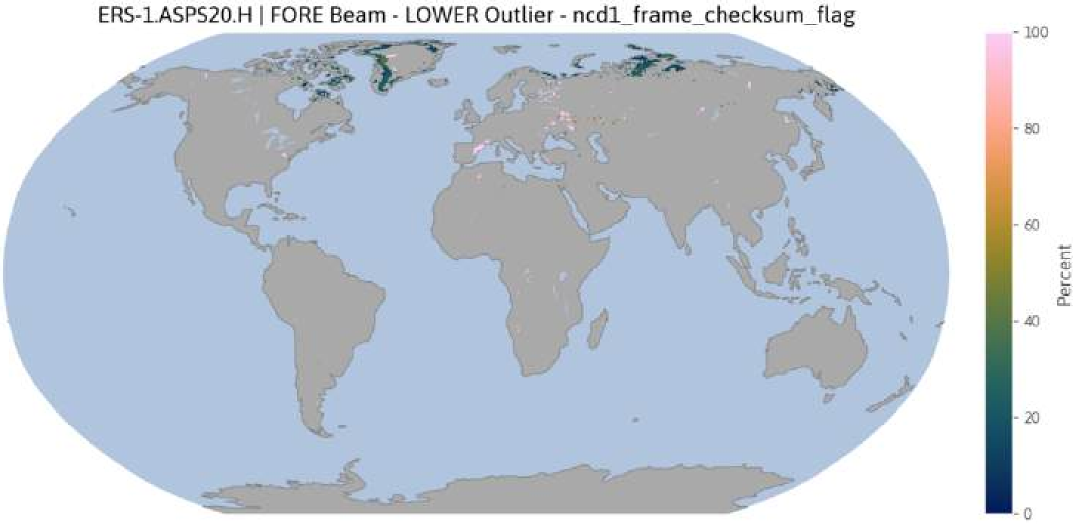

Figure A.19: Lower outliers (in percent) that have been flagged by the node confidence data field “Frame Checksum flag” for the Fore beam in `ERS-1.ASPS20.H`.

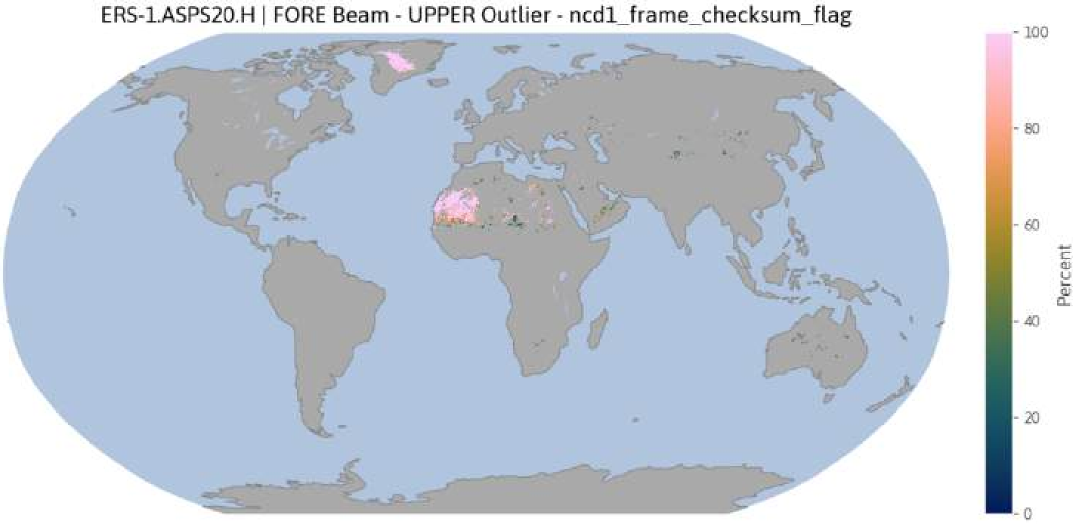

Figure A.20: Upper outliers (in percent) that have been flagged by the node confidence data field “Frame Checksum flag” for the Fore beam in `ERS-1.ASPS20.H`.

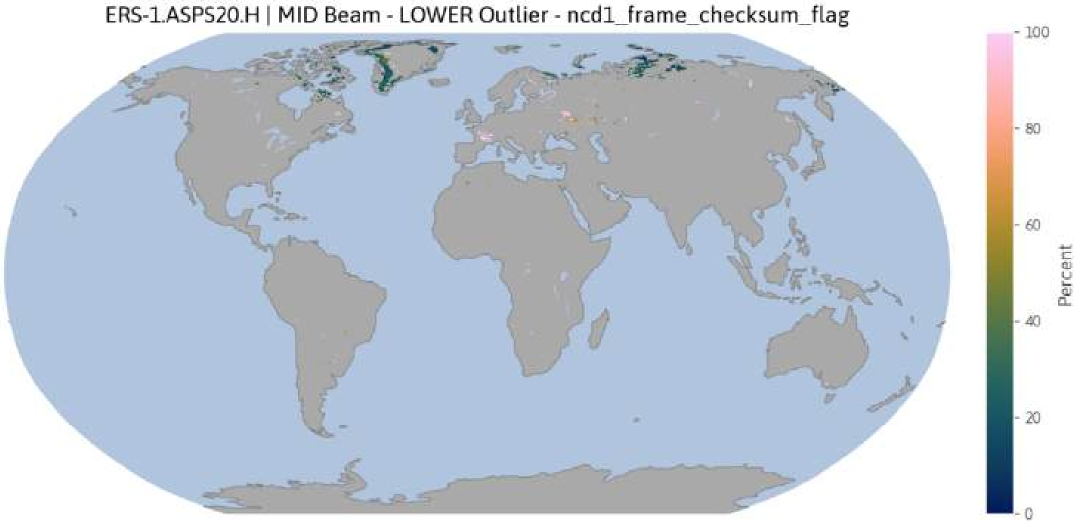

Figure A.21: Lower outliers (in percent) that have been flagged by the node confidence data field “Frame Checksum flag” for the Mid beam in `ERS-1.ASPS20.H`.

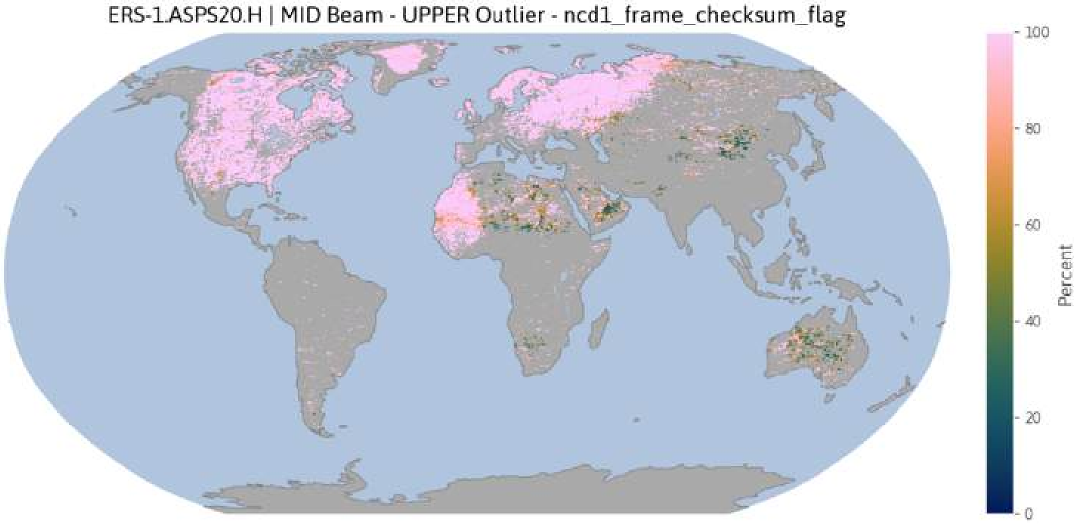

Figure A.22: Upper outliers (in percent) that have been flagged by the node confidence data field “Frame Checksum flag” for the Mid beam in `ERS-1.ASPS20.H`.

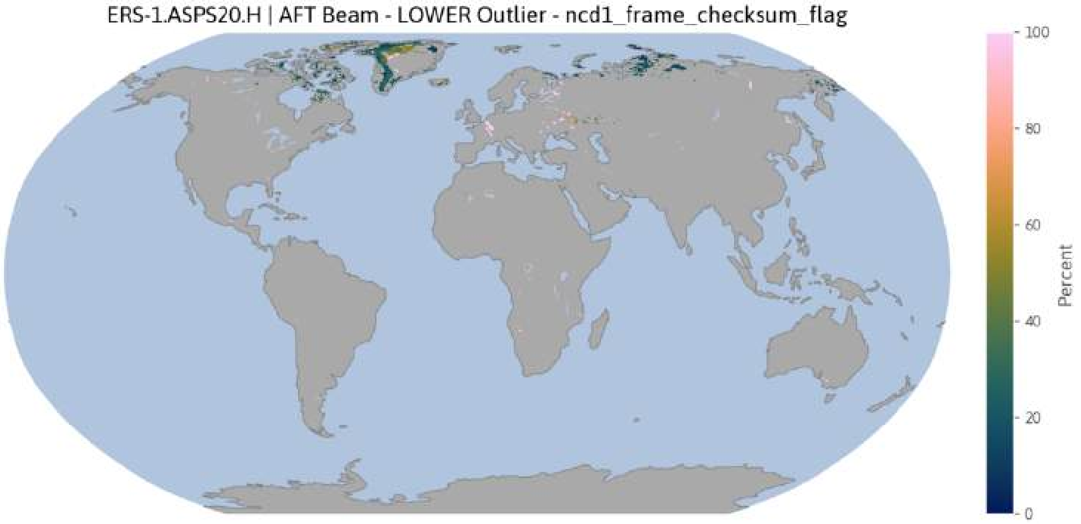

Figure A.23: Lower outliers (in percent) that have been flagged by the node confidence data field “Frame Checksum flag” for the Aft beam in `ERS-1.ASPS20.H`.

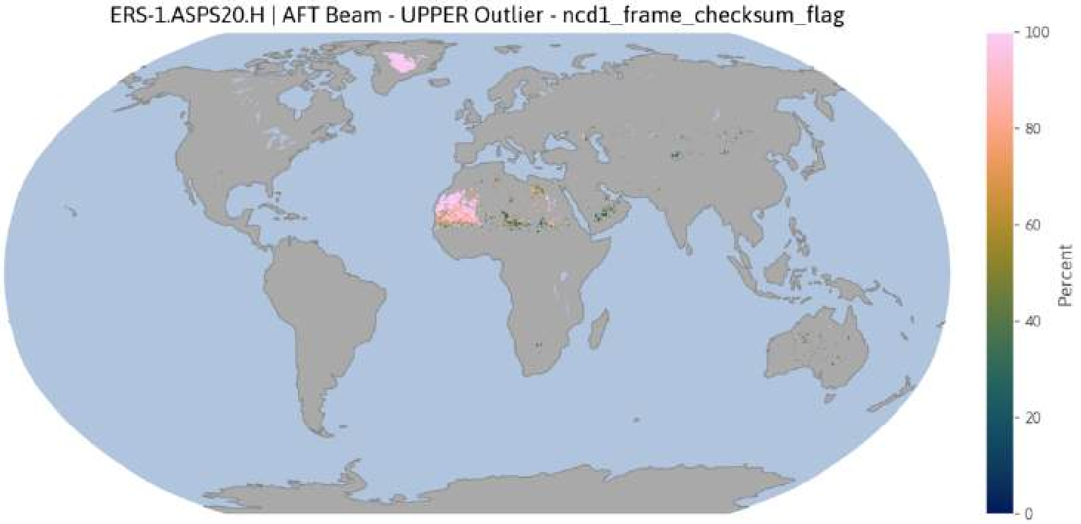

Figure A.24: Upper outliers (in percent) that have been flagged by the node confidence data field “Frame Checksum flag” for the Aft beam in `ERS-1.ASPS20.H`.

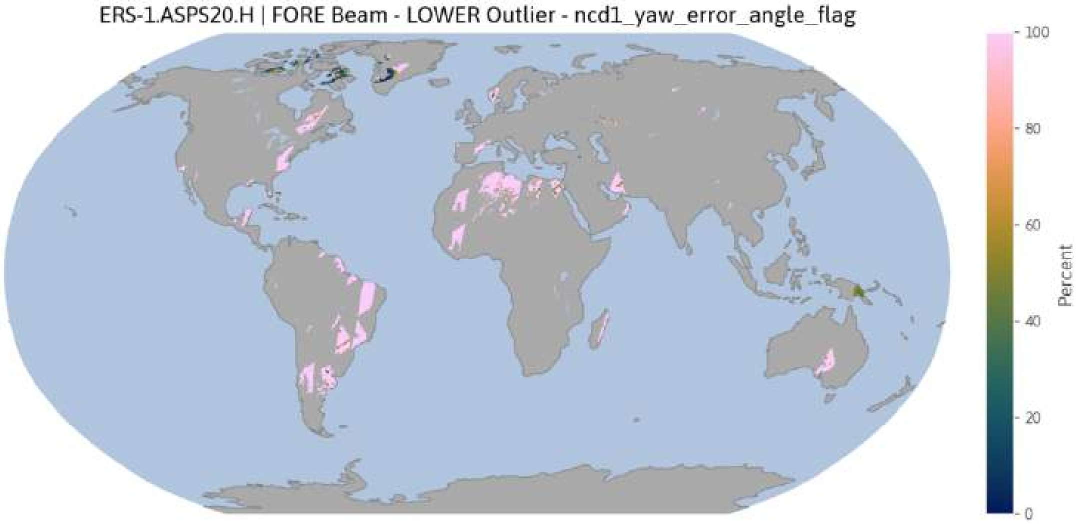

Figure A.25: Lower outliers (in percent) that have been flagged by the node confidence data field “Yaw Error Angle flag” for the Fore beam in `ERS-1.ASPS20.H`.

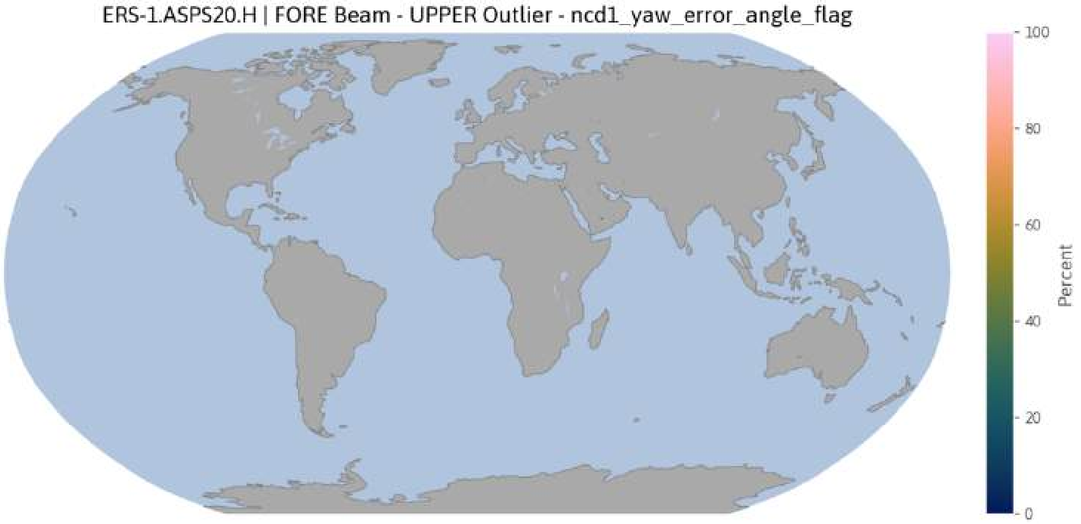

Figure A.26: Upper outliers (in percent) that have been flagged by the node confidence data field “Yaw Error Angle flag” for the Fore beam in `ERS-1.ASPS20.H`.

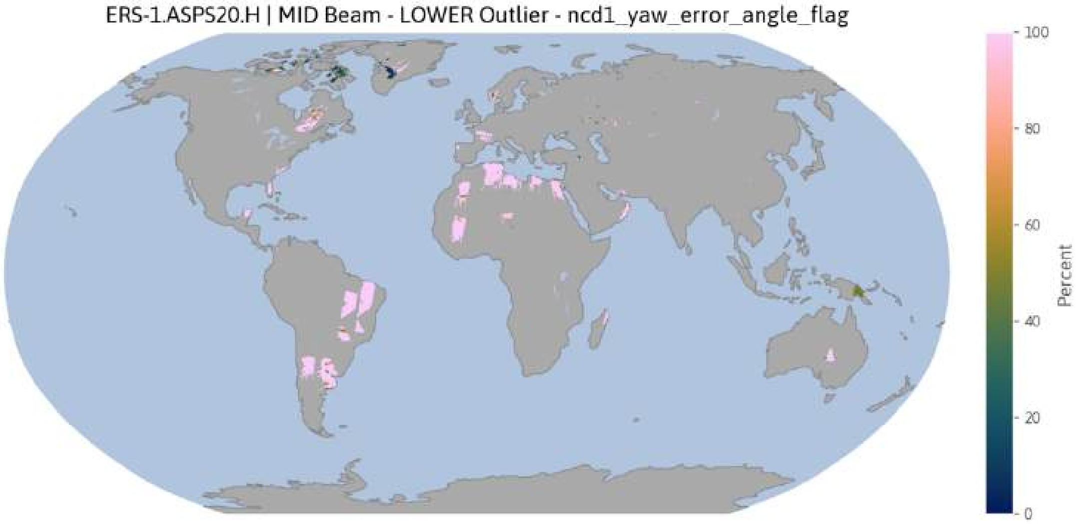

Figure A.27: Lower outliers (in percent) that have been flagged by the node confidence data field “Yaw Error Angle flag” for the Mid beam in `ERS-1.ASPS20.H`.

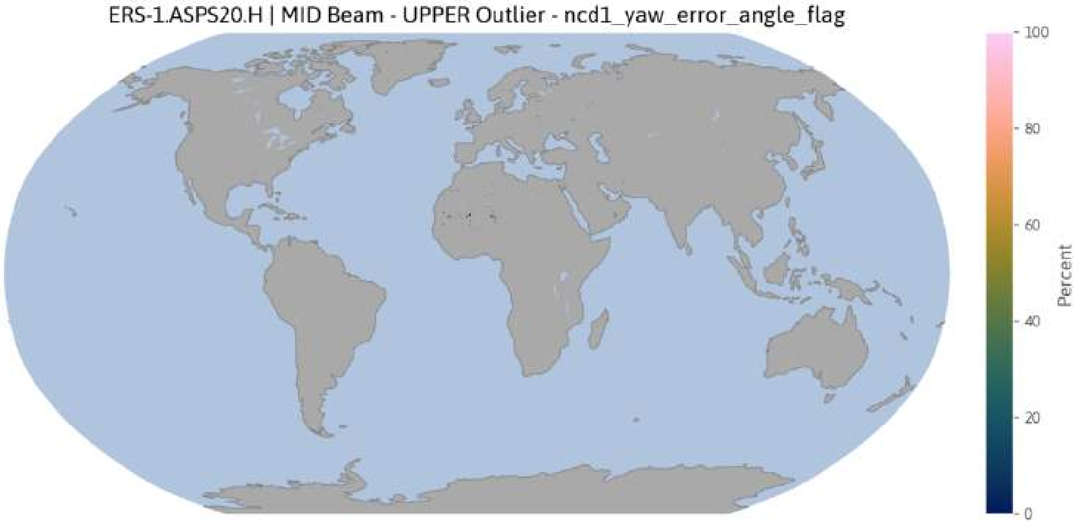

Figure A.28: Upper outliers (in percent) that have been flagged by the node confidence data field “Yaw Error Angle flag” for the Mid beam in `ERS-1.ASPS20.H`.

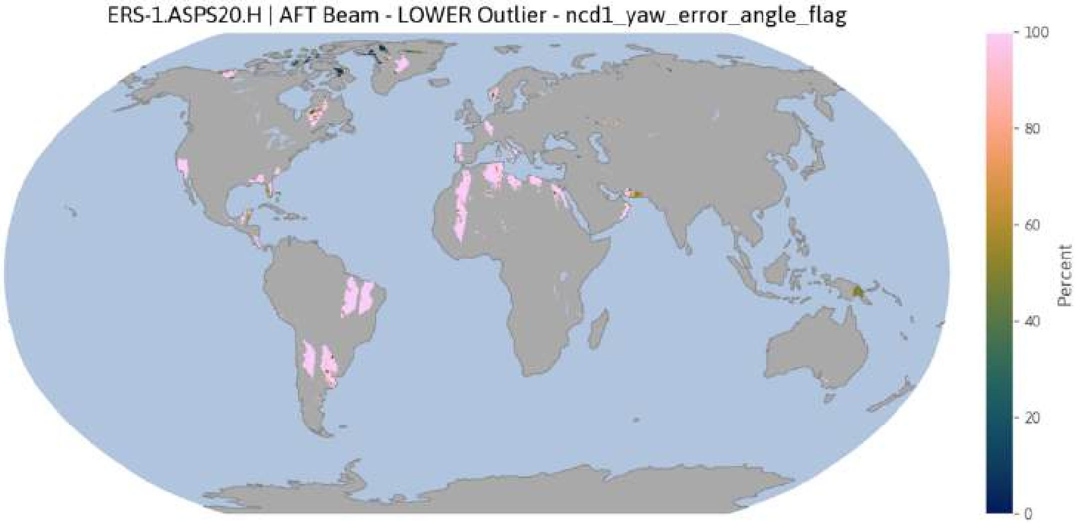

Figure A.29: Lower outliers (in percent) that have been flagged by the node confidence data field “Yaw Error Angle flag” for the Aft beam in `ERS-1.ASPS20.H`.

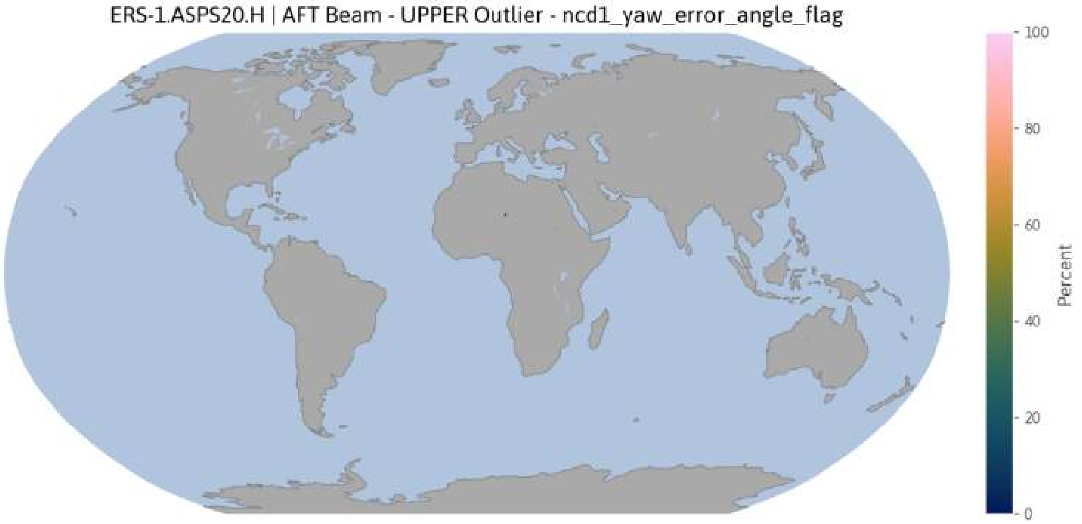

Figure A.30: Upper outliers (in percent) that have been flagged by the node confidence data field “Yaw Error Angle flag” for the Aft beam in `ERS-1.ASPS20.H`.

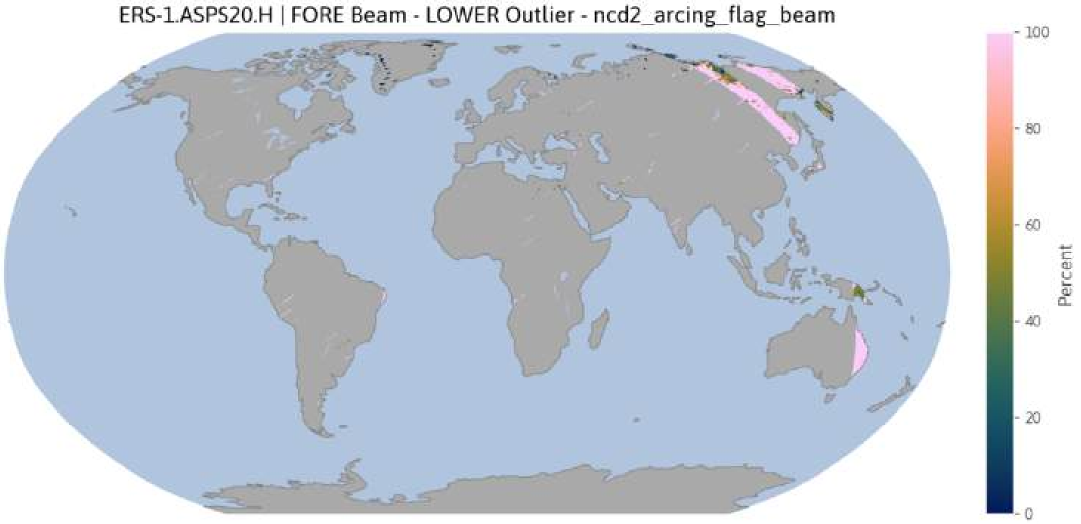

Figure A.31: Lower outliers (in percent) that have been flagged by the node confidence data field “Arcing flag” for the Fore beam in `ERS-1.ASPS20.H`.

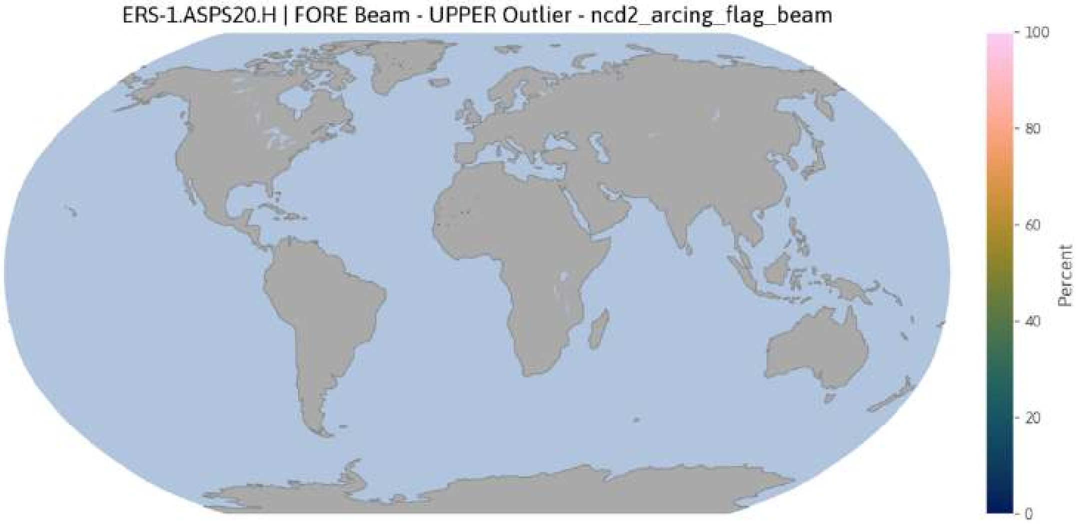

Figure A.32: Upper outliers (in percent) that have been flagged by the node confidence data field “Arcing flag” for the Fore beam in `ERS-1.ASPS20.H`.

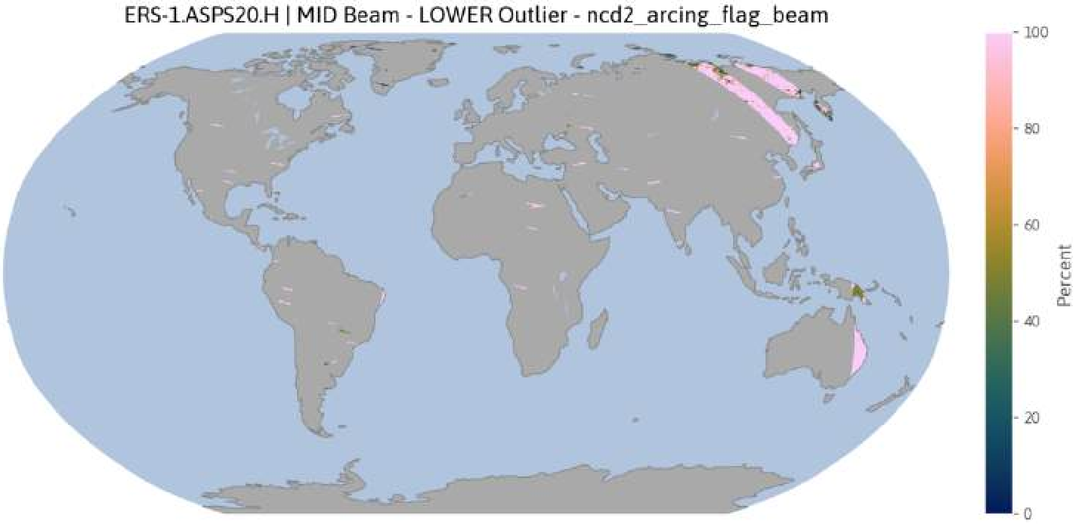

Figure A.33: Lower outliers (in percent) that have been flagged by the node confidence data field “Arcing flag” for the Mid beam in `ERS-1.ASPS20.H`.

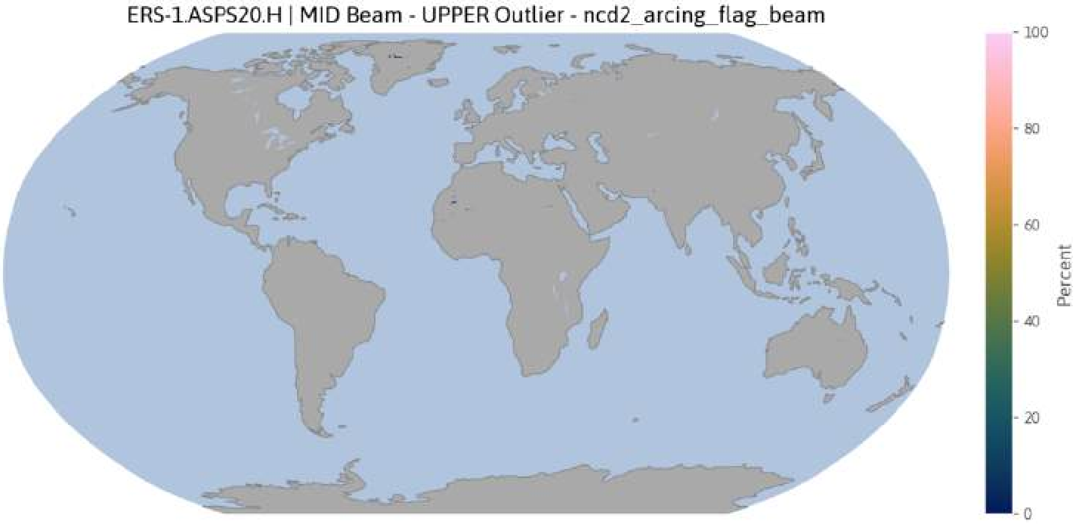

Figure A.34: Upper outliers (in percent) that have been flagged by the node confidence data field “Arcing flag” for the Mid beam in `ERS-1.ASPS20.H`.

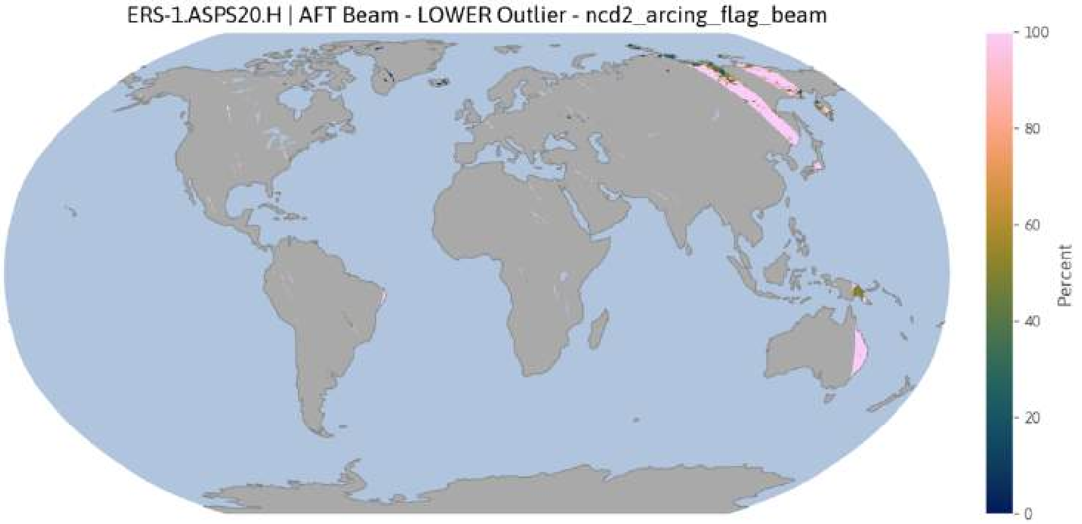

Figure A.35: Lower outliers (in percent) that have been flagged by the node confidence data field "Arcing flag" for the Aft beam in `ERS-1.ASPS20.H`.

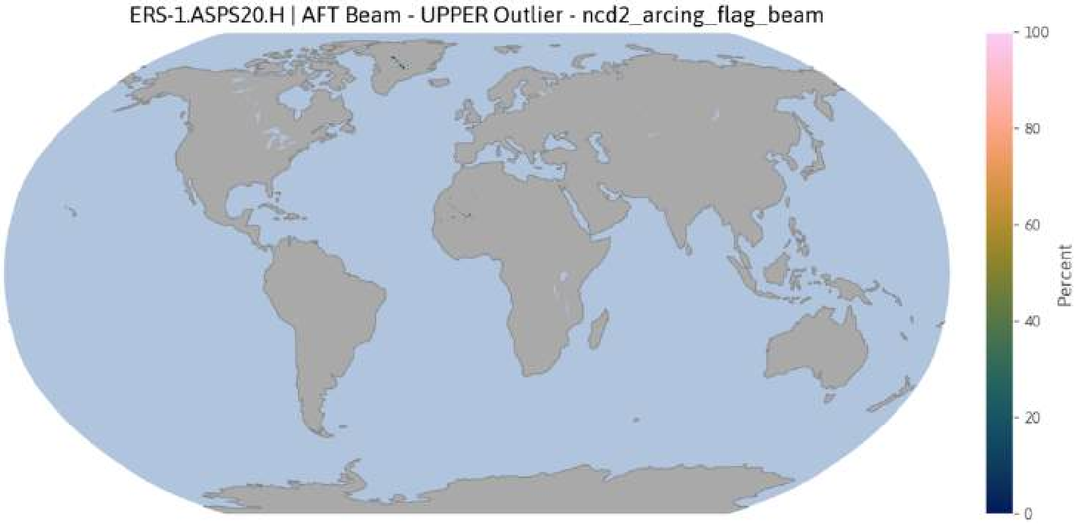

Figure A.36: Upper outliers (in percent) that have been flagged by the node confidence data field "Arcing flag" for the Aft beam in `ERS-1.ASPS20.H`.

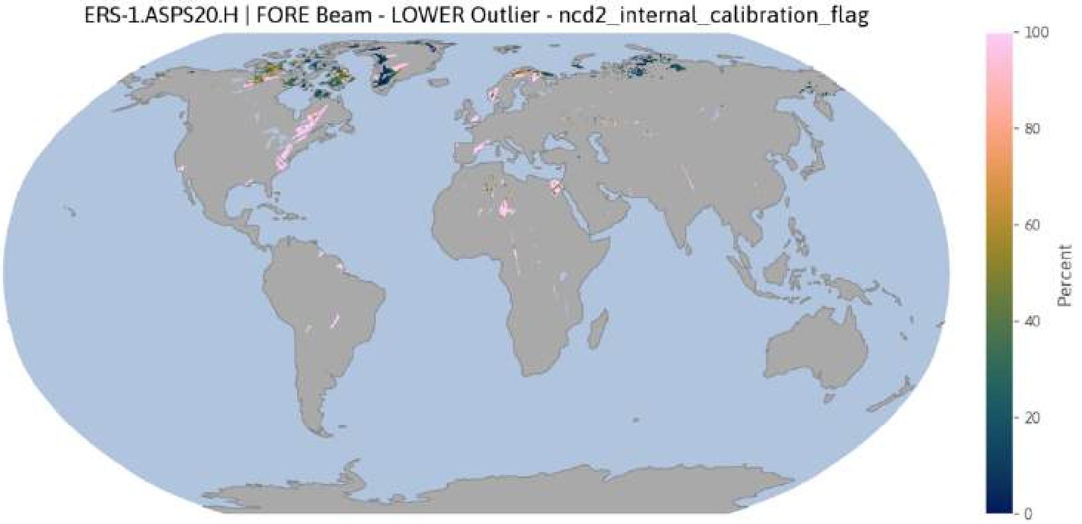

Figure A.37: Lower outliers (in percent) that have been flagged by the node confidence data field “Internal calibration flag” for the Fore beam in `ERS-1.ASPS20.H`.

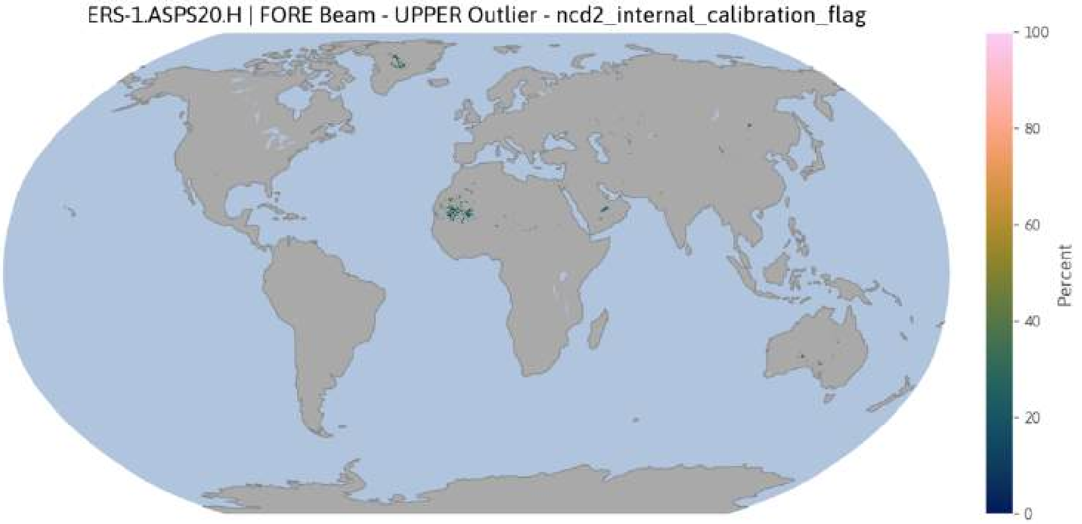

Figure A.38: Upper outliers (in percent) that have been flagged by the node confidence data field “Internal calibration flag” for the Fore beam in `ERS-1.ASPS20.H`.

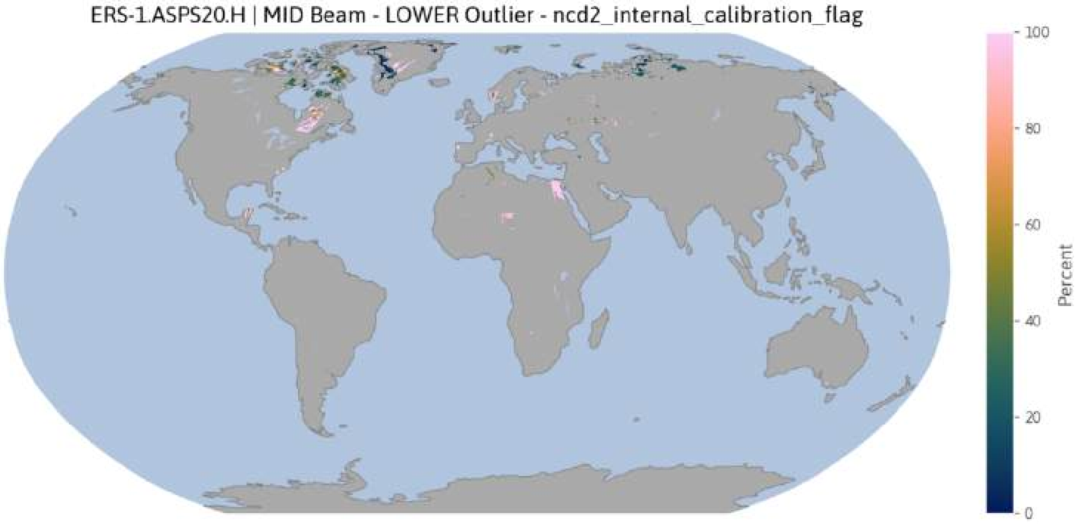

Figure A.39: Lower outliers (in percent) that have been flagged by the node confidence data field “Internal calibration flag” for the Mid beam in `ERS-1.ASPS20.H`.

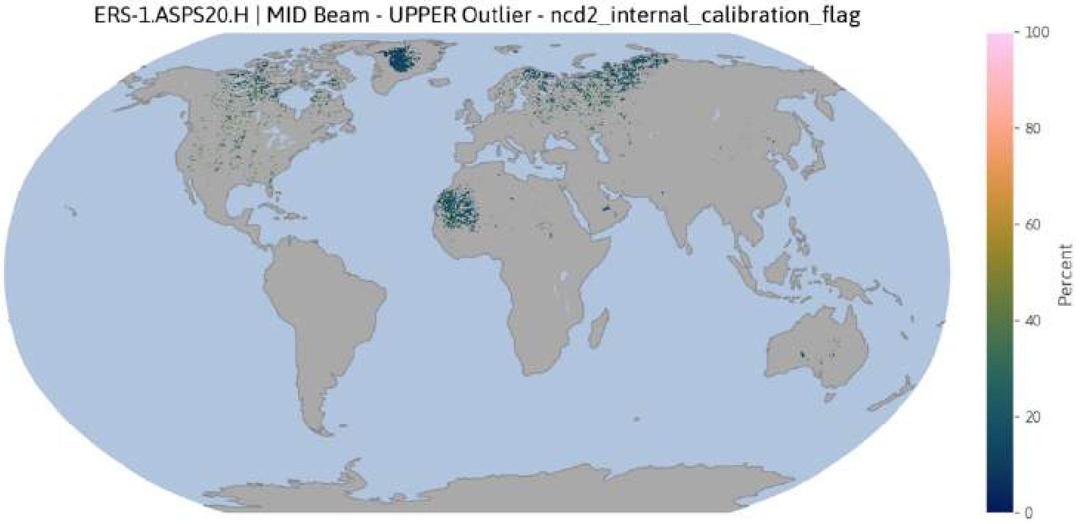

Figure A.40: Upper outliers (in percent) that have been flagged by the node confidence data field “Internal calibration flag” for the Mid beam in `ERS-1.ASPS20.H`.

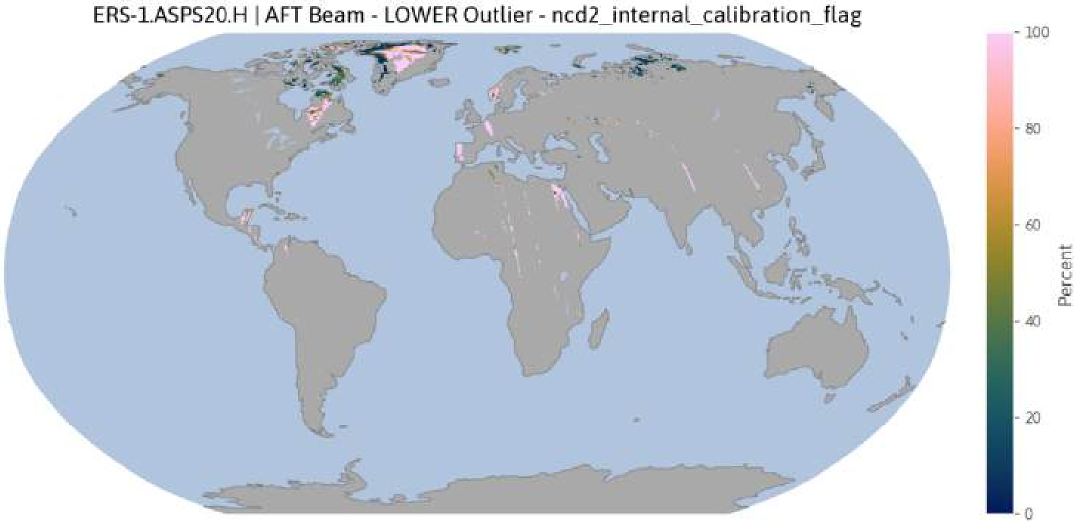

Figure A.41: Lower outliers (in percent) that have been flagged by the node confidence data field “Internal calibration flag” for the Aft beam in `ERS-1.ASPS20.H`.

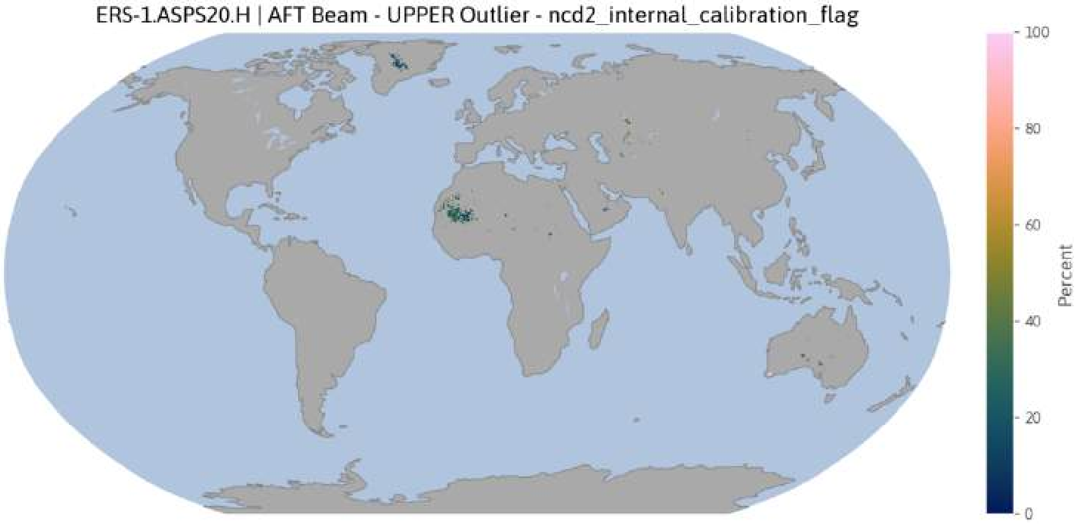

Figure A.42: Upper outliers (in percent) that have been flagged by the node confidence data field “Internal calibration flag” for the Aft beam in `ERS-1.ASPS20.H`.

A.2. ERS-2 outlier detection

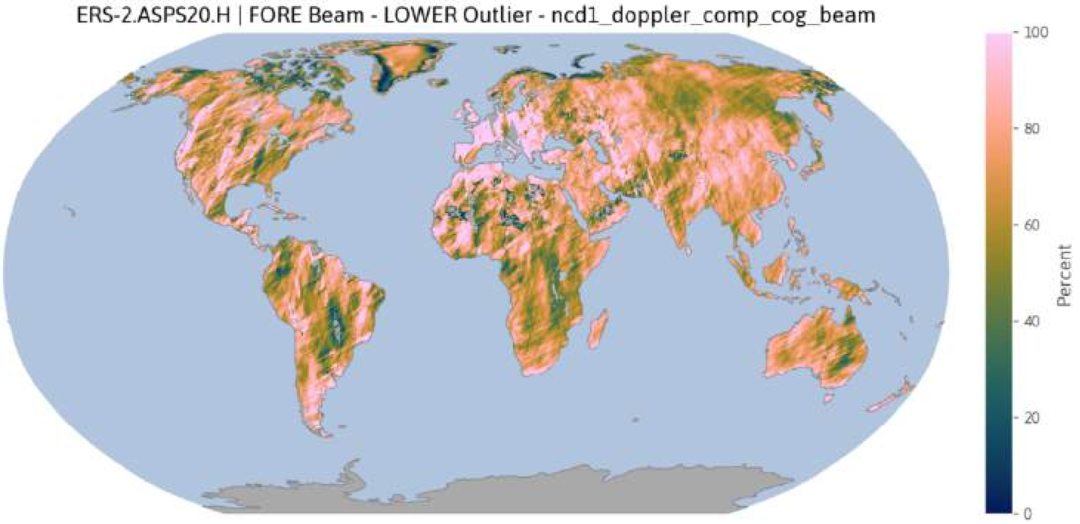

Figure A.43: Lower outliers (in percent) that have been flagged by the node confidence data field “Doppler Compensation Center of Gravity (CoG) flag” for the Fore beam in `ERS-2.ASPS20.H`.

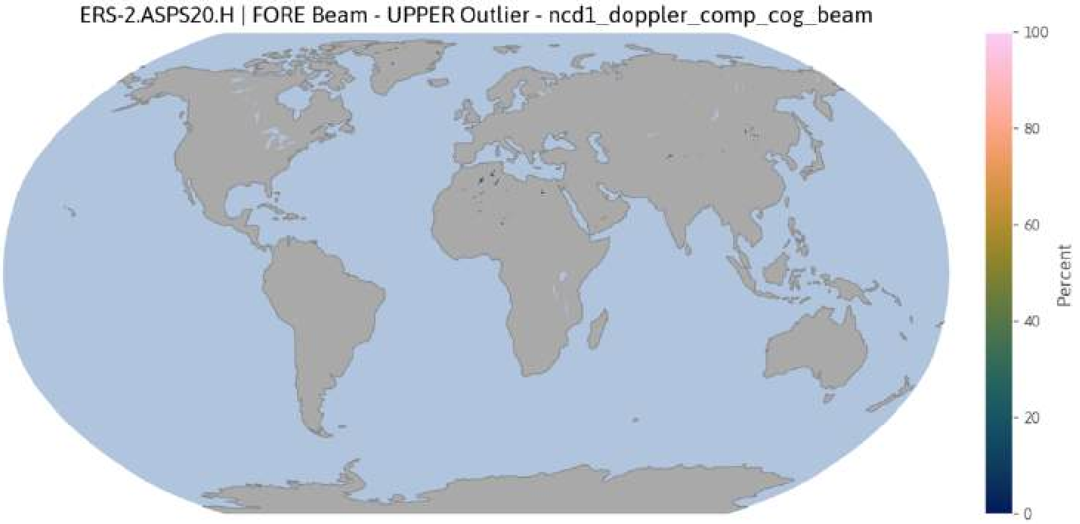

Figure A.44: Upper outliers (in percent) that have been flagged by the node confidence data field “Doppler Compensation Center of Gravity (CoG) flag” for the Fore beam in `ERS-2.ASPS20.H`.

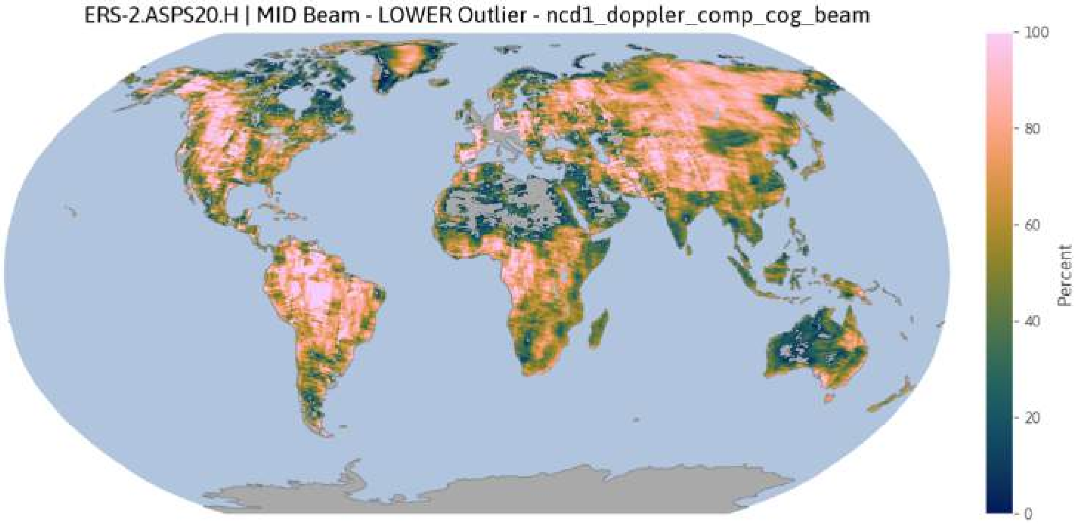

Figure A.45: Lower outliers (in percent) that have been flagged by the node confidence data field “Doppler Compensation Center of Gravity (CoG) flag” for the Mid beam in `ERS-2.ASPS20.H`.

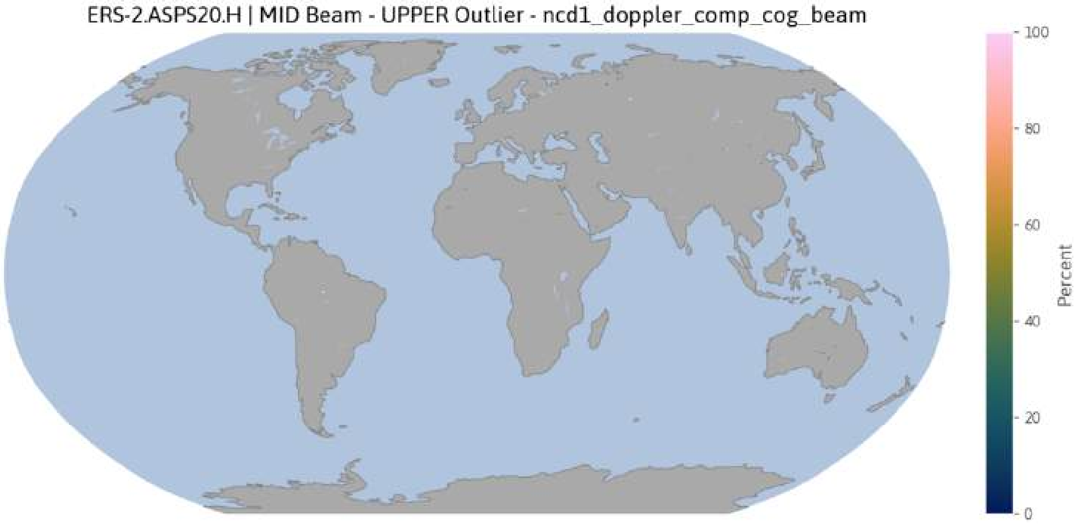

Figure A.46: Upper outliers (in percent) that have been flagged by the node confidence data field “Doppler Compensation Center of Gravity (CoG) flag” for the Mid beam in `ERS-2.ASPS20.H`.

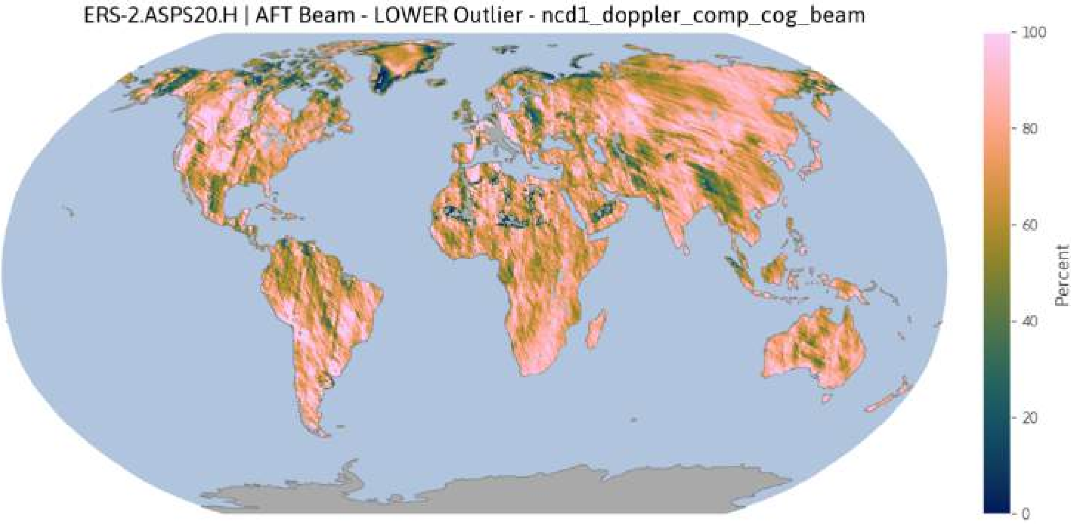

Figure A.47: Lower outliers (in percent) that have been flagged by the node confidence data field “Doppler Compensation Center of Gravity (CoG) flag” for the Aft beam in `ERS-2.ASPS20.H`.

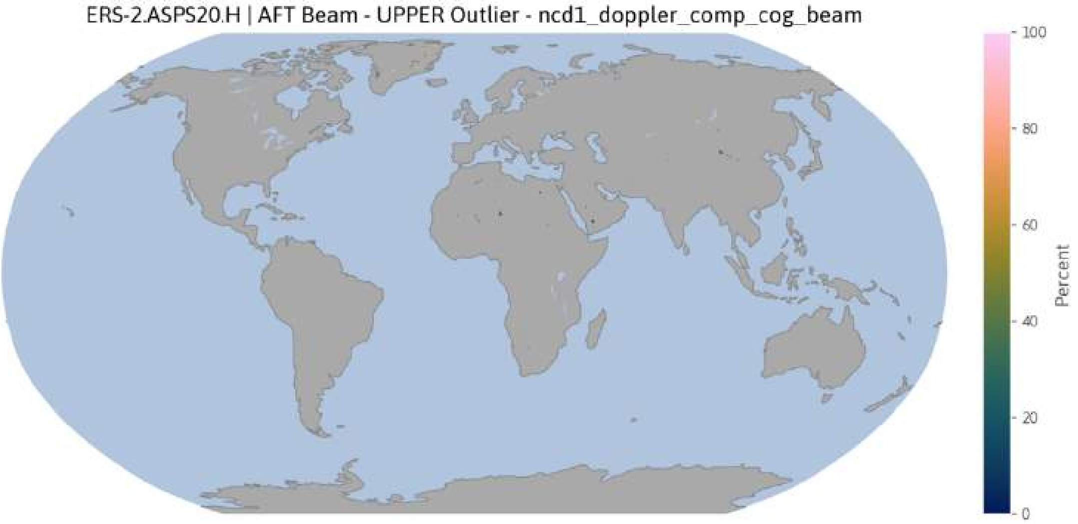

Figure A.48: Upper outliers (in percent) that have been flagged by the node confidence data field “Doppler Compensation Center of Gravity (CoG) flag” for the Aft beam in `ERS-2.ASPS20.H`.

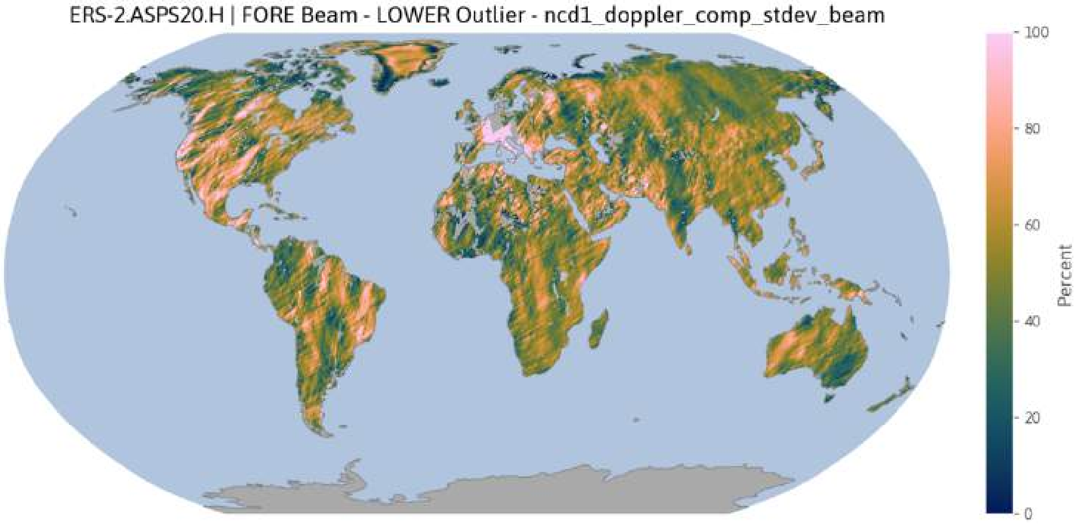

Figure A.49: Lower outliers (in percent) that have been flagged by the node confidence data field "Doppler Compensation Stdev flag" for the Fore beam in `ERS-2.ASPS20.H`.

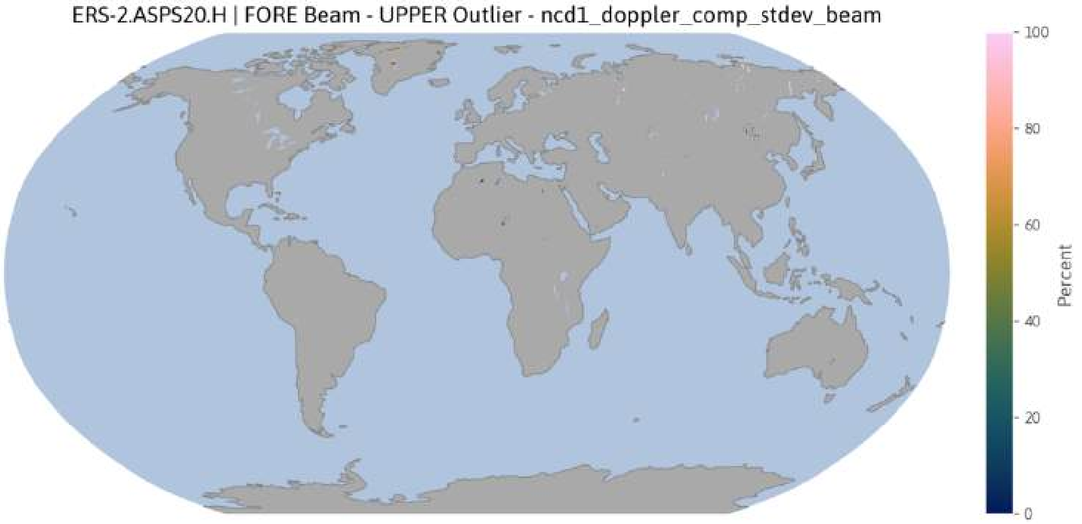

Figure A.50: Upper outliers (in percent) that have been flagged by the node confidence data field "Doppler Compensation Stdev flag" for the Fore beam in `ERS-2.ASPS20.H`.

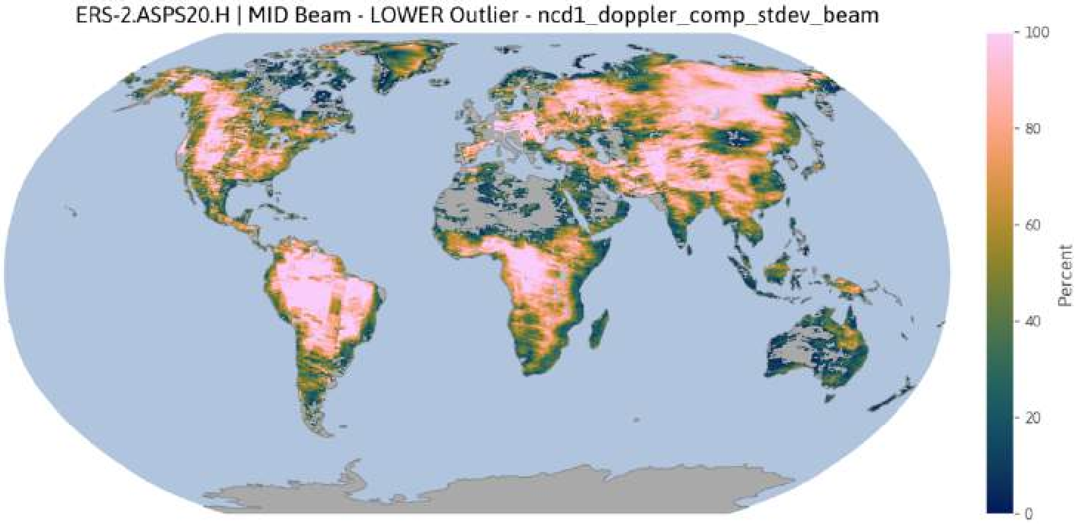

Figure A.51: Lower outliers (in percent) that have been flagged by the node confidence data field “Doppler Compensation Stdev flag” for the Mid beam in `ERS-2.ASPS20.H`.

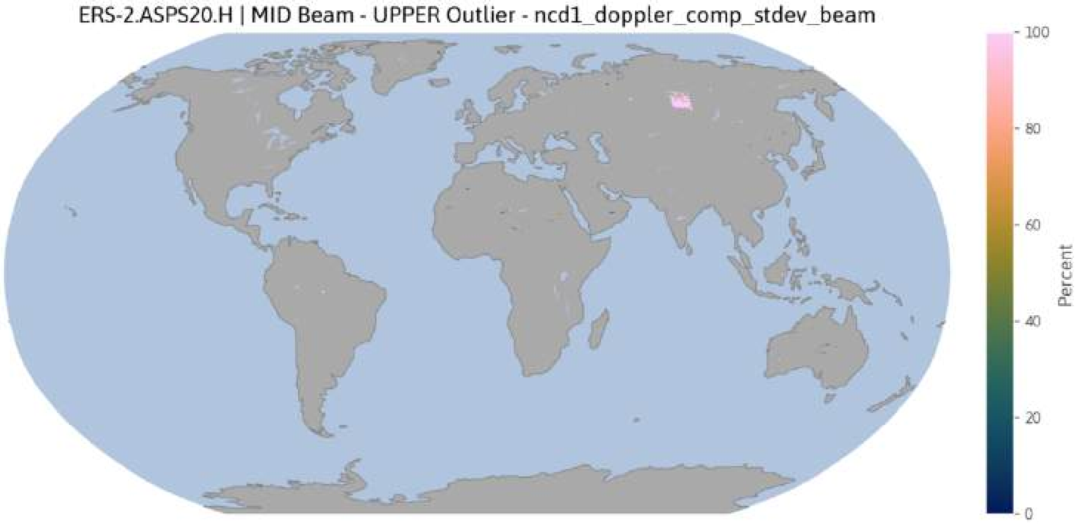

Figure A.52: Upper outliers (in percent) that have been flagged by the node confidence data field “Doppler Compensation Stdev flag” for the Mid beam in `ERS-2.ASPS20.H`.

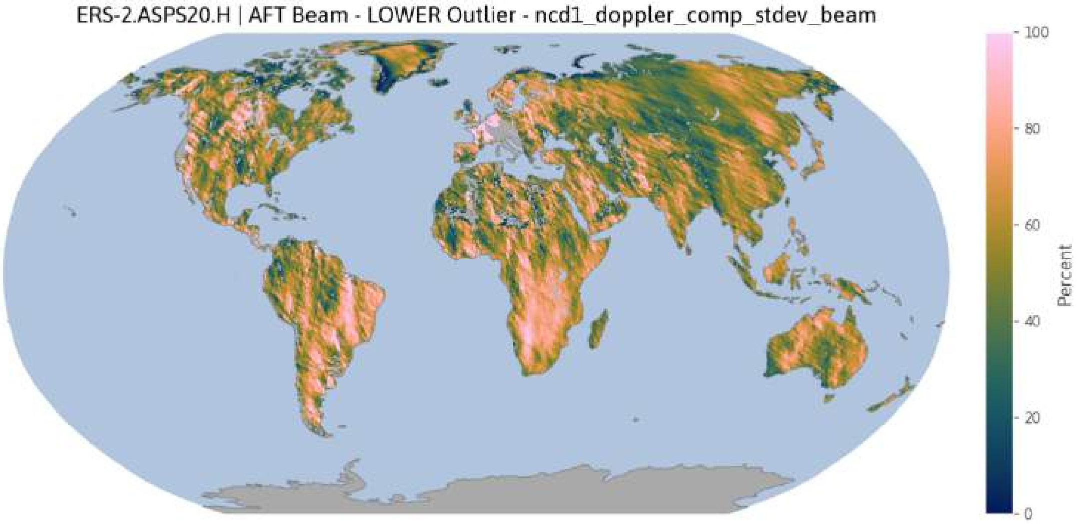

Figure A.53: Lower outliers (in percent) that have been flagged by the node confidence data field “Doppler Compensation Stdev flag” for the Aft beam in `ERS-2.ASPS20.H`.

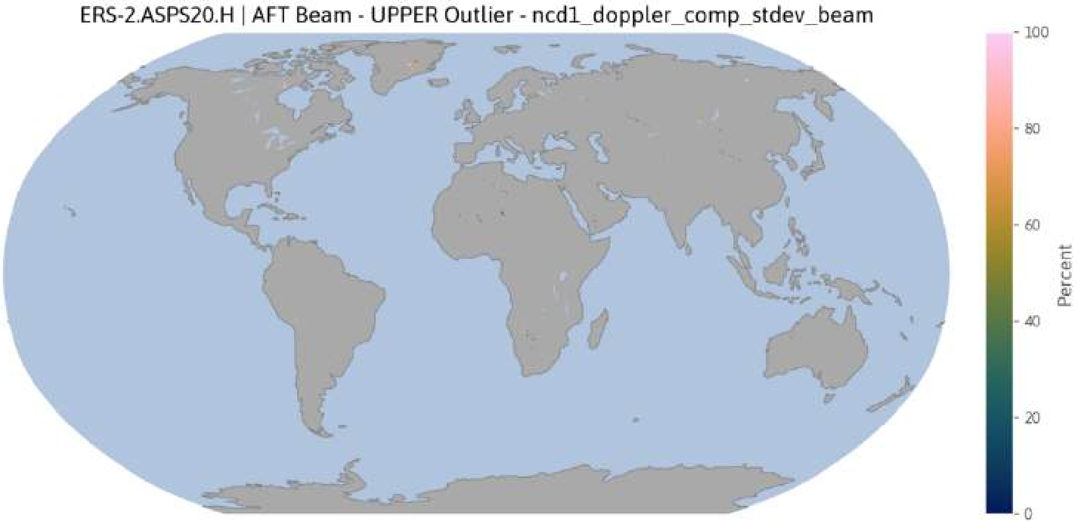

Figure A.54: Upper outliers (in percent) that have been flagged by the node confidence data field “Doppler Compensation Stdev flag” for the Aft beam in `ERS-2.ASPS20.H`.

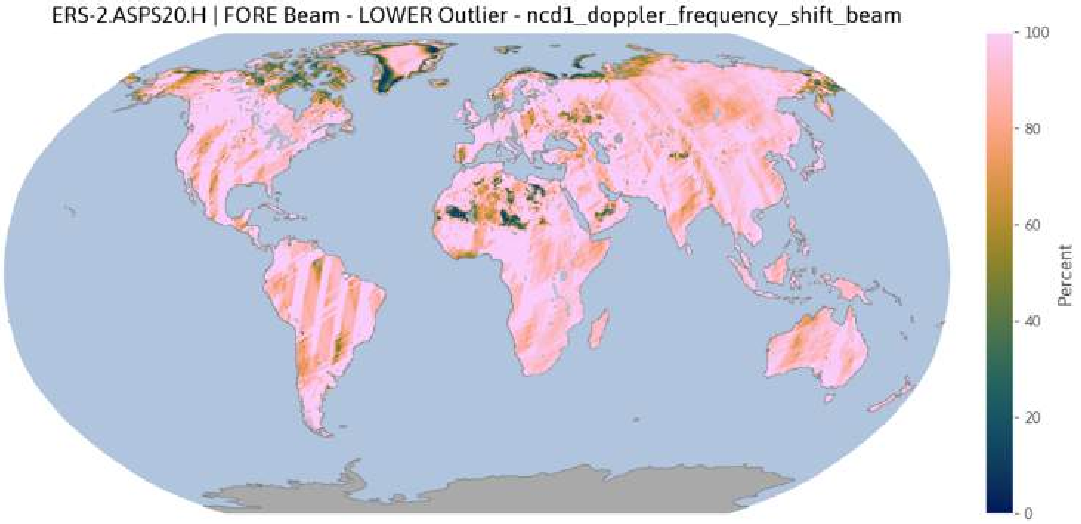

Figure A.55: Lower outliers (in percent) that have been flagged by the node confidence data field “Doppler Frequency Shift flag” for the Fore beam in `ERS-2.ASPS20.H`.

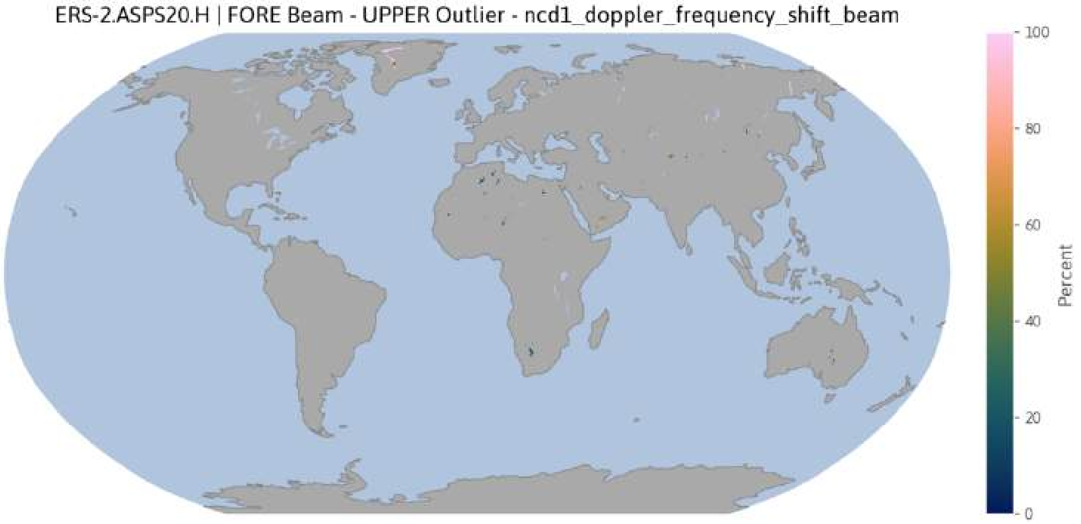

Figure A.56: Upper outliers (in percent) that have been flagged by the node confidence data field “Doppler Frequency Shift flag” for the Fore beam in `ERS-2.ASPS20.H`.

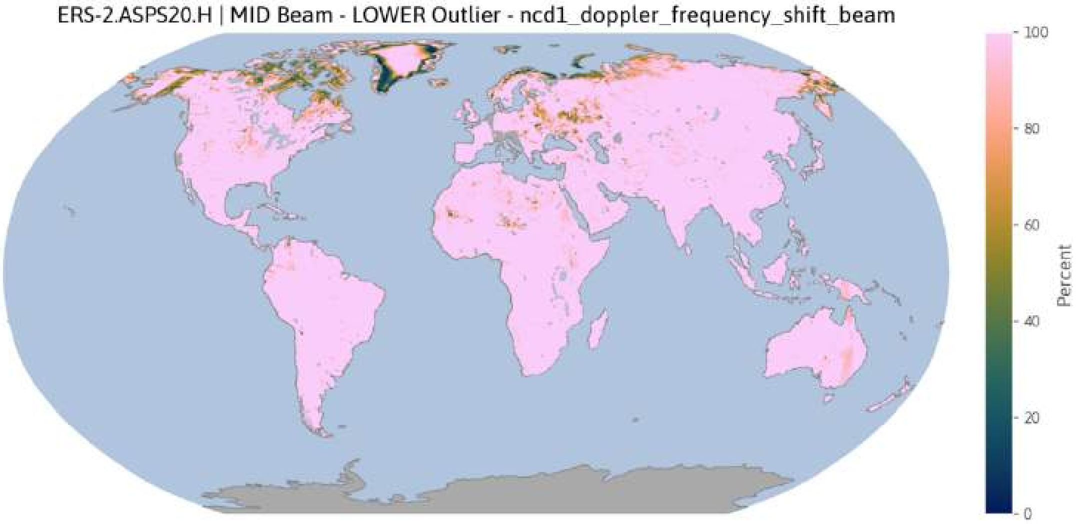

Figure A.57: Lower outliers (in percent) that have been flagged by the node confidence data field “Doppler Frequency Shift flag” for the Mid beam in `ERS-2.ASPS20.H`.

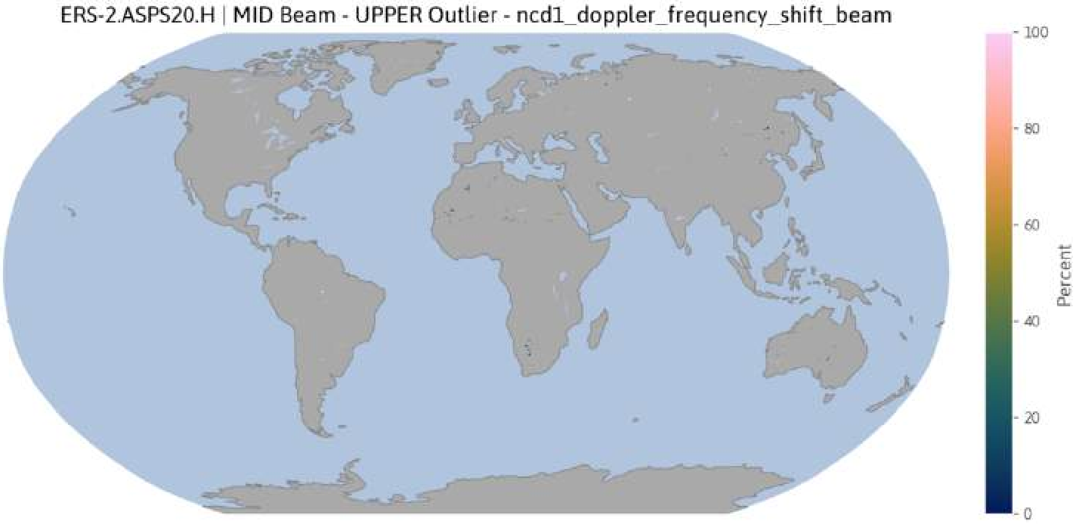

Figure A.58: Upper outliers (in percent) that have been flagged by the node confidence data field “Doppler Frequency Shift flag” for the Mid beam in `ERS-2.ASPS20.H`.

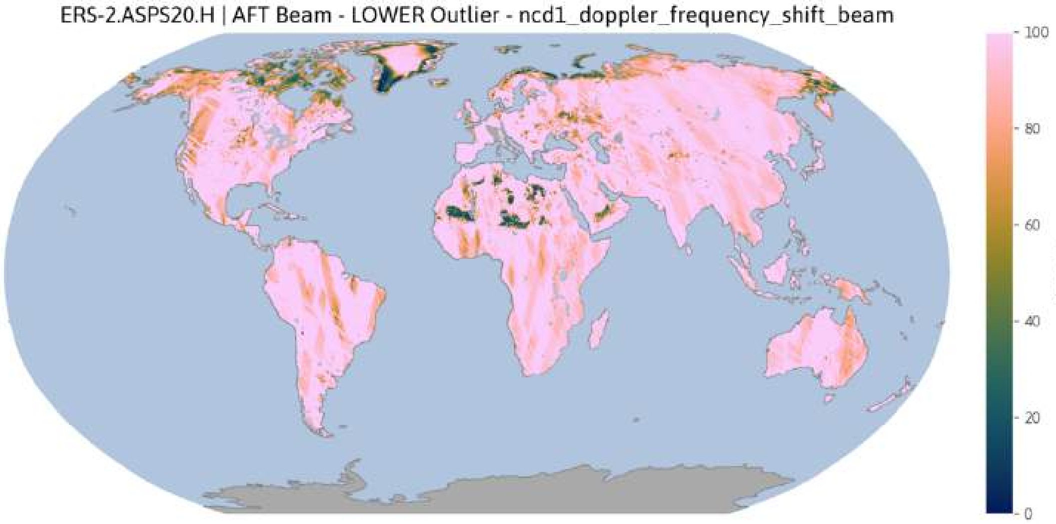

Figure A.59: Lower outliers (in percent) that have been flagged by the node confidence data field "Doppler Frequency Shift flag" for the Aft beam in `ERS-2.ASPS20.H`.

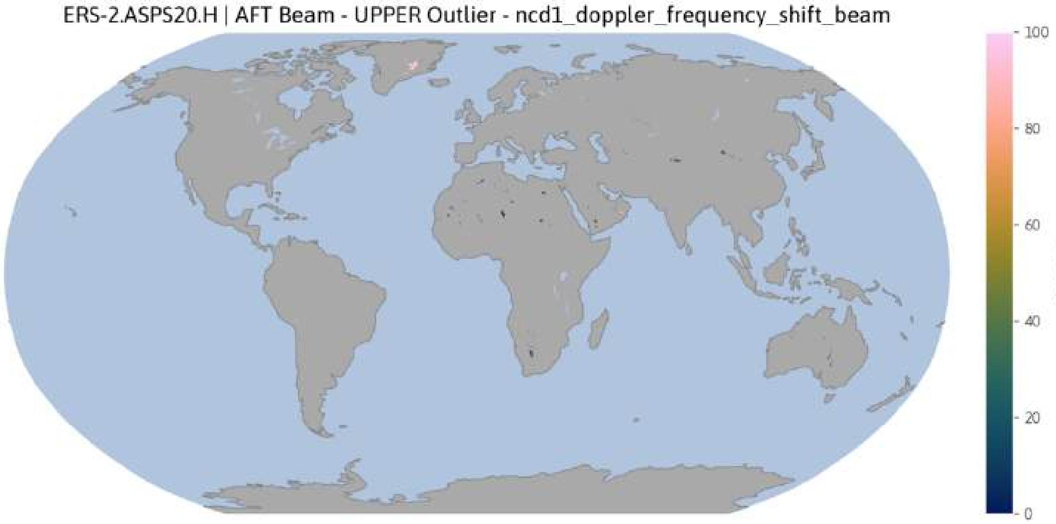

Figure A.60: Upper outliers (in percent) that have been flagged by the node confidence data field "Doppler Frequency Shift flag" for the Aft beam in `ERS-2.ASPS20.H`.

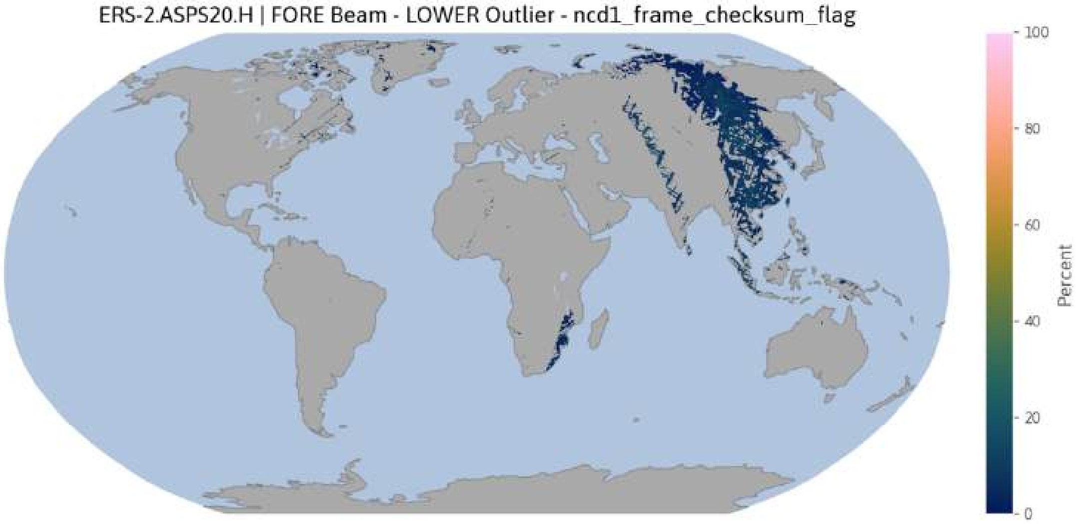

Figure A.61: Lower outliers (in percent) that have been flagged by the node confidence data field "Frame Checksum flag" for the Fore beam in `ERS-2.ASPS20.H`.

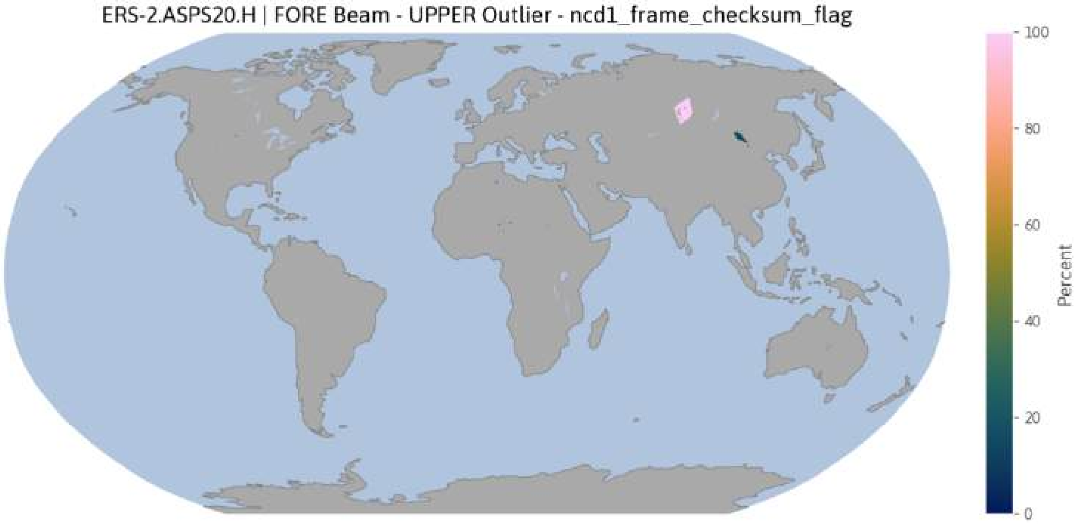

Figure A.62: Upper outliers (in percent) that have been flagged by the node confidence data field "Frame Checksum flag" for the Fore beam in `ERS-2.ASPS20.H`.

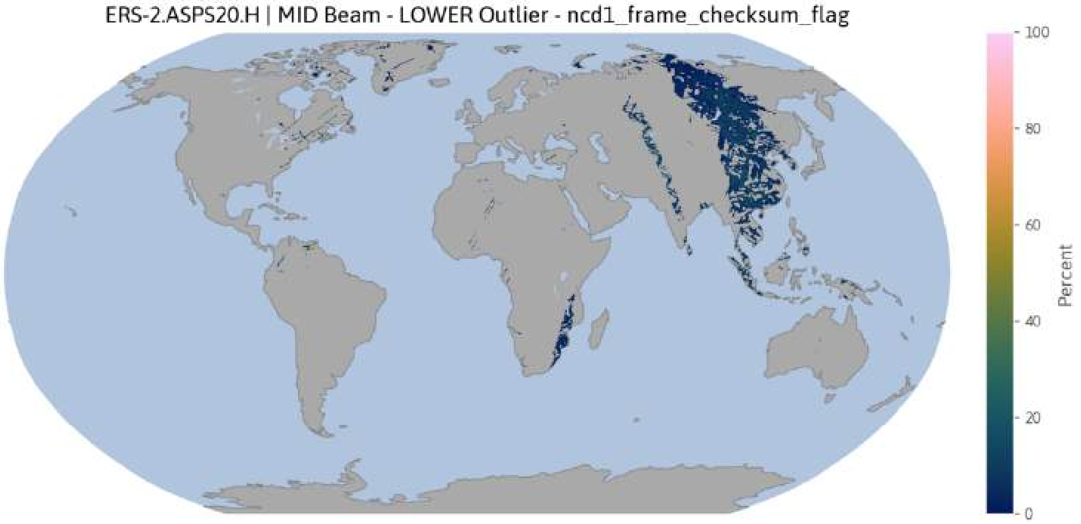

Figure A.63: Lower outliers (in percent) that have been flagged by the node confidence data field "Frame Checksum flag" for the Mid beam in `ERS-2.ASPS20.H`.

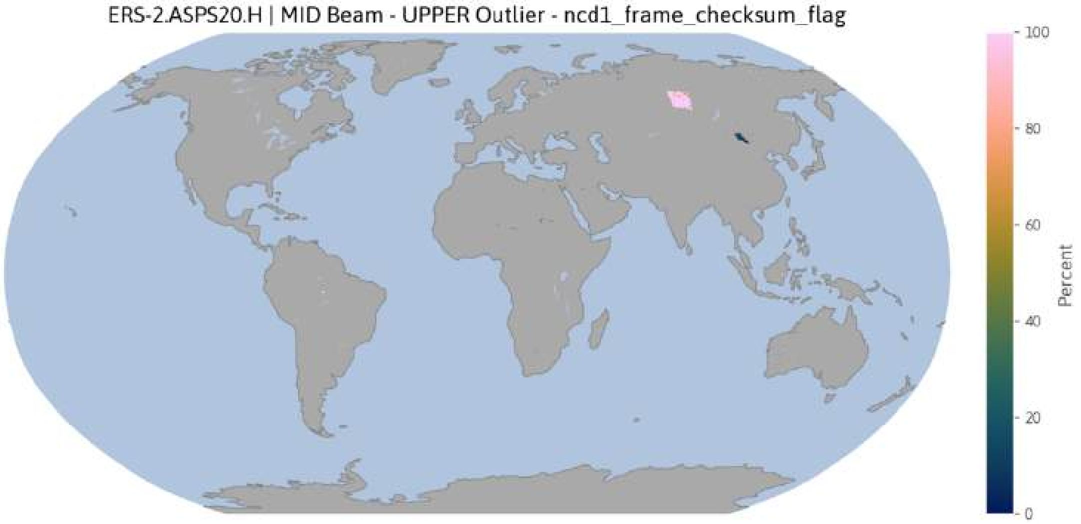

Figure A.64: Upper outliers (in percent) that have been flagged by the node confidence data field "Frame Checksum flag" for the Mid beam in `ERS-2.ASPS20.H`.

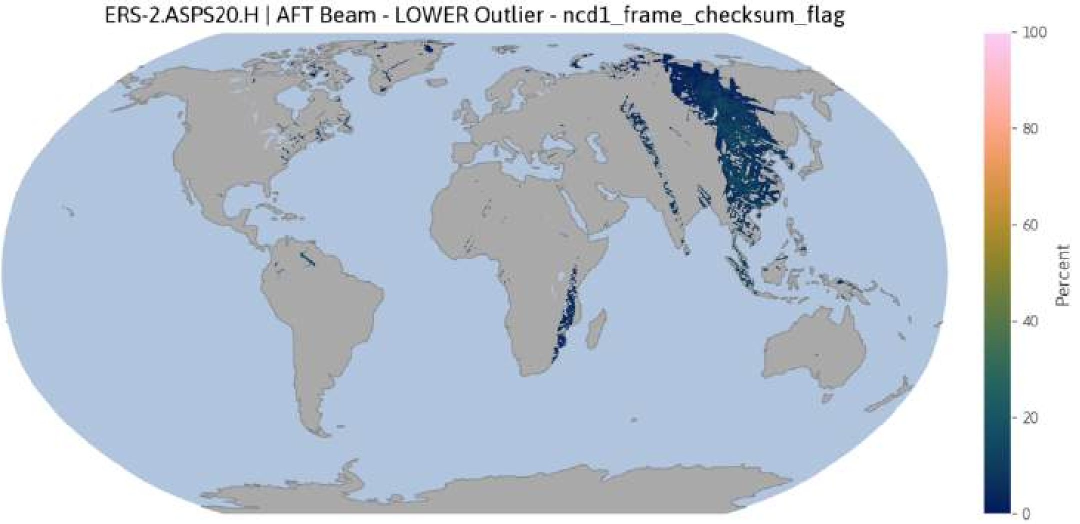

Figure A.65: Lower outliers (in percent) that have been flagged by the node confidence data field “Frame Checksum flag” for the Aft beam in `ERS-2.ASPS20.H`.

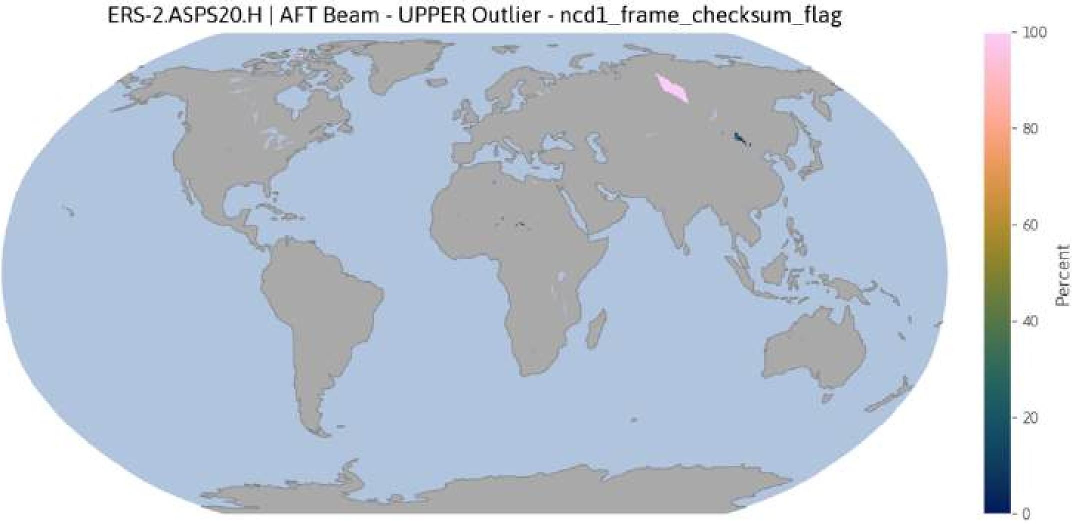

Figure A.66: Upper outliers (in percent) that have been flagged by the node confidence data field “Frame Checksum flag” for the Aft beam in `ERS-2.ASPS20.H`.

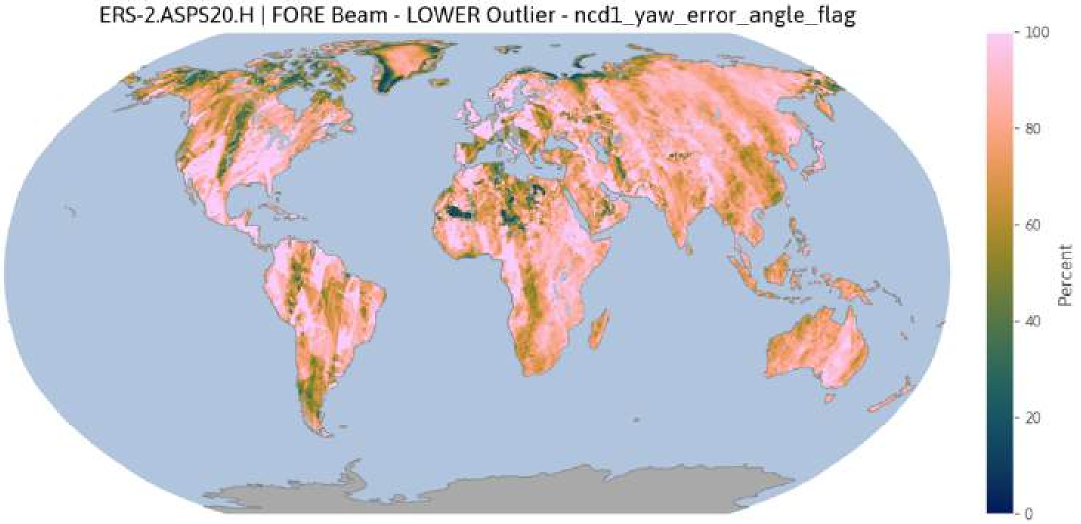

Figure A.67: Lower outliers (in percent) that have been flagged by the node confidence data field “Yaw Error Angle flag” for the Fore beam in `ERS-2.ASPS20.H`.

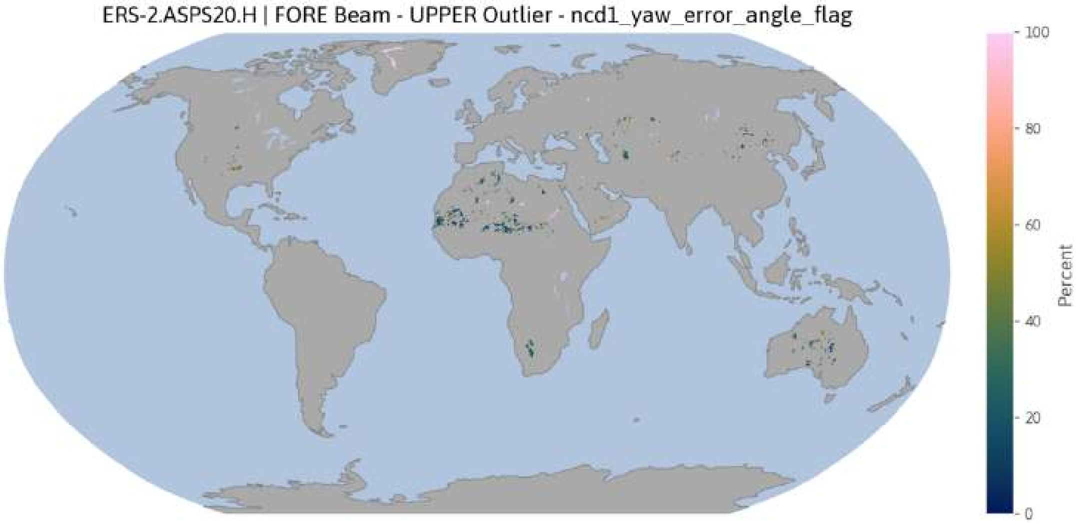

Figure A.68: Upper outliers (in percent) that have been flagged by the node confidence data field “Yaw Error Angle flag” for the Fore beam in `ERS-2.ASPS20.H`.

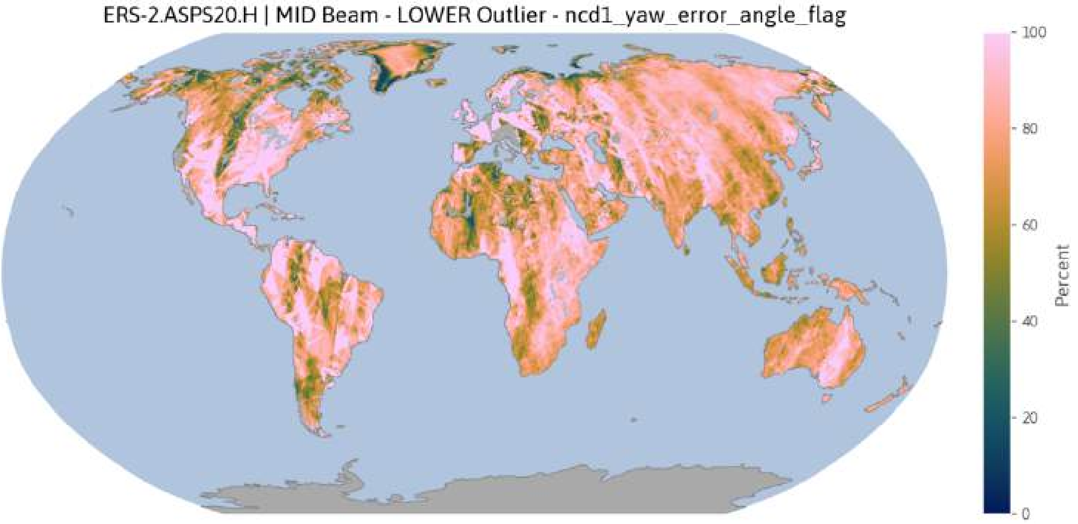

Figure A.69: Lower outliers (in percent) that have been flagged by the node confidence data field “Yaw Error Angle flag” for the Mid beam in `ERS-2.ASPS20.H`.

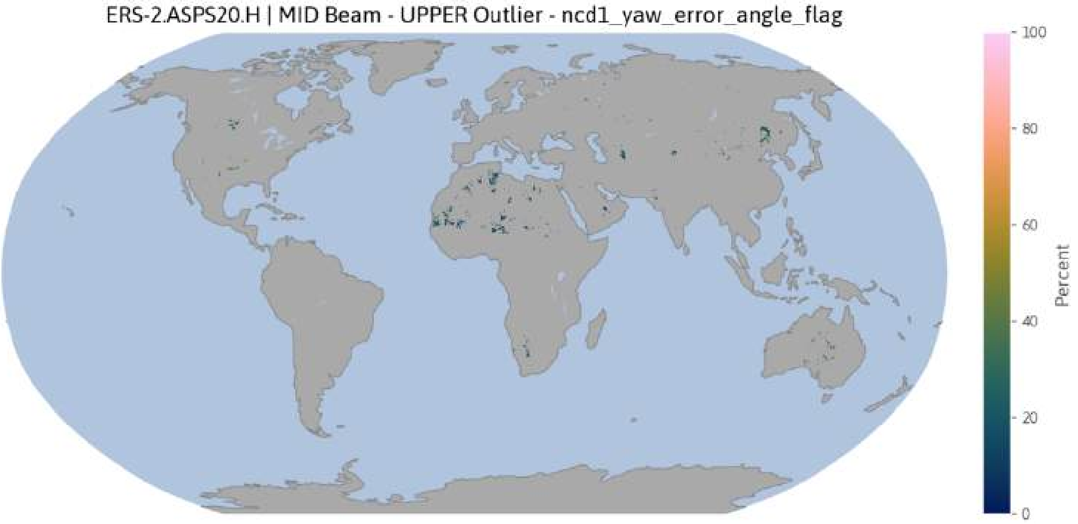

Figure A.70: Upper outliers (in percent) that have been flagged by the node confidence data field “Yaw Error Angle flag” for the Mid beam in `ERS-2.ASPS20.H`.

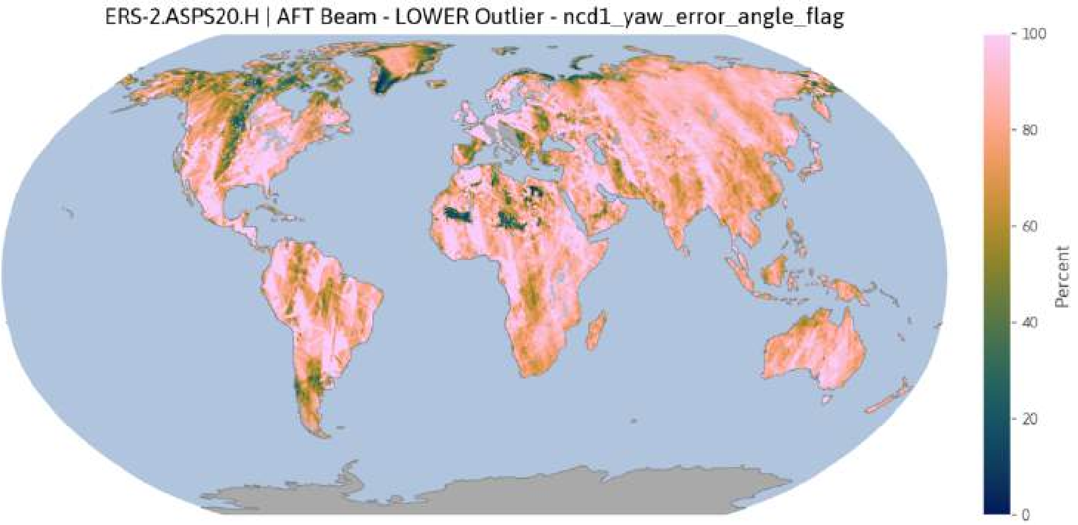

Figure A.71: Lower outliers (in percent) that have been flagged by the node confidence data field “Yaw Error Angle flag” for the Aft beam in `ERS-2.ASPS20.H`.

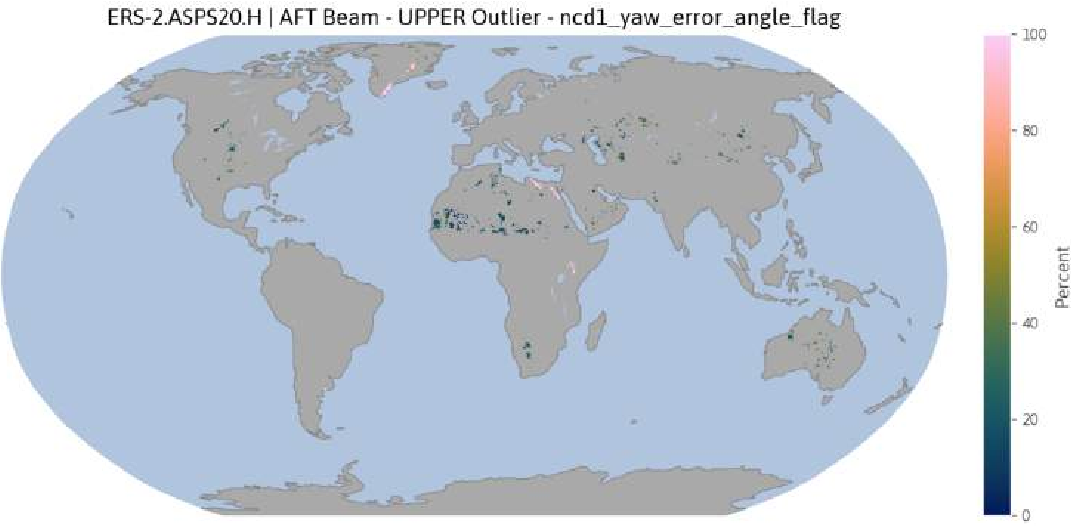

Figure A.72: Upper outliers (in percent) that have been flagged by the node confidence data field “Yaw Error Angle flag” for the Aft beam in `ERS-2.ASPS20.H`.

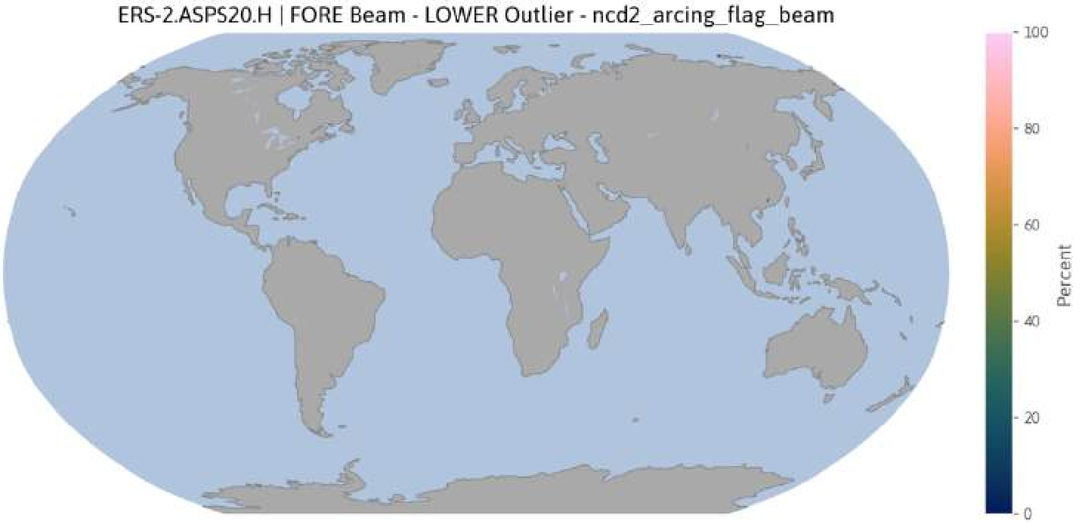

Figure A.73: Lower outliers (in percent) that have been flagged by the node confidence data field “Arcing flag” for the Fore beam in `ERS-2.ASPS20.H`.

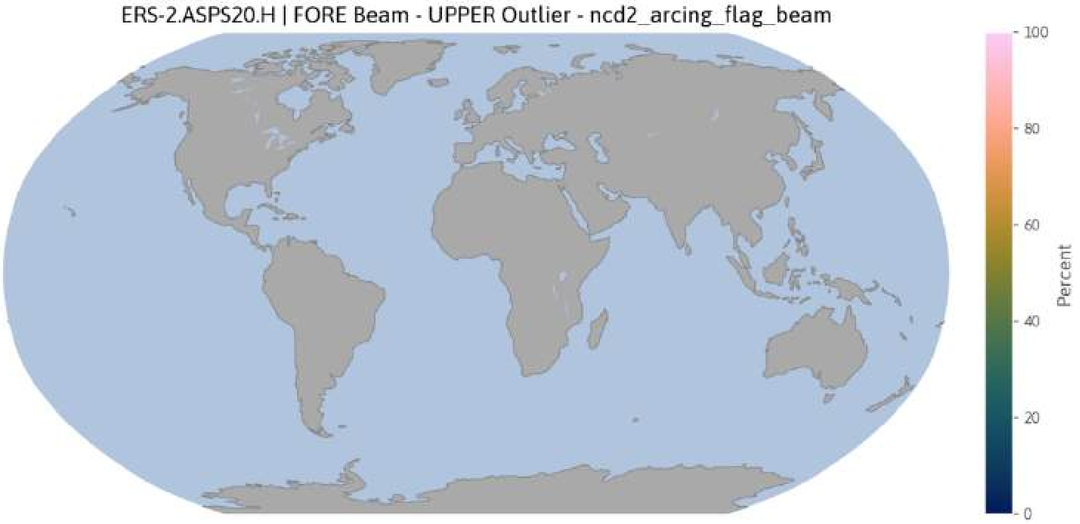

Figure A.74: Upper outliers (in percent) that have been flagged by the node confidence data field “Arcing flag” for the Fore beam in `ERS-2.ASPS20.H`.

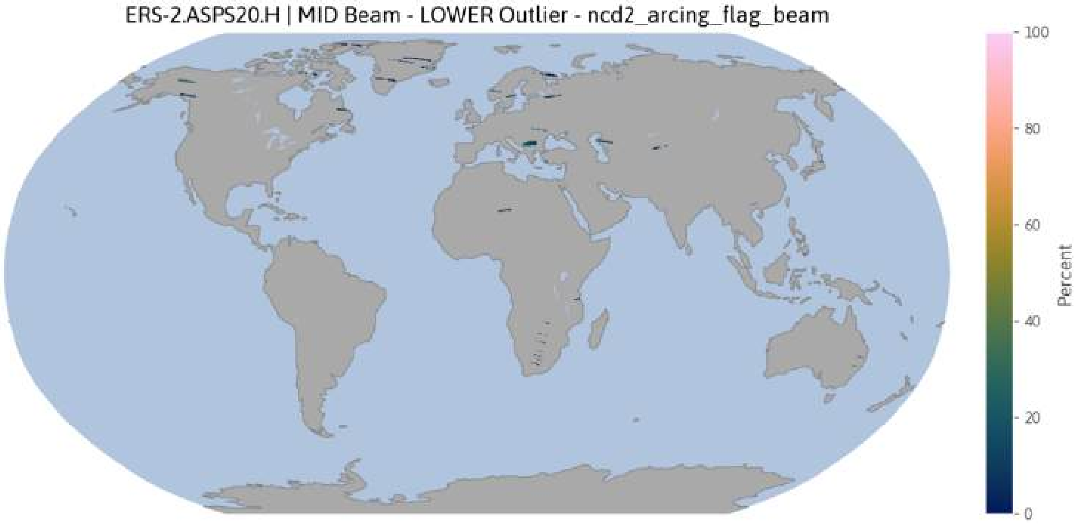

Figure A.75: Lower outliers (in percent) that have been flagged by the node confidence data field "Arcing flag" for the Mid beam in `ERS-2.ASPS20.H`.

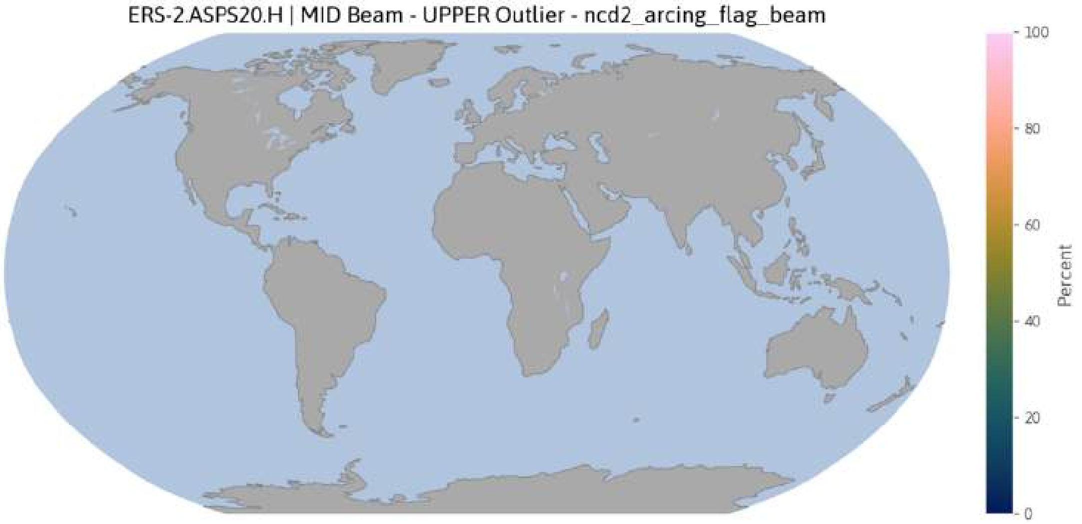

Figure A.76: Upper outliers (in percent) that have been flagged by the node confidence data field "Arcing flag" for the Mid beam in `ERS-2.ASPS20.H`.

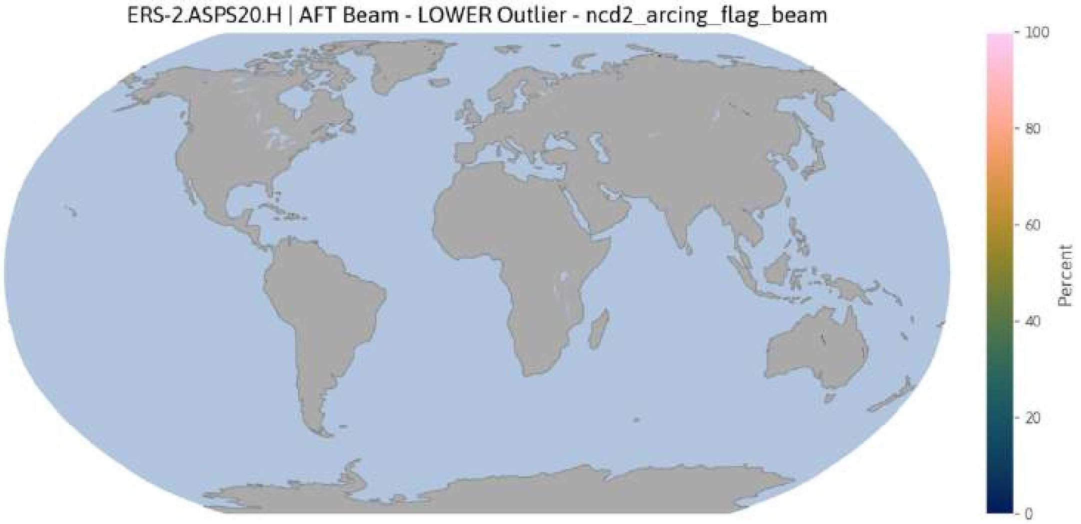

Figure A.77: Lower outliers (in percent) that have been flagged by the node confidence data field “Arcing flag” for the Aft beam in `ERS-2.ASPS20.H`.

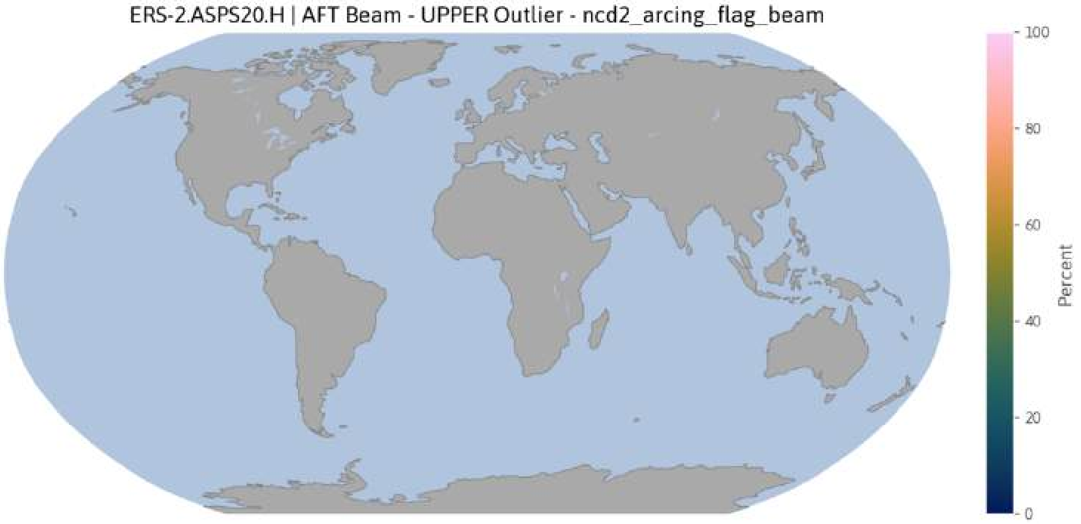

Figure A.78: Upper outliers (in percent) that have been flagged by the node confidence data field “Arcing flag” for the Aft beam in `ERS-2.ASPS20.H`.

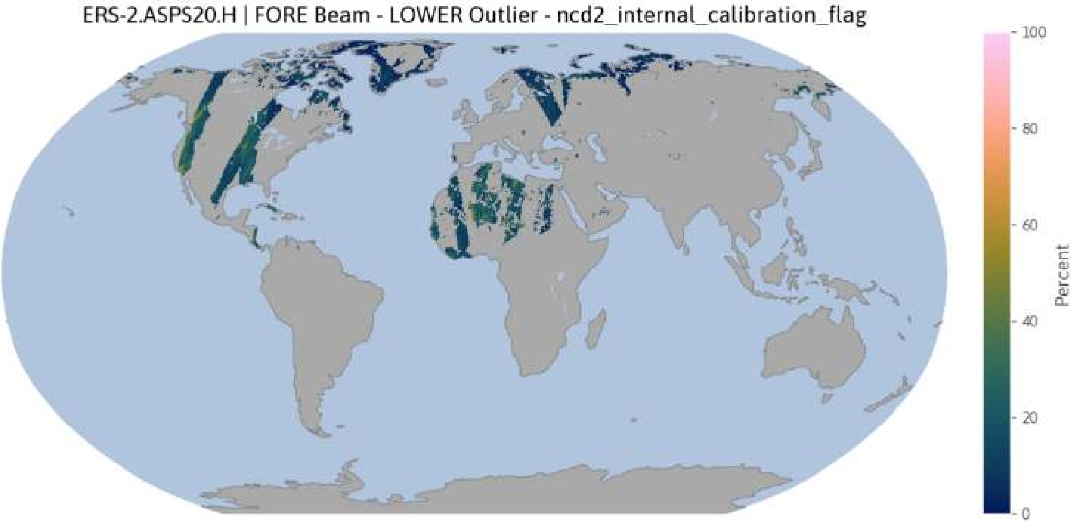

Figure A.79: Lower outliers (in percent) that have been flagged by the node confidence data field “Internal calibration flag” for the Fore beam in `ERS-2.ASPS20.H`.

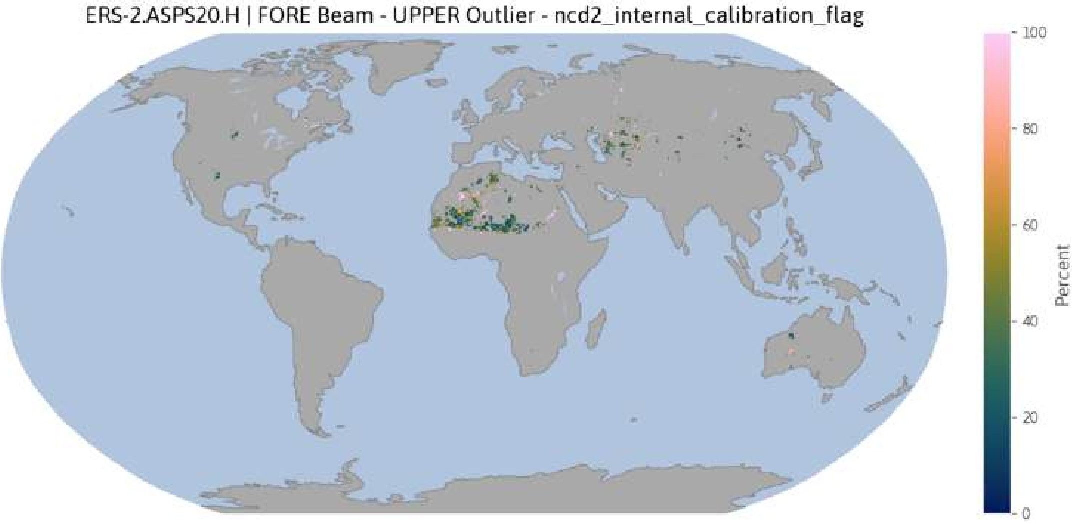

Figure A.80: Upper outliers (in percent) that have been flagged by the node confidence data field “Internal calibration flag” for the Fore beam in `ERS-2.ASPS20.H`.

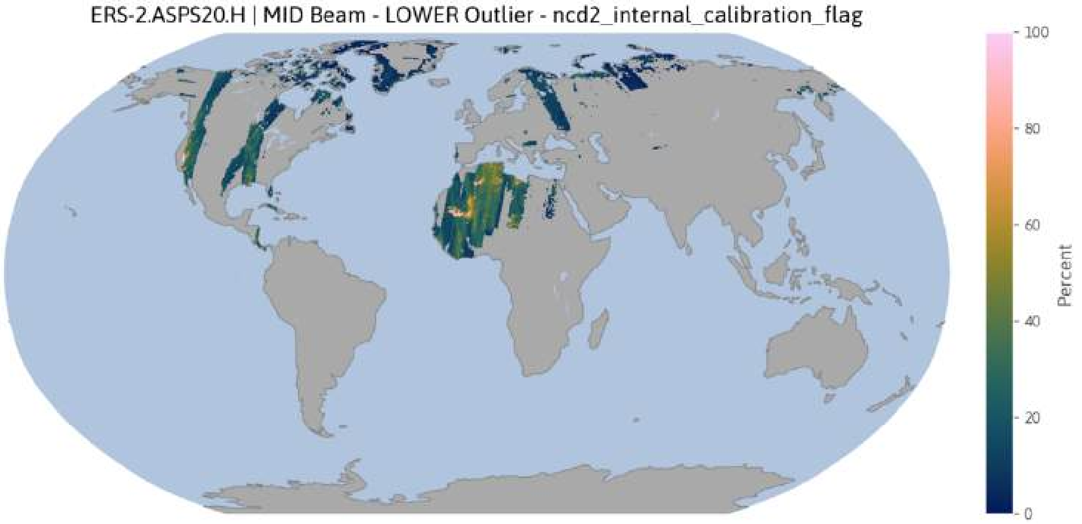

Figure A.81: Lower outliers (in percent) that have been flagged by the node confidence data field "Internal calibration flag" for the Mid beam in `ERS-2.ASPS20.H`.

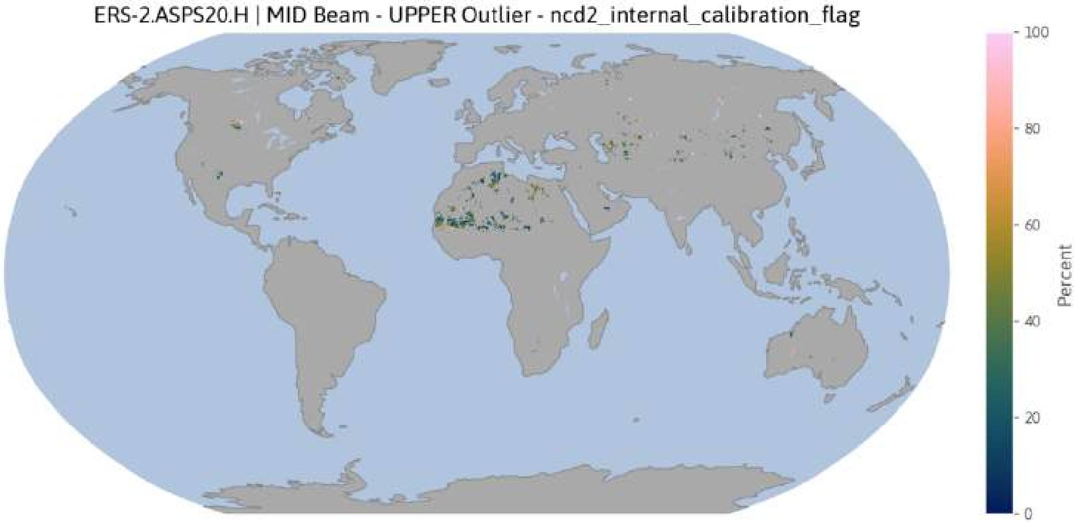

Figure A.82: Upper outliers (in percent) that have been flagged by the node confidence data field "Internal calibration flag" for the Mid beam in `ERS-2.ASPS20.H`.

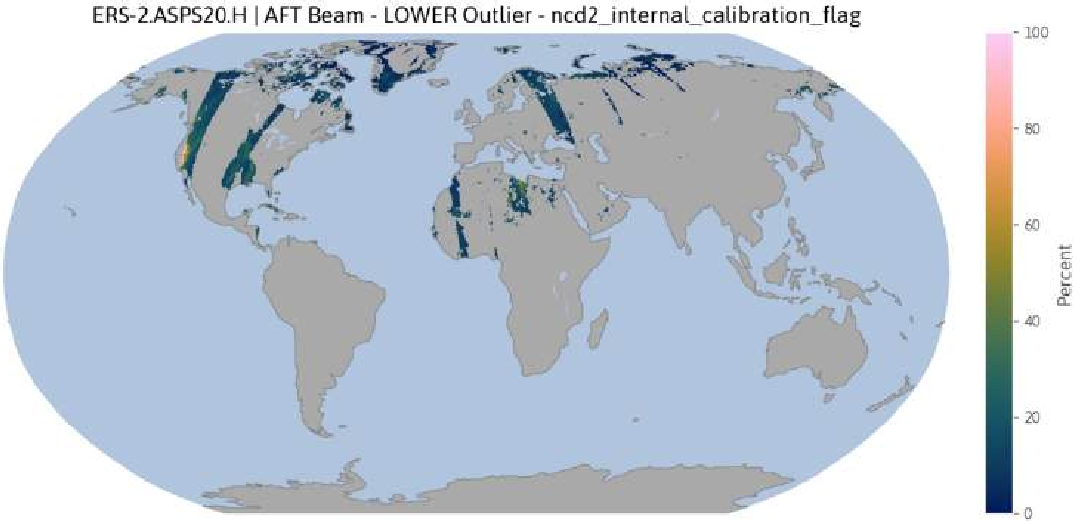

Figure A.83: Lower outliers (in percent) that have been flagged by the node confidence data field "Internal calibration flag" for the Aft beam in `ERS-2.ASPS20.H`.

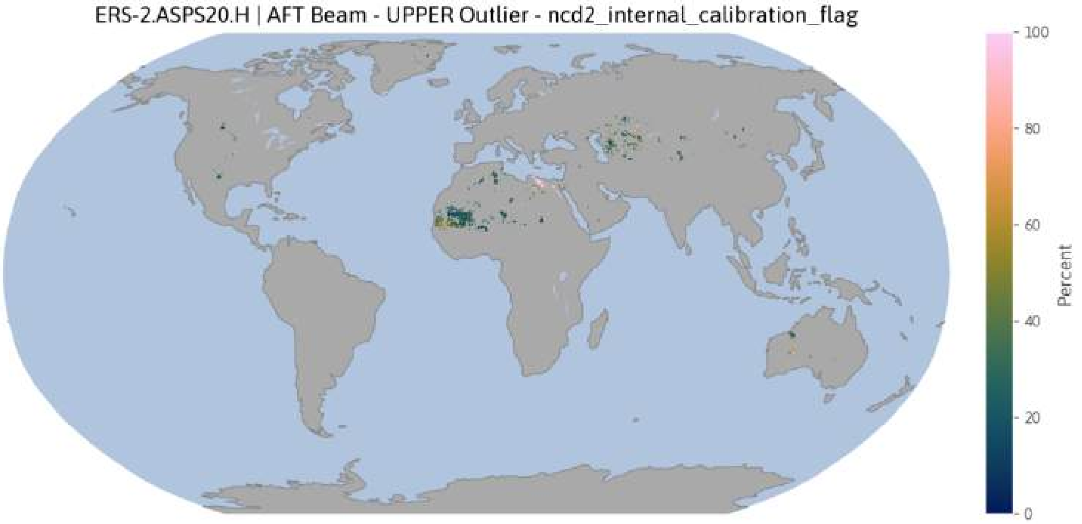

Figure A.84: Upper outliers (in percent) that have been flagged by the node confidence data field "Internal calibration flag" for the Aft beam in `ERS-2.ASPS20.H`.